University of Stavanger

Faculty of Science and Technology

MASTER'S THESIS

Study program: MSc in Petroleum Engineering Specialization: Well Engineering	Spring semester, 2015 Open access
Author: Shreyansh Divyankar	…… (Author's signature)
Faculty supervisor: Jan Aage Aasen External supervisor(s):	
Thesis title: Horizontal well oriented perforation skin factor: A numerical analysis of skin factor reduction by off-setting perforation phasing from 360^{O} to $350^{O}/10^{O}$	
Credits (ECTS): 30	
Key words: Horizontal well Oriented perforation Skin factor reduction Finite element modelling Isotropic reservoir Anisotropic reservoir	Pages: 60 + enclosure: 116 Stavanger, June 15, 2015

Acknowledgements

First and foremost, I wish to express my sincere gratitude to my faculty supervisor Dr. Jan Aage Aasen. His support, guidance and constant motivational feedback has been instrumental in seeing this work to fruitition.

It has been a real pleasure working under his supervision and I would like to thank him for his patience and input pertaining to understanding of the problem statement, research methodolgy and analysis of the simulation results.

I would like to use the opportunity to thank the technical faculty at the department of Drilling Engineering. I have had the privelage of receiving lectures from a truly remarkable team of academic faculty and their advices and suggestions significantly contributed to the formulation and outcome of this thesis.

I thank my colleagues Mr. Velarasan Masilamani for his help with the finite element modeling software and Ms. Ekaterina Wiktorski for her valuable assistance with linear regression techniques. I would also like to thank Mr. Jaspreet Singh Sachdeva for his valuable input while compiling the report.

I would like to thank Ms. Marthe Seland Andersson for being a constant source of motivation, support and morale.

The most special thanks goes to my family. Their confidence and trust in me has been a source of motivation over the years and is a driving force towards the successful completion of this academic program.

Abstract

Formation damage has been a major topic of research and cased and perforated skin factor quantification has received significant attention which has resulted in some truly remarkable publications. The inherent importance of the skin factor in analysing completion efficiency makes it a relevant topic of research and hence this thesis work was undertaken to better understand the effects of orienting the perforations from 360^O to $350^O/10^O$ on the perforation skin factor.

One of the practical reasons for off-setting the perforations is to provide more space for explosives and hence achieve deeper formation penetration. However, as shown in this work though numerical methods, orienting the perforations has additional significant effects in terms of perforation skin factor reduction in horizontal wells. This reduction effect is observed in both isotropic and anisotropic reservoir settings and is more pronounced for configurations involving smaller diameter boreholes and shorter perforation penetration.

Detailed survey of pertinent literature which forms the foundation of cased and perforated skin factor analysis is presented at the outset and this is used for establishing the theoretical basis for analysing the results obtained from finite element modeling. The results from the finite element modeling are presented subsequently and the same is used to derive conclusions regarding the perforation skin factor reduction effect due to off-setting the perforations. Recommendations for refining the work and future possibilities for expanding the results presented herein are also included. Details of the finite element modeling procedure are presented in a comprehensive manner for the interested reader.

As a part of the thesis work, detailed numerical simulation runs were carried out for three borehole sizes, wherein each borehole size was assigned three different values of perforation tunnel length. Three different types of reservoir setting were applied to study the behaviour of perforation skin factor, depending on the ratio of horizontal to vertical permeability. A total of fifty-four (54) simulation cases were rigourously developed and the output results from all these cases are presented in appendices.

Table of Contents

List of Figures

List of Tables

Chapter 1: Introduction and problem statement

Oriented perforations are commonly used in horizontal wells as a sand prevention measure. In the public domain there is a good perforation skin factor model available. However, this model is limited to in-line oriented perforations. Commonly the shots are fired upwards at 350°/10° phasing and three reasons for this practice can be mentioned:

1. The 20° degree offset between each perforation tunnel gives reduced flow restriction (reduced perforation skin) compared to perforations arranged in a straight line
2. The staggered pattern provides additional space for the shaped charges (more explosives)
3. Extra space between each perforation tunnel (less risk for sand collapse)

The objective of the thesis work is to develop a horizontal well perforation skin factor correlation for 350°/ 10° phasing. In the original vertical perforation skin factor FEM was used to generate the needed coefficient for a semi analytical solution. The same technique was employed to obtain the horizontal well perforation skin factor described above. The intention is to use a similar approach for the new correlation that will be produced as a part of the thesis work.

The primary aim of the thesis is to obtain a correlation for the horizontal perforation skin for 350°/10° phasing based on the zero -degree phasing model published by Furui et al (2002). The vertical fracture solution by Pratts (1961) gives an overall perforation skin factor for the zero - degree case (inline perforations):

$S_{360} = Ln\ (4r_W / L_P)$

The objective is to calculate the (two - dimensional) flow into two vertical fractures spaced twenty degrees apart using the ANSYS finite element model (FEM). The thermal elements in ANSYS have an option that allows the element to model steady -state fluid flow through porous media. With this option the thermal parameters are interpreted as analogous flow parameters. The simulation of an anisotropic system is readily performed by assigning different values of permeability in the x, y and z directions. The output from ANSYS gives $S_{350/10}$.

From experience data and physical reasoning we know that 350°/10° phasing decreases the skin compared to inline perforations. The productivity gain going from inline perforation to 350°/10° phasing is approximately described as:

$\Delta S = S_{360} - S_{350/10}$

This is the desired result and it is expected to be a function of L_P/r_W and anisotropy ratio.

Chapter 2: Literature review and theoretical description of model

The region in the immediate vicinity of the borehole is critical in terms of well performance. Any permeability changes in the said region can have far reaching consequences based on the nature and magnitude of the permeability changes mentioned herein. A zone of reduced permeability is caused due to phenomenon related to drilling damage (e.g. drilling mud invasion) and completion damage (e.g. crushed zone due to perforation or plugged sand management equipment). In many cases the permeability can actually be improved from its initial or damaged state and this forms much of the rationale behind stimulation jobs being carried out today. Skin factor is a very useful analytical tool which is used to quantify (in dimensionless terms) these changes in the critical "near borehole" region and is defined in the Schlumberger oilfield glossary as follows:

'A dimensionless factor calculated to determine the production efficiency of a well by comparing actual conditions with theoretical or ideal conditions. A positive skin value indicates some damage or influences that are impairing well productivity. A negative skin value indicates enhanced productivity, typically resulting from stimulation'

2.1: Analytical equations for quantifying skin factor

The mathematical equation for radial pressure distribution caused by an oil well which is draining an infinite reservoir is given by Golan and Curtis (2003) as following:

$$p\,(r) = p_{wf} + \frac{141.2 q_o \mu_o B_o}{kh} \ln\left({}^{r}/_{r_w}\right) \ldots\ldots\ldots\ldots\ldots\ldots\ldots\ldots\ldots\ldots\ldots\ldots \text{Eq (1)}$$

Where:

q_o = oil flow rate in STB/D

μ_o = oil viscosity in cp

B_o = Oil Formation Value Factor, reservoir bbl/STB

k = permeability in mD

h = pay zone thickness, in feet

p and p_{wf} = reservoil and well flowing pressures, in psia

r and r_w = reservoir and well radius, in feet

This equation is developed using several simplifying assumptions, which are listed as follows:

- Reservoir has uniform thickness
- The well crosses the entire reservoir thickness
- Flow is assumed to be ideal
- Formation is assumed to be homogeneous (isotropic permeability) throughout the reservoir
- Uncased and ideally clean wellbore

- Darcy`s law should be valid for fluid flow modeling in the entire system

Using the same simplifying assumptions, Golan and Curtis (2003) conclude that the equation for pseudo-steady state flow can be written in terms of $\Delta P = p_R - p'_{wf}$, where p'_{wf} indicates the wellbore flowing pressure for the case of an ideal well producing under assumption of ideal radial model and is as follows:

$$p(r) - p'_{wf} = \frac{141.2 q_o \mu_o B_o}{kh} \ln[(r_e/r_w) - 0.75] \ldots\ldots\ldots\ldots\ldots\ldots\ldots\ldots \text{Eq (2)}$$

However, a real well will seldom produce under the conditions of the ideal well model as the permeability in the vicinity of the borehole is altered due to various operations carried out over the life cycle of the well. As discussed earlier, these permeability changes can be either detrimental or beneficial. In addition, changes from ideal behavior are also caused due to flow restrictions in the perforations and convergence to perforations, which in diameter is just fraction of net pay zone. The overall result as concluded by Golan and Curtis (2003) is that the pressure distribution in an actual well differs from that in the ideal well, difference being larger near the wellbore and diminishes away from the wellbore as the radius approaches reservoir radius.

This additional pressure drop between ideal and non ideal wellbores can be expressed as $\Delta p_s = p'_{wf} - p_{wf}$ and this is usually termed as pressure loss due to 'skin'. A dimensionless skin factor s, proportional to Δp_s can be mathematically defined as:

$$S = \frac{kh}{141.2 q_o B_o \mu_o} \Delta p_s \ldots\ldots\ldots\ldots\ldots\ldots\ldots\ldots\ldots\ldots\ldots\ldots\ldots\ldots\ldots\ldots \text{Eq (3)}$$

$$\text{Or, } \Delta p_s = 141.2 \frac{q_o B_o \mu_o}{kh} S \ldots\ldots\ldots\ldots\ldots\ldots\ldots\ldots\ldots\ldots\ldots\ldots\ldots\ldots\ldots\ldots \text{Eq (4)}$$

Adding the equations for pressure loss due to skin factor and pseudo steady state pressure distribution, i.e. Eq (2) + Eq (4) incorporates the dimensionless skin factor in the flow equation:

$$p(r) - p_{wf} = \frac{141.2 q_o \mu_o B_o}{kh} \ln[(r_e/r_w) - 0.75 + S] \ldots\ldots\ldots\ldots\ldots\ldots\ldots\ldots \text{Eq (5)}$$

Rearranging the previous equation and solving for rate gives:

$$q_o = \frac{kh\,(p_R - p_{wf})}{141.2 \mu_o B_o [\ln(r_e/r_w) - 0.75 + S]} \ldots\ldots\ldots\ldots\ldots\ldots\ldots\ldots\ldots\ldots\ldots\ldots \text{Eq (6)}$$

Skin can also be included in to the analysis of flow efficiency, which is defined as the ratio between actual and ideal flow rates. Mathematically it can conveniently be expressed as:

$$\text{Flow Efficiency} = E_F = \frac{\ln(r_e/r_w) - 0.75}{\ln(r_e/r_w) - 0.75 + S} \ldots\ldots\ldots\ldots\ldots\ldots\ldots\ldots\ldots\ldots \text{Eq (7)}$$

2.2: Pressure drop due to skin factor in horizontal wells

Examination of the equation for Δp_s readily reveals that pressure drop due to skin is a function of q/h, i.e. rate of fluid entry per unit length of wellbore. Hence, for horizontal wells we can state that pressure drop due to skin can be given by:

$$\Delta p_s = 141.2 \frac{q_o B_o \mu_o}{kL} S \ldots\ldots\ldots\ldots\ldots\ldots\ldots\ldots\ldots\ldots\ldots\ldots\ldots\ldots\ldots\ldots\ldots\ldots \text{Eq (8)}$$

Parameter L is the length of the horizontal section. It is stated by Joshi (1990) that for the same skin factor, additional pressure drop in a horizontal well is much lower than that in a vertical well and this can be attributed to low fluid entry per unit length L of wellbore. It is also important to note that the permeability being used in horizontal well calculations is the effective reservoir permeability and is given by $K = \sqrt{K_v K_H}$ (K_V is vertical permeability and K_H is horizontal permeability).

2.3: Skin factor in cased and perforated wells

Cased and perforated wells have become one of the most common completion techniques due to the inherent control they provide over oil and gas production and mitigation of problems like sand production. Analysis of productivity and skin factor in cased and perforated wells is significantly more complex than the same in openhole completions, primarily due to the 3 dimensional nature of the flow. Other complexities arise from the following factors:

- The spiral distributions of perforations in the vertical direction, creating a 3D convergence effect
- The presence of the wellbore, which acts as a barrier to flow in to perforations in itself

Much work has been done in this field and two papers published clearly stand out. “Semi analytical productivity models for perforated completions” by M. Karakas and S.M. Tariq presents a reliable cased and perforated skin model for vertical wells and much of the approach followed by the authors has been applied in this work. “A new skin factor model for perforated horizontal wells” published by K. Furui, D. Zhu and A.D. Hill furthers the work started by M. Karakas and S.M. Tariq by presenting a skin factor model for horizontal wells. They have also incorporated the effect of direction of perforations with respect to maximum permeability direction. Both these models report the results for in-line perforations. However, it is an industry practice to offset the perforations by 20^O. This work takes inspiration and guidance from the abovementioned papers to arrive at a model for $350^O/10^O$ perforation skin factor. In the upcoming sections, the results reported by Karakas and Tariq (1991) and Furui et al (2002) will be briefly discussed before laying out the theoretical groundwork of this thesis.

2.3.1: Cased & perforated skin factor model developed by Karakas and Tariq (1991)

This section refers to SPE paper #18247 titled “semi analytical productivity models for perforated completions” authored by Karakas and Tariq (1991) and published in SPE Production Engineering in February 1991. The authors have utilized finalized element modeling for solution of the second order partial differential equation which gives the pressure distribution for various well and perforation configurations. In their paper Karakas and Tariq (1991) have first considered the simpler 2D steady state flow problem, which provides a reasonable mathematical model under the assumption of very high perforation density/ low perforation spacing. Using an accurate 2D finite element model, the authors establish the dependency of skin factor on angular perforation phasing, perforation penetration and well radius. The wellbore effect is quantified in terms of a wellbore

pseudo-skin. Nomenclature to be used subsequently in this section (which has not been defined previously) is as follows:

Ɵ = angle between two successive perforations

n_S = number of perforations per foot of the formation, inversely proportional to perforation shot density h

h = 1/ n_S

Assumptions regarding the porous media and fluid (oil) contained therein are as follows:

- Reservoir is made up of single layer cylindrical formation with constant thickness
- Reservoir fluid (oil) is single phase and incompressible (density = constant)
- Flow from reservoir to well is laminar
- The reservoir radius is significantly larger than the perforation penetration radius
- Anisotropy ratio is constant throughout the reservoir

With these assumptions, the task at hand is reduced to solving the steady state potential equation with suitable boundary conditions. The authors assume constant pressure at reservoir radius and inside the well as outer and inner boundary conditions. The pressure drop inside the perforation is assumed to be negligible. The steady state flow in to the perforation is given by Karakas and Tariq (1991) as following:

$$q_P = \frac{2\pi k h_t((p_e - p_w)}{\mu[ln(r_e/r_w) + S_t]} \dots\dots\dots\dots\dots\dots\dots\dots\dots\dots\dots\dots\dots\dots\dots\dots\dots\dots\dots\dots\dots . \text{Eq (9)}$$

S_t is the total skin factor in the abovementioned formula. It is a combination of effects due to perforation and any other permeability damage to the formation and is expressed as $S_t = S_p + S_{dp}$. S_p indicates the relative efficiency of a perforated well compared to that of an ideal openhole completion (geometrical skin in an undamaged formation) whereas the damage skin factor S_{dp} is an estimate of treatable skin (primarily due to damage caused during drilling and completion activities) in perforated completions. S_p can be expressed by the following mathematical expression used by Furui et al (2002):

$$S_P = \left(\frac{J_O}{J_P} - 1\right) ln(r_b/r_w) \dots\dots\dots\dots\dots\dots\dots\dots\dots\dots\dots\dots\dots\dots\dots\dots\dots\dots \text{Eq (10)}$$

J_O = Productivity Index of ideal openhole completion

J_P = Productivity index estimated by finite element modeling (FEM) simulator for the specific perforation condition

r_b = Radius where effect of perforation is not felt (taken as 32” in this thesis work)

r_w = Well radius

Dimensionless parameters introduced by Karakas and Tariq (1991) are as follow:

$$\text{Dimensionless perforation spacing} = h_D = (h/L_p)\sqrt{K_H/K_V}$$

$$\text{Dimensionless perforation radius} = r_{pD} = \left(r_p/2h\right)\left(1+\sqrt{K_V/K_H}\right)$$

$$\text{Dimensionless well radius} = r_{wD} = r_w/(L_P + r_w)$$

The authors obtained a 2D solution by neglecting all vertical flow in to the perforations (reasonable assumption to make if the perforation shot density is sufficiently high), thus making the flow in to perforations independent of vertical coordinates. Using the stated plane flow conditions and utilizing the effective well radius concept developed by Prats (1961) for vertically fractured wells, the overall perforation skin can be expressed by:

$$S_P \approx S_H = \ln\left(\frac{r_W}{r_{we}}\right) \ldots\ldots\ldots\ldots\ldots\ldots\ldots\ldots\ldots\ldots\ldots\ldots\ldots\ldots\ldots\ldots\ldots\ldots\ldots\ldots \text{Eq (11)}$$

The effective well radius, r_{we} as defined by Prats [6] is given by:

$$r_{we}(\theta) = \begin{cases} {}^1\!/_4\, L_P \text{ if } \theta = 0 \text{ degree} \\ \alpha_\theta (r_w + L_P) \text{ otherwise} \end{cases}$$

In the paper, values of α_Θ were obtained by finite element simulation for all phasing except 0 and 360 degrees. It is important to note that equation 11 is only valid for negligible wellbore radius (extremely small r_{wD}). In the presence of a normal borehole, the wellbore blockage effect can be quite significant for certain perforation geometries and hence the simulated S_P will always be higher than the calculated S_H. They derived the mathematical equation for wellbore pseudo-skin by subtracting the value of S_H from the overall perforation skin factor S_P (obtained by FEM) and the equation is as follows:

$$S_{wb}(\theta) = C_1 exp[C_2(\theta) r_{wD}] \ldots\ldots\ldots\ldots\ldots\ldots\ldots\ldots\ldots\ldots\ldots\ldots\ldots\ldots\ldots\ldots\ldots\ldots\ldots\ldots \text{Eq (12)}$$

Values of C_1 and C_2 as functions of perforation phasing are presented as Table #2 in the original paper presented by Karakas and Tariq (1991).

The vertical convergent flow in to perforations causes an additional pressure drop and therefore adversely affects productivity. This additional pressure drop has been quantified as a vertical pseudo-skin (S_V) by the authors. Assuming a small dimensionless well radius, the perforation skin factor for the 3D case can be expressed as:

$$S_{P,3D} \approx S_H + S_V \ldots\ldots\ldots\ldots\ldots\ldots\ldots\ldots\ldots\ldots\ldots\ldots\ldots\ldots\ldots\ldots\ldots\ldots\ldots\ldots \text{Eq (13)}$$

$S_{P,\,3D}$ was obtained through FEM by the authors. The dependence of S_V on other dimensionless parameters can be easily determined by subtracting S_H (obtained from equation 11) from the simulated $S_{P,\,3D}$. Based on this, the authors present a mathematical relation for approximating vertical pseudo-skin as a function of dimensionless spacing and radius as follows:

$$S_V = 10^a h_D^{b-1} r_{pD}^b \ldots\ldots\ldots\ldots\ldots\ldots\ldots\ldots\ldots\ldots\ldots\ldots\ldots\ldots\ldots\ldots\ldots\ldots\ldots\ldots \text{Eq (14)}$$

Where $a = a_1 log_{10} r_{pD} + a_2$ and $b = b_1 r_{pD} + b_2$. Table #4 in the paper presents all values of a_1, a_2, b_1 and b_2. As expected, S_V increases with dimensionless perforation spacing and decreases with dimensionless perforation radius. They also report that major wellbore effects can be sufficiently accounted for by the 2D wellbore

pseudo-skin discussed in *Eq* (12). The paper also discusses other significant effects such as crushed zone effect, anisotropy effects, damaged zone effects etc., however since these topics are not being investigated in the current thesis work, they are not reviewed herein.

2.3.2: Cased and perforated skin factor model for horizontal wells developed by Furui et al (2002)

This section refers to the SPE Paper #77363 titled 'a new skin factor model for perforated horizontal wells' authored by Furui et al (2002) and presented at the SPE Annual Technical Conference and Exhibition, 29 September-2 October, San Antonio, Texas. The perforation skin model for vertical well presented in section 2.3.1 cannot account for the orientation of the horizontal well with the anisotropic permeability field and hence is not suitable for application to perforated horizontal completions. The horizontal well model presented by Furui et al (2002) proves that perforations have an inherent relation with the direction of maximum permeability, enhancing flow when normal and leading to significant positive skin if parallel to the maximum permeability direction. Nomenclature used in this section which has not been previously defined is as follows:

m = Number of perforations per plane, analogous to Θ in Karakas and Tariq model

K_x, K_y, K_z = Principal permeabilities in x, y and z axis

α = Perforation orientation with the direction of maximum permeability

Assumptions made regarding the porous media and the fluids are as follows:

- Steady state, viscous flow of incompressible single phase fluid (oil)
- Effect of gravity is negligible
- Fluid enters the well only through perforations
- Anisotropy is constant throughout the reservoir
- Pressure drop inside the perforations is negligible

The perforation skin factor S_p indicates the relative efficiency of a perforated well with an ideal openhole condition. FEM was used to solve the steady state pressure diffusivity equation for different perforation conditions under suitable inner and outer boundary conditions and the results were compared with the ideal openhole productivity to determine the perforation skin factor using *Eq* (10), i.e.,

$$S_P = \left(\frac{J_O}{J_P} - 1\right) ln(r_b/r_w)$$

Similar to Karakas and Tariq model, Furui et al (2002) divided the perforation skin factor in to three identifiable components:

$$S_P = S_{2D} + S_{wb} + S_{3D} \ldots\ldots\ldots\ldots\ldots\ldots\ldots\ldots\ldots\ldots\ldots\ldots\ldots\ldots\ldots \text{Eq (15)}$$

It is stated in the work of Furui et al (2002) and Prats (1961) that the 2D plane flow behavior is analogous to flow behavior in an infinite conductivity fractured well. For unidirectional perforation (m = 1), the similarity between fracture and high shot density perforation tunnels can be utilized and S_{2D} can be given by:

$$S_{2D} = \ln\left(\frac{4r_w}{l_P}\right) = \ln\left(\frac{4}{l_{pD}}\right) \text{ where } l_{pD} \text{ is } l_P/r_w \ldots\ldots\ldots\ldots\ldots\ldots\ldots\ldots\ldots\ldots \text{Eq (16)}$$

As *m* approaches infinity, effective well radius approaches to $r_w + l_p$ and the S_{2D} is given by:

$$S_{2D} = \ln\left(\frac{r_w}{r_w + l_p}\right) = \ln\left(\frac{1}{1 + l_{pD}}\right) \ldots\ldots\ldots\ldots\ldots\ldots\ldots\ldots\ldots\ldots\ldots\ldots\ldots \text{Eq (17)}$$

For other values of m, i.e. *m* = 2, 3, 4 etc. the value of S_{2D} should lie between those given by Eq (16) and Eq (17). Furui et al (2002) suggest the following interpolation:

$$S_{2D} = a_m ln\left(\frac{4}{l_{pD}}\right) + (1 - a_m) ln\left(\frac{1}{1 + l_{pD}}\right) \ldots\ldots\ldots\ldots\ldots\ldots\ldots\ldots\ldots \text{Eq (18)}$$

Numerical values of a_m are generated using numerical modeling and presented in Table #1 in the paper published by Furui et al (2002). For including effect of azinmuth of perforation tunnel with maximum permeability direction, the authors calculate effective perforation length and equivalent wellbore radius by applying coordinate transformation in equivalent isotropic space to obtain:

$$l_{p,eff} = l_p\left(\sqrt{k_y/k_z}\, sin^2\alpha + \sqrt{k_z/k_y}\, cos^2\alpha\right)^{0.5} \ldots\ldots\ldots\ldots\ldots\ldots\ldots\ldots\ldots\ldots \text{Eq (19)}$$

$$r_{w,eq} = \frac{r_w}{2}\left[\sqrt[4]{k_y/k_z} + \sqrt[4]{k_z/k_y}\right] \ldots\ldots\ldots\ldots\ldots\ldots\ldots\ldots\ldots\ldots\ldots\ldots\ldots\ldots \text{Eq (20)}$$

Substituting from Eq (19) and Eq (20) in Eq (16) (for *m* = 1) gives:

$$S_{2D} = ln\left(\frac{4}{l_{pD}}\right) + ln\left[\frac{\sqrt{k_y/k_z} + 1}{2\left(cos^2\alpha + \left(k_y/k_z\right)sin^2\alpha\right)^{0.5}}\right] \ldots\ldots\ldots\ldots\ldots\ldots\ldots \text{Eq (21)}$$

The additional second term provides the quantification of effect of anisotropy and perforation orientation on plane flow skin factor.

Similarly, for *m* = 2, Eq (17) can be modified by using Eq (18) and (19) in the following way:

$$S_{2D} = a_2 ln\left(\frac{4}{l_{pD}}\right) + (1 - a_2) ln\left(\frac{1}{1 + l_{pD}}\right) + ln\left[\frac{\sqrt{k_y/k_z} + 1}{2\left(cos^2\alpha + \left(k_y/k_z\right)sin^2\alpha\right)^{0.5}}\right] \ldots\ldots\ldots\ldots\ldots\ldots eq \text{ (22)}$$

Furui et al (2002) report that the effects of anisotropy and perforation orientation for *m* > 3 are negligible and direct application of Eq (18) will give accurate values, as verified by comparing with simulation results.

The wellbore blockage pseudo-skin has been calculated by the authors in a similar way as discussed in the previous section, i.e., $S_{wb} = S_{FEM} - S_{2D}$. The wellbore skin will be positive for any perforation condition and its correlation on the basis of FEM simulation results is:

$$S_{wb} = b_m\left\{{}^{c_m}/_{l_{pD,eff}} + exp\left[{}^{-c_m}/_{l_{pD,eff}}\right]\right\} \ldots\ldots\ldots\ldots\ldots\ldots\ldots\ldots\ldots\ldots \text{Eq (23)}$$

Where:

$$l_{pD,eff} = \begin{cases} l_{pD}\left[\dfrac{(k_y/k_z)sin^2\alpha + cos^2\alpha}{(k_y/k_z)cos^2\alpha + sin^2\alpha}\right]^{0.675} & \text{for } m = 1 \\ l_{pD}\left[\dfrac{1}{(k_y/k_z)cos^2\alpha + sin^2\alpha}\right]^{0.625} & \text{for } m = 2 \\ l_{pD} & \text{for } m = 3 \text{ and } 4 \end{cases}$$

The values of b_m and c_m are presented in Table #2 in the paper authored by Furui et al (2002). It is important to note that in their work the authors have replaced the wellbore with a permeable formation, permeability of which is equal to that of the reservoir as opposed to Karakas and Tariq (1991) who assumed extremely small wellbore radius.

For low shot densities the flow geometry around perforation becomes complicated due to which the authors executed a 3D FEM analysis. Output of this analysis was S_{FEM} which was used to find correlation for 3D convergent flow skin according to $S_{3D} = S_{FEM} - S_{2D} - S_{wb}$. The 3D wellbore skin was assumed to be equal to one determined by 2D analysis for all practical perforation conditions.

2.4: Theoretical basis for work carried out for the thesis

Extensive FEM simulations were carried out to estimate the solution of second order partial differential equation for thermal diffusivity for different well and perforation configurations. The thermal transmissibility was used as an analogue to pressure transmissibility (which is a direct function of permeability) and in this manner solution from ANSYS Thermal under suitable inner and outer boundary conditions, i.e. the temperature distribution, was interpreted to be pressure distribution. The exact same approach was followed by Karakas and Tariq (1991) and is reasonably accurate due to the similarity between steady state pressure and temperature transmissibility equations. Detailed step wise description of the FEM simulation process will be presented in chapter 5. The aim of this section is to define the analytical procedure used in the calculations and assumptions therein.

Ideal openhole condition was assumed to be the one wherein all of the pressure on the outer boundary (320 bars) was acting on the wellbore. The pressure inside the wellbore (inner boundary condition) was set to be 80 bars. FEM simulations were carried out to determine the pressure distribution from the outer boundary to the tip of the perforation for the cases of inline and oriented perforations. Baseline case for maximum expected perforation skin factor was established by setting $K_Y = 0$. This correlates to a pay zone with very low net to gross ratio consisting of thin sand layers heavily interlaced with shale (hence negligible vertical permeability). In the next step, these simulations were carried out for both the isotropic and anisotropic (K_H/K_V = 1 and 10) cases. Having obtained the pressure distributions, the final step was to equate this data to the skin factor to determine if there was any reduction in skin factor by virtue of orienting the perforations from 360^{O} to 350^{O}/10^{O}. Starting point for this was the radial flow equation used by Karakas and Tariq (1991), i.e. Eq (9):

$$q_P = \frac{2\pi k h_t((p_e - p_w)}{\mu[ln(r_e/r_w) + S_t]}$$

We are investigating the steady state 2D flow behavior in the immediate vicinity of the borehole (ignoring far field effects) and hence the use of radial flow equation is valid. In the ideal openhole condition, where all the pressure from the outer boundary is acting on the wellbore, S_t by definition would be equal to 0. This conclusion was used to calculate the ideal openhole flow rate. Adding the inline perforations (m = 1 or $\Theta = 0^O$ or 360^O) in the model led to lesser pressure from the outer boundary being transmitted to the tip of the perforations, as expected. This in effect would be the reservoir pressure experienced by the well and correlates directly to the additional pressure drop in the vicinity of the borehole. This reduced pressure was used in the abovementioned flow formula (keeping $S_t = 0$ as the skin effect is reflected in the reduced pressure itself) and the perforation flow rate was calculated for inline 360^O perforations.

In the next step, the model was modified to include $350^O/10^O$ oriented perforations with the same inner and outer boundary conditions as before to determine the pressure distribution. The pressure at the tip of the perforation was, as expected, higher than in the case of inline perforations and this was used to calculate the perforation flow rate for oriented perforations. Having obtained the flow rates for different perforation configurations S_P was calculated by *Eq* (10) following the work of Furui et al (2008), i.e.:

$$S_P = \left(\frac{J_O}{J_P} - 1\right) ln(r_b/r_w)$$

Wherein r_b was set to be 32" for all cases. The reason for selecting r_b = 32" is that this dimensioning accommodates the maximum number of elements and nodes that can be built in to the non-commercial student version of the software ANSYS Mechanical APDL (at the finest meshing density). Any size greater than 32" would result in number of elements exceeding the allowable limit, creating an error message and terminating the simulation run. The same procedure was carried out for isotropic and anisotropic behavior, setting K_H/K_V = 1 and 10 for obtaining the results. It is important to state all the assumptions in this work:

- The reservoir no-flow boundary is assumed to be far from the well relative to perforation near wellbore effects
- Steady state radial flow geometry is assumed to be the flow in the near borehole region
- Maximum permeability direction was assumed to be in the horizontal plane
- Steady state, viscous flow of incompressible single phase fluid (oil)
- Perforation shot density is high enough to neglect any 3D convergent flow in to perforations
- Effect of gravity is negligible
- Fluid enters the well only through perforations and the borehole is assigned the same permeability as the formation [same approach as Furui et al (2002)] to correctly place the perforations in the model
- Anisotropy, when accounted for, is constant throughout the reservoir
- Pressure drop inside the perforations is negligible
- Outer boundary condition is 320 bar at 32" and inner boundary condition in 80 bar at the root of the perforation

- Total pressure drops in the borehole vicinity are used for quantifying S_P. In theory, the total pressure drop reflects the pressure drops caused by perforation skin and formation damage skin. However since the focus of the thesis is to identify the effect on perforation skin due to orienting the perforations, the formation damage skin in all cases is assumed to be zero
- Due to software limitations because of the non-commercial student license, it was not possible to place the offline perforations in oriented degrees. The oriented perforations are represented by their projected area (calculated using simple trigonometric transformation) in *X-Y* plane

Placement of the well on the Cartesian coordinate system of ANSYS is as follows:

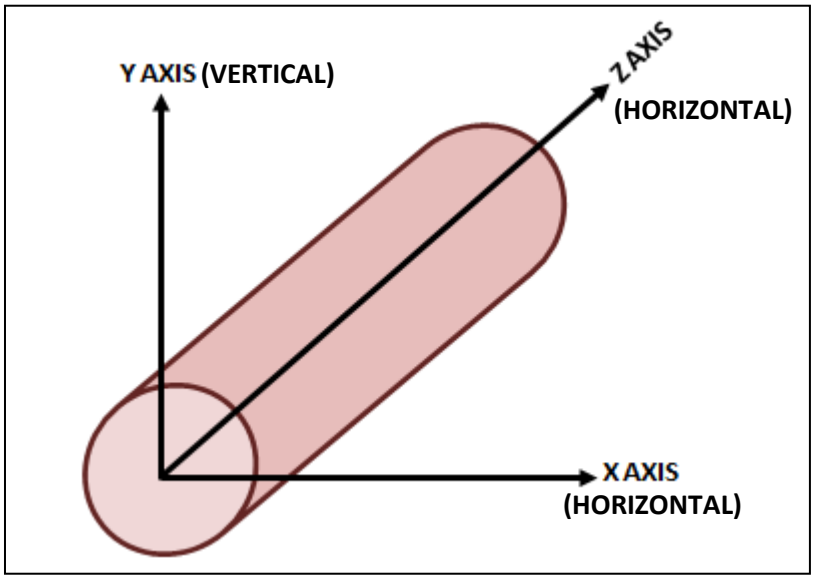

Figure 1: Placement of the well in Cartesian coordinate system

This concludes the literature survey directly pertinent to the thesis work. Readers who are interested in a more detailed insight into the analysis of perforation skin factor and the application of finite element modeling therein are referred to the works of Prats (1961), Tariq (1987), Pucknel and Clifford (1991), Andrews et al (2008) and Brooks and Haggerty (2011).

Chapter 3: Results of finite element modeling (FEM) simulations

The iso-parametric thermal elements in ANSYS have an option that allows the element to model steady-state fluid flow through porous media as discussed by Karakas and Tariq (1991). The thermal transmissibility parameters (T_{XX}, T_{YY} and T_{ZZ}) are interpreted as analogous fluid flow parameters in the (x, y and z directions) and the pressure distribution is obtained from the numerical solution of the following second order partial differential equation (the model provides temperature distribution which is equivalent to pressure distribution):

$$\frac{\partial}{\partial x}\left(T_{XX}\frac{\partial T}{\partial x}\right)+\frac{\partial}{\partial y}\left(T_{YY}\frac{\partial T}{\partial y}\right)+\frac{\partial}{\partial z}\left(T_{ZZ}\frac{\partial T}{\partial z}\right)=0 \ldots\ldots\ldots\ldots\ldots\ldots\ldots\ldots\ldots\ldots\ldots\ldots\ldots \text{Eq (24)}$$

3.1: Results for baseline case of maximum expected perforation skin factor (K_H/K_V = infinity)

For this set of simulations, the software only requires the value of $T_{xx,}$ the inherent assumption being that flow is only along the x axis. With this assumption, *Eq* (24) is simplified to:

$$\frac{\partial}{\partial x}\left(T_{XX}\frac{\partial T}{\partial x}\right)=0 \ldots\ldots\ldots\ldots\ldots\ldots\ldots\ldots\ldots\ldots\ldots\ldots\ldots\ldots\ldots\ldots\ldots\ldots\ldots\ldots \text{Eq (25)}$$

This can be considered similar to thin horizontal layers with very poor vertical permeability. Results from the FEM simulations are presented in the successive sections.

3.1.1: Results for 2.4" borehole

The simulated values of *Sp* for inline and *350/10^O* are as follows:

Well radius (inches)	Skin factor from FEM	$l_{pD} = l_p/r_w$		
		1.25	2.5	3.75
2.4"	$S_{p\ 360}$	4.317	2.59	1.55
	$S_{p\ 350/10}$	1.757	1.177	0.863
Decrease in skin		59.30%	54.56%	44.32%

Table 1: Effect of orienting the perforation by 20^O for 2.4" well radius, K_H/K_V = infinity

The values reported in the table are plotted as follows:

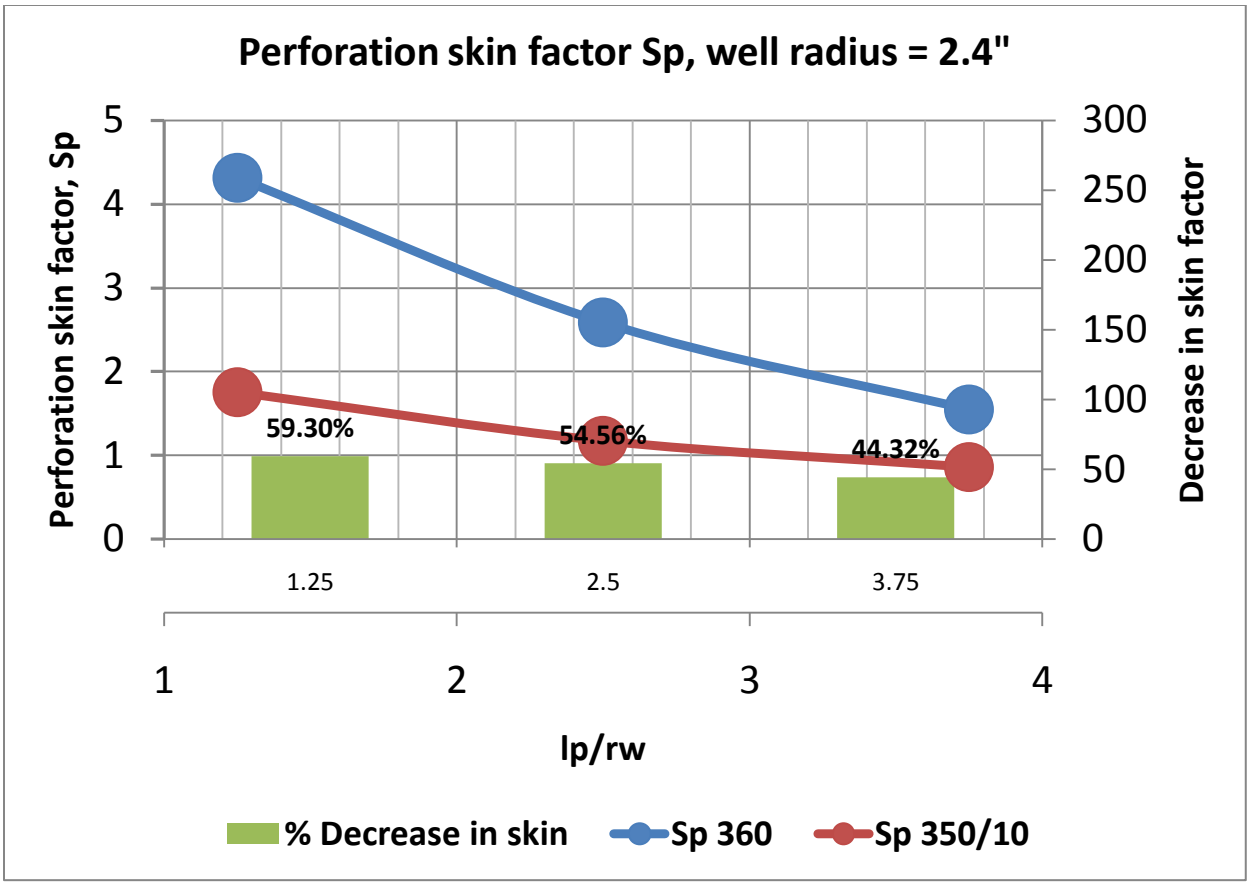

Figure 2: Perforation skin factor for r_w = 2.4" and K_H/K_V = infinity

As expected, there is significant reduction in perforation skin going from inline to oriented perforations. Initial high values of inline perforations can be attributed to the small size of the borehole and hence high plane flow and wellbore pseudo-skin. However, we can observe the advantages of using *350^{O}/10^{O}* phasing in terms of mitigation of high perforation skin factors for small/slim sized boreholes. It is reasonable to conclude that orienting the perforations reduces both the plane flow skin (S_{2D}) and the wellbore pseudo-skin. Another important observation is that percentage reduction of skin factor decreases with increasing l_{pD}. This is attributed to larger effective well radius resulting from increasing the perforation length (l_p).

3.1.2: Results for 3" borehole

The simulated values of *Sp* for inline and *350^{O}/10^{O}* are as follows:

Well radius (inches)	Skin factor from FEM	$l_{pD} = l_p/r_w$		
		1	2	3
3"	$S_{p\ 360}$	4.396	2.305	1.14
	$S_{p\ 350/10}$	2.142	1.42	1.014
Decrease in skin		51.27%	38.39%	11.05%

Table 2: Effect of orienting the perforation by 20^{O} for 3" well radius, K_H/K_V = infinity

The values reported in table 2 are plotted as follows:

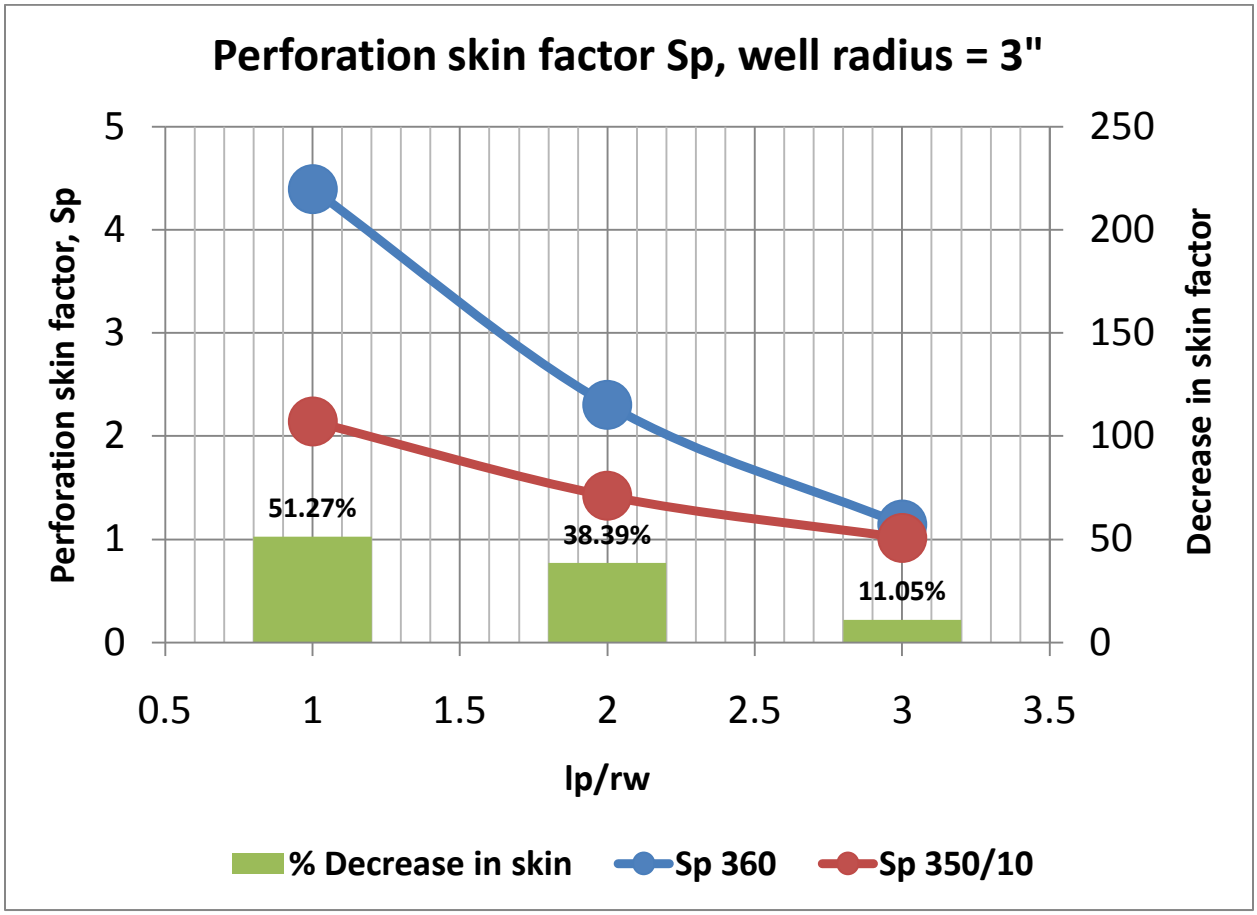

Figure 3: Perforation skin factor for r_w = 3" and K_H/K_V = infinity

It is noted that having increased the borehole size, the reduction in perforation skin factor is not very large for the largest perforation size (9"). However, the reduction is still quite significant for the smaller perforation sizes (3" and 6").

3.1.3: Results for 4.3" borehole

The simulated values of *Sp* for inline and $350^O/10^O$ are as follows:

Well radius (inches)	Skin factor from FEM	$l_{pD} = l_p/r_w$		
		0.7	1.4	2.09
4.3"	$S_{p\ 360}$	4.683	2.007	1.35
	$S_{p\ 350/10}$	2.372	1.698	1.204
Decrease in skin		49.35%	15.40%	10.81%

Table 3: Effect of orienting the perforation by 20^O for 4.3" well radius, K_H/K_V = infinity

The values in table 3 are plotted as follows:

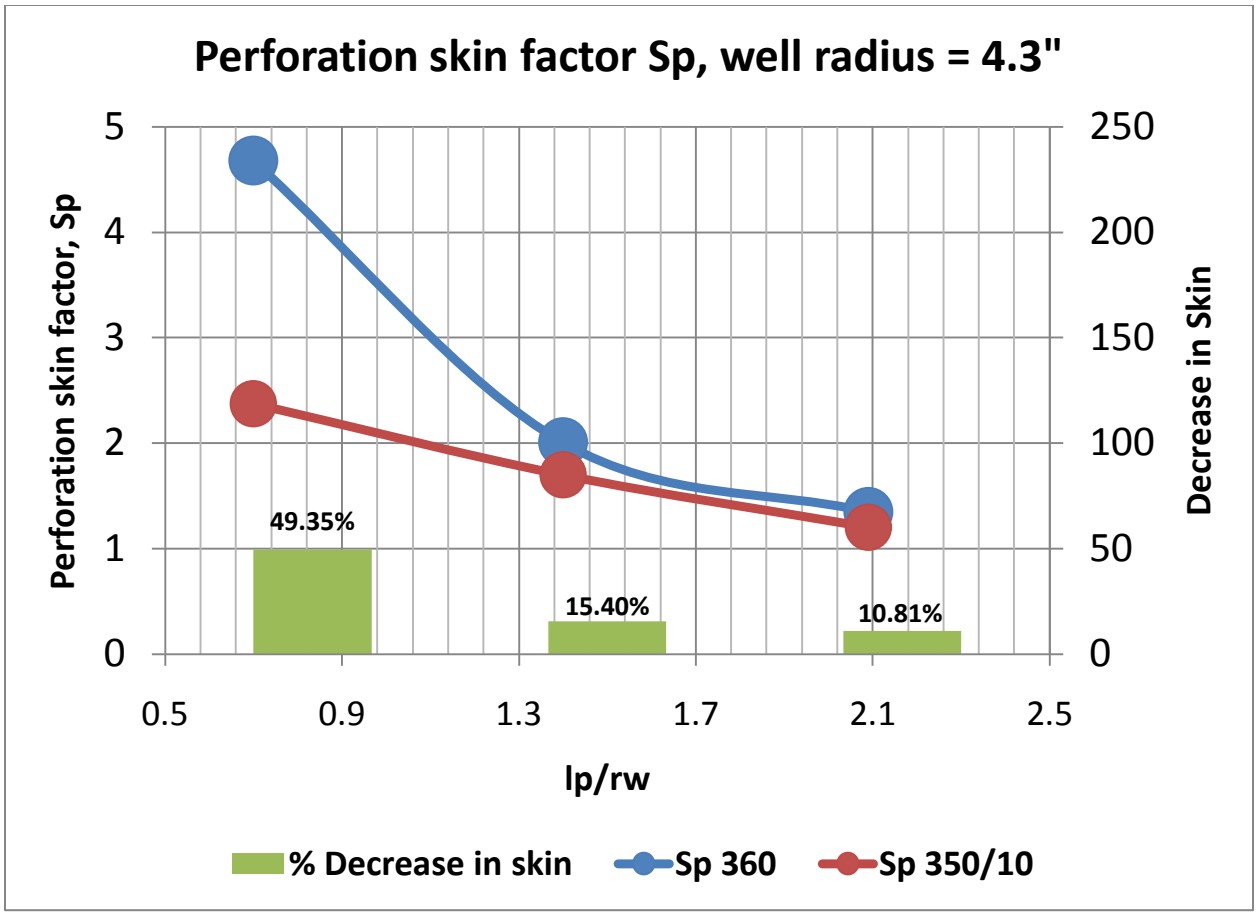

Figure 4: Perforation skin factor for r_w = 4.3" and K_H/K_V = infinity

The effect of increasing the wellbore radius is quite visible for perforation l_{pD} = 1.4 and 2.09 (perforation sizes 6" and 9") wherein the reduction in skin factor with oriented perforations is not very high. As stated previously, this is due to the increasing effective radius ($r_{WE} = r_W + l_P$). From these simulations, it is apparent that the oriented perforations offer maximum advantage (in terms of % reduction of perforation skin factor) in configurations wherein the borehole diameter and perforation length are small compared to the reservoir radius.

3.2: Isotropic and anisotropic results

For these simulations, the software requires the value of T_{xx}, T_{YY} and T_{ZZ}. This reflects a realistic scenario wherein flow paths are established over x, y and z axis. Since 2D FEM simulation is being carried out (by virtue of the plane model created, as explained in chapter 5), Eq (24) is simplified to:

$$\frac{\partial}{\partial x}\left(T_{XX}\frac{\partial T}{\partial x}\right)+\frac{\partial}{\partial y}\left(T_{YY}\frac{\partial T}{\partial y}\right) \ldots\ldots\ldots\ldots\ldots\ldots\ldots\ldots\ldots\ldots\ldots\ldots\ldots\ldots\ldots\ldots\ldots\ldots \text{Eq (26)}$$

This is a much closer analogue to real radial flow due to the assumption of high perforation shot density and under the given circumstances, provides a more refined understanding of the behavior of perforation skin factor. Pressure distribution simulations for inline and oriented perforations have been carried out for 2 cases (K_H/K_V = 1 and 10) and the results are presented in successive sections.

3.2.1: Isotropic reservoir, $K_H/K_V = 1$

Results for different borehole diameters are presented in the subsequent sections.

3.2.2.1: Results for 2.4" borehole:

Well radius (inches)	Skin Factor from FEM	$l_{pD} = l_p/r_w$		
		1.25	2.5	3.75
2.4"	$S_{p\ 360}$	4.317	2.266	1.4
	$S_{p\ 350/10}$	1.473	0.962	0.699
Decrease in skin		65.88%	57.55%	50.07%

Table 4: Effect of orienting the perforation by 20^{O} for 2.4" well radius, $K_H/K_V = 1$

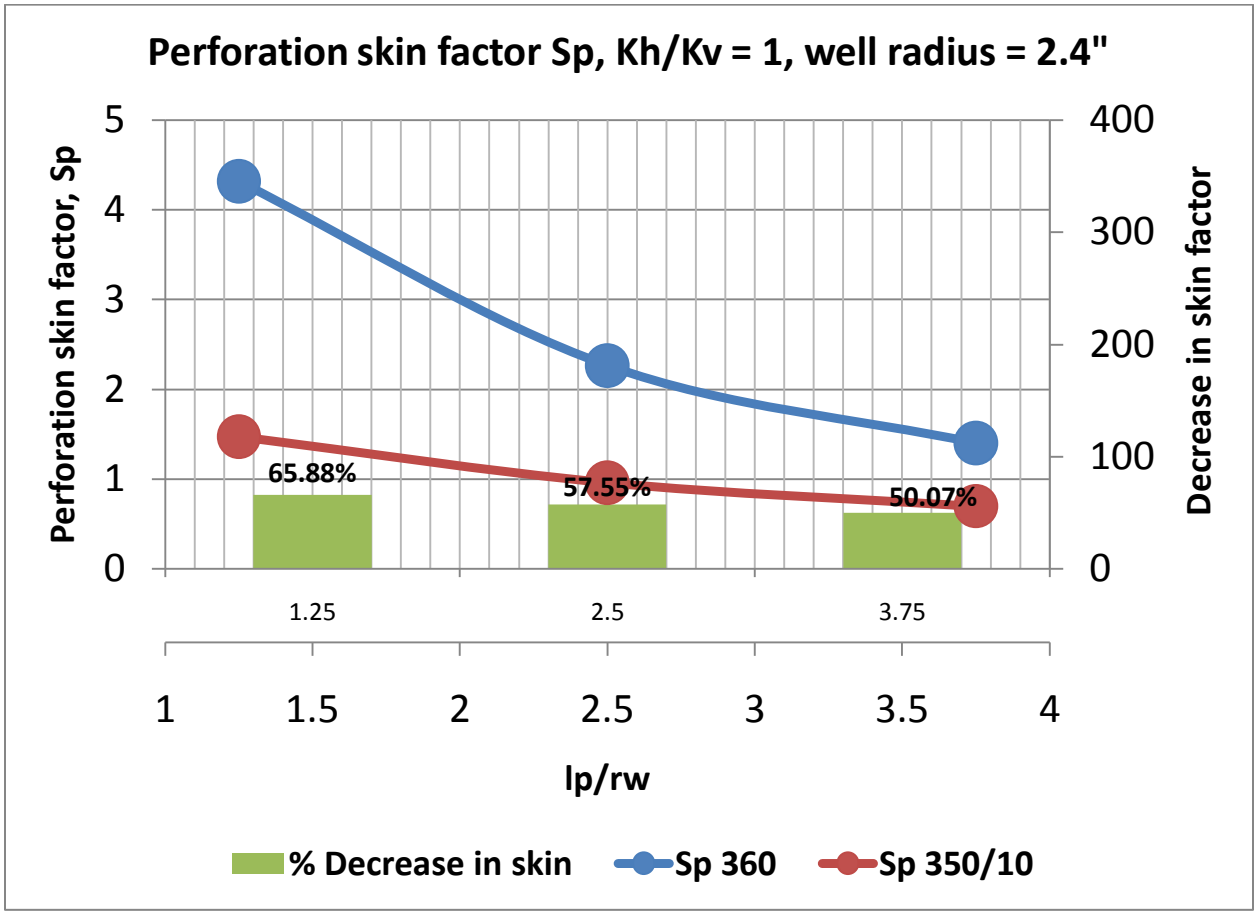

Figure 5: Perforation skin factor for $r_w = 2.4$" and $K_H/K_V = 1$

Two important observations can be made from the presented data. The perforation skin factor for the isotropic case is lesser than that from the established baseline case of maximum expected S_P (this is logical due to improved spatial flow conditions) and oriented perforations are more effective at reducing the perforation skin factor for K_H/K_V = 1. The previous observation that oriented perforations are extremely beneficial for small borehole and perforation diameter holds true herein also.

3.2.2.2: Results for 3" borehole:

Simulation results are as follows:

Well radius (inches)	Skin Factor from FEM	$l_{pD} = l_p/r_w$		
		1	2	3
3"	$S_{p\ 360}$	3.49	2.06	1.31
	$S_{p\ 350/10}$	1.40	0.94	0.69
Decrease in skin		60.02%	54.67%	47.63%

Table 5: Effect of orienting the perforation by 20^O for 3" well radius, $K_H/K_V = 1$

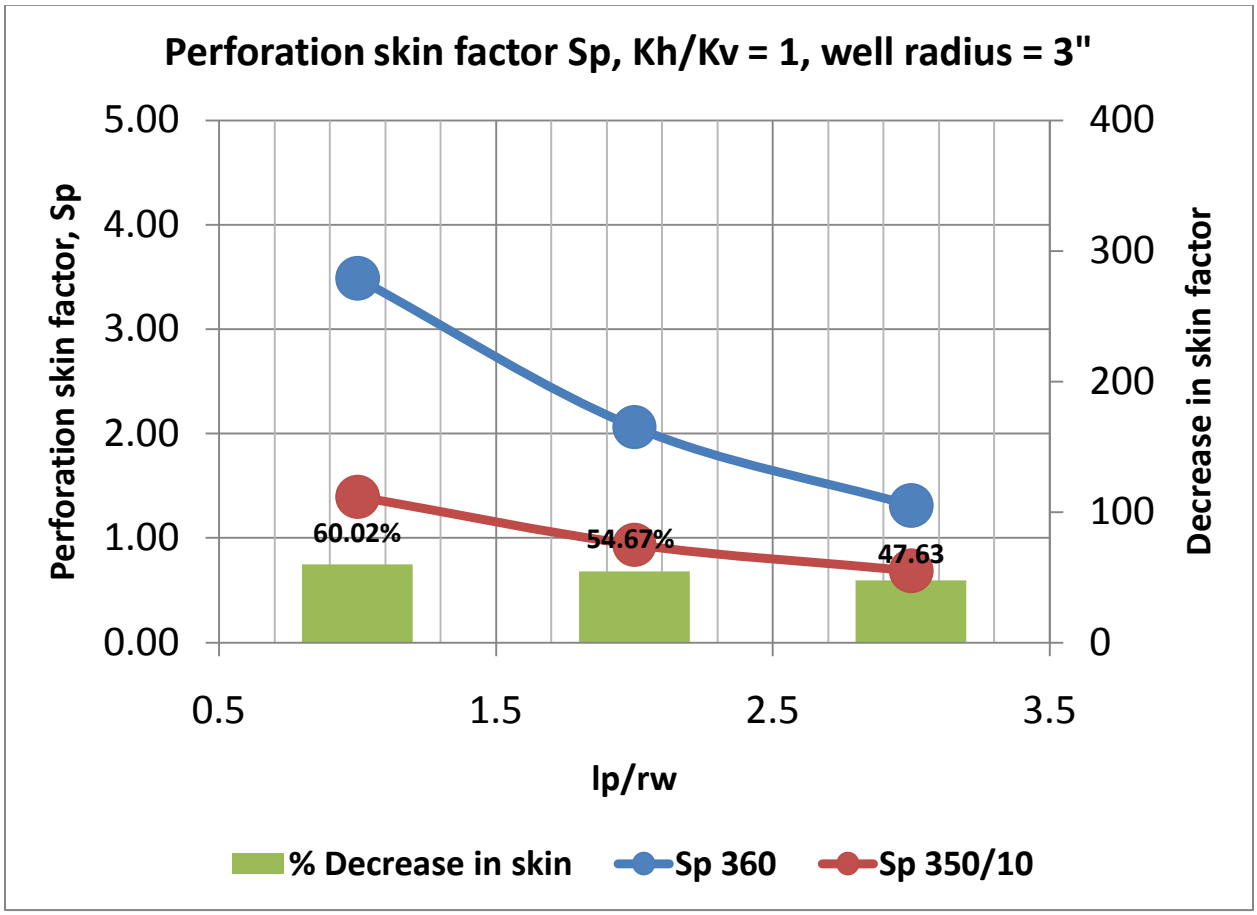

Figure 6: Perforation skin factor for $r_w = 3"$ and $K_H/K_V = 1$

An important observation is that even though with increasing borehole diameter the perforation skin factor is reducing significantly. Oriented perforations are much more effective at decreasing the perforation skin factor in anisotropic medium than in isotropic medium. This suggests a strong functional relationship between perforation orientation and magnitude and direction of formation anisotropy.

3.2.2.3: Results for 4.3" borehole:

Simulation results are as follows:

Well radius (inches)	Skin Factor from FEM	$l_{pD} = l_p/r_w$		
		0.7	1.4	2.09
4.3"	$S_{p\ 360}$	3.80	1.88	1.11
	$S_{p\ 350/10}$	1.34	0.83	0.61
Decrease in skin		64.76%	55.98%	44.80%

Table 6: Effect of orienting the perforation by 20^O for 4.3" well radius, $K_H/K_V = 1$

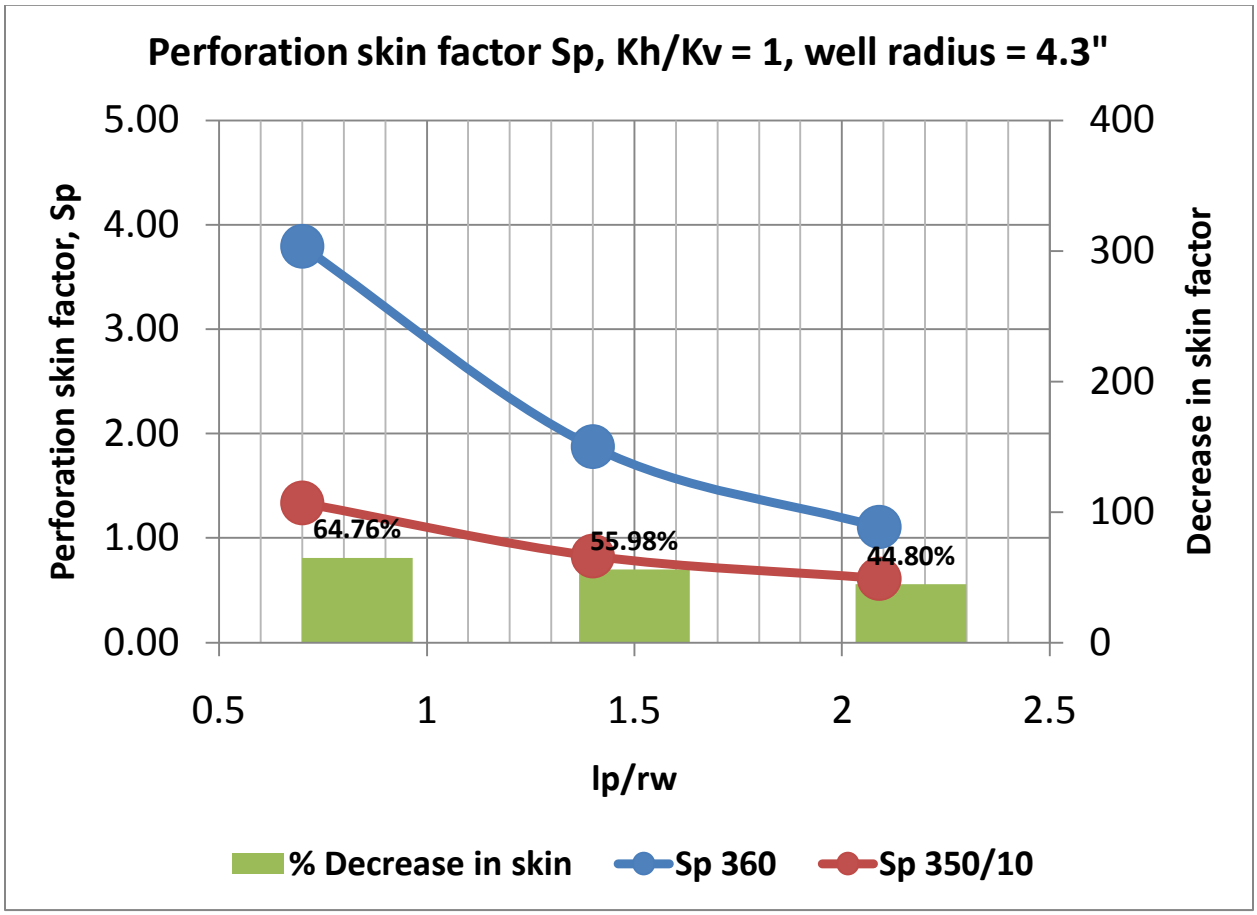

Figure 7: Perforation skin factor for $r_w = 4.3$" and $K_H/K_V = 1$

The perforation skin factor, as expected, is reduced due to the increasing borehole size. However oriented perforations are much more effective at reducing the perforation skin factor in anisotropic medium than in isotropic medium, irrespective of the size of the borehole and length of perforations.

3.2.2: Anisotropy, $K_H/K_V = 10$

This represents an ideal condition for horizontal well, wherein the horizontal permeability is much greater than the vertical permeability. Perforations are modeled to be perpendicular to the maximum permeability direction, i.e. the x axis.

3.2.2.1: Results for 2.4" borehole

The simulation results from FEM are as follows:

Well radius (inches)	Skin Factor from FEM	$l_{pD} = l_p/r_w$		
		1.25	2.5	3.75
2.4"	$S_{p\ 360}$	1.20	0.58	0.36
	$S_{p\ 350/10}$	0.83	0.38	0.24
Decrease in skin		31.23%	33.93%	34.37%

Table 7: Effect of orienting the perforation by 20^{O} for 2.4" well radius, $K_H/K_V = 10$

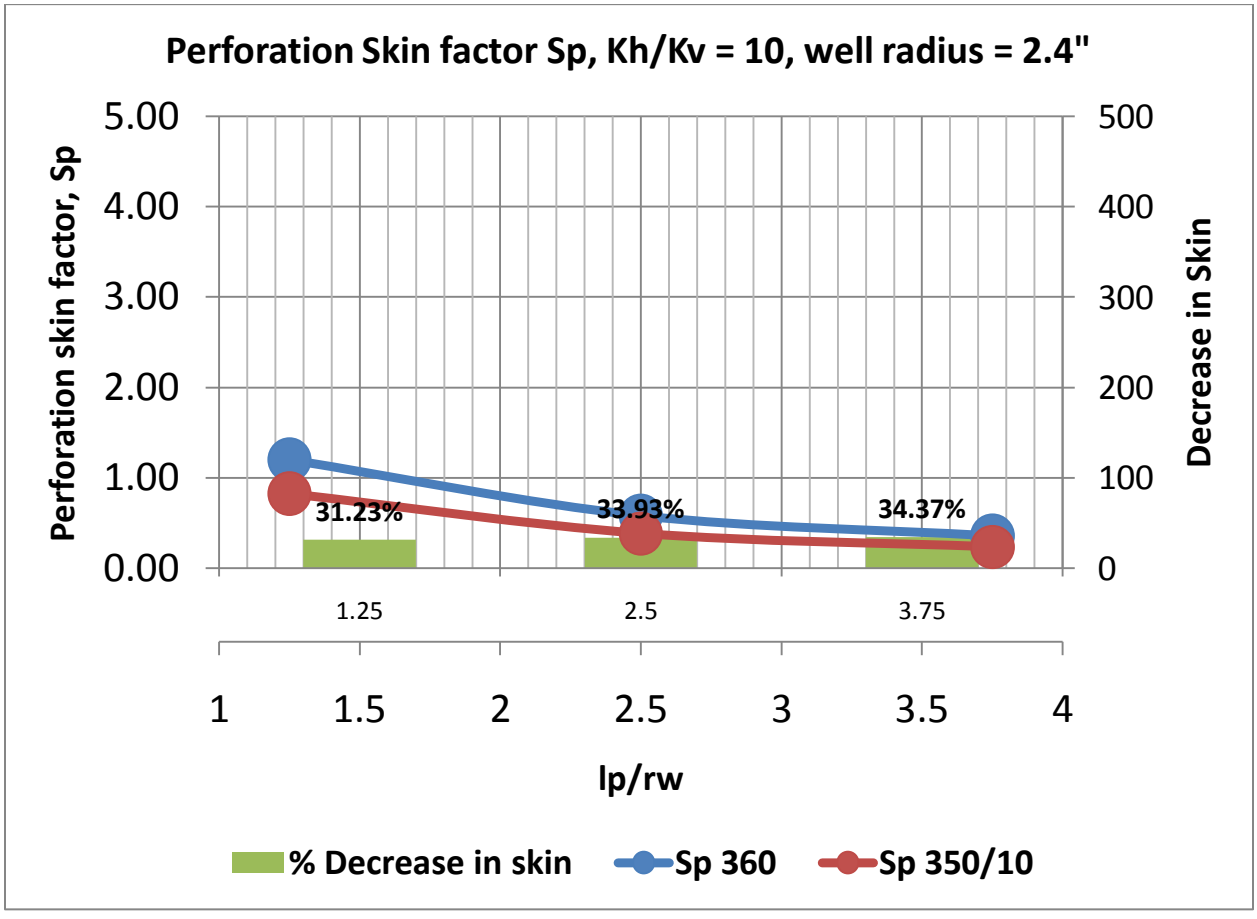

Figure 8: Perforation skin factor for $r_w = 2.4$" and $K_H/K_V = 10$

The most interesting observation is the considerable decrease in perforation skin factor in the case of favorable anisotropy. This is attributed to superior flow conditions and correct orientation of perforations to the direction

of maximum permeability (x).Oriented perforations are still decreasing the perforation skin factor but the magnitude is not as pronounced as it was in previous cases.

3.2.2.2: Results for 3" borehole

Simulation results are as follows:

Well radius (inches)	Skin Factor from FEM	$l_{pD} = l_p/r_w$		
		1	2	3
3"	$S_{p\ 360}$	0.79	0.39	0.38
	$S_{p\ 350/10}$	0.74	0.39	0.24
Decrease in skin		6.56%	0.00%	37.36%

Table 8: Effect of orienting the perforation by 20^{O} for 3" well radius, K_H/K_V= 10

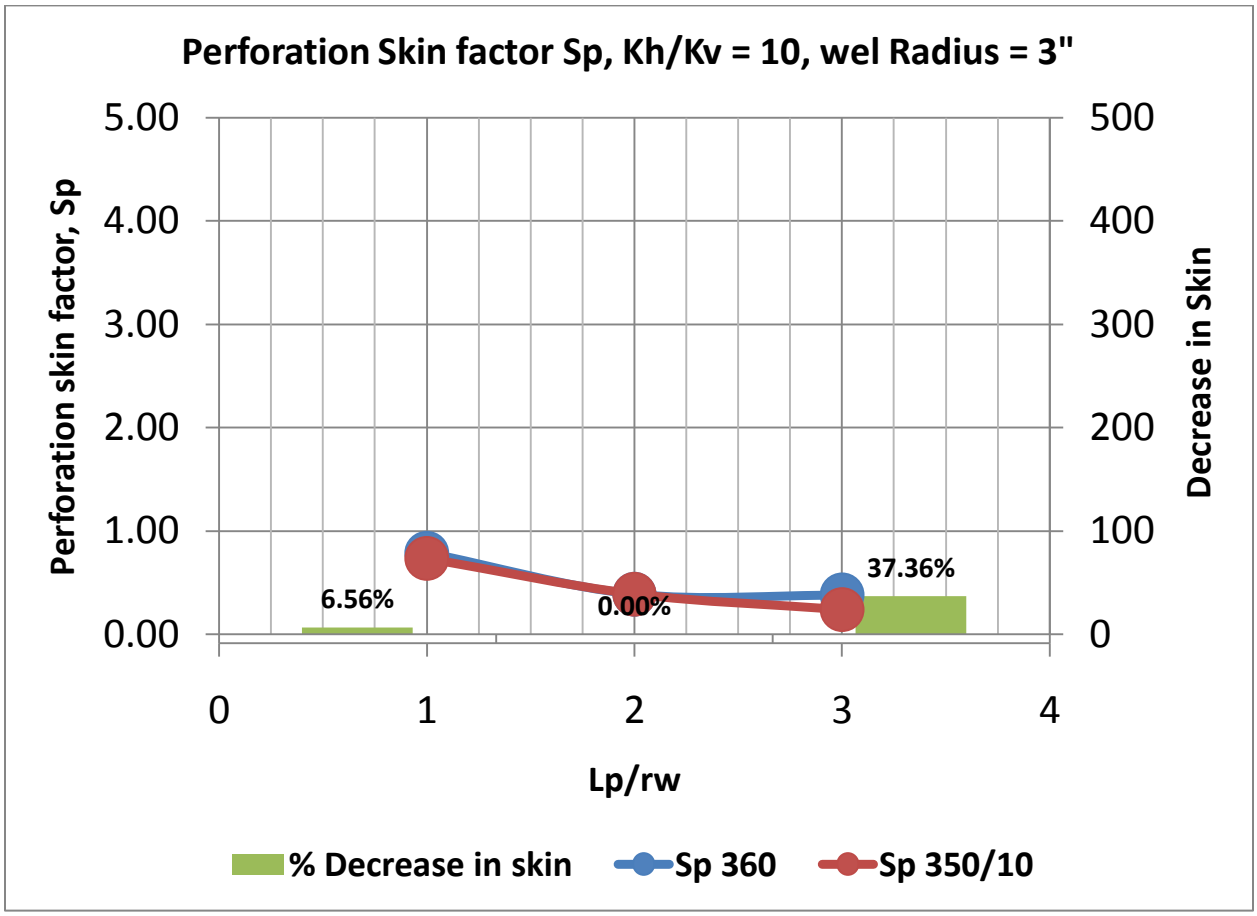

Figure 9: Perforation skin factor for r_w = 3" and K_H/K_V= 10

There appears to be no significant change in perforation skin factor, except for the greatest perforation length. This might be due to minor simulation error and possible reasons for the same would be discussed in chapter 4.

3.2.2.3: Results for 4.3" borehole

Simulation results are as follows:

Well radius (inches)	Skin Factor from FEM	$l_{pD} = l_p/r_w$		
		0.7	1.4	2.09
4.3"	$S_{p\ 360}$	1.00	0.48	0.25
	$S_{p\ 350/10}$	0.58	0.32	0.19
Decrease in skin		41.94%	32.77%	25.93%

Table 9: Effect of orienting the perforation by 20^O for 4.3" well radius, $K_H/K_V = 10$

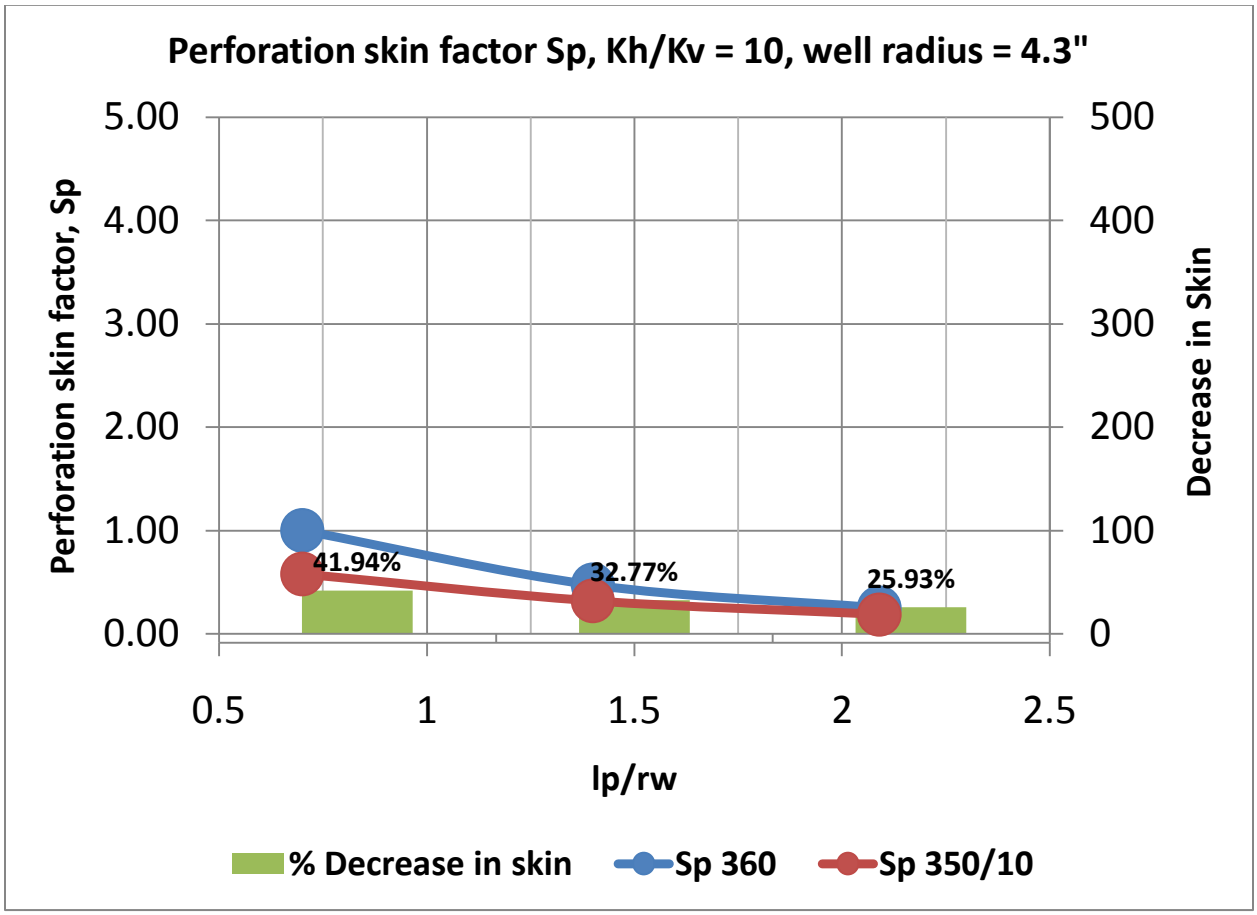

Figure 10: Perforation skin factor for $r_w = 4.3$" and $K_H/K_V = 10$

The trends of perforation skin factor for this borehole diameter follows the trends established in the previous sections.

Chapter 4: Analysis of perforation skin factor $S_{P\_350/10}$ obtained through finite element modeling

This chapter covers the analysis of oriented perforation skin factors for isotropic and anisotropic cases. The purpose of the data analysis is to determine S_P as a function of l_{pD} (l_P/r_W) by combining all different curves (obtained for different borehole and formation configurations) in to one correlation. The discussion that follows herein attempts to put all these variables in to one correlation by utilizing the regression tool kit provided as an add-on in Microsoft Excel.

4.1: Regression analysis

This section provides a brief description of regression analysis and is directly referred from Freedman (2005) wherein excellent literature is available for statistical regression. In statistics, regression analysis is a statistical process for estimating the relationships among variables. It includes many techniques for modeling and analyzing several variables, primary focus being on the relationship between a dependent variable (in our case S_P) and one or more independent variables (in our case, l_{pD} and r_W). Regression analysis helps one understand how the typical value of the dependent variable (or 'criterion variable') changes when any one of the independent variables is varied, while the other independent variables are held fixed. In all cases, the estimation target is a function of the independent variables called the regression function. In regression analysis, it is also of interest to characterize the variation of the dependent variable around the regression function which can be described by a probability distribution, Freedman (2005). Two of the most common regression techniques are linear and non linear regression analysis.

Microsoft Excel provides a data analysis module which makes linear regression analysis possible. In linear regression, data are modeled using linear predictor functions, and unknown model parameters are estimated from the data. Such models are called linear models. Most commonly, linear regression refers to a model in which the conditional mean of Y for a given value of X is an affine function of X (Freedman, 2005). Nonlinear regression is a form of regression analysis in which observational data are modeled by a function which is a nonlinear combination of the model parameters and depends on one or more independent variables. The data are fitted by a method of successive approximations (Bethea et al, 1985).

4.2: Regression analysis for $S_{P\_350/10}$ for the established baseline case of maximum expected perforation skin factor

In the previous chapter, 3 different curves for $S_{P\_350/10}$ were presented for 3 different borehole radii, i.e. 2.4", 3" and 4.3". The perforation skin factor was plotted as a function of l_{pD} for all the three borehole radii and we examined the effect of going to $350^O/10^O$ phasing from inline phasing. This section will attempt to combine these 3 curves into one single equation, wherein dependency of perforation skin can be expressed as a function of both l_{pD} and r_W. The plot of all the oriented perforation skin factors with respect to l_{pD} is as follows:

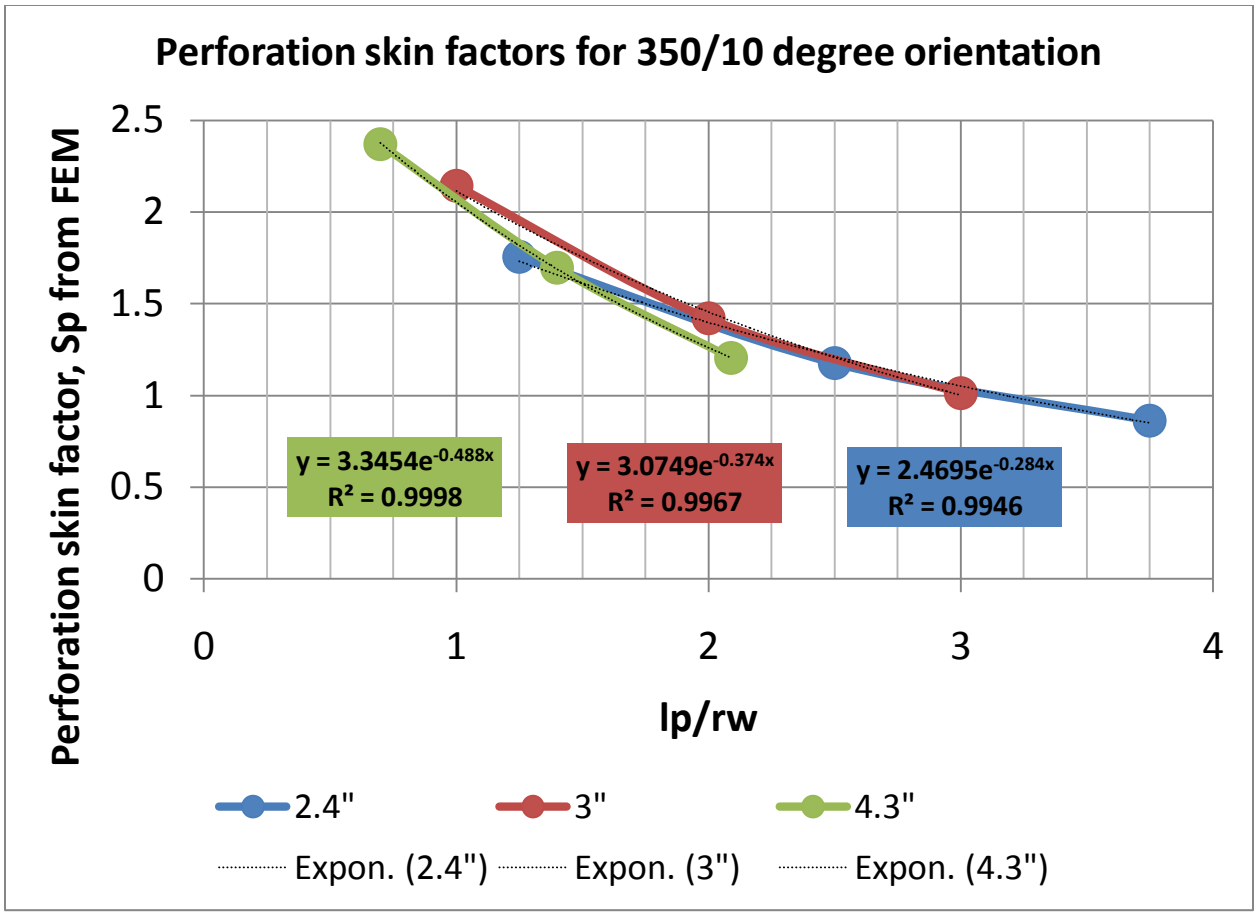

Figure 11: Oriented perforation skin factor for K_H/K_V = infinity

It should be mentioned herein that the trend that was expected (i.e. decreasing S_p with increasing borehole radius is not very apparent here. This may be due to one or a combination of the following reasons:

- Insufficient mesh density and number of nodes while carrying out FEM simulations (the software ANSYS is only available via a student license and there are restrictions to how highly dense the mesh can be)
- Slight miscalculation regarding the analogy between pressure and thermal transmissibility parameters
- Iso-parametric elemental shape degeneracy, which were encountered during some of the simulation runs
- Possible error in placement of inner boundary condition

This is the best possible correlation that could be obtained and hence is being used in this thesis work. Different trend-line fitting options were tried and it was found that the exponential trend line gives the best fit (highest coefficient of regression R^2), closely followed by linear trend-line. The exponential trend lines with their corresponding equations and R^2 values are presented in figure 10. Ideally, since the best fit is an exponential line it would have yielded accurate results if non linear forced regression was carried out, i.e. observational data should have been modeled by a function which was an exponential combination of the model parameters and dependant on l_{pD} and r_W. However, excel only provides linear regression tool and due to time-frame constraints

and with the purpose of keeping the analysis simple, linear regression was carried out. Input, output and error values are reported in the subsequent tables.

Input Summary			Output	
Sp_350/10	LpD	Rw	$S_{P\_Regression}$	Error
1.757	1.25	2.4	1.957875	0.102598
1.177	2.5	2.4	1.32875	0.114205
0.863	3.75	2.4	0.699625	-0.23352
2.142	1	3	2.0837	-0.02798
1.42	2	3	1.5804	0.101493
1.014	3	3	1.0771	0.058583
2.372	0.7	4.3	2.23469	-0.06144
1.698	1.4	4.3	1.88238	0.09795
1.204	2.09	4.3	1.535103	0.215688

Table 10: Input and output parameters for regression analysis, $S_{P\_350/10}$ for K_H/K_V = infinity

Regression Statistics	
Multiple R	0.94697043
R Square	0.89675299
Adjusted R Square	0.86233732
Standard Error	0.19080563
Observations	9

ANOVA					
	df	SS	MS	F	Significance F
Regression	2	1.897269	0.94864	26.06	0.0011006
Residual	6	0.218441	0.03641		
Total	8	2.11571			

	Coefficients	Standard Error	t Stat	P-value	Lower 95%	Upper 95%	Lower 95.0%	Upper 95.0%
Intercept	2.623934	0.395217	6.639226	0.0006	1.656873	3.591	1.65687	3.590994
LpD	-0.503303	0.077034	-6.53351	0.0006	-0.691799	-0.313	-0.6918	-0.31481
Rw	-0.036597	0.091139	-0.402	0.7019	-0.2596	0.186	-0.25961	0.186412

Table 11: Regression coefficients, $S_{P\_350/10}$ for K_H/K_V = infinity

The regression is acceptable as long as the significance F is less than 0.05. Our value of significance F from regression is 0.0011006 and hence the regression is correct. However it should be cautioned that the R^2 value for the regression is low (0.897) and this lack of accuracy is clearly reflected in the error calculated between $S_{P\_Regression}$ and $S_{P\_350/10}$ .This lack of accuracy is due to error in FEM modeling, the identification and correction of which remains one of the first priorities in terms of carrying this work forward in the future. Linear regression equation for $S_{P\_350/10}$ is given as:

$$S_{P\_350/10} = 2.624 - 0.5033 l_{pD} - 0.0366 r_W \ldots\ldots\ldots\ldots\ldots\ldots\ldots\ldots\ldots\ldots\ldots\ldots\ldots\ldots Eq\ (27)$$

The presence of r_w in Eq (27) is undesirable. Attempts were made to carry out regression with r_{wD} (dimensionless) however the results were highly erroneous due to large spread of the data set. This can be resolved with non linear regression.

4.3: Regression analysis for $S_{P\_350/10}$ for $K_H/K_V = 1$

The plot of all the oriented perforation skin factors with respect to L_{pD} for $K_H/K_V = 1$ is as follows:

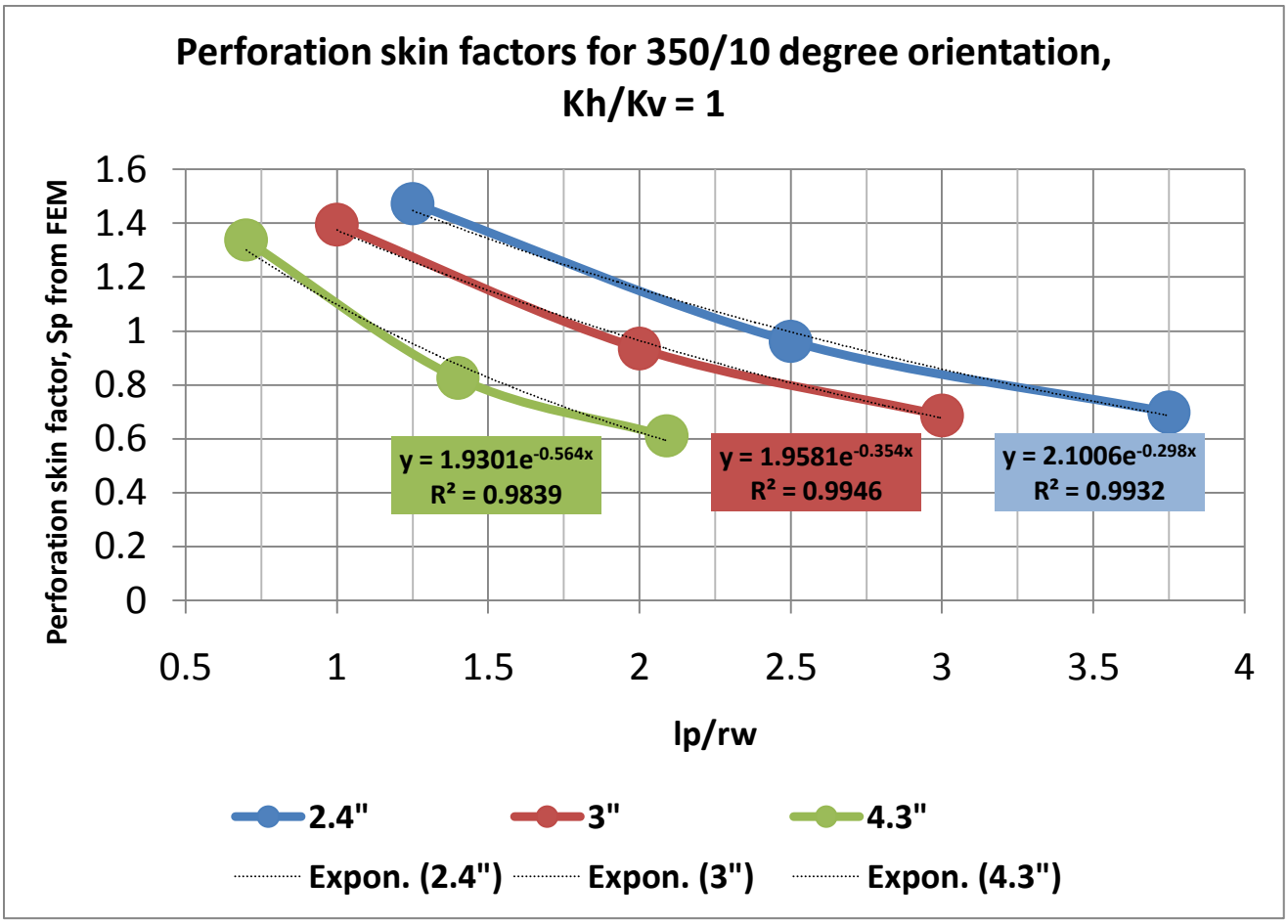

Figure 12: Oriented perforation skin factors for $K_H/K_V = 1$

The expected trend of decreasing S_P with increasing borehole radius is observed and this validates the accuracy of the FEM simulations for $K_H/K_V = 1$. Out of all the possible trend-line fitting options, exponential trend-line again provided the best fit (highest R^2 values as shown on the plot). This again brings us to the simplifying assumption of using linear regression primarily due to the constraints of time frame lack of non-linear regression tools. Input, output and error values are reported in the subsequent tables.

INPUT SUMMARY			Output	Error
Sp_350/10	LpD	Rw	$S_{P\_Regression}$	
1.473	1.250	2.400	1.465	-0.005
0.962	2.500	2.400	1.021	0.058
0.699	3.750	2.400	0.577	-0.211
1.395	1.000	3.000	1.396	0.001
0.936	2.000	3.000	1.041	0.101
0.687	3.000	3.000	0.686	-0.002
1.338	0.698	4.300	1.162	-0.151
0.826	1.395	4.300	0.914	0.096
0.611	2.093	4.300	0.667	0.084

Table 12: Input and output parameters for regression analysis, $S_{P\_350/10}$ for $K_H/K_V = 1$

Regression Statistics	
Multiple R	0.958
R Square	0.918
Adjusted R Square	0.891
Standard Error	0.109
Observations	9.000

ANOVA					
	df	SS	MS	F	Significance F
Regression	2	0.7978	0.3989	33.6	0.0006
Residual	6	0.0712	0.0119		
Total	8	0.8691			

	Coefficients	Standard Error	t Stat	P-value	Lower 95%	Upper 95%	Lower 95.0%	Upper 95.0%
Intercept	2.53976	0.22569	11.253	0.00003	1.98751	3.092	1.98751	3.09202
LpD	-0.35533	0.04397	-8.082	0.00019	-0.46291	-0.248	-0.46291	-0.24775
Rw	-0.26275	0.05206	-5.047	0.00234	-0.39012	-0.135	-0.39012	-0.13537

Table 13: Regression coefficients, $S_{P\_350/10}$ for $K_H/K_V = 1$

The regression is acceptable as long as the significance F is less than 0.05. Our value of significance F from regression is 0.0006 and hence the regression is correct. Moreover all our P-values are less than 0.05 which again is an additional proof of the accuracy of the regression modeling. It should be noted that the R^2 value for the regression is high (0.918) and degree of statistical match is clearly reflected in the error calculated between

$S_{P\_Regression}$ and $S_{P\_350/10}$ in table 12 (very low). This further validates the FEM analysis to be reasonably accurate for the purpose of this thesis work. Linear regression equation for $S_{P\_350/10}$ is given as:

$$S_{P\_350/10} = 2.5398 - 0.3553 l_{pD} - 0.2628 r_W \ldots\ldots\ldots\ldots\ldots\ldots\ldots\ldots\ldots\ldots Eq\ (28)$$

The presence of r_w in Eq (28) is undesirable. Attempts were made to carry out regression with r_{wD} (dimensionless) however the results were highly erroneous due to large spread of the data set. This can be resolved with non linear regression.

4.3 Regression analysis for $S_{P\_350/10}$ for the K_H/K_V = 10

The plot of all the oriented perforation skin factors with respect to l_{pD} for K_H/K_V = 10 is as follows:

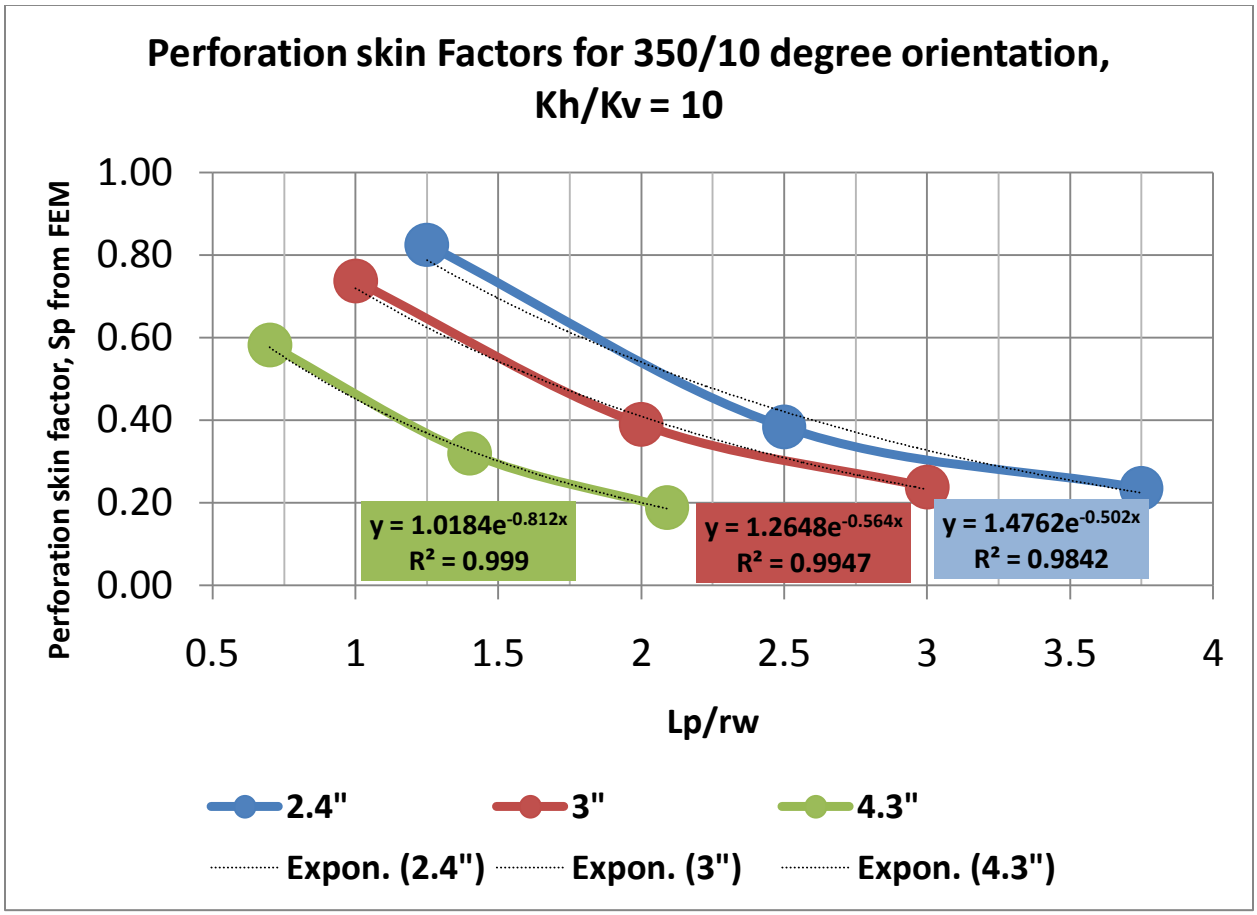

Figure 13: Oriented perforation skin factors for K_H/K_V = 10

The expected trend of decreasing S_P with increasing borehole radius is observed and this once again validates the accuracy of the FEM simulations for K_H/K_V = 1o. Out of all the possible trend-line fitting options, exponential trend-line provided the best fit (highest R^2 values as shown on the plot). This again brings us to the simplifying assumption of using linear regression primarily due to the constraints of time frame and lack of non-linear regression tools. Input, output and error values are reported in the subsequent tables.

INPUT SUMMARY			Output	Error
Sp_350/10	LpD	Rw	$S_{P\_Regression}$	
0.825	1.25	2.4	0.778	-0.06034
0.384	2.50	2.4	0.470	0.183191
0.235	3.75	2.4	0.162	-0.45138
0.737	1.00	3	0.719	-0.02574
0.391	2.00	3	0.472	0.172792
0.239	3.00	3	0.226	-0.05795
0.583	0.70	4.3	0.530	-0.0985
0.320	1.40	4.3	0.358	0.107426
0.188	2.09	4.3	0.187	-0.01042

Table 14: Input and output parameters for regression analysis, $S_{P\_350/10}$ for $K_H/K_V = 10$

Regression Statistics	
Multiple R	0.968270542
R Square	0.937547843
Adjusted R Square	0.916730458
Standard Error	0.066313814
Observations	9

ANOVA					
	df	*SS*	*MS*	*F*	*Significance F*
Regression	2	0.3961004	0.19805	45.0368	0.00024
Residual	6	0.0263851	0.00440		
Total	8	0.4224855			

	Coefficients	*Standard Error*	*t Stat*	*P-value*	*Lower 95%*	*Upper 95%*	*Lower 95.0%*	*Upper 95.0%*
Intercept	1.571936	0.1373513	11.4446	2.67E-05	1.23585	1.9080	1.23585	1.908023
LpD	-0.2465234	0.0267572	-9.2133	9.22E-05	-0.3119960	-0.181	-0.31199	-0.18105
Rw	-0.2022074	0.0316803	-6.3828	0.000696	-0.2797262	-0.125	-0.27973	-0.12469

Table 15: Regression coefficients, $S_{P\_350/10}$ for $K_H/K_V = 10$

The regression is acceptable as long as the significance F is less than 0.05. Our value of significance F from regression is 0.00024 and hence the regression is correct. Moreover all our P-values are less than 0.05 which

again is an additional proof of the accuracy of the regression modeling. It should be noted that the R^2 value for the regression is the highest in all simulations which have been analysed in this work (0.938) and degree of statistical match is clearly reflected in the error calculated between $S_{P\_Regression}$ and $S_{P\_350/10}$ in table 14 (very low). This further validates the FEM analysis to be reasonably accurate for the purpose of this thesis work. Linear regression equation for $S_{P\_350/10}$ is given as:

$$S_{P\_350/10} = 1.5719 - 0.2465 l_{pD} - 0.2022 r_W \quad \text{Eq (29)}$$

The presence of r_w in *Eq* (29) is undesirable. Attempts were made to carry out regression with r_{wD} (dimensionless) however the results were highly erroneous due to large spread of the data set. This can be resolved with non linear regression.

4.4: Analysis of skin factor reduction due to off-setting the perforation

Final step in the analysis process is the quantification of reduction in skin factor when we go from 360^O phasing to 350^O/10^O phasing. Following are the plots for skin factor reduction:

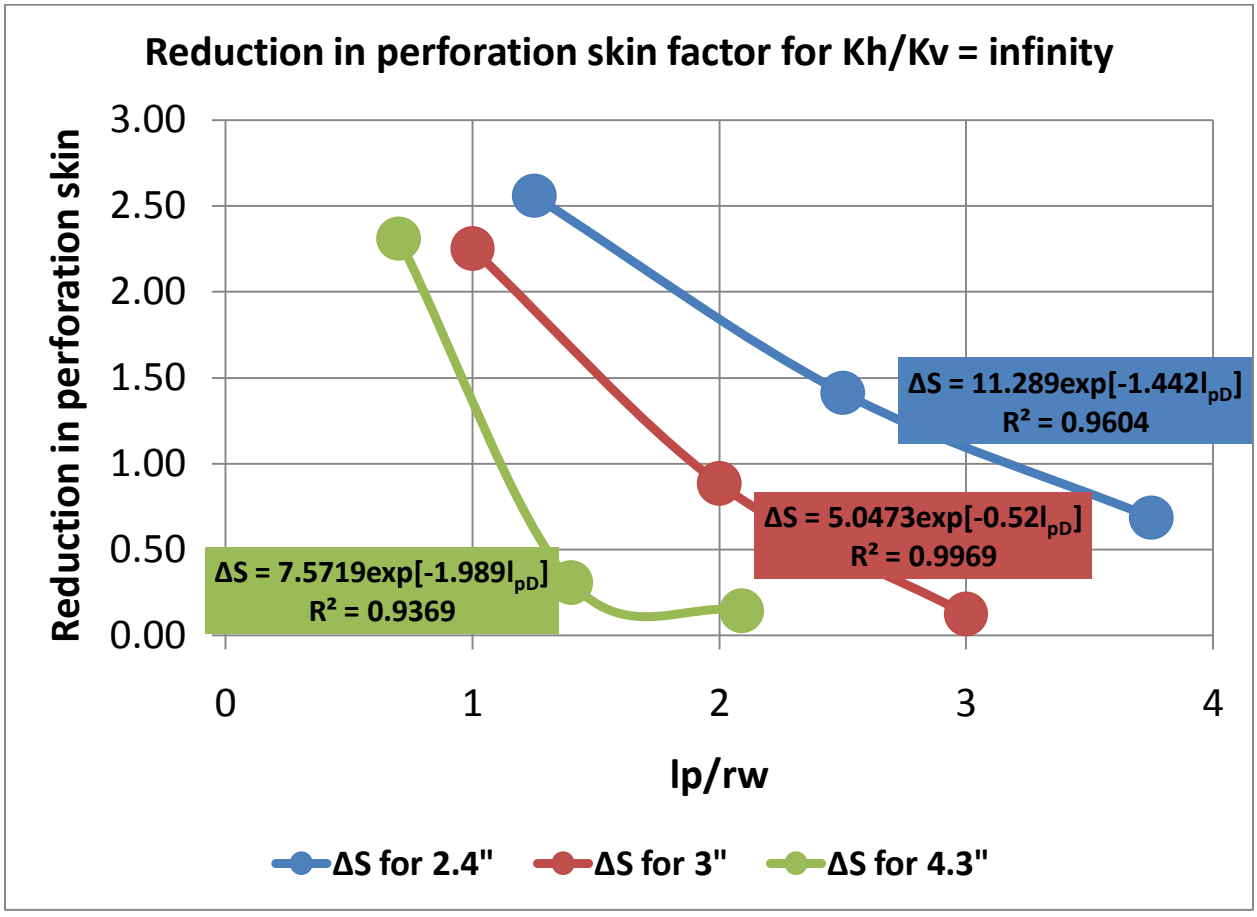

Figure 14: Skin factor reduction for K_H/K_V = infinity

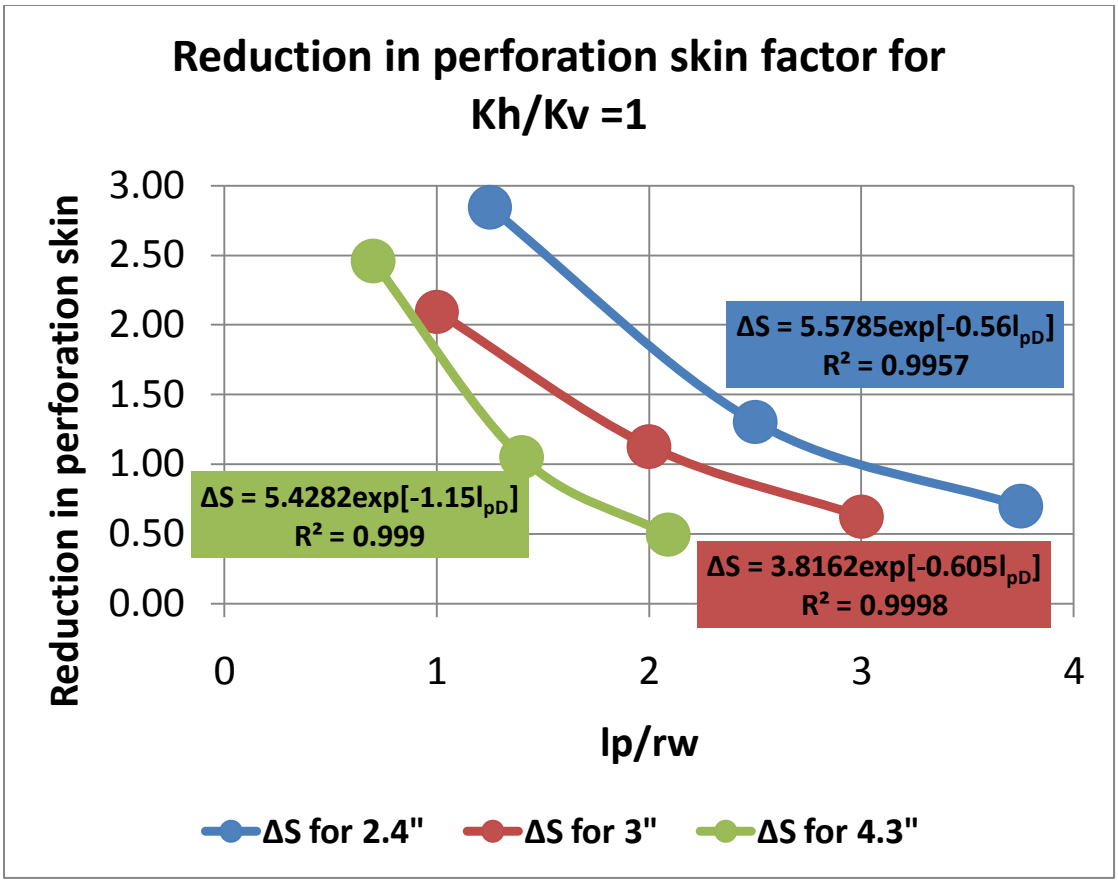

Figure 15: Skin factor reduction for $K_H/K_V = 1$

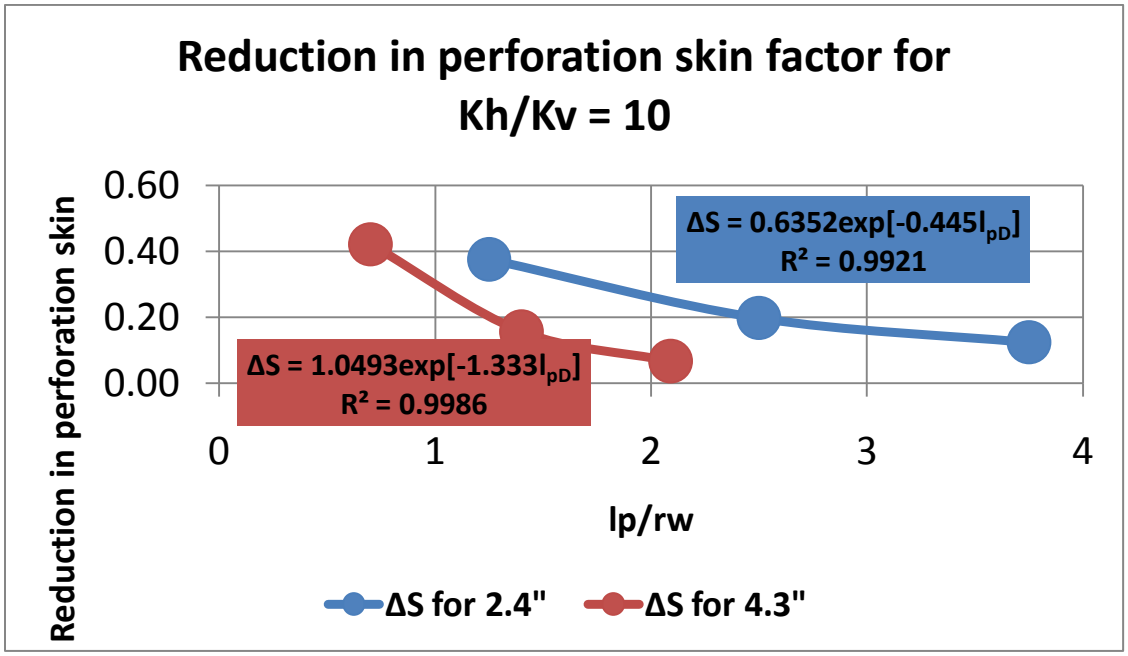

Figure 16: Skin factor reduction for $K_H/K_V = 10$

It is evident upon examination of figures 14 to 16 that ΔS has an exponential trend with l_{pD} and the generalized equation for skin factor reduction can be stated to be:

$$\Delta \boldsymbol{S} = \boldsymbol{C_m exp}\left[\boldsymbol{C_n} * \boldsymbol{l_{pD}}\right] \ldots\ldots\ldots\ldots\ldots\ldots\ldots\ldots\ldots\ldots\ldots\ldots\ldots\ldots\ldots\ldots \boldsymbol{Eq}\ (\mathbf{30})$$

Different values of C_m and C_n are plotted on the figures 14-16 and it is evident that these values are a function of well radius r_w. Linear regression analysis was attempted in excel to arrive at a general equation, using both the well radius and its dimensionless counterpart. However the results were highly erroneous due to the large spread of data, with the coefficient of regression R^2 not even exceeding 0.35. This is a severe limitation of linear regression and it is possible to arrive at a general equation in terms of dimensionless well radius using non linear regression techniques.

4.5: Conclusion and outline for future work aimed towards publication

In conclusion, several significant newly discovered areas which require further investigation are:

- The effect of orienting the perforations was quantified by FEM and a general equation for skin factor reduction was derived based on thorough numerical modeling and is presented above as *Eq* (30). This remains to be verified by physical experiments and is one of the primary focus points for future continuation of the research work
- Taking inspiration from the work of Furui et al (2002), the author intends to derive equations for equivalent well radius and equivalent perforation length which would incorporate the anisotropy ratio and orientation of perforations with respect to direction of maximum permeability by carrying out coordinates transformation in equivalent isotropic space. Furui et al (2003) present this transformation as follows, *Eq* (19) and *Eq* (20):

$$l_{p,eff} = l_p \left(\sqrt{k_y/k_z}\, sin^2\alpha + \sqrt{k_z/k_y}\, cos^2\alpha\right)^{0.5}$$

$$r_{w,eq} = \frac{r_w}{2}\left[\sqrt[4]{k_y/k_z} + \sqrt[4]{k_z/k_y}\right]$$

- The objective is to obtain an equivalent transformation for the $350^O/10^O$ oriented perforation system and substitute it in *Eq* (30) to come up with a robust analytical derivative of *Eq* (30) which would verify the simulation results with analytical calculations

Areas of improvement regarding the process of finite element modeling are as follows:

- Using the commercial version of the finite element modeling software for detailed modeling, this is expected to take care of some errors noticed during the simulation runs by finer meshing
- Using the commercial version of the finite element modeling software to place oriented perforations as per their actual orientation, instead of taking the projected area
- More extensive simulation runs, involving more well radii and perforation lengths to arrive at better correlations
- Use of advanced non linear (exponential) regression techniques to estimate correct and unified correlations for $S_{P\_350/10}$ and ΔS

Chapter 5: Stepwise description of finite element modeling simulations

5.1 Introduction

As per the 'ANSYS Mechanical APDL Thermal Analysis Guide', the basis of thermal analysis is a heat balance equation obtained from the principal of conservation of energy. The finite element solution which is performed via ANSYS Mechanical APDL calculates nodal temperatures, and then uses the nodal temperatures to calculate steady state temperature distribution over the entire model for heat transfer through conduction and convection. A steady state loading condition is one wherein heat storage effects are independent of time. The thermal parameter thus calculated (i.e. temperature distribution) is considered equivalent to pressure distribution (Karakas and Tariq). As per 'ANSYS Mechanical APDL Modeling & Meshing Guide', model generation refers to the generation of nodes and elements that represent the spatial volume and connectivity of the actual system. The modeling process can be summarized in the following steps:

- Enter the software preprocessor (*PREP7*) and initiate the model building session using solid modeling procedures
- Establish a working plane if it is desired to have a customized one, however we use the default working plane which is the same as the global Cartesian coordinates (x, y and z)
- Specify the element type (this directly determines the number of nodes, i.e. number of points at which the numerical solution for the second order partial differential equation will be solved to generate a temperature distribution model)
- Generate basic geometries (circles and rectangles in our case) and use Boolean operators to define the connectivity of the system
- Create nodes and elements by 'meshing' the solid model

After successfully creating the model and meshing, the final step is to apply the loads and obtain the finite element solution. The sections that follow cover the entire modeling and solution methodology in detail.

5.2 Modeling and simulation methodology

The first step in the process is to launch ANSYS Mechanical APDL v.13 and set the preference to 'thermal' through the graphic user interface (GUI) as shown in figure 14:

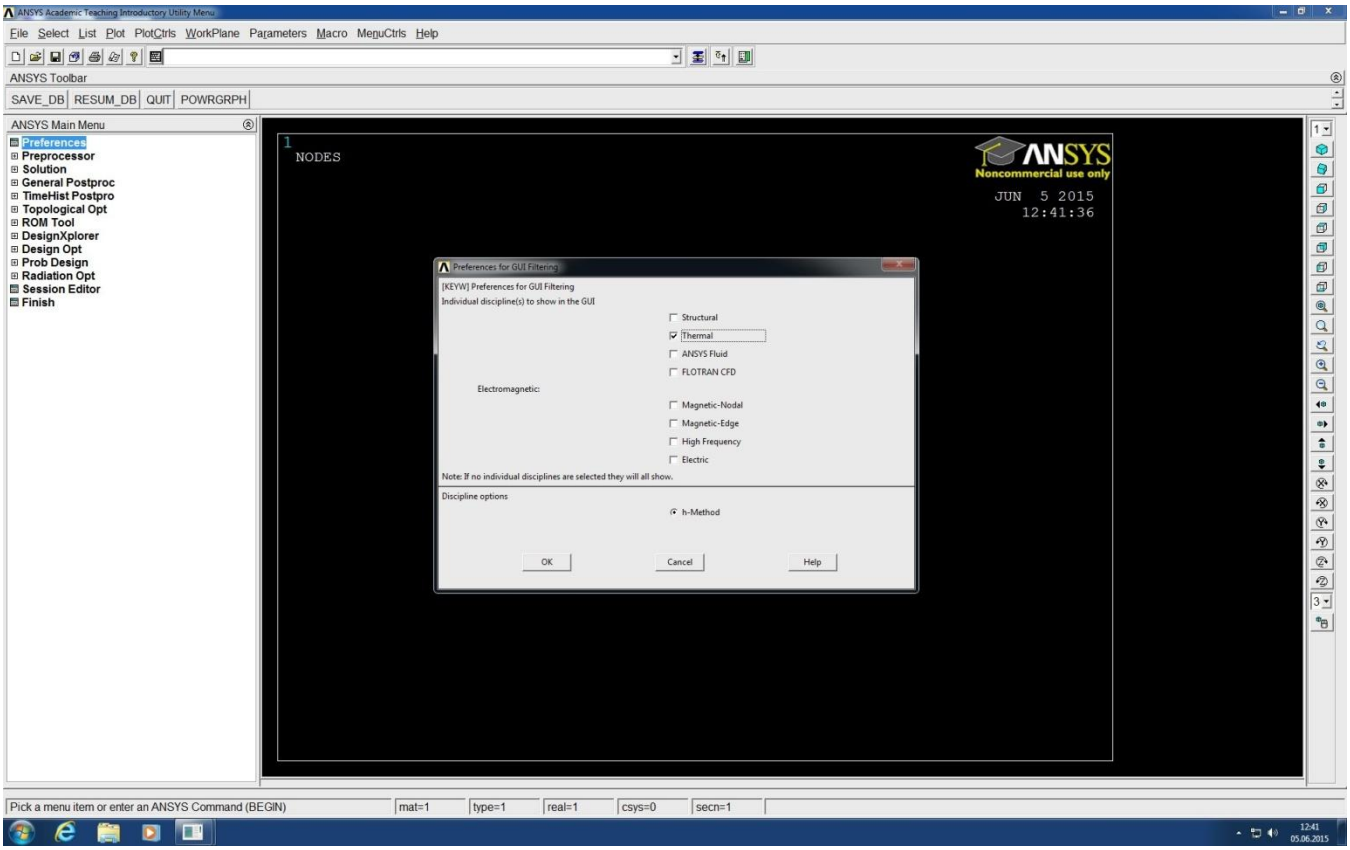

Figure 17: Preference selection through the ANSYS GUI

This loads all the required sub-routines for thermal analysis in to the preprocessor for subsequent modeling and meshing steps. In the next step, the building blocks of the model, i.e. elements are specified. The 2D iso-parametric element *PLANE55* is selected and its specifications regarding geometry and placement of nodes (denoted by solid fill circles) are as follows (ANSYS Mechanical APDL element reference guide):

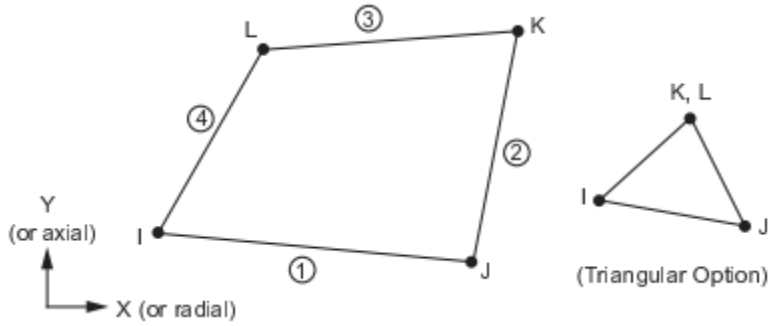

Figure 18: Geometry of element PLANE55 with placement of nodes (ANSYS Mechanical APDL element reference guide)

Figure 16 shows the method of specifying *PLANE55* as the element to be used in the model and its hierarchical position in the ANSYS GUI:

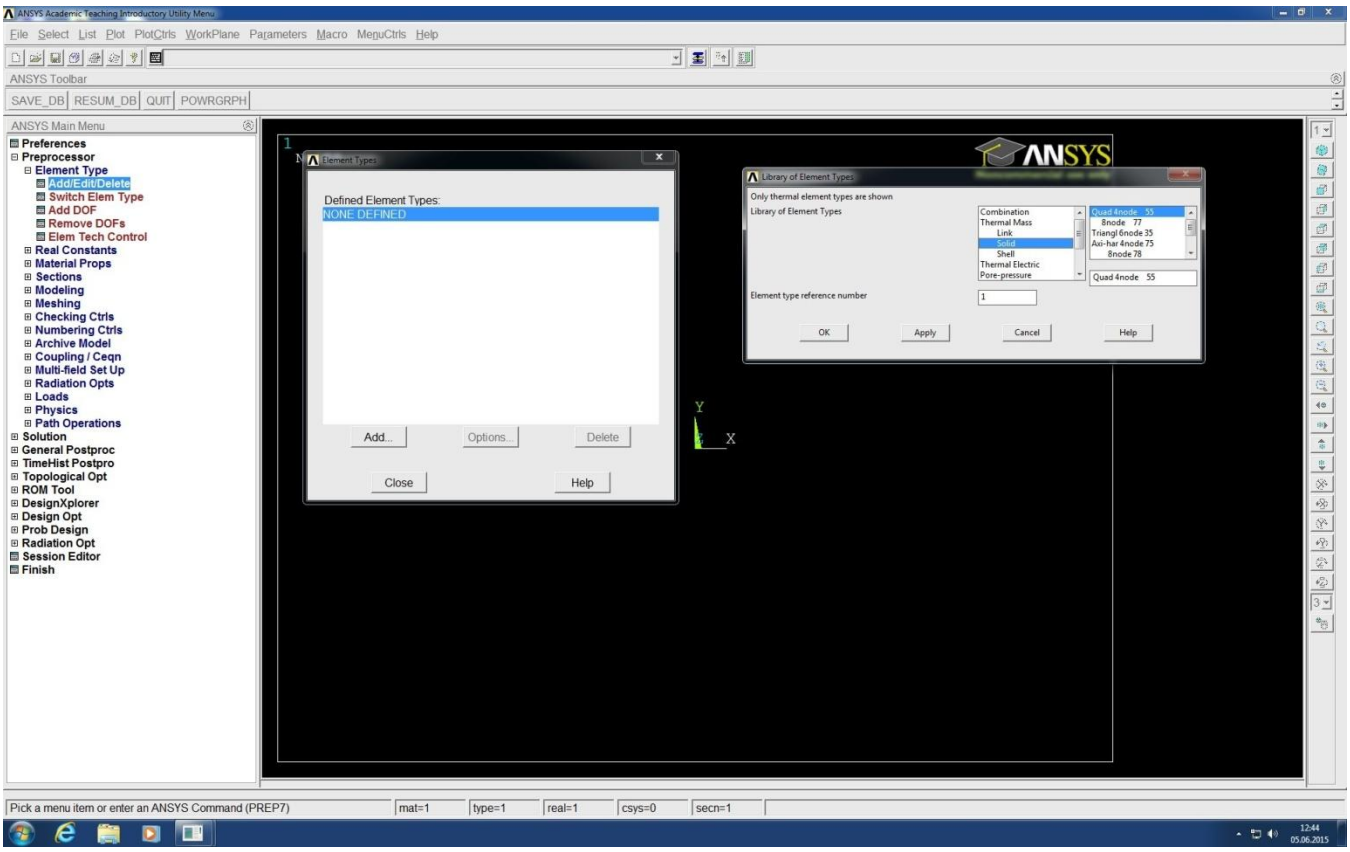

Figure 19: Element selection through the ANSYS GUI

The next step is to input the material properties. This requires us to specify the method of heat transfer dominant in the system and the behavior of material properties (i.e. thermal transmissibility). Conduction is set up as the dominant mechanism of heat transfer because the steady state heat transfer equation for conduction is the closest analogue to pressure distribution under the same steady state conditions (Karakas and Tariq, 1991). Simulations have been carried out for 2 sets of material property behavior. In the terminology inbuilt into the software, the first set of simulations is for 'isotropic' behavior. This implies that the specified thermal property (i.e. thermal transmissibility *TXX*) is the only one acting throughout the system. As stated earlier, this resembles a reservoir with $K_V = 0$. The second set of simulations is for 'orthotropic' behavior. Simply put, herein the software considers the values of thermal transmissibility to be varying along the entire 3 axis' and we input 3 distinct values, *TXX*, *TYY* and *TZZ* (*TZZ* is irrelevant as the model is 2D, only existing in X-Y plane). Putting TXX = TYY simulates the isotropic reservoir behavior where $K_H = K_V$. The case of $K_H = 10*K_V$ has also been investigated under the 'orthotropic' simulations to study the behavior of reservoir anisotropy. It is an assumption herein that the thermal transmissibility parameter is analogous to reservoir permeability (Karakas and Tariq, 1991) and hence the heat balance equation, which is numerically solved by the software, provides a pressure distribution model under specified inner and outer boundary conditions. Figures 17 and 18 provide the hierarchical position of the material model input option in the ANSYS GUI.

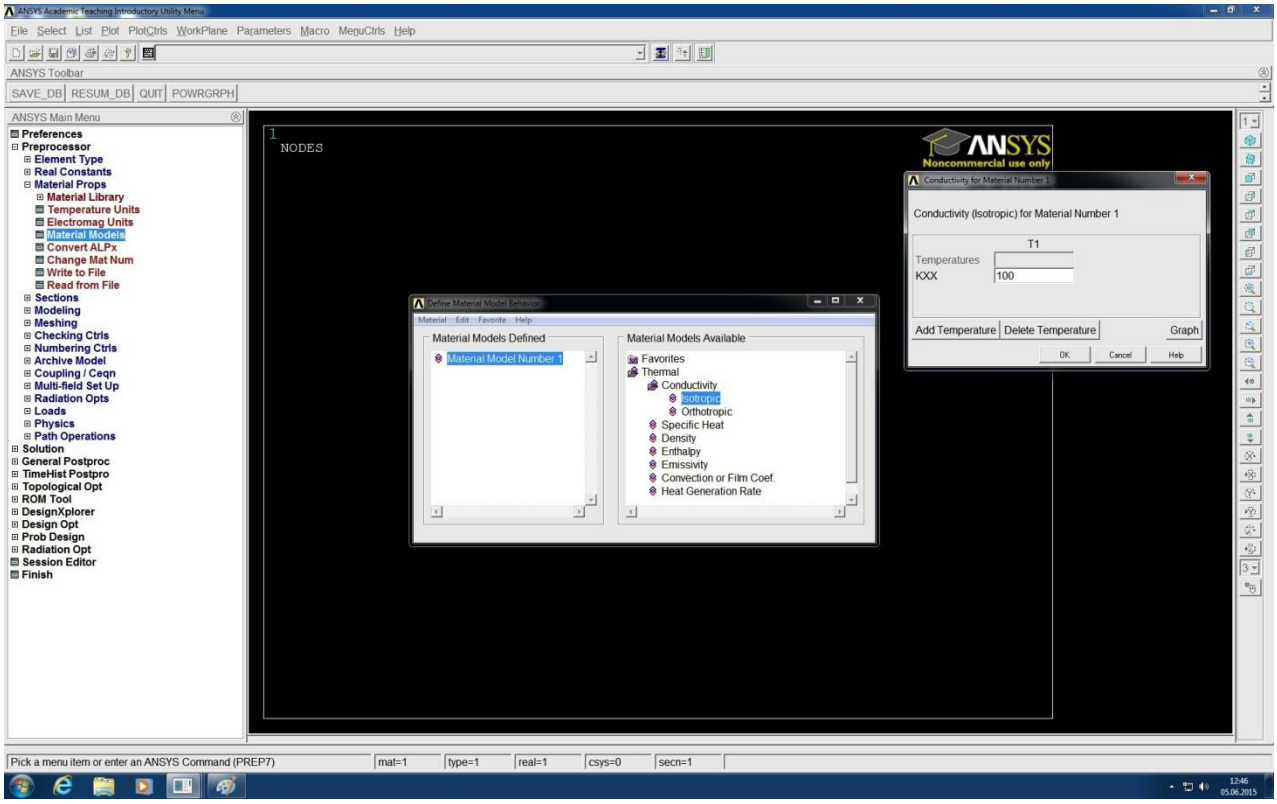

Figure 20: Input process for formation permeability through the ANSYS GUI

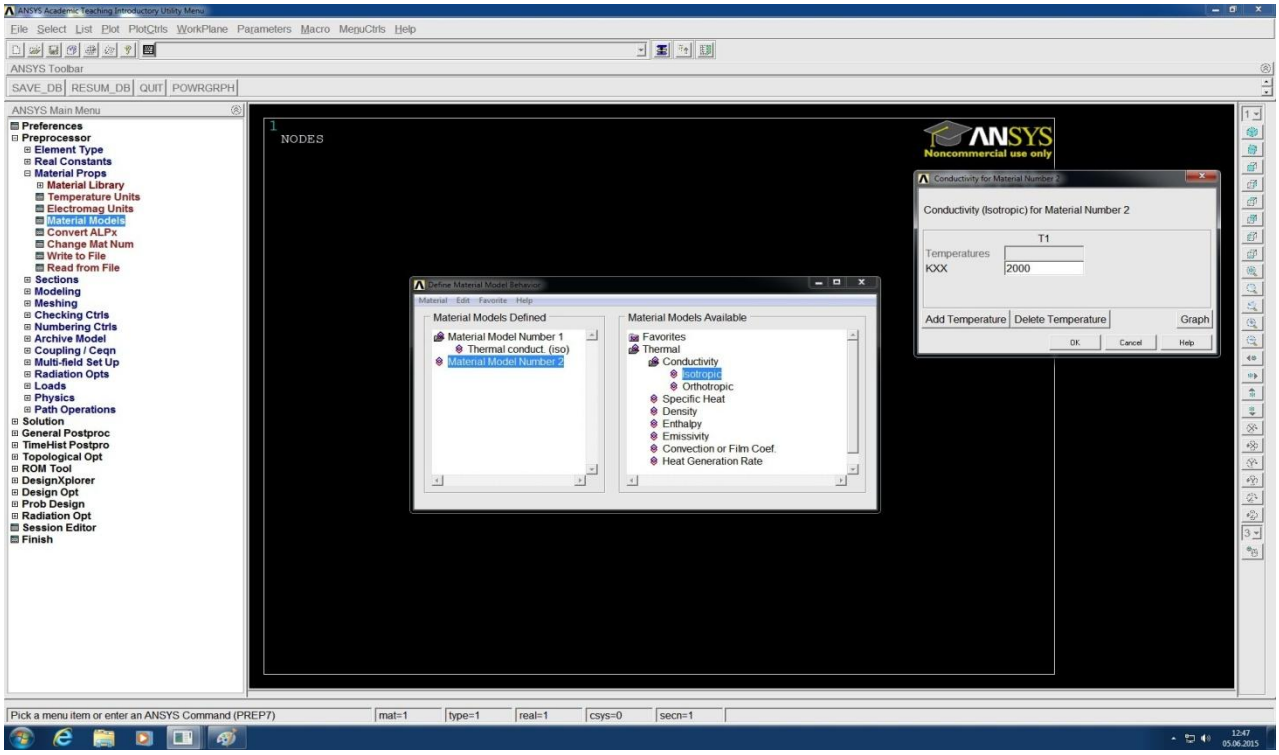

Figure 21: Input process for perforation permeability through the ANSYS GUI

Having configured the element and material behavior, the next task at hand is to create a geometrical representation of the well and perforation configuration. This is done by using, what is known in the software`s terminology, as 'primitives'. Primitives are basic geometric shapes which can be input to the working plane and made to interact with each other in a way which is representative of the real phenomenon being modeled. Primarily two primitives have been used extensively in the modeling process, circles with annulus and rectangles. Circles with annulus has been used to model well to perforation tip and perforation tip to reservoir boundary by putting in appropriate radii. The process and its place in GUI hierarchy are shown in figures 19 and 20.

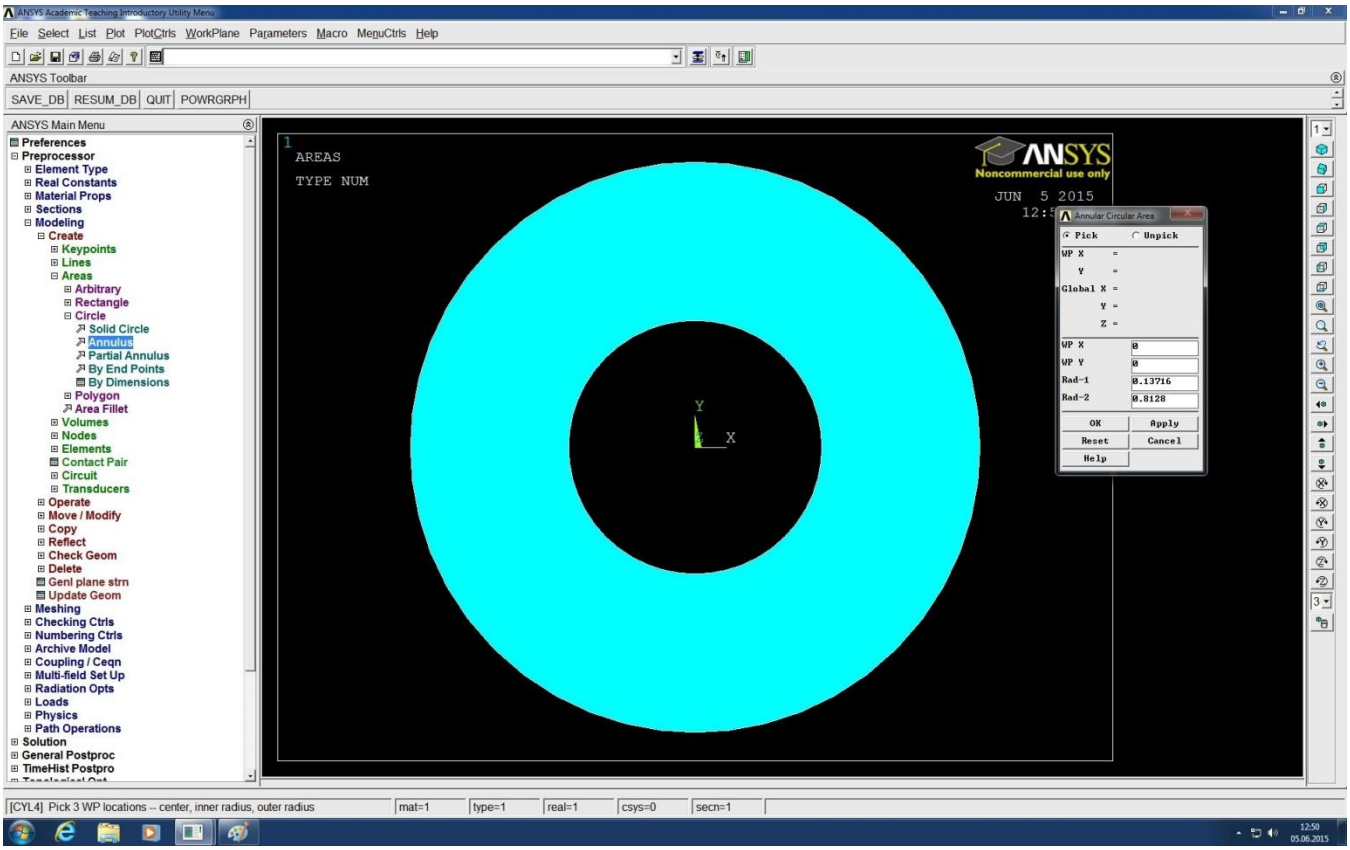

Figure 22: Modeling from the well to perforation tip, inner radius = well radius & outer radius = well radius + perforation tunnel length

The small dialog box in figure 19 is for the next annular circle that is going to be inserted in the active working plane. The inner radius for the second circle will be equivalent to well radius plus perforation length and the outer radius will be the reservoir radius. For all the simulation runs, reservoir radius was kept constant at 32". This was done due to the limitations of the student version of the software. A radius higher than 32" resulted in the number of nodes exceeding the allowed limits.

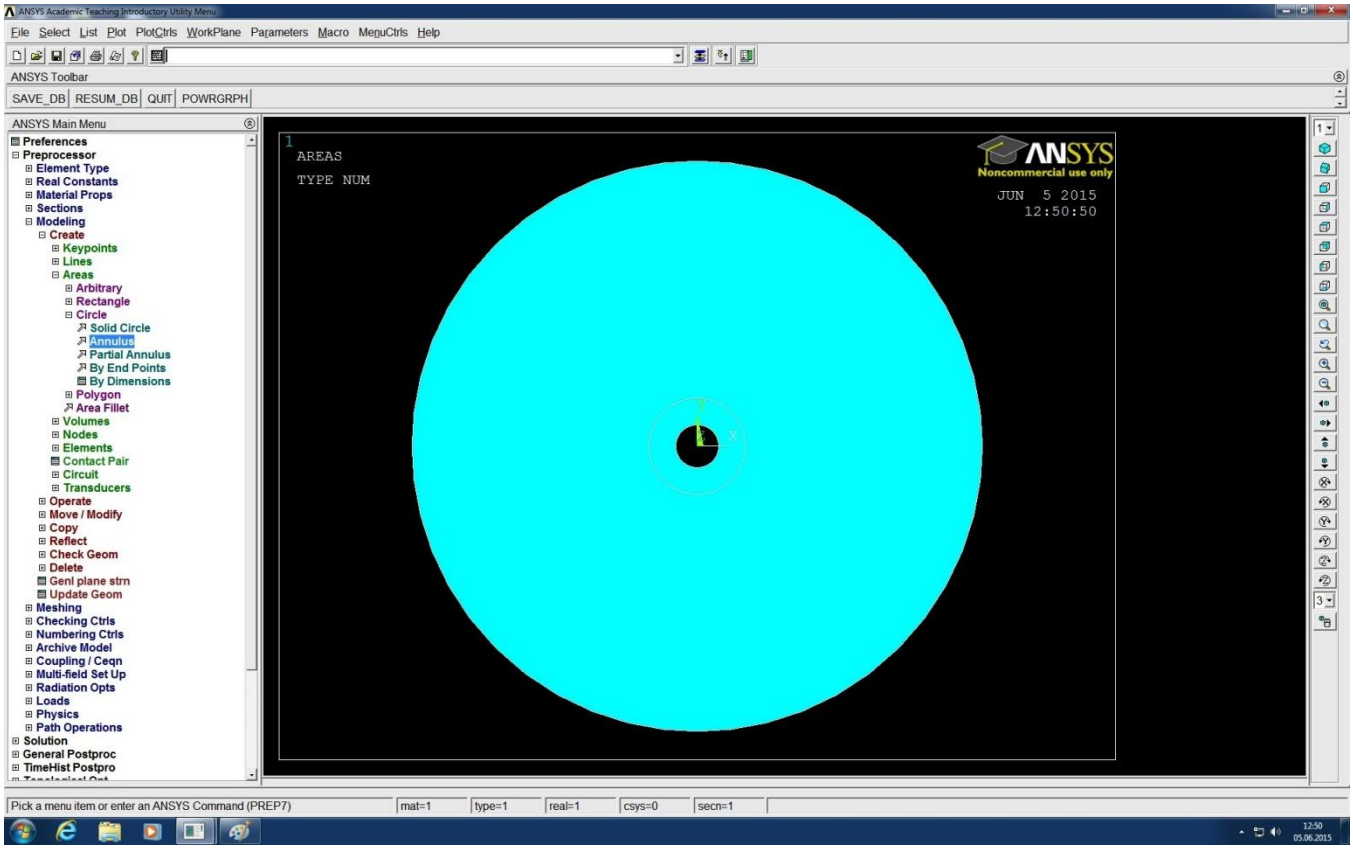

Figure 23: Modeling from the perforation tip to the reservoir radius, inner radius = well radius + perforation tunnel length & outer radius = 32"

Figure 20 represents the well and the boundary of the investigation radius (the radius beyond which the effects of perforation are not felt and reservoir pressure is constant). The inner black circle represents the borehole surrounded by another circle the diameter of which is the perforation tunnel length. Finally, the last circle extends from the tip of the perforation to the boundary of investigation radius. All these circles are independent of each other, however for the calculation from outer boundary to inner boundary to work; these circles should interact with each other in a unified manner.

This can be done by accessing the operate subroutine found in the modeling routine of the software. ANSYS provides 'Boolean operators', tools which can be used to establish connectivity between different geometric primitives which form the model. The Boolean operator termed 'glue' is applied to all the circles on the work plane. The results in the software treating the 2 different circles as one whole during the approximation of the numerical solution, hence providing a continuous and stable solution all the way from the outer boundary (investigation radius = 32") to the inner boundary (well radius). The application of the glue operator is shown in figure 21. The small dialog box in the figure enables the user to pick the areas which have to be glued together (in our case, the 2 circles).

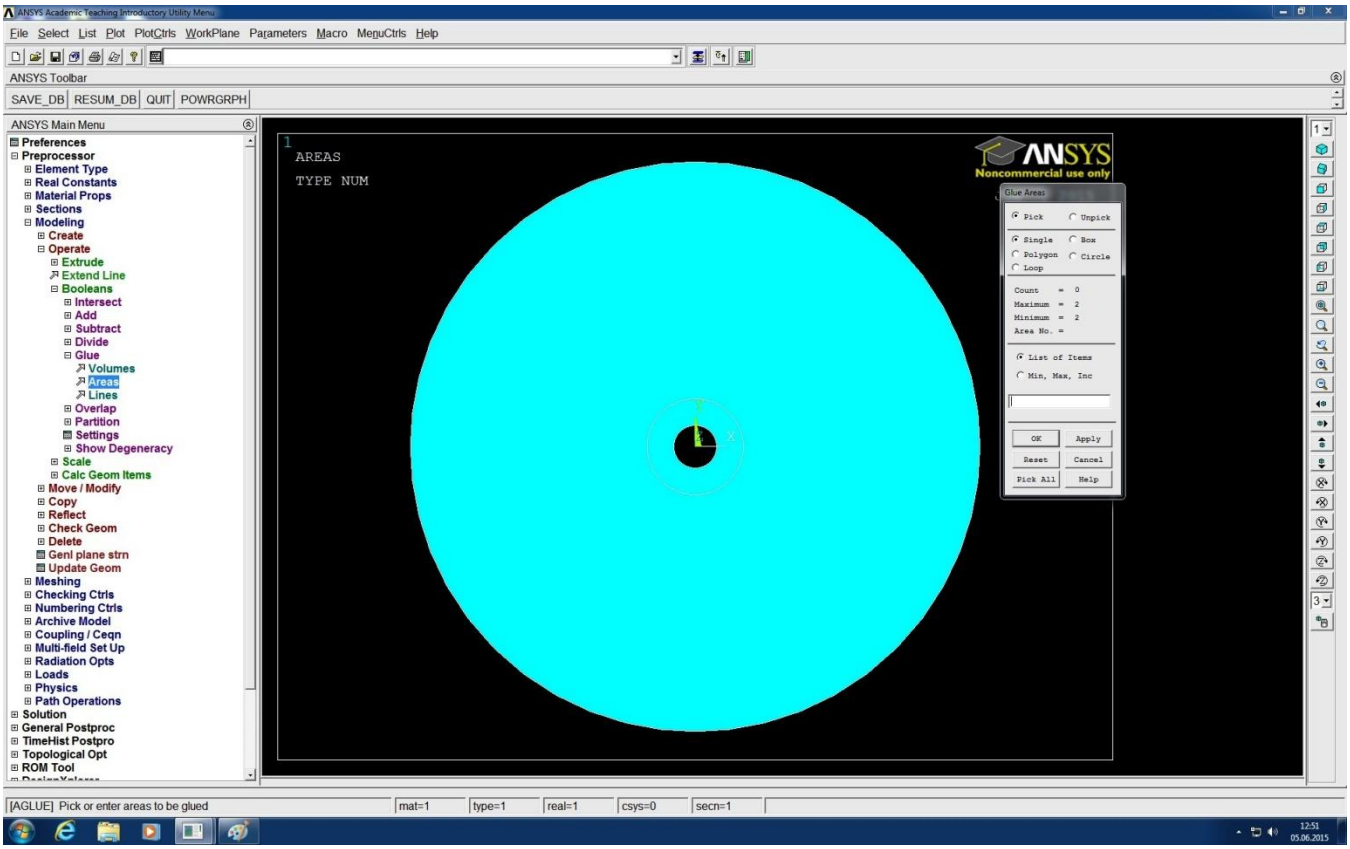

Figure 24: Using the Boolean operator 'glue through the ANSYS GUI

The next step is to include the perforation in the model and specify as to how it interacts with the existing components of the system. For the purpose of 2D analysis, the perforation can be assumed to be a thin rectangular strip with constant width of 2" and length equal to that of the perforation tunnel. Hence a rectangular primitive is used for modeling the perforation and placing it on the existing coordinate system.

The perforation strip is modeled to interact with the existing geometry by using the Boolean operator termed 'overlap'. This operator sets the area covered by the perforation strip to take precedence over the underlying formation area. This is the desired result because we have set two different material models, one for the formation and one for the perforation. In area where perforation and formation are overlapping, we want the material properties specified for perforation to takeover so that the numerical solution is a real representation of the physical phenomenon being modeled herein. Figure 22 shows the process of including a rectangular strip as perforation and figure 23 exhibits how the 'overlap' operator can be used for setting the mode of interaction between the perforation and rest of the model.

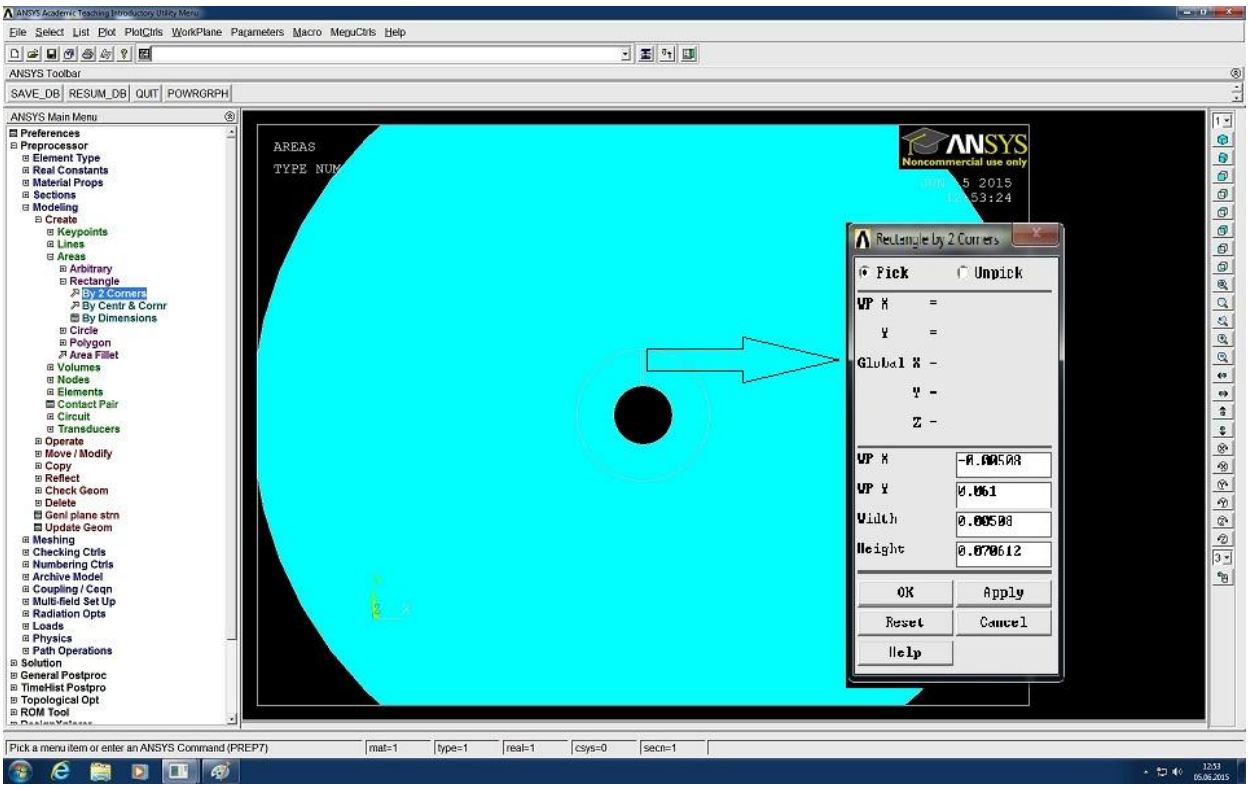

Figure 25: Using a rectangular primitive to model the perforation through ANSYS GUI

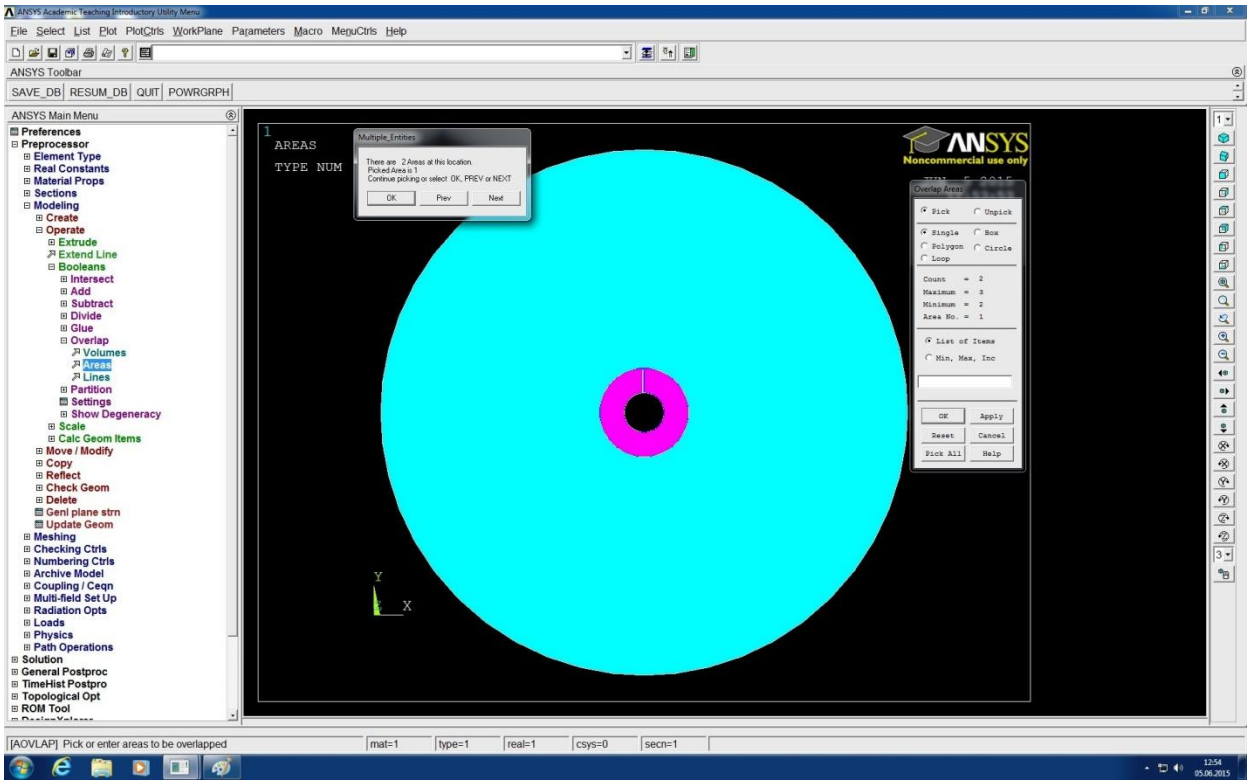

Figure 26: Using the Boolean operator 'overlap' to superimpose the perforation over the model through the ANSYS GUI

This concludes the modeling work. Now, the model has to be meshed. This directly implies to dividing the modeled geometry in to the specified element (*PLANE55*) for node generation and assigning material properties to different parts of the model (the perforation has to be assigned the material model 2 and the formation has to be assigned material model 1). This task can be accomplished through the meshing tool which is accessed through the meshing subroutine in the GUI as shown in figure 24.

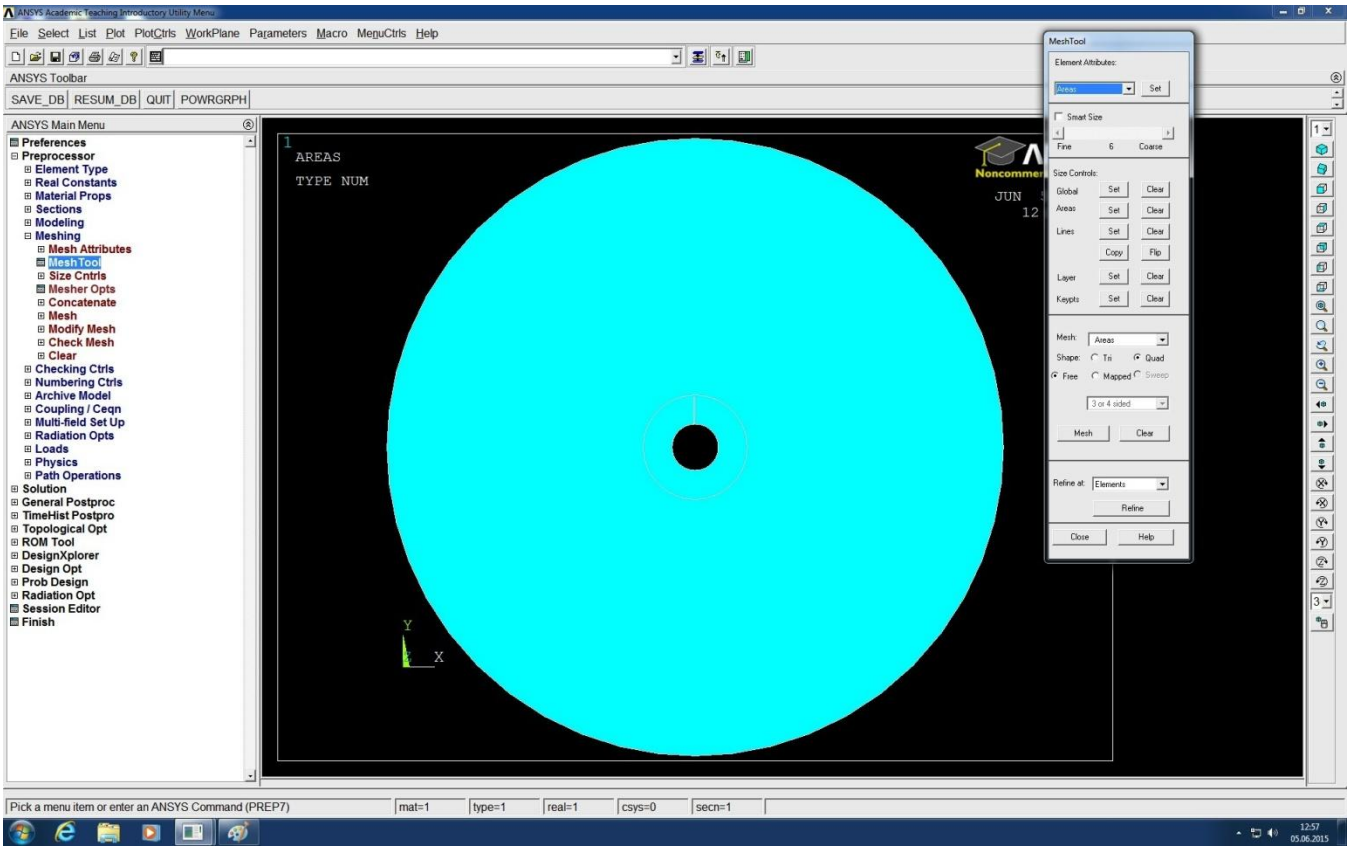

Figure 27: Accessing the meshing tool through the ANSYS GUI

Once the meshing tool is active, different areas can be selected to assign element and material model. In this model, we will assign the iso-parametric element *PLANE55* to the entire geometry; however 2 different material models will be used.

As stated earlier the perforations will be assigned material model 2 (which has a very high transmissibility) and the formation will be assigned material model 1. Varying transmissibility between 2 models is expected to simulate the reality wherein there is a large contrast between formation and perforation permeability; to an extent that perforations can be considered to be acting like infinitely conducting fractures, given that the condition of very high shot density is satisfied (Furui et al). Figures 25-27 illustrates how to achieve this through the GUI.

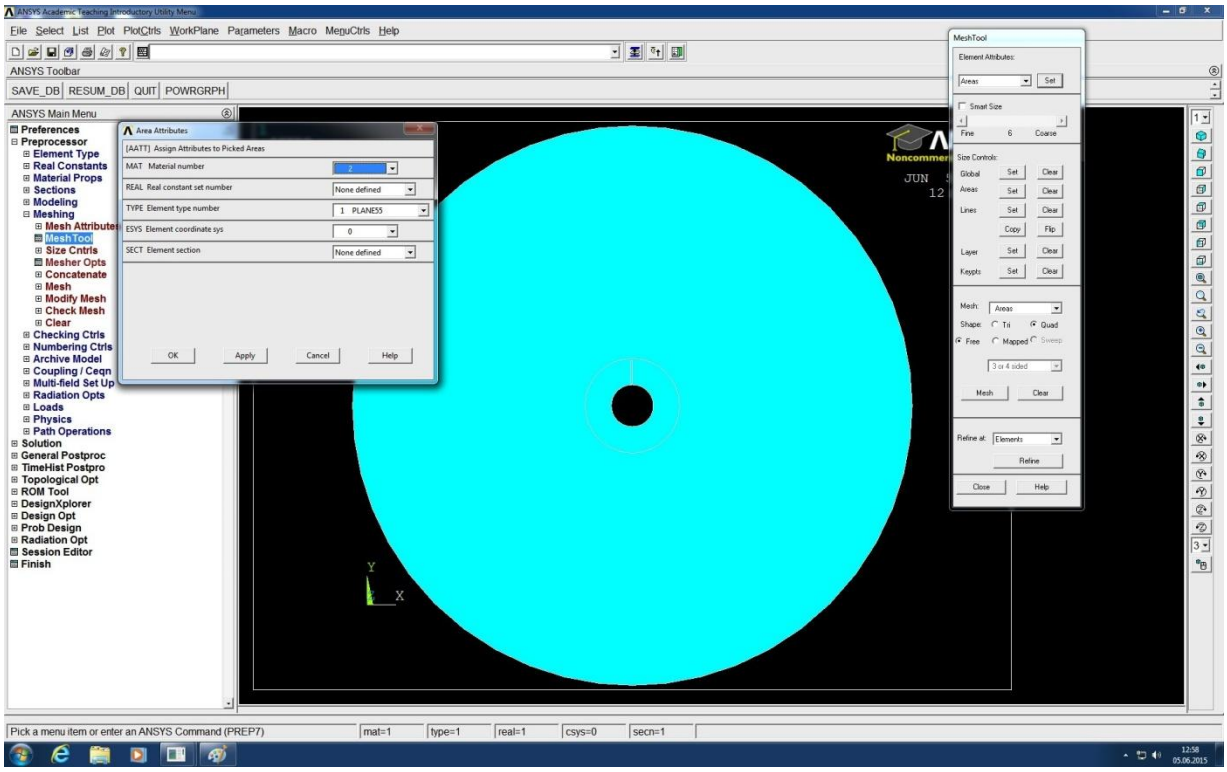

Figure 28: Assigning element and material model to perforation through the ANSYS GUI

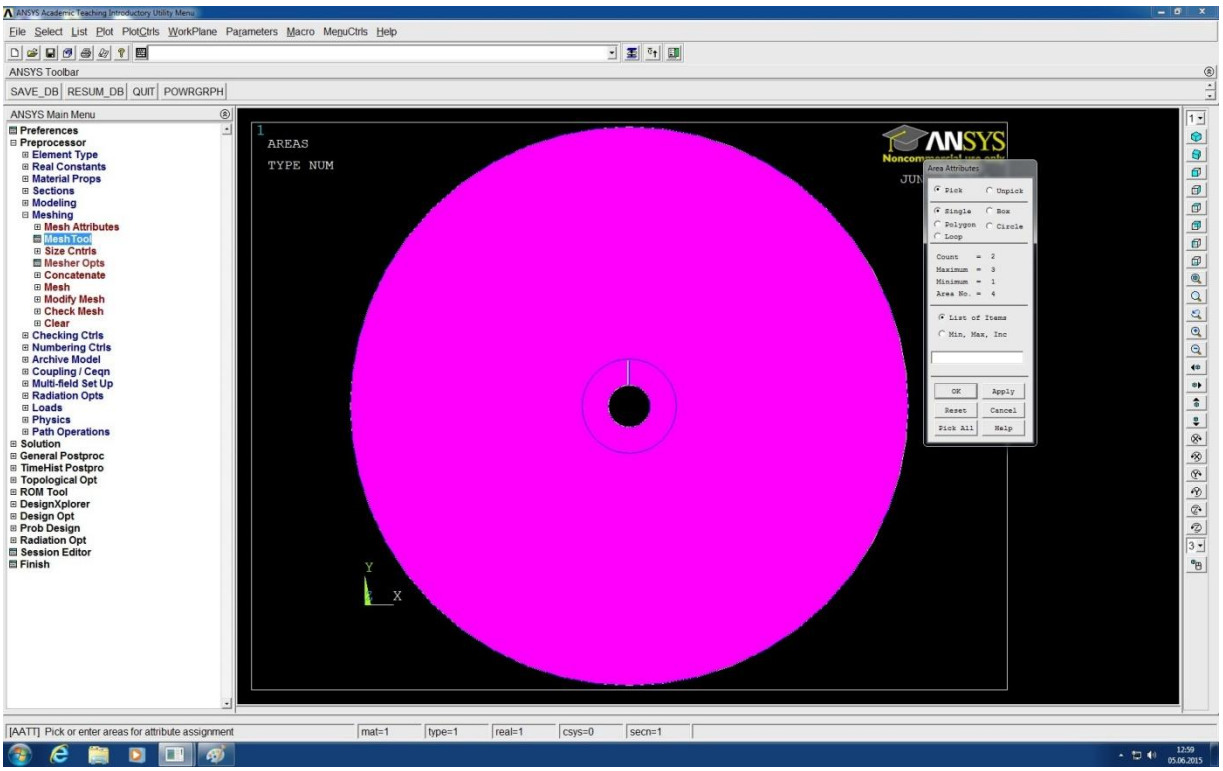

Figure 29: Selecting rest of the remaining area for element and material model assignment

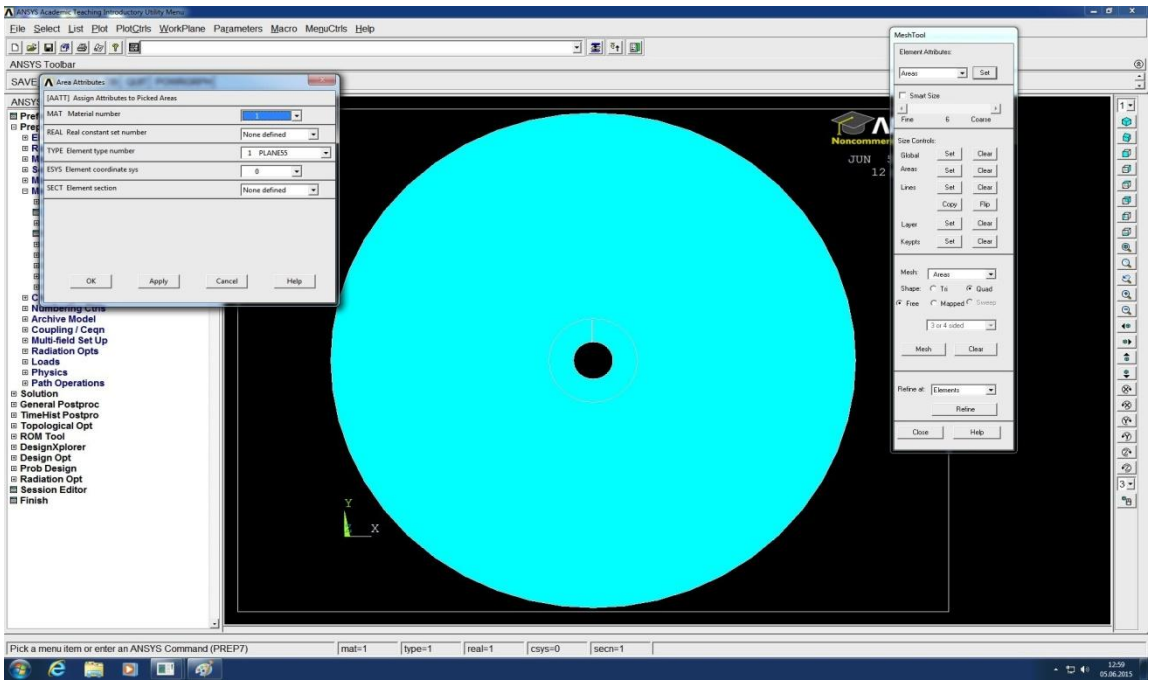

Figure 30: Assigning element and material model to the formation through the ANSYS GUI

Having assigned all the relevant information, the next step is to mesh the model. The entire model area is selected, smart size is activated and set to 1 (finest meshing possible in the non commercial version) in the mesh tool window and the command to mesh the model is issued. The meshed model is given in figures 28 and 29.

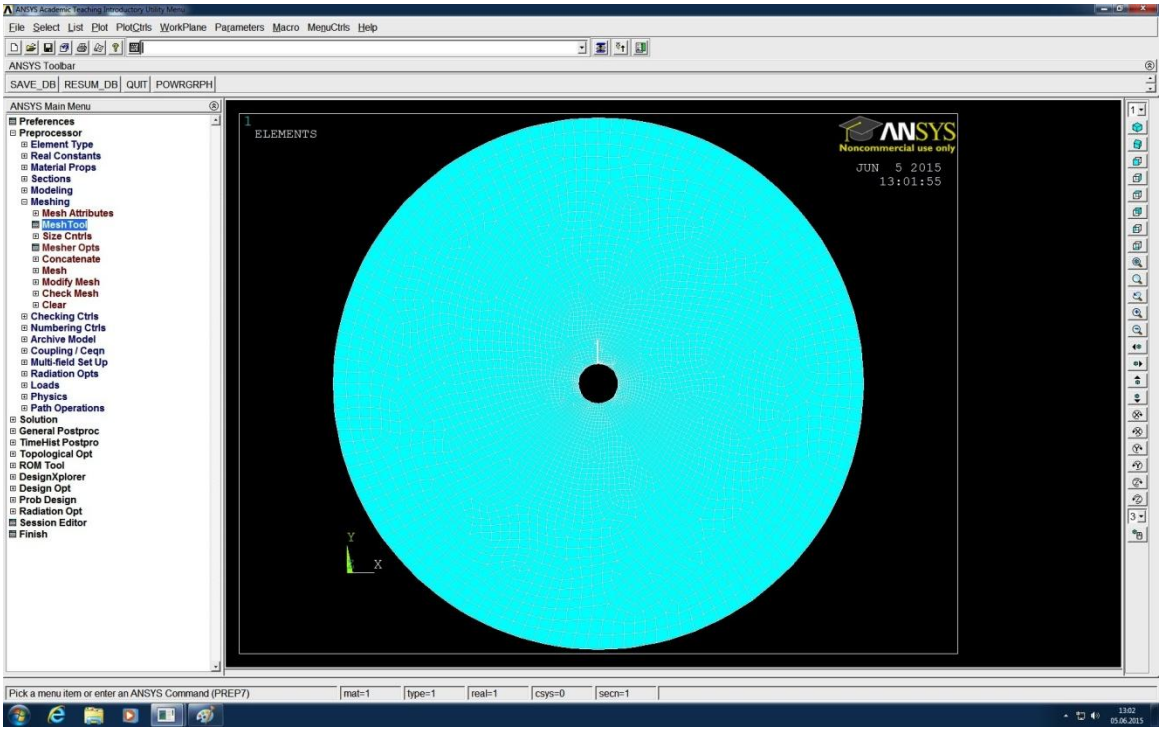

Figure 31: Meshing completed, i.e. the model is successfully divided into elements

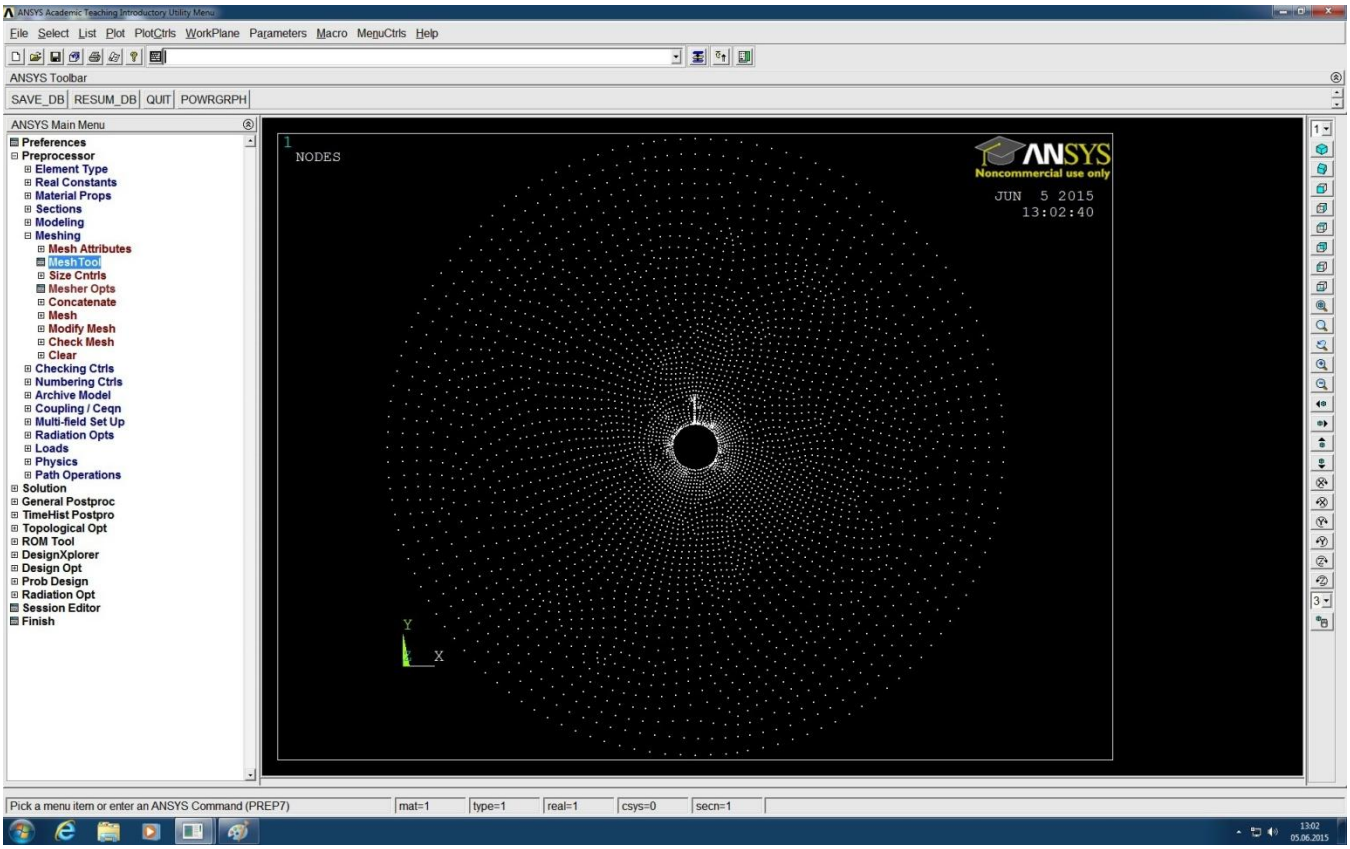

Figure 32: Placement of nodes in the meshed model (note the high nodal density around the well and the perforation)

This concludes the work that has to be carried out in the meshing sub-routine of the ANSYS pre-processor. We are now ready to exit the pre-processor and make the final input for numerical solution. This is done by accessing the routine named 'solution'. This section enables us to apply loads over the model that we have created and meshed and obtain a numerical solution for the steady state heat transfer (conduction) equation. The temperature distribution model thus created is considered analogous to pressure distribution and the values are used for skin factor calculation.

Since this is a 2D model, the outer boundary is represented by 4 lines and a temperature of 320 ^{O}C is applied to these lines as outer boundary condition. For the purpose of this work, this is same as reservoir pressure of 320 bar. As for the inner boundary condition, 80 ^{O}C is applied at the root of the perforation and same as before, this is considered equal to a well flowing pressure of 80 bar. A convection field is set up inside the wellbore to account for any major pressure changes occurring due to flow of fluid in the well, however this is not necessary as it was found during simulations that the said effects are nearly negligible. Having applied all the loads, the last step is to solve for the current load step. All the steps mentioned above are shown in figures 30 to 35.

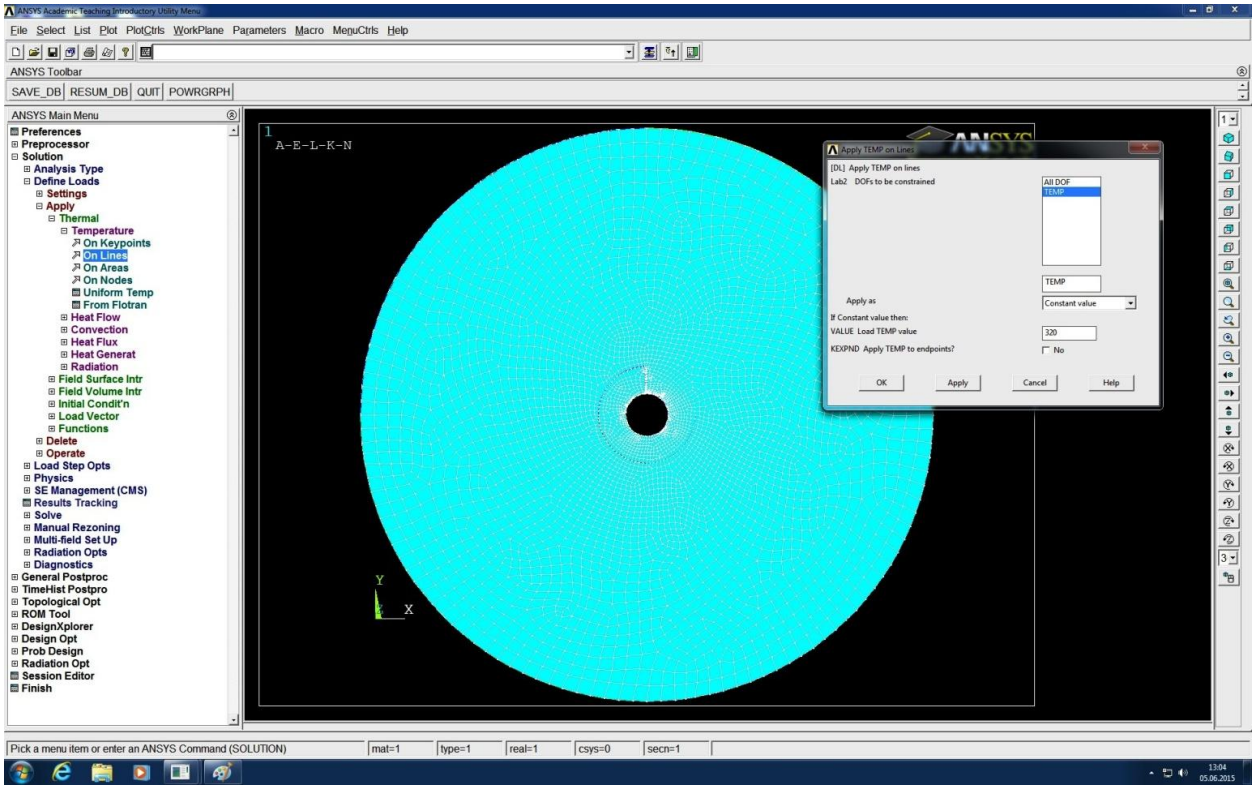

Figure 33: Application of load on the outer boundary

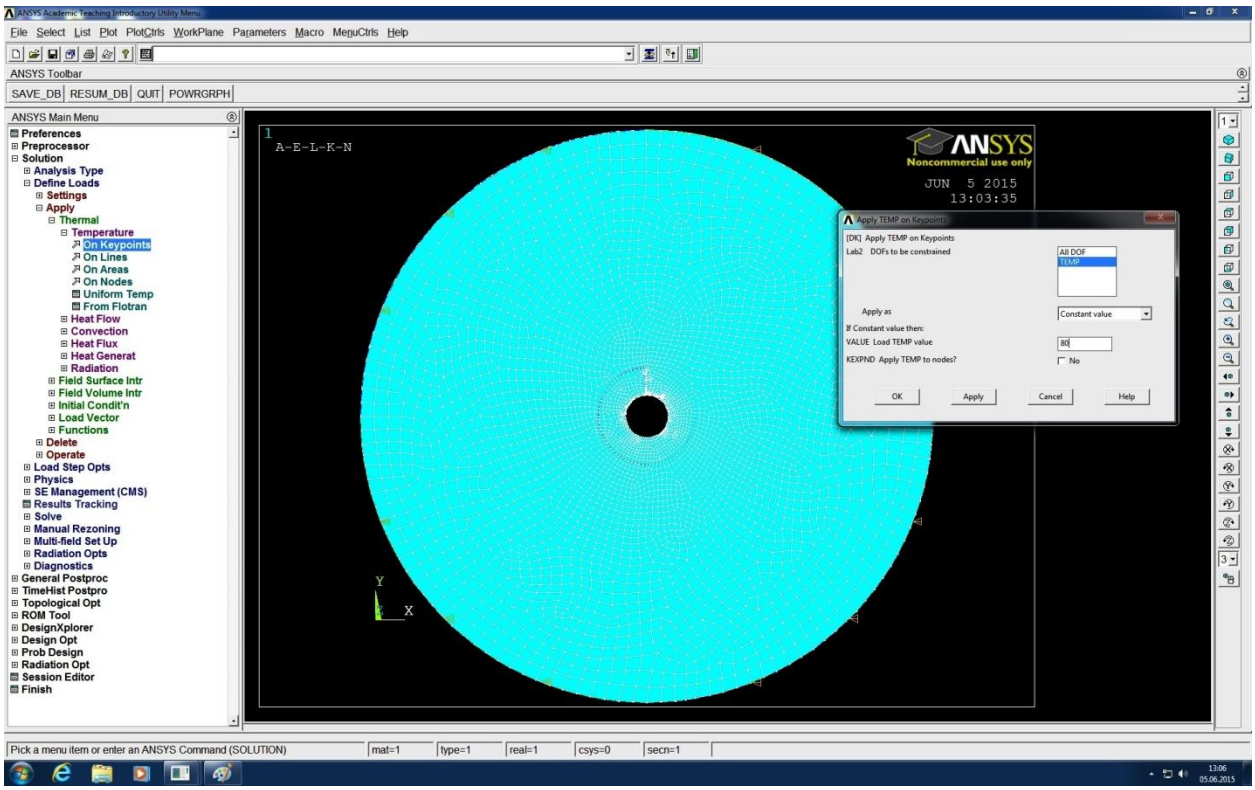

Figure 34: Application of load on the inner boundary (root of the perforation)

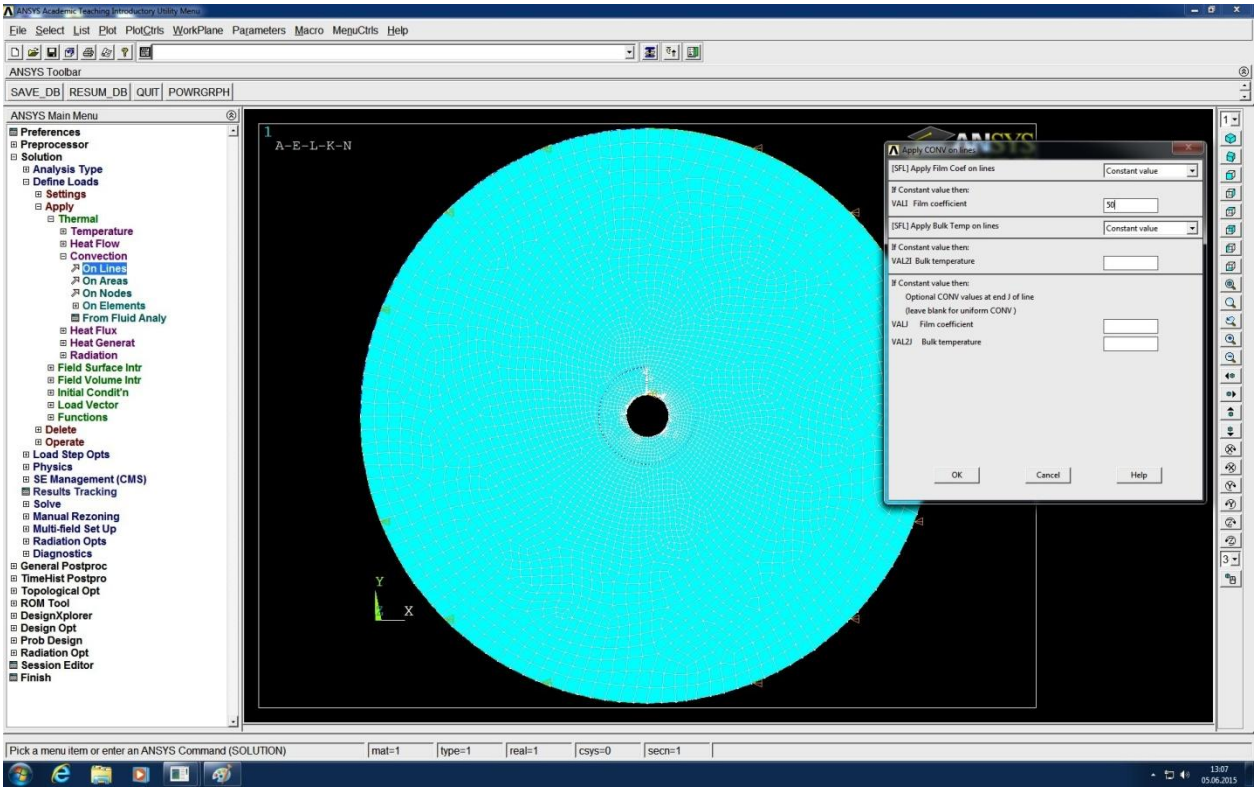

Figure 35: Application of convection inside the well to account for fluid flow effects

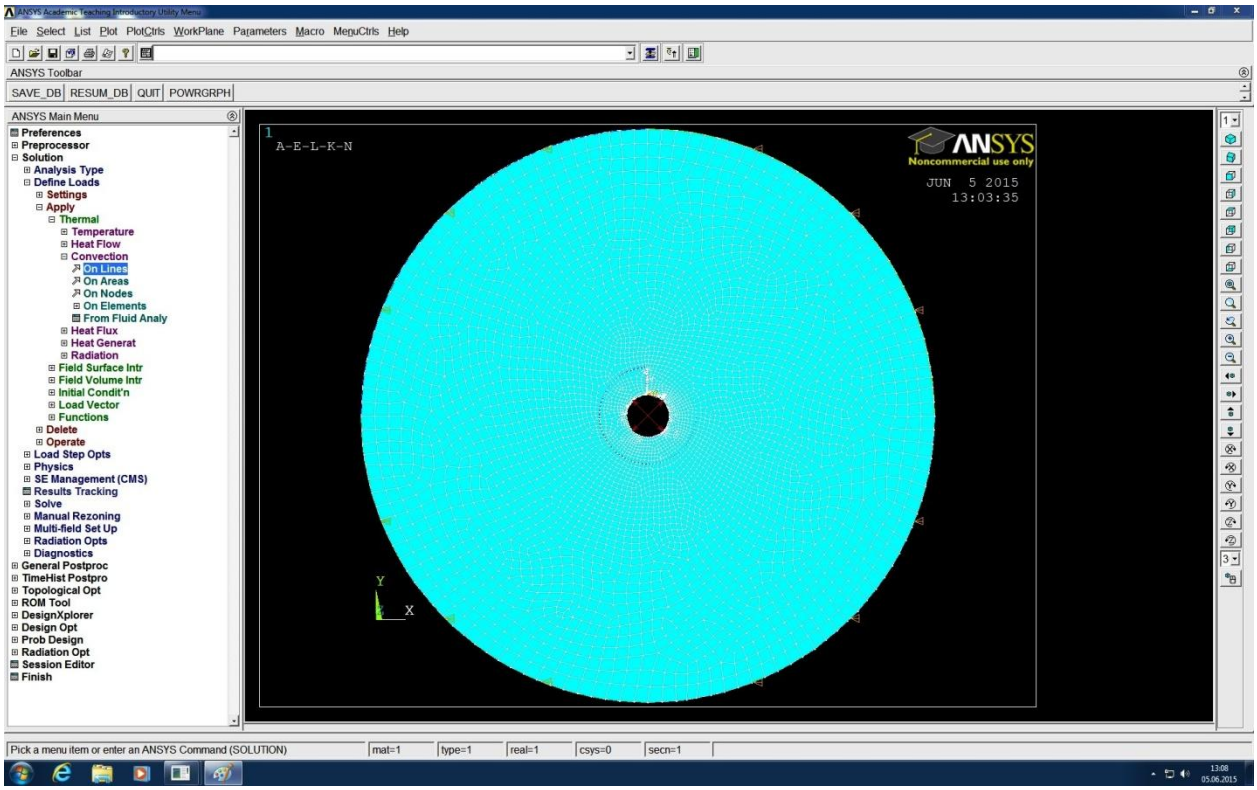

Figure 36: Model with all the loading data

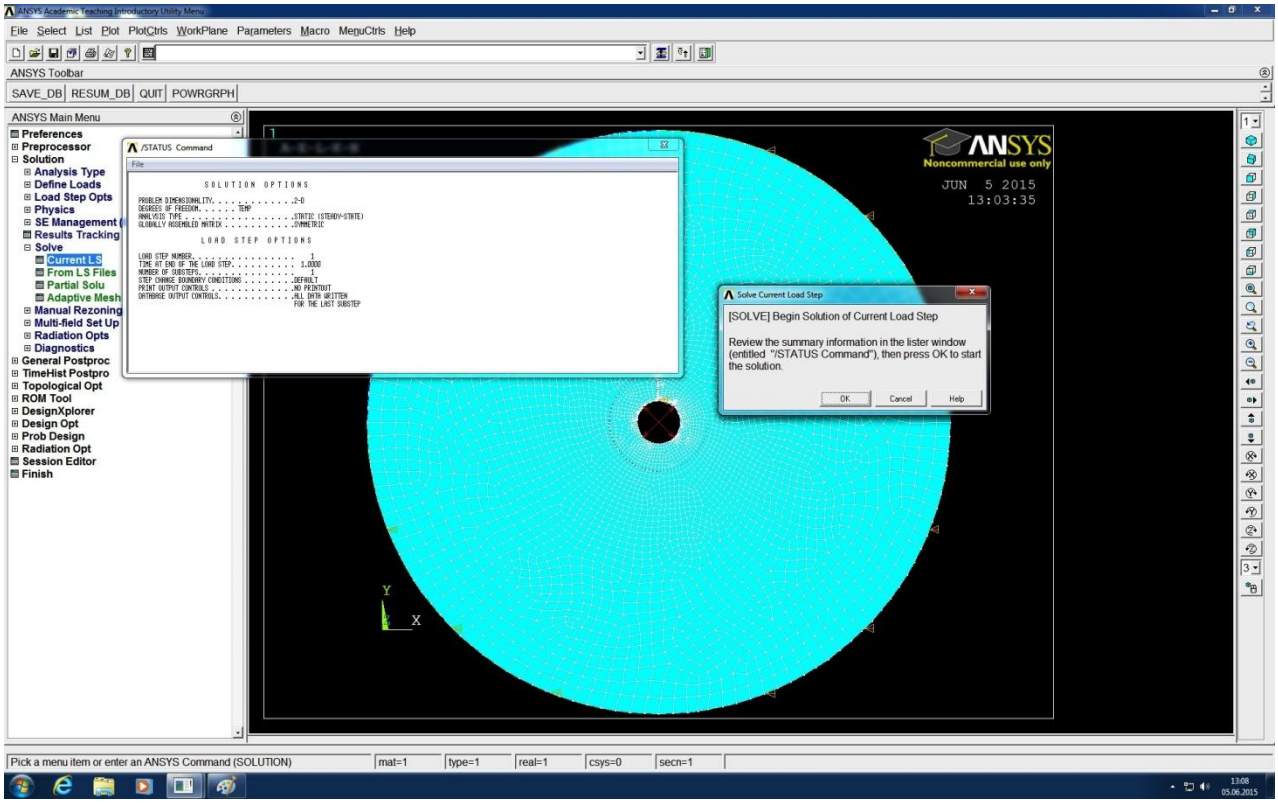

Figure 37: Solving for the current load step

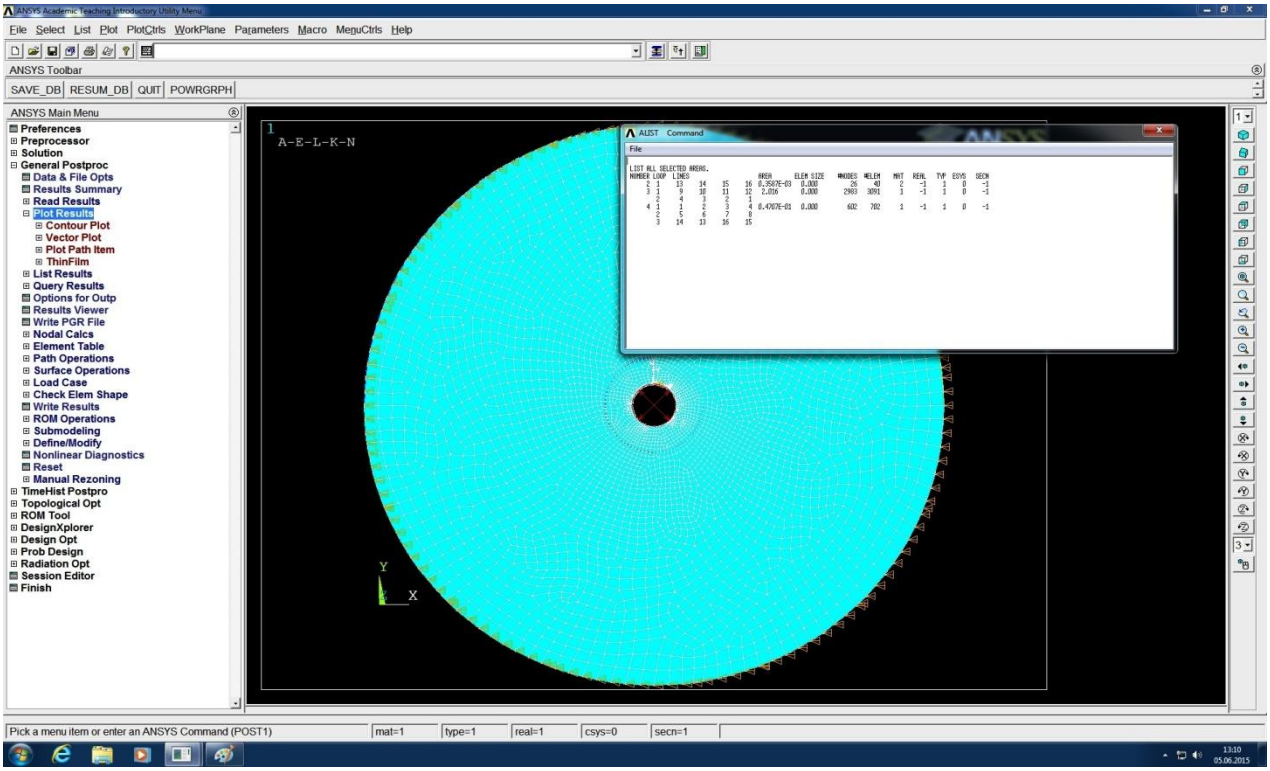

Figure 38: Solved model with information regarding number of nodes

This concludes the simulation run. There are a variety of options available for viewing the results and all of them can be found under the subroutine 'general postproc'. The preferred method is to view the distribution model as a contour plot and this can be easily managed through 'general postproc' as shown in the following figures:

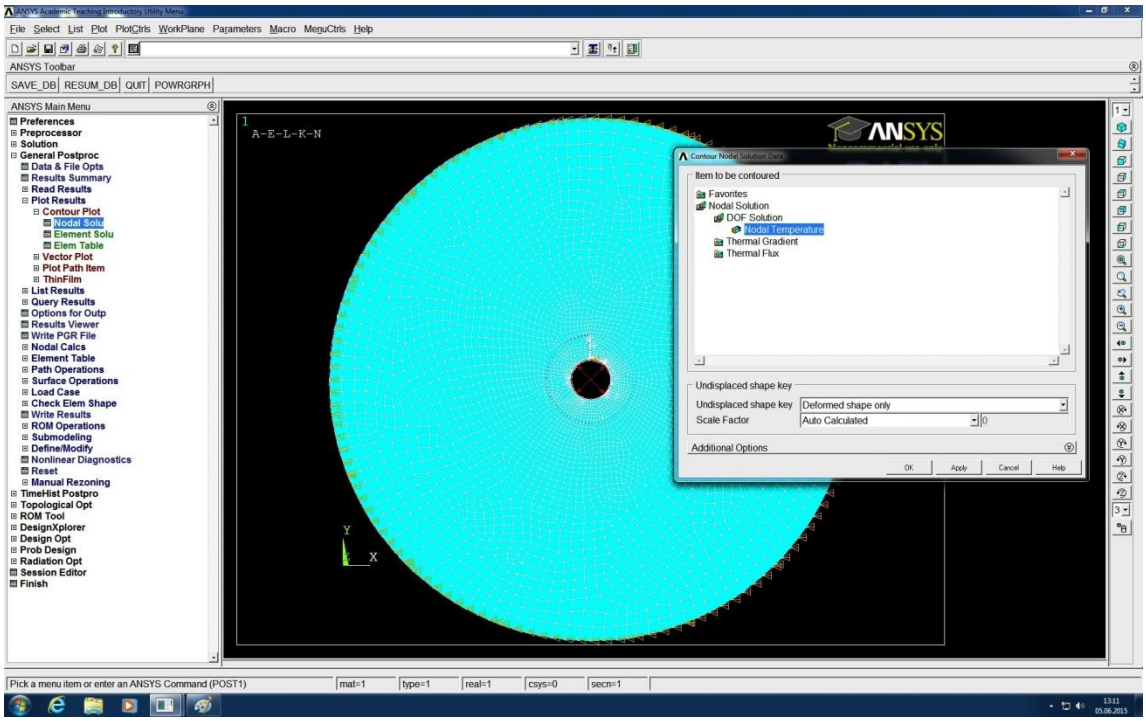

Figure 39: Issuing the command to view the result as a contour plot

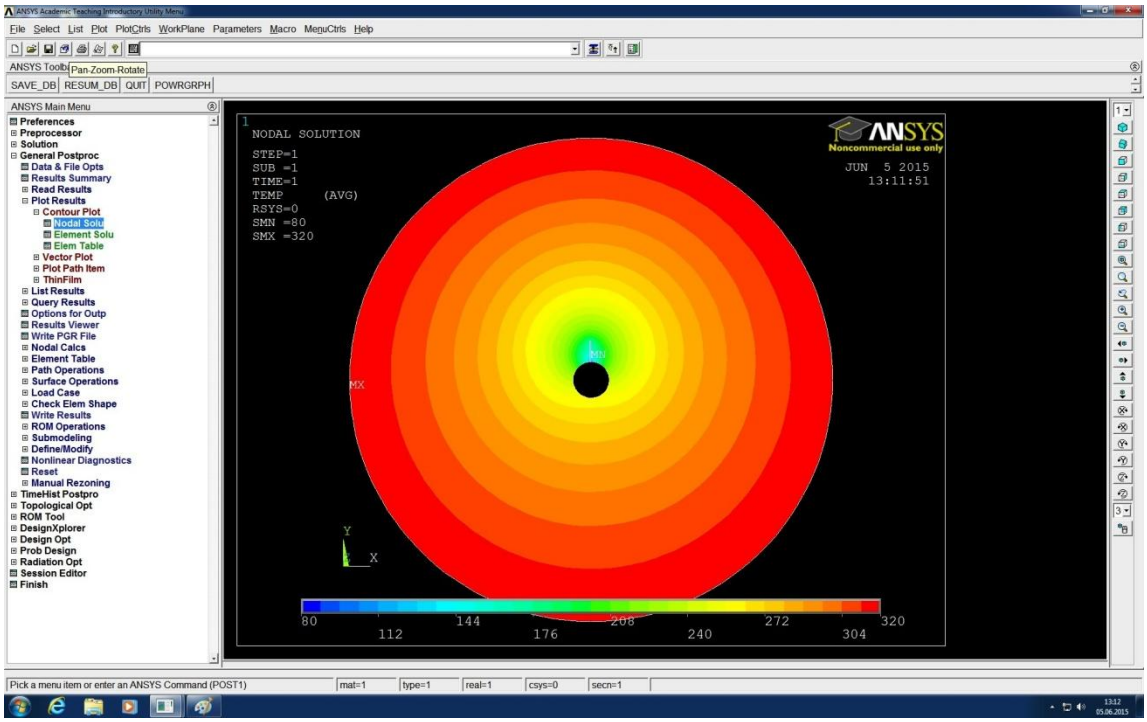

Figure 40: the numerical solution of the load step presented as a contour plot

This concludes the methodology for creating and solving a model for non oriented perforations. For oriented perforations, the entire process is same however we add two rectangular primitives instead of one. The coordinates of these two primitives are calculated by simple trigonometric transformation of oriented perforations' coordinates and two equivalent rectangular strips are used to simulate the effect of off-setting the perforations by 20^{O}. Figures 40, 41 and 42 are presented herein to demonstrate how the oriented perforations appear on the GUI.

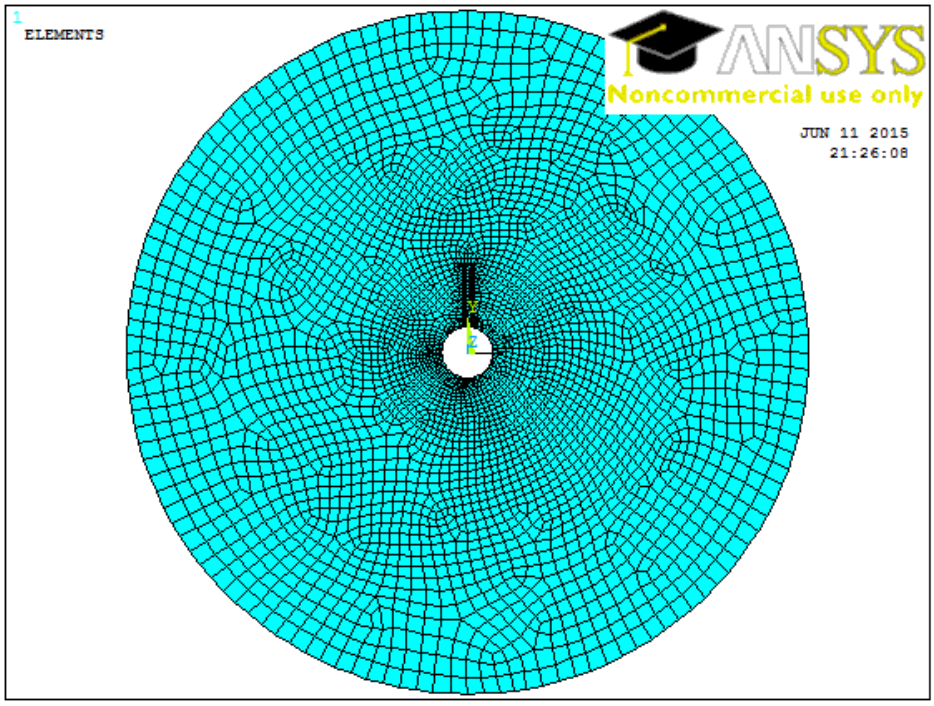

Figure 41: Meshed model for oriented perforations

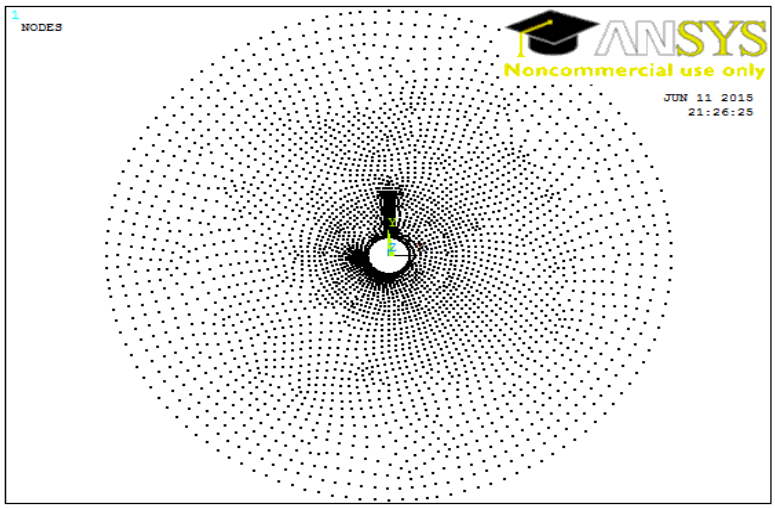

Figure 42: Nodal distribution for oriented perforations

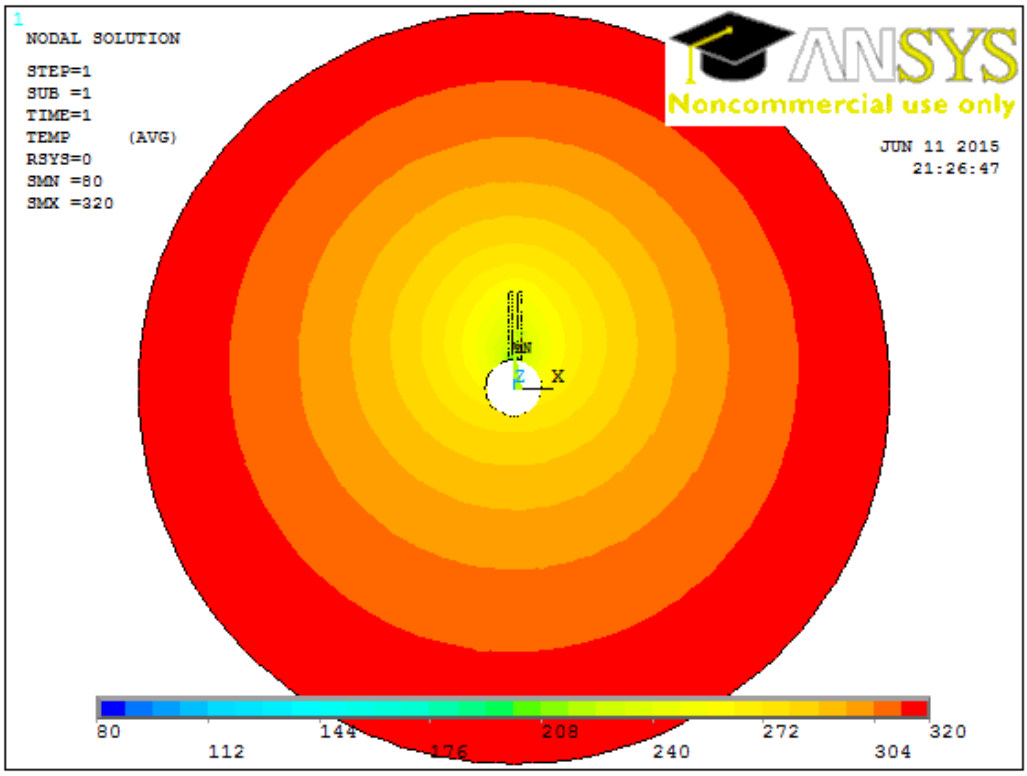

Figure 43: Numerical solution of the load step presented as a contour plot

REFERENCES

Andrews, J., Kjørholt, H., and Jøranson, H. 2005. Production Enhancement from Sand Management Philosophy: A Case Study from Statfjord and Gullfaks. SPE Paper 94511 presented at SPE European Formation Damage Conference held in Scheveningen, The Netherlands, 25-27 May.

Andrews, J.S., Jøranson, H., and Raaen, A.M. 2008. Oriented Perforating as a Sand Prevention Measure - Case Studies from a Decade of Field Experience Validating the Method Offshore Norway. OTC Paper 19130 presented at 2008 Offshore Technology Conference held in Houston, Texas, USA, 5-8 May.

ANSYS Mechanical APDL Element Reference. Release 15, November 2013. Canonsborg, Pennsylvania: ANSYS Inc.

ANSYS Mechanical APDL Modeling and Meshing Guide. Release 15, November 2013. Canonsborg, Pennsylvania: ANSYS Inc.

ANSYS Mechanical APDL Thermal Analysis Guide. Release 15, November 2013. Canonsborg, Pennsylvania: ANSYS Inc.

Bellarby, J. 2010. *Well Completion Design*. *Reprint 2010. First Edition 2009.* Oxford, U.K.: Elsevier.

Bethea, R. M., Duran, B. S., and Boullion, T. L. 1985. *Statistical Methods for Engineers and Scientists.* New York: Marcel Dekker.

Brooks, J.E., and Haggerty, D. 2011. Laboratory Simulation of Flow Through a Perforation. SPE Paper 144187 presented at SPE European Formation Damage Conference held in Noordwijk, The Netherlands, 7-10 June.

Freedman, D.A. 2005. *Statistical Models: Theory and Practice.* Cambridge University Press

Furui, K., Zhu, D., and Hill, A.D. 2002. A Rigorous Formation Damage Skin Factor and Reservoir Inflow Model for a Horizontal Well. SPE Paper 74698 presented at SPE International Sypmosium and Exhibition on Formation Damage Control, Lafayette, Louisiana, 20-21 February.

Furui, K., Zhu, D., and Hill, A.G. 2002. A New Skin Factor Model for Perforated Horizontal Wells. SPE Paper 77363 presented at SPE Annual Technical Conference and Exhibition, San Antonio, Texas, 29 September-2 October.

Golan, M., and Whitson, C.H. 1996. *Well Performance. Second Edition.* Norwegian University of Science and Technology. Trondheim, Norway: Tapir Akademisk Forlag.

Joshi, S.D. 1991. *Horizontal Well Technology. First Edition.* Tulsa, Oklahoma: Pennwell Publishing Company.

Karakas, M. and Tariq, S.M. 1991. Semianalytical Productivity Models for Perforated Completions. *SPE Production Engineering* **6** (01): 73-82, February. SPE Paper 18247.

Karakas, M. and Tariq, S.M. 1990. Supplement to SPE Paper 18247, Semianalytical Productivity Models for Perforated Completions. Available from SPE, Richardson, Texas, USA.

Linear Regression. 2015. Retrieved 05th May 2015 from http://en.wikipedia.org/wiki/Linear_regression

Non Linear Regression. 2015. Retrieved 10th May 2015 from http://en.wikipedia.org/wiki/Nonlinear_regression

Prats, M. 1961. Effect of Vertical Fracture on Reservoir Behavior- Incompressible Fluid Case. *Society of Petroleum Engineers Journal* **1** (02): 105-118, June. SPE Paper 1575-G.

Pucknell, J.K. and Clifford, P.G. 1991. Calculation of Total Skin Factors. SPE Paper 23100 presented at Offshore Europe Conference held in Aberdeen, 3-6 September.

Regression Analysis. 2015. Retrieved 05th May 2015 from http://en.wikipedia.org/wiki/Regression_analysis

Regression. 2015. Retrieved 15th May 2015 from http://www.excel-easy.com/examples/regression.html

Skin. 2015. Retrieved 15th April 2015 from http://www.glossary.oilfield.slb.com/en/Terms/s/skin.aspx

Tariq, S.M. 1987. Evaluation of Flow Characteristics of Perforations Including Nonlinear Effects With the Finite Element Method. *SPE Production Engineering* **2** (02): 104-112, May. SPE Paper 12781.

Tariq, S.M., Ichara, M.J., and Ayestaran L. 1989. Performance of Perforated Completions in the Presence of Anisotropy, Laminations or Natural Fractures. *SPE Production Engineering* **4** (04): 376-384, November. SPE Paper 14320-PA.

APPENDIX A: CALCULATION TABLES

Case 1: K_H/K_V = Infinity (case of zero vertical permeability)

Non Oriented Perforation (360 degree phasing)														
BH Radius (in)	Perforation Length (in)	P_res (bar)_FEM	P_BH (bar)	S2D_Pratts	Lp/rw	P_res (ideal)	Txx=kh/u	Ideal OH Rate	Perforation Flow Rate	Jo	Jp	Jo/Jp	Sp	Rwd
2.4	3	170	80	1.163	1.25	320	100	58187.05	21820.14	242.446	90.917	2.667	4.317	0.444
2.4	6	200	80	0.470	2.50	320	100	58187.05	29093.52	242.446	121.223	2.000	2.590	0.286
2.4	9	230	80	0.065	3.75	320	100	58187.05	36366.91	242.446	151.529	1.600	1.554	0.211
3	3	164	80	1.386	1.00	320	100	63672.21	22285.27	265.301	92.855	2.857	4.396	0.500
3	6	201.6	80	0.693	2.00	320	100	63672.21	32260.59	265.301	134.419	1.974	2.305	0.333
3	9	242	80	0.288	3.00	320	100	63672.21	42978.74	265.301	179.078	1.481	1.140	0.250
4.3	3	152	80	1.746	0.70	320	100	75092.64	22527.79	312.886	93.866	3.333	4.683	0.589
4.3	6	200	80	1.053	1.40	320	100	75092.64	37546.32	312.886	156.443	2.000	2.007	0.417
4.3	9	248	80	0.648	2.09	320	100	75092.64	52564.85	312.886	219.020	1.429	0.860	0.323

Table 16: Perforation skin factor calculation for 360 degree phasing

Oriented Perforations (350/10 degree phasing)														
BH Radius (in)	Perforation Length (in)	P_res (bar)_FEM	P_BH (bar)	S2D_Pratts	Lp/rw	P_res (ideal)	Txx=kh/u	Ideal OH Rate	Perforation Flow Rate	Jo	Jp	Jo/Jp	Sp	Rwd
2.4	3	223	80		1.25	320	100	58187.05	34669.78	242.446	144.457	1.678	1.757	0.444
2.4	6	245	80		2.50	320	100	58187.05	40003.60	242.446	166.682	1.455	1.177	0.286
2.4	9	260	80		3.75	320	100	58187.05	43640.29	242.446	181.835	1.333	0.863	0.211
3	3	206	80		1.00	320	100	63672.21	33427.91	265.3009	139.283	1.905	2.142	0.500
3	6	230	80		2.00	320	100	63672.21	39795.13	265.3009	165.813	1.600	1.420	0.333
3	9	248	80		3.00	320	100	63672.21	44570.55	265.3009	185.711	1.429	1.014	0.250
4.3	3	190	80		0.70	320	100	75092.64	34417.46	312.886	143.406	2.182	2.372	0.589
4.3	6	210	80		1.40	320	100	75092.64	40675.18	312.886	169.480	1.846	1.698	0.417
4.3	9	230	80		2.09	320	100	75092.64	46932.90	312.886	195.554	1.600	1.204	0.323

Table 17: Perforation skin factor calculation for 350/10 degree phasing

Case 2: K_H/K_V = 1 (isotropic reservoir)

Non Oriented Perforation (360 degree phasing)															
BH Radius (in)	Perforation Length (in)	P_res (bar)_FEM	P_BH (bar)	S2D_Pratts	Lp/rw	P_res (ideal)	Txx	Tyy	Tzz	Average T=kh/u	Ideal OH Rate	Perforation Flow Rate	Jo	Jp	Jo/Jp	Sp (= S2D + Swb)
2.4	3	170	80		1.25	320	100	100	100	100	58187.048	21820.143	242.446	90.9172626	2.667	4.317
2.4	6	208	80		2.50	320	100	100	100	100	58187.048	31033.092	242.446	129.304551	1.875	2.266
2.4	9	235.8	80		3.75	320	100	100	100	100	58187.048	37773.092	242.446	157.387883	1.540	1.400
3	3	177	80		1.00	320	100	100	100	100	63672.213	25734.186	265.301	107.225776	2.474	3.490
3	6	208.2	80		2.00	320	100	100	100	100	63672.213	34011.574	265.301	141.714892	1.872	2.064
3	9	234.4	80		3.00	320	100	100	100	100	63672.213	40962.457	265.301	170.676905	1.554	1.312
4.3	3	163	80		0.70	320	100	100	100	100	75092.637	25969.537	312.886	108.206404	2.892	3.797
4.3	6	204	80		1.40	320	100	100	100	100	75092.637	38797.863	312.886	161.657761	1.935	1.878
4.3	9	234.7	80		2.09	320	100	100	100	100	75092.637	48403.462	312.886	201.681093	1.551	1.107

Table 18: Perforation skin factor calculation for 360 degree phasing

Horizontal well oriented perforation skin factor: A numerical analysis of skin factor reduction by off-setting perforation phasing from 360^{O} to $350^{O}/10^{O}$

Oriented Perforation (350/10 degree phasing)																
BH Radius (in)	Perforation Length (in)	P_res (bar)_FEM	P_BH (bar)	S2D_Pratts	Lp/rw	P_res (ideal)	Txx	Tyy	Tzz	Average T=kh/u	Ideal OH Rate	Perforation Flow Rate	Jo	Jp	Jo/Jp	Sp (= S2D + Swb)
2.4	3	233	80		1.25	320	100	100	100	100	58187.048	37094.243	242.446	154.559	1.569	1.473
2.4	6	255	80		2.50	320	100	100	100	100	58187.048	42428.056	242.446	176.784	1.371	0.962
2.4	9	269	80		3.75	320	100	100	100	100	58187.048	45822.300	242.446	190.926	1.270	0.699
3	3	231	80		1.00	320	100	100	100	100	63672.213	40060.434	265.301	166.918	1.589	1.395
3	6	252	80		2.00	320	100	100	100	100	63672.213	45631.753	265.301	190.132	1.395	0.936
3	9	266	80		3.00	320	100	100	100	100	63672.213	49345.965	265.301	205.608	1.290	0.687
4.3	3	224	80		0.70	320	100	100	100	100	75092.637	45055.582	312.886	187.732	1.667	1.338
4.3	6	250	80		1.40	320	100	100	100	100	75092.637	53190.618	312.886	221.628	1.412	0.826
4.3	9	264	80		2.09	320	100	100	100	100	75092.637	57571.022	312.886	239.879	1.304	0.611

Table 19: Perforation skin factor calculation for 350/10 degree phasing

Case 2: $K_H/K_V = 10$ (anisotropic reservoir)

Non Oriented Perforation (360 degree phasing)																
BH Radius (in)	Perforation Length (in)	P_res (bar)_NO	P_BH (bar)	S2D_Pratts	Lp/rw	P_res (ideal)	Txx	Tyy	Tzz	AvgT=Kh/u	Ideal OH Rate	Perforation Flow Rate	Jo	Jp	Jo/Jp	Sp
2.4	3	244	80		1.25	320	1000	100	100	550	320028.764	218686.322	1333.453	911.193	1.463	1.200
2.4	6	276	80		2.50	320	1000	100	100	550	320028.764	261356.824	1333.453	1088.987	1.224	0.581
2.4	9	290.8	80		3.75	320	1000	100	100	550	320028.764	281091.931	1333.453	1171.216	1.139	0.359
3	3	260	80		1.00	320	1000	100	100	550	350197.174	262647.88	1459.155	1094.366	1.333	0.789
3	6	286	80		2.00	320	1000	100	100	550	350197.174	300585.908	1459.155	1252.441	1.165	0.391
3	9	286.7	80		3.00	320	1000	100	100	550	350197.174	301607.316	1459.155	1256.697	1.161	0.381
4.3	3	240	80		0.70	320	1000	100	100	550	413009.504	275339.67	1720.873	1147.249	1.500	1.004
4.3	6	274	80		1.40	320	1000	100	100	550	413009.504	333849.349	1720.873	1391.039	1.237	0.476
4.3	9	293	80		2.09	320	1000	100	100	550	413009.504	366545.935	1720.873	1527.275	1.127	0.254

Table 20: Perforation skin factor calculation for 360 degree phasing

Oriented Perforation (350/10 degree phasing)																
BH Radius (in)	Perforation Length (in)	P_res (bar)_NO	P_BH (bar)	S2D_Pratts	Lp/rw	P_res (ideal)	Txx	Tyy	Tzz	Average T=kh/u	Ideal OH Rate	Perforation Flow Rate	Jo	Jp	Jo/Jp	Sp
2.4	3	262	80		1.25	320	1000	100	100	550	320028.764	242688.480	1333.453	1011.202	1.319	0.825
2.4	6	289	80		2.50	320	1000	100	100	550	320028.764	278691.716	1333.453	1161.215	1.148	0.384
2.4	9	300	80		3.75	320	1000	100	100	550	320028.764	293359.701	1333.453	1222.332	1.091	0.235
3	3	263	80		1.00	320	1000	100	100	550	350197.174	267025.345	1459.155	1112.606	1.311	0.737
3	6	286	80		2.00	320	1000	100	100	550	350197.174	300585.908	1459.155	1252.441	1.165	0.391
3	9	298	80		3.00	320	1000	100	100	550	350197.174	318095.766	1459.155	1325.399	1.101	0.239
4.3	3	266	80		0.70	320	1000	100	100	550	413009.504	320082.366	1720.873	1333.677	1.290	0.583
4.3	6	287	80		1.40	320	1000	100	100	550	413009.504	356220.698	1720.873	1484.253	1.159	0.320
4.3	9	299.4	80		2.09	320	1000	100	100	550	413009.504	377559.522	1720.873	1573.165	1.094	0.188

Table 21: Perforation skin factor calculation for 350/10 degree phasing

APPENDIX B: Finite element modeling simulation results for K_H/K_V = infinity

(Isobaric contour plots and pressure distribution plots from ANSYS Mechanical APDL)

Well radius (inches)	2.4
Perforation length (inches) and type	3
Perforation phasing	360

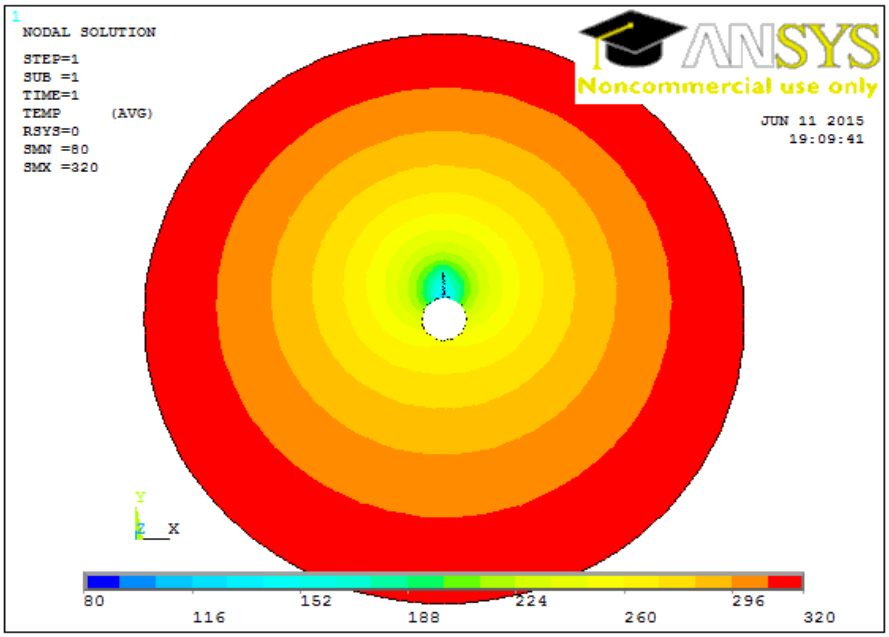

Figure 44: Isobaric contour plot

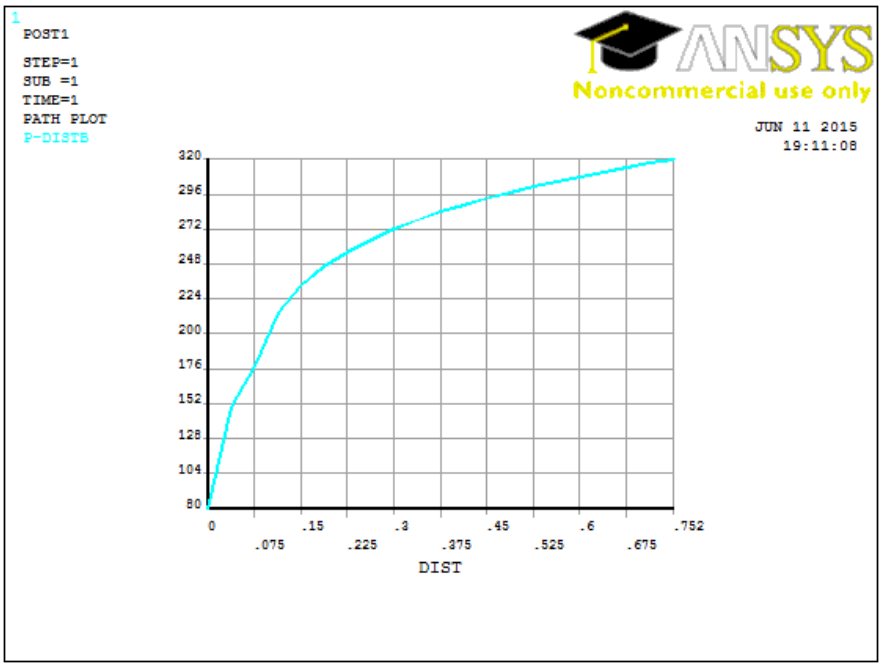

Figure 45: Pressure distribution from inner boundary to outer boundary

Well radius (inches)	2.4
Perforation length (inches) and type	6
Perforation phasing	360

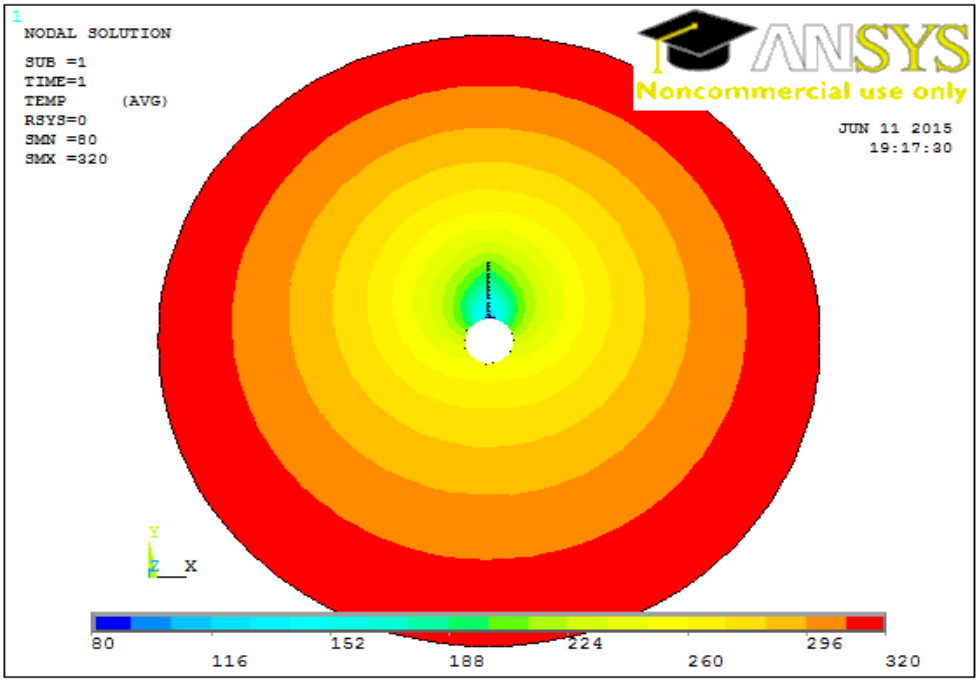

Figure 46: Isobaric contour plot

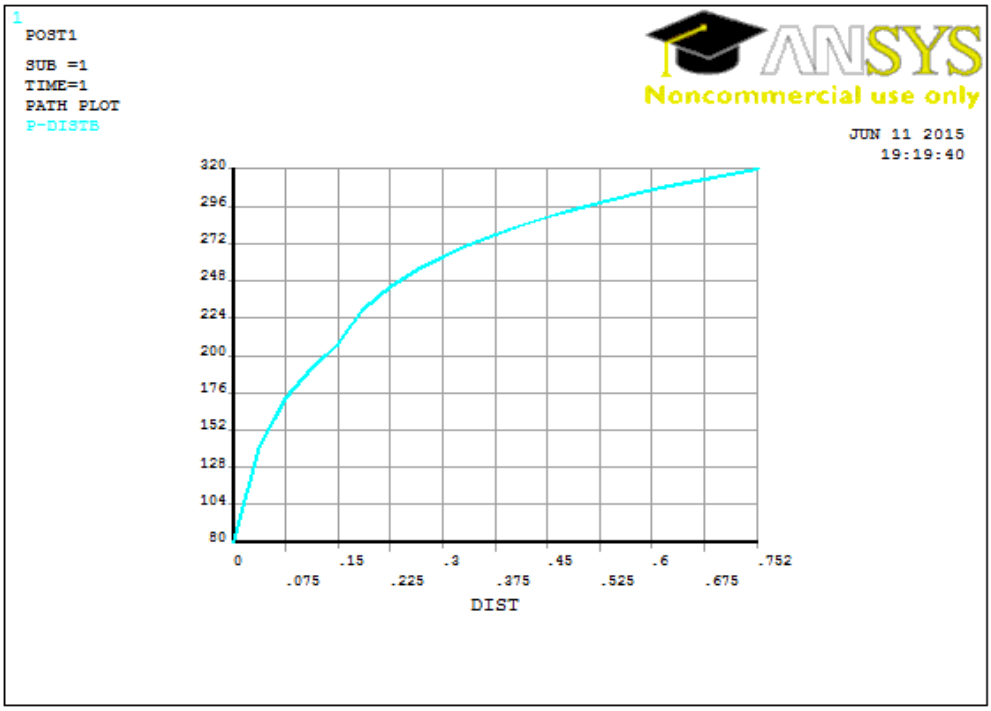

Figure 47: Pressure distribution from inner boundary to outer boundary

Well radius (inches)	2.4
Perforation length (inches) and type	9
Perforation phasing	360

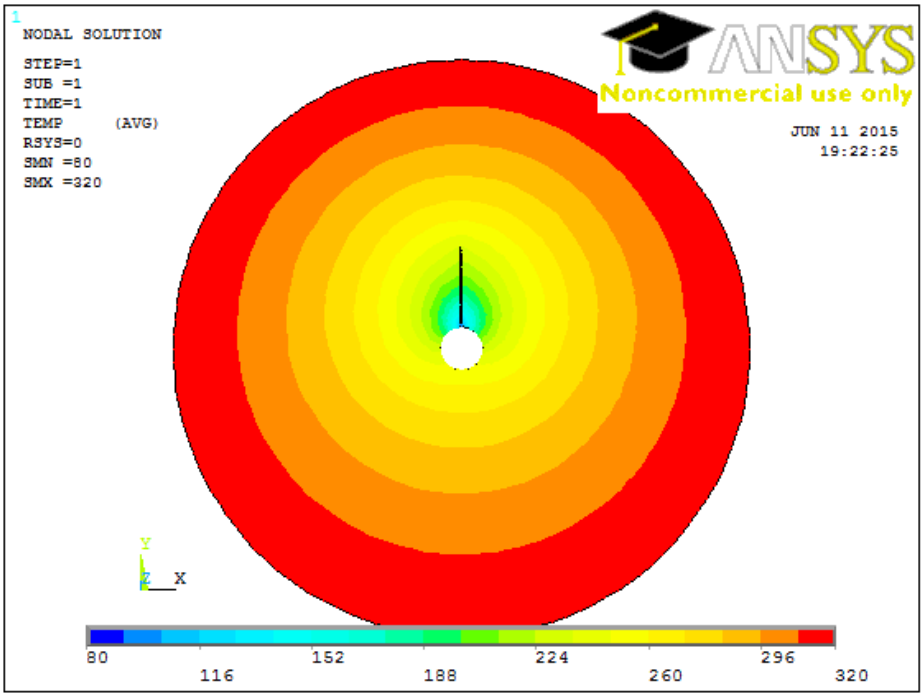

Figure 48: Isobaric contour plot

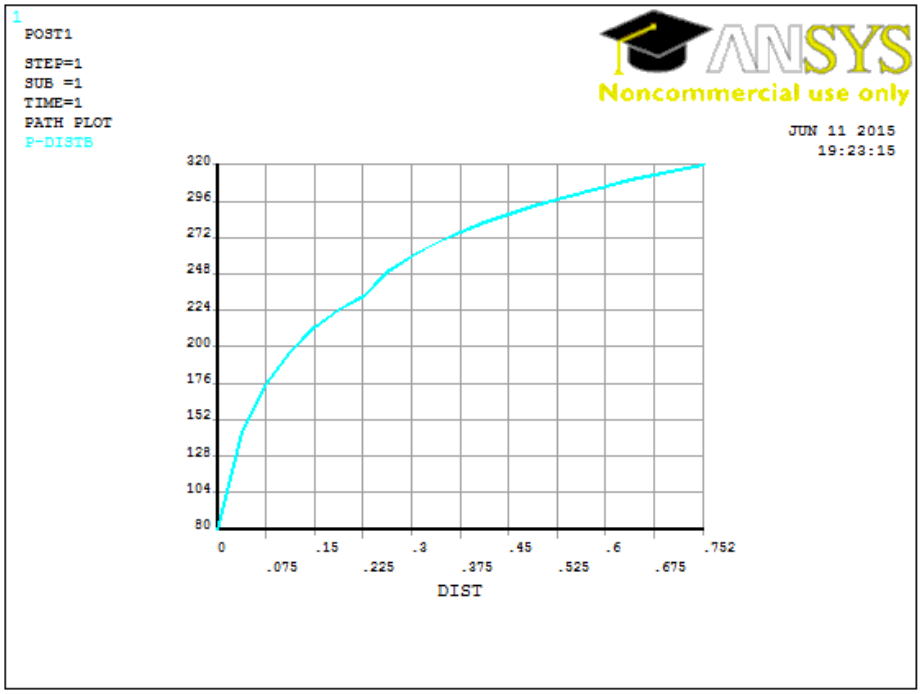

Figure 49: Pressure distribution from inner boundary to outer boundary

Well radius (inches)	3
Perforation length (inches) and type	3
Perforation phasing	360

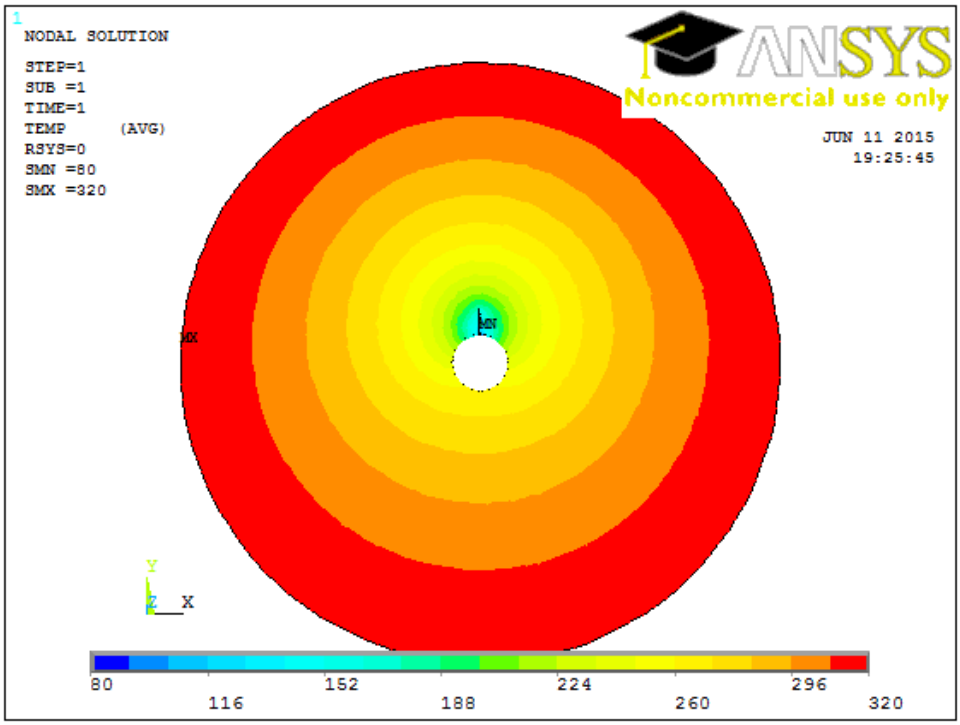

Figure 50: Isobaric contour plot

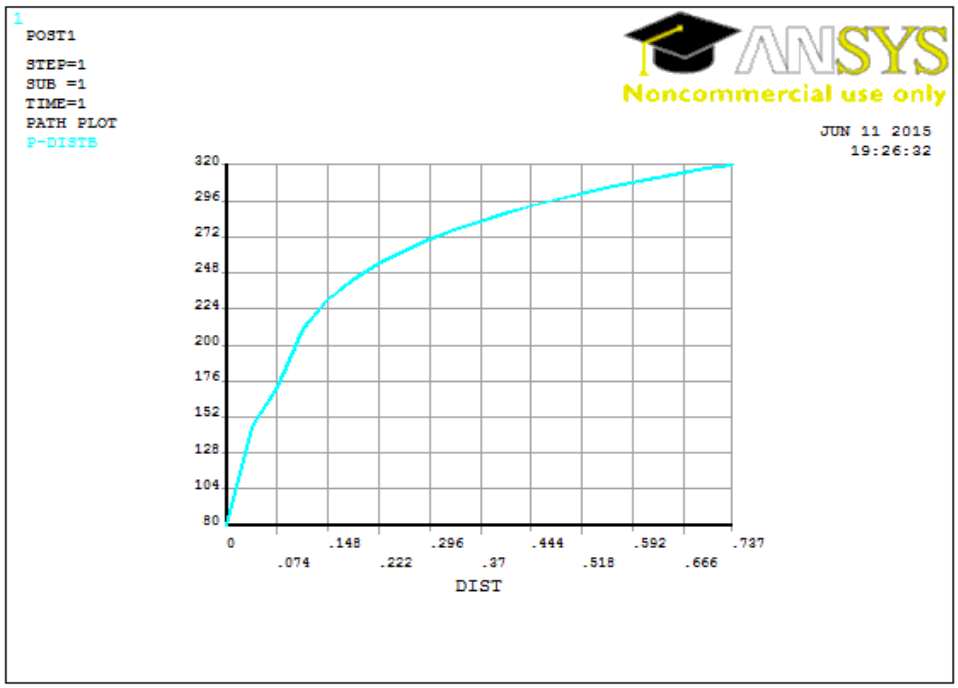

Figure 51: Pressure distribution from inner boundary to outer boundary

Well radius (inches)	3
Perforation length (inches) and type	6
Perforation phasing	360

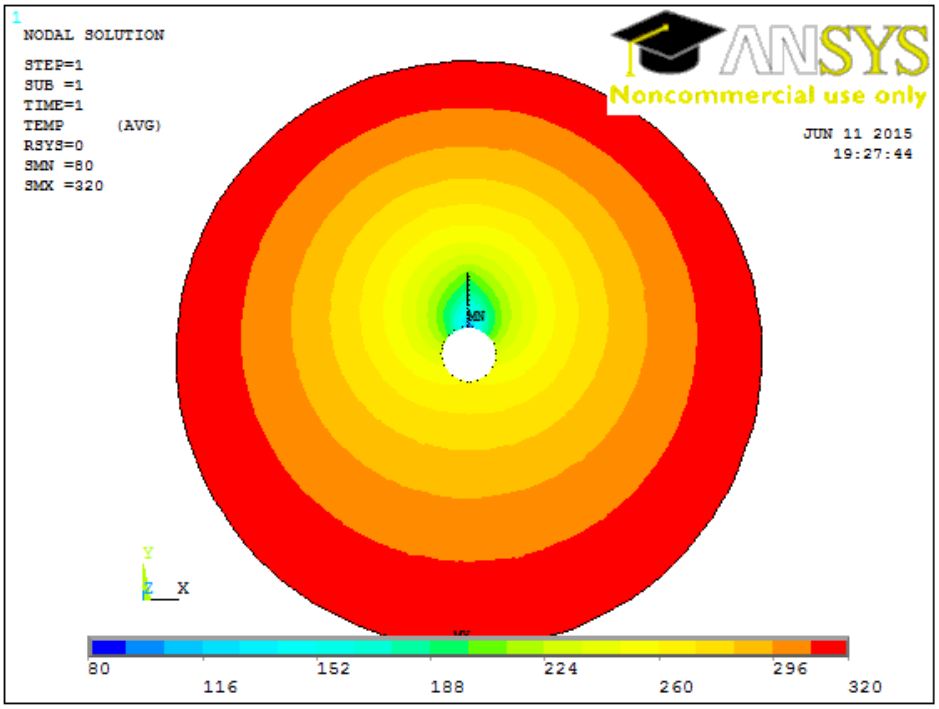

Figure 52: Isobaric contour plot

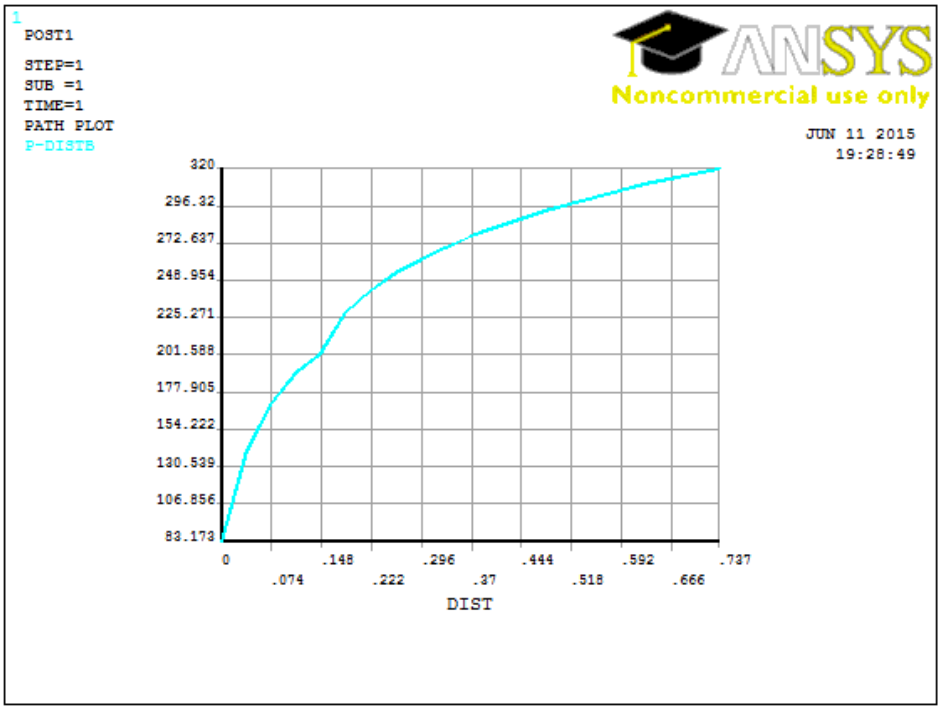

Figure 53: Pressure distribution from inner boundary to outer boundary

Well radius (inches)	3
Perforation length (inches) and type	9
Perforation phasing	360

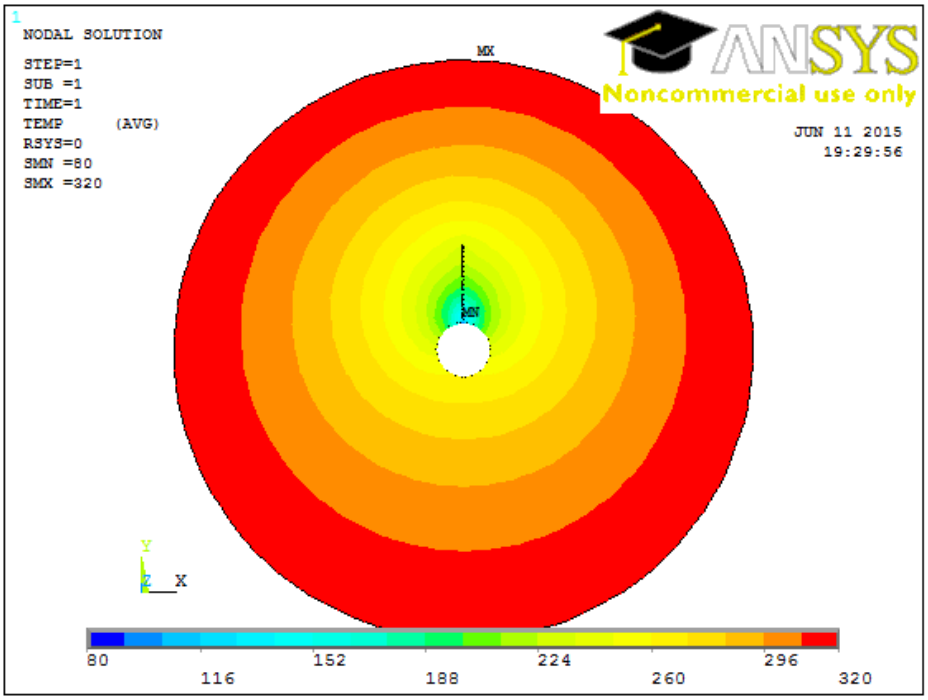

Figure 54: Isobaric contour plot

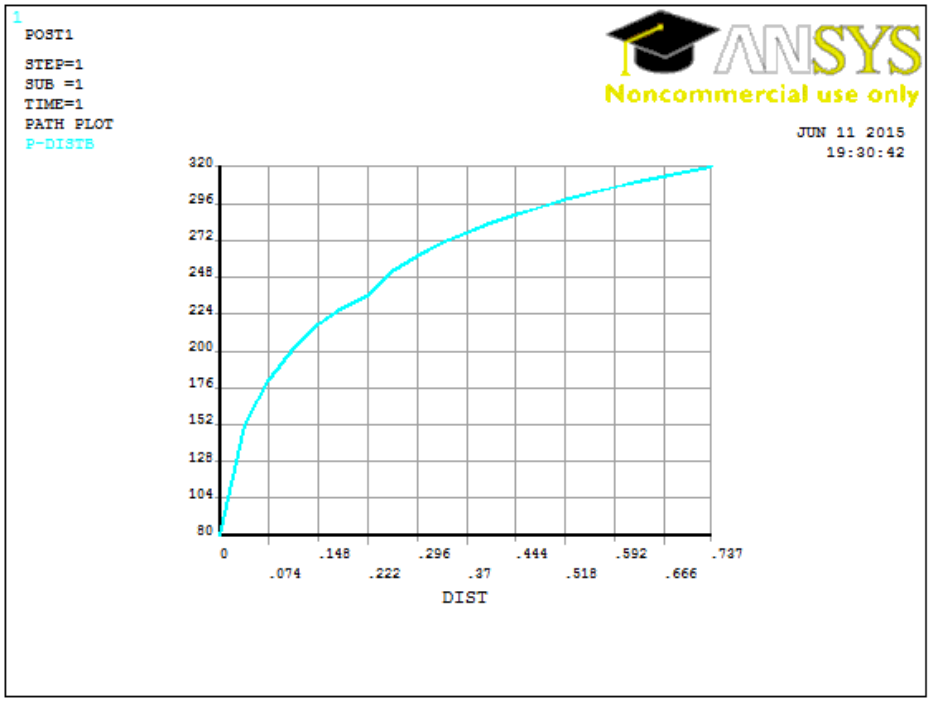

Figure 55: Pressure distribution from inner boundary to outer boundary

Well radius (inches)	4.3
Perforation length (inches) and type	3
Perforation phasing	360

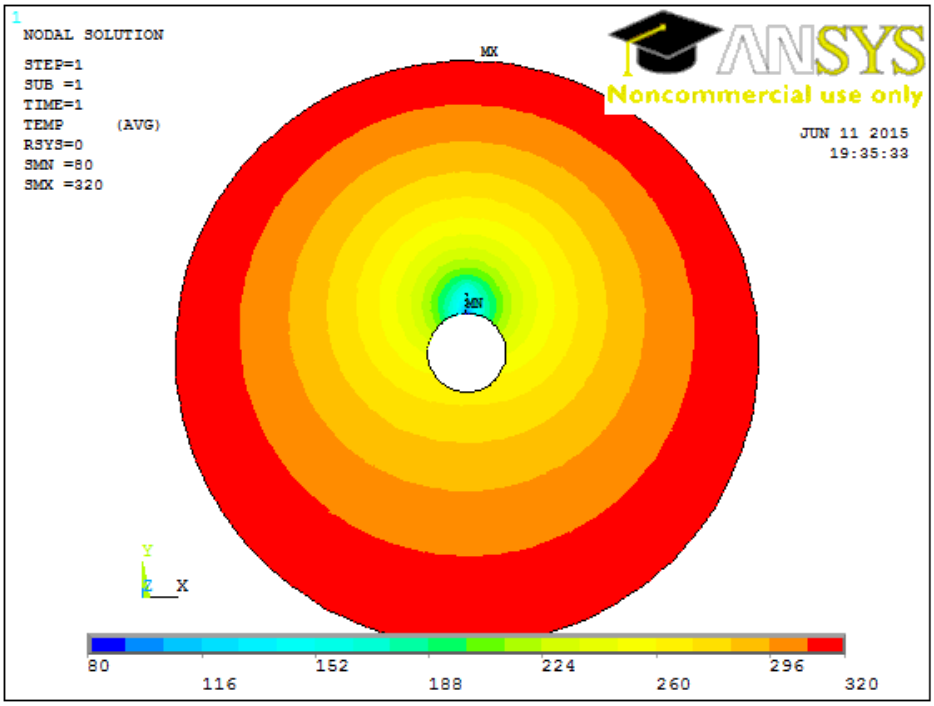

Figure 56: Isobaric contour plot

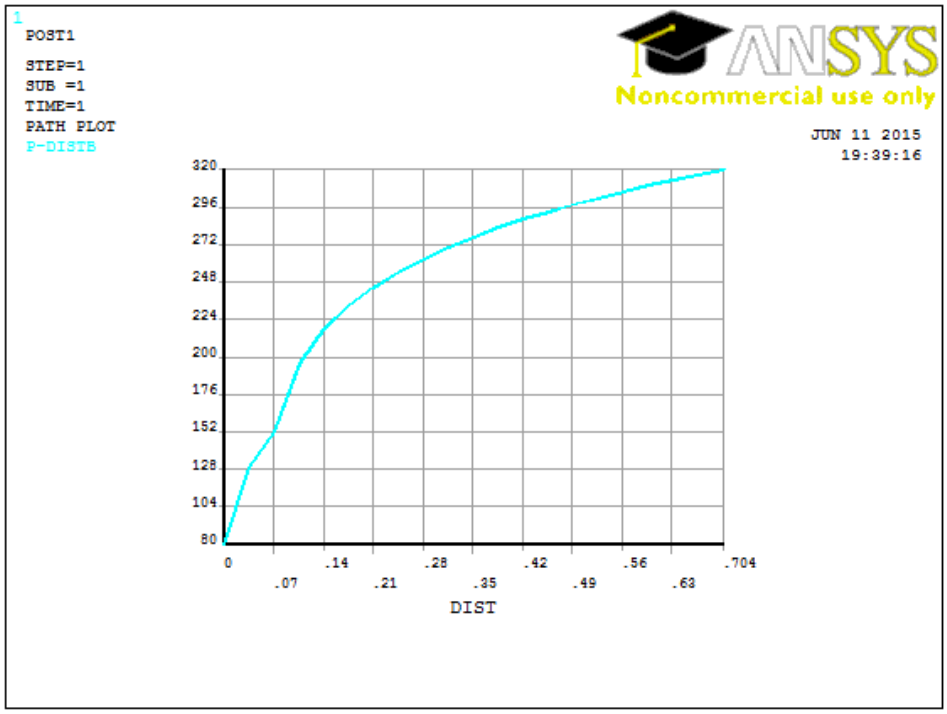

Figure 57: Pressure distribution from inner boundary to outer boundary

Well radius (inches)	4.3
Perforation length (inches) and type	6
Perforation phasing	360

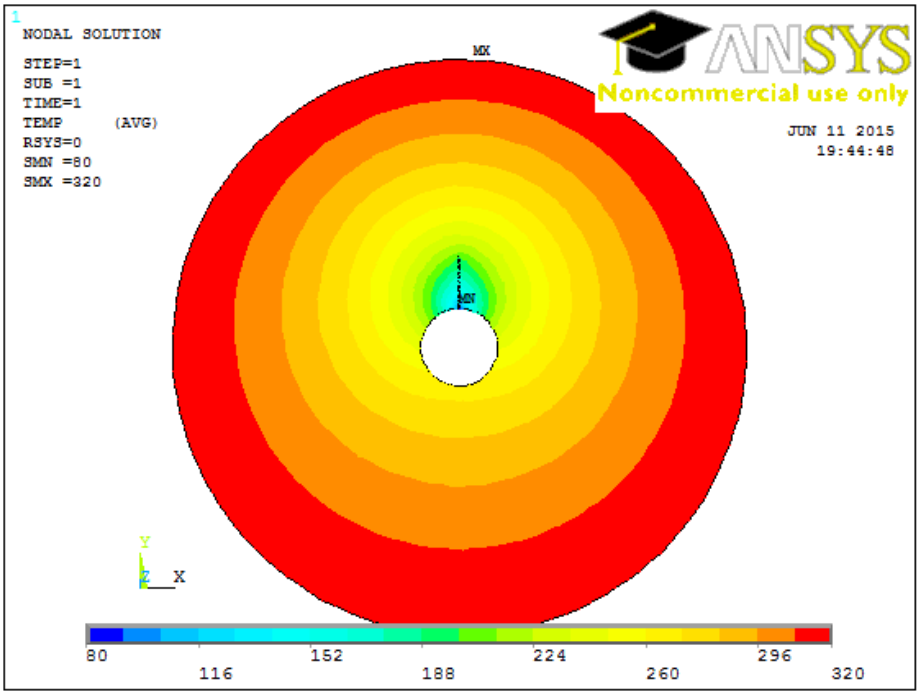

Figure 58: Isobaric contour plot

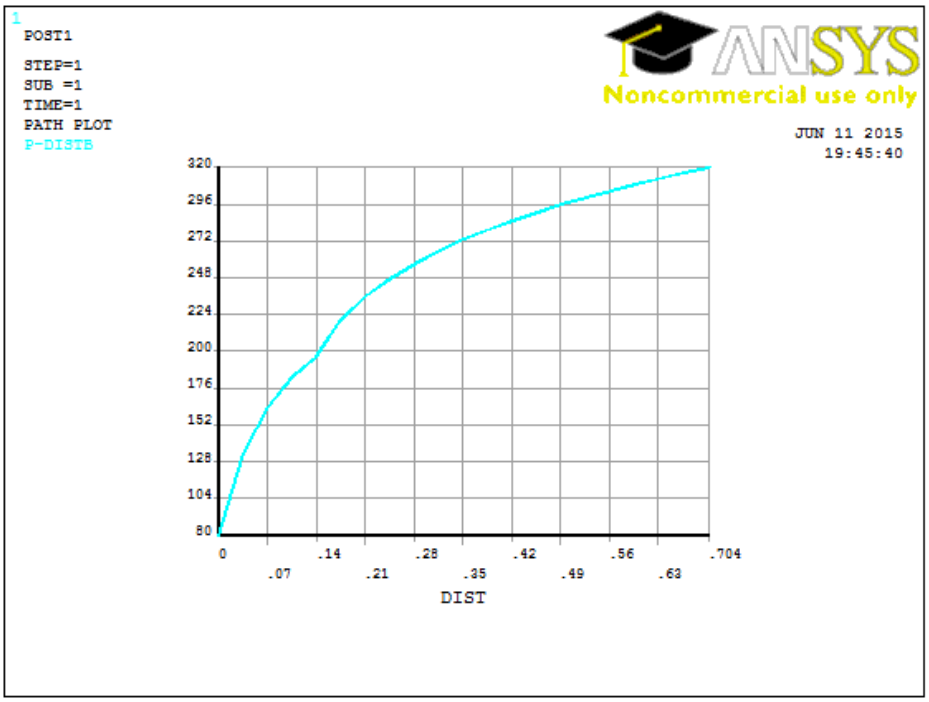

Figure 59: Pressure distribution from inner boundary to outer boundary

Well radius (inches)	4.3
Perforation length (inches) and type	9
Perforation phasing	360

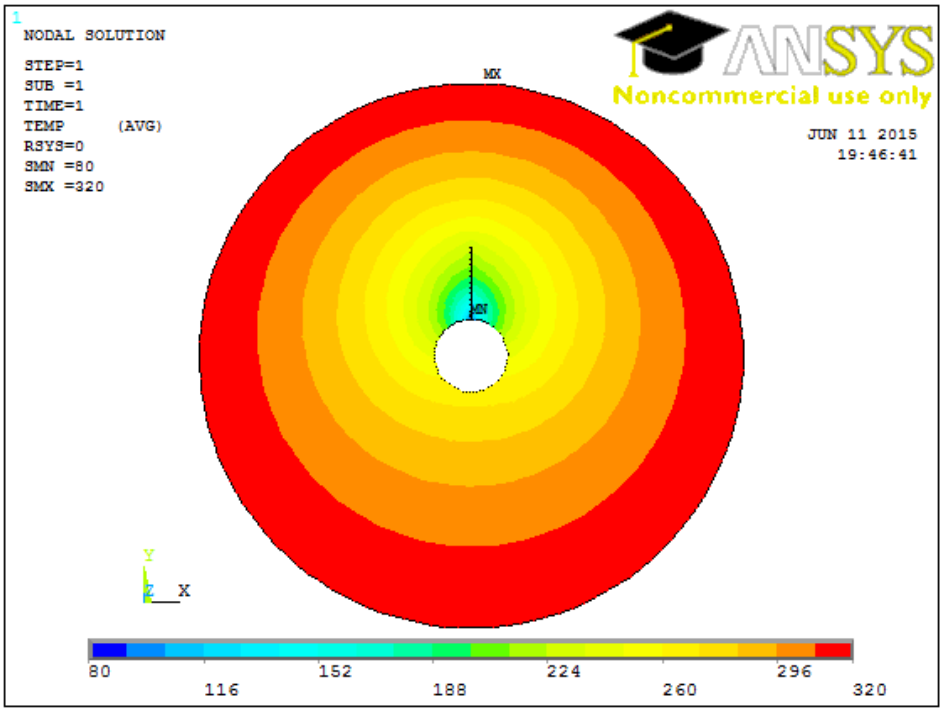

Figure 60: Isobaric contour plot

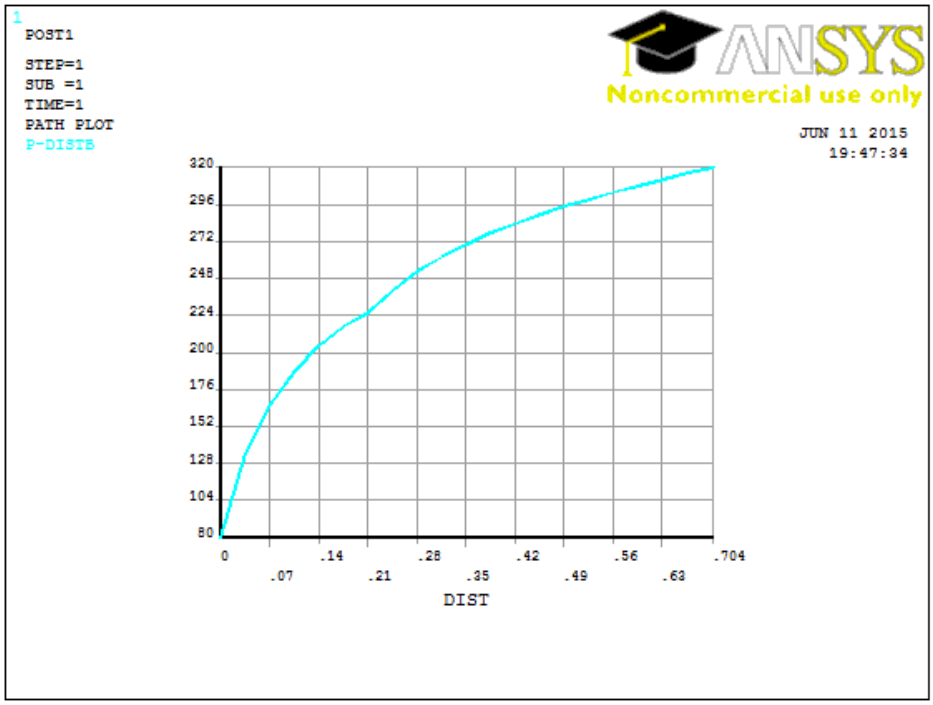

Figure 61: Pressure distribution from inner boundary to outer boundary

Well radius (inches)	2.4
Perforation length (inches) and type	3
Perforation phasing	350/10

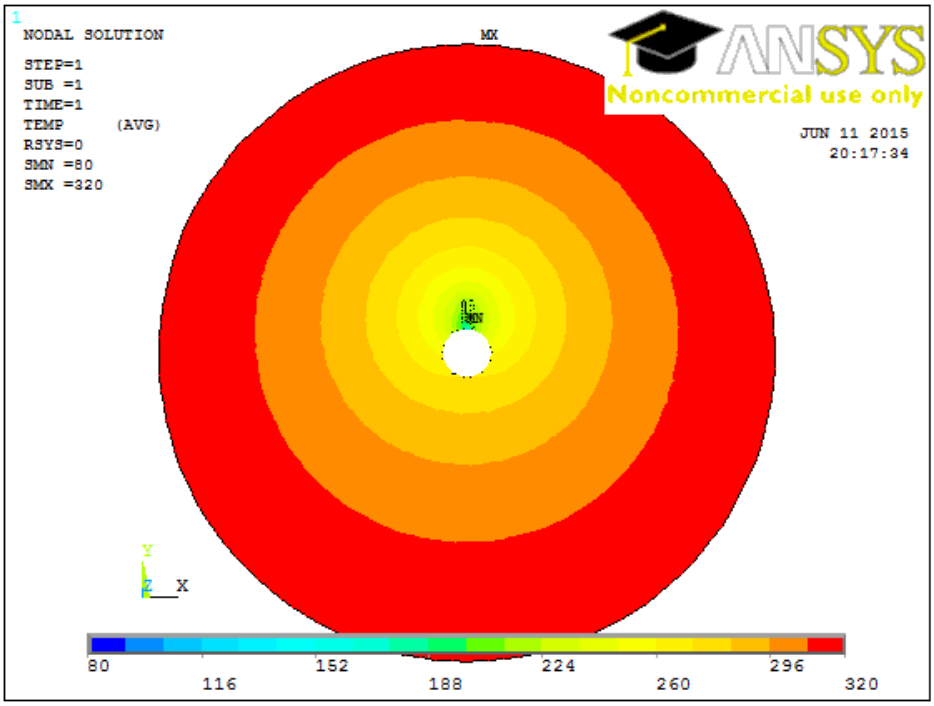

Figure 62: Isobaric contour plot

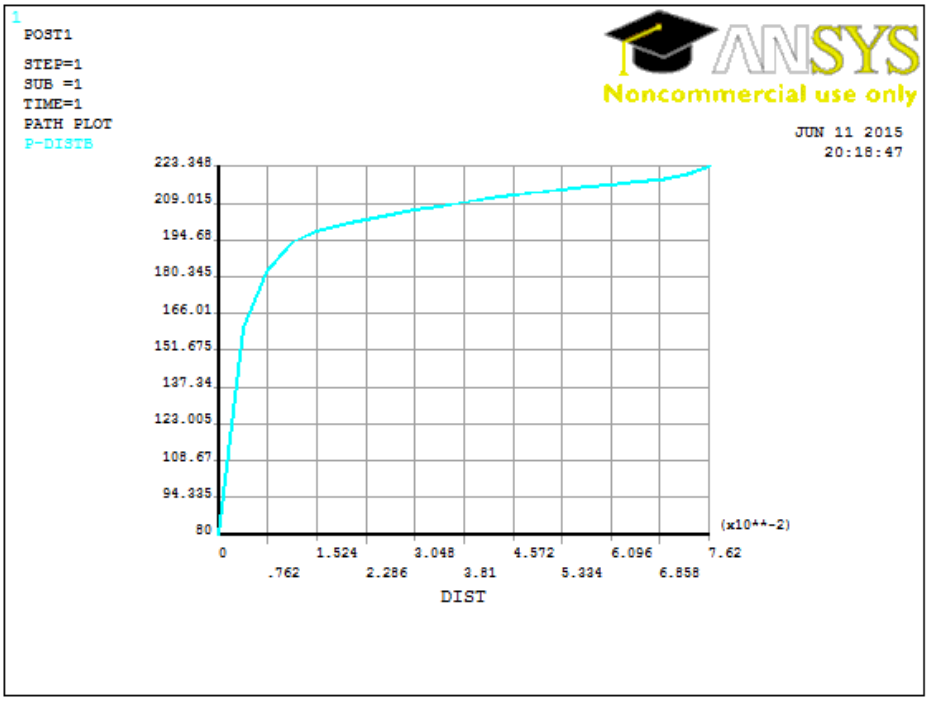

Figure 63: Pressure distribution from inner boundary to the tip of perforation tunnel

Well radius (inches)	2.4
Perforation length (inches) and type	6
Perforation phasing	350/10

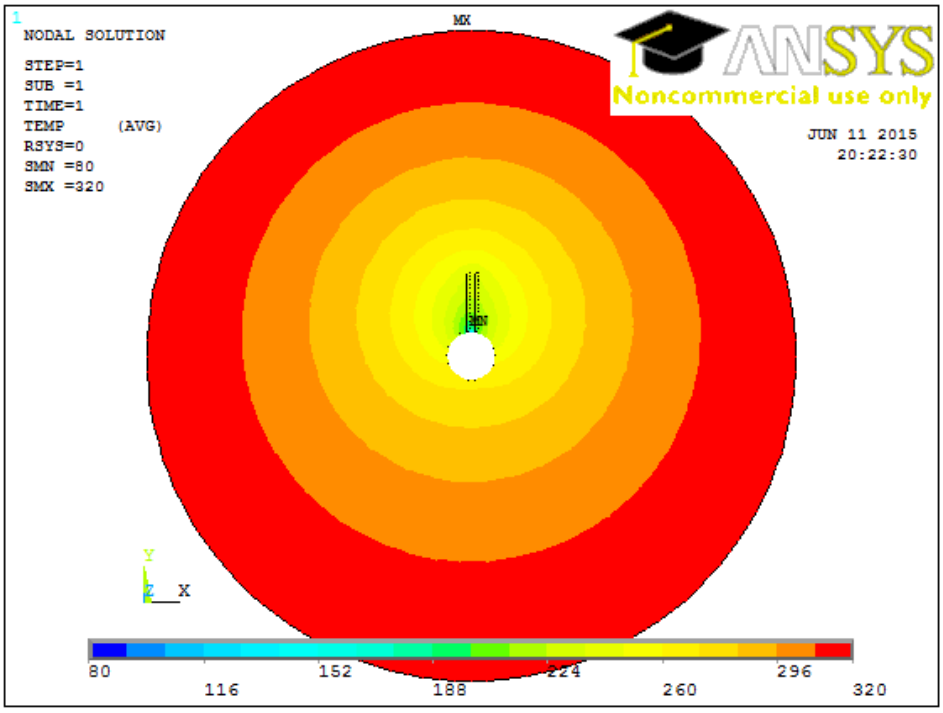

Figure 64: Isobaric contour plot

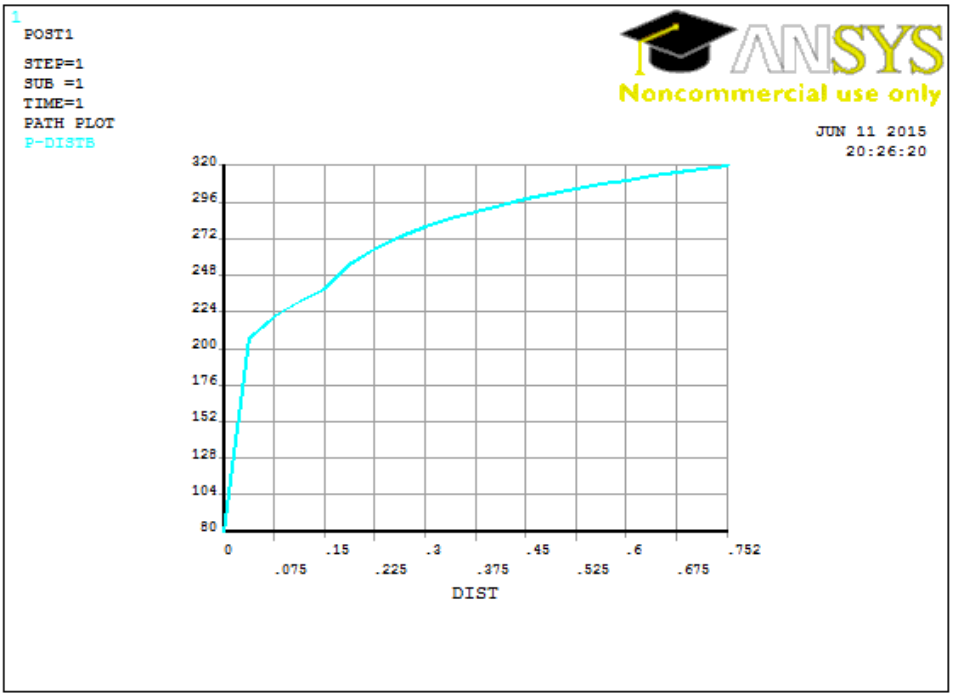

Figure 65: Pressure distribution from inner boundary to outer boundary

Well radius (inches)	2.4
Perforation length (inches) and type	9
Perforation phasing	350/10

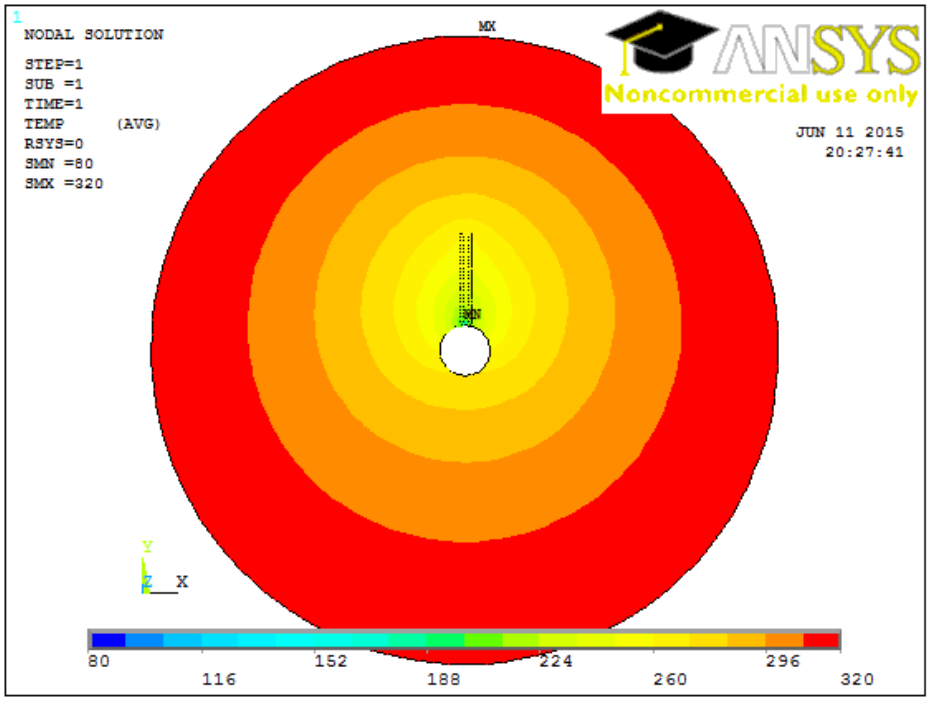

Figure 66: Isobaric contour plot

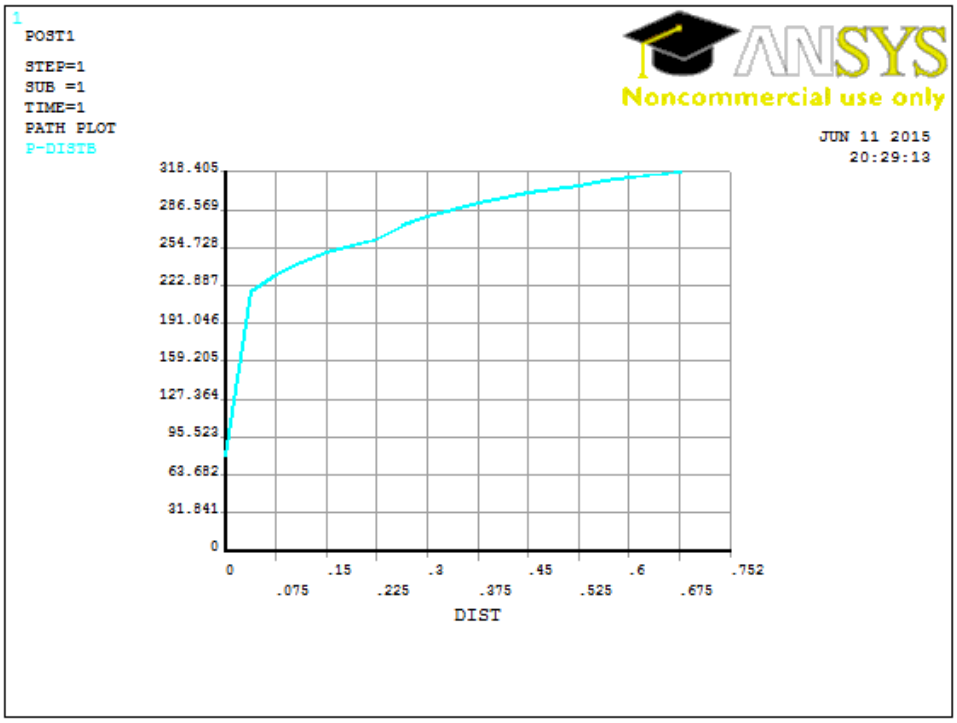

Figure 67: Pressure distribution from inner boundary to outer boundary

Well radius (inches)	3
Perforation length (inches) and type	3
Perforation phasing	350/10

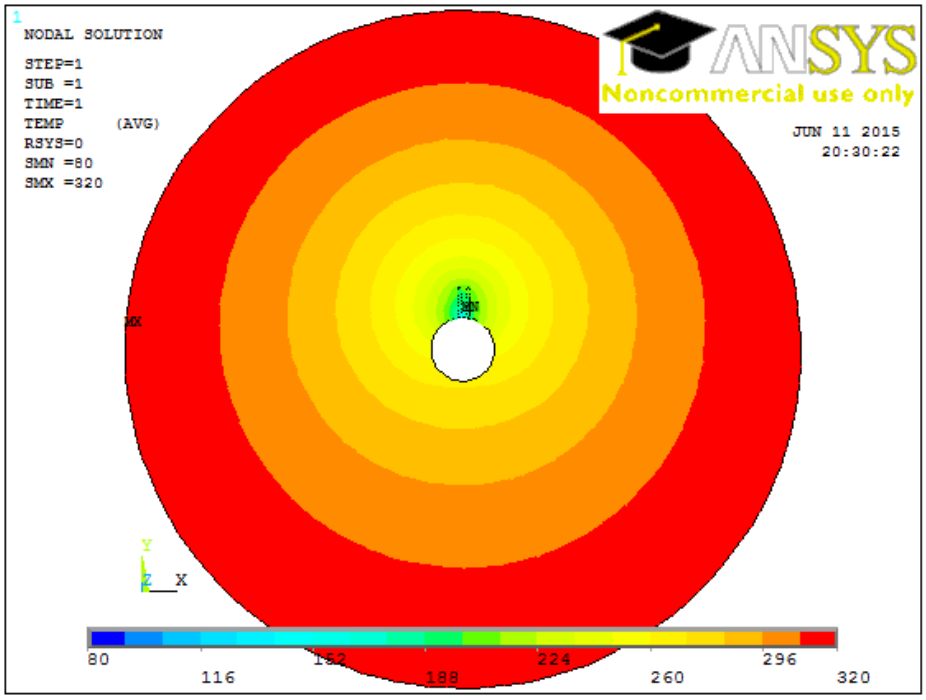

Figure 68: Isobaric contour plot

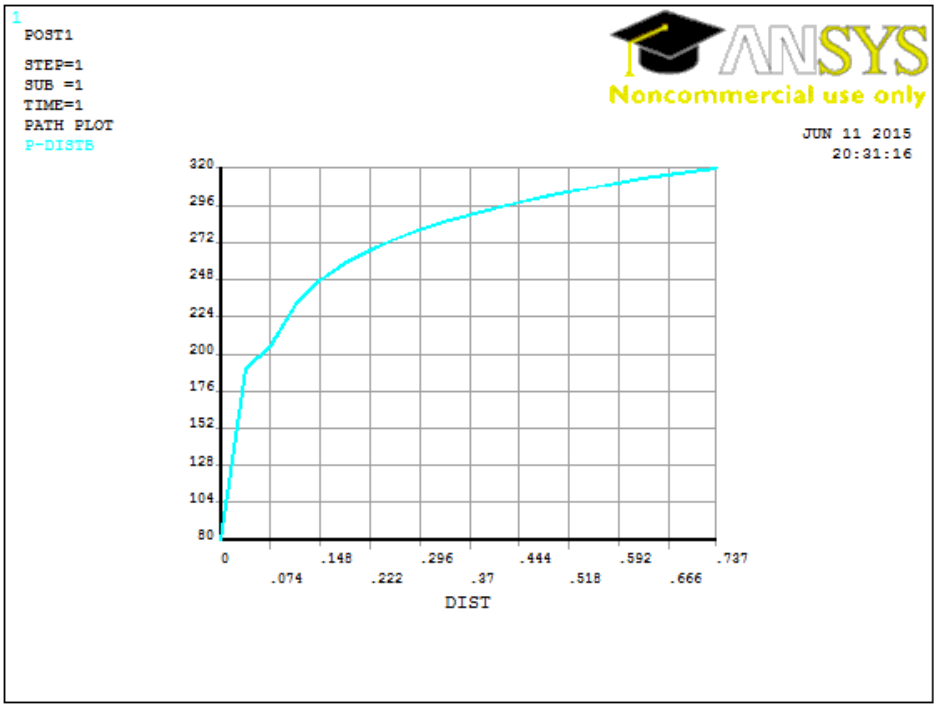

Figure 69: Pressure distribution from inner boundary to outer boundary

Well radius (inches)	3
Perforation length (inches) and type	6
Perforation phasing	350/10

Figure 70: Isobaric contour plot

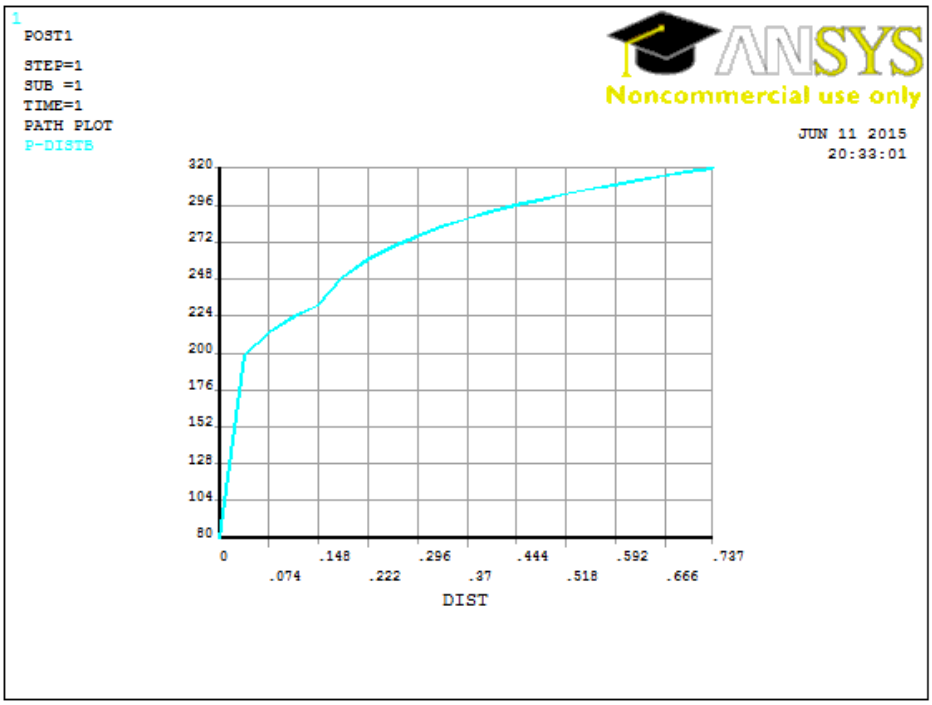

Figure 71: Pressure distribution from inner boundary to outer boundary

Well radius (inches)	3
Perforation length (inches) and type	9
Perforation phasing	350/10

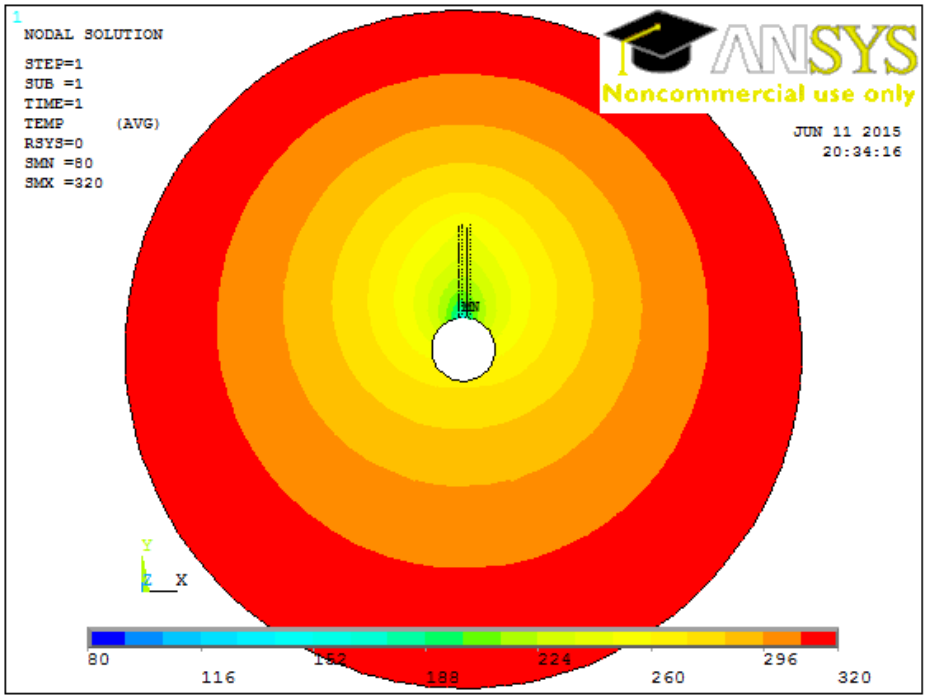

Figure 72: Isobaric contour plot

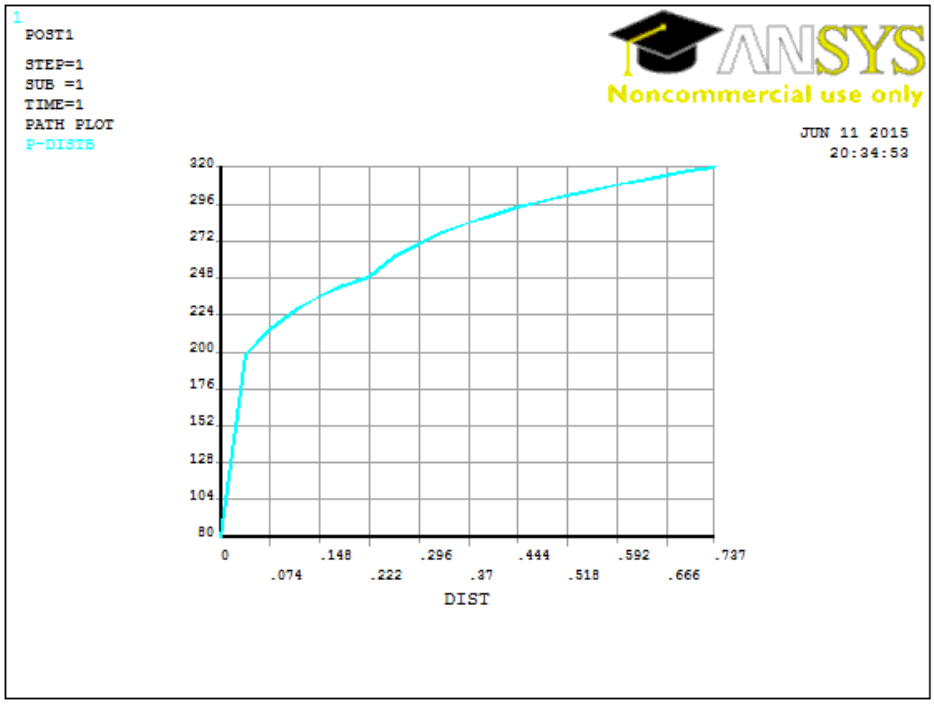

Figure 73: Pressure distribution from inner boundary to outer boundary

Well radius (inches)	4.3
Perforation length (inches) and type	3
Perforation phasing	350/10

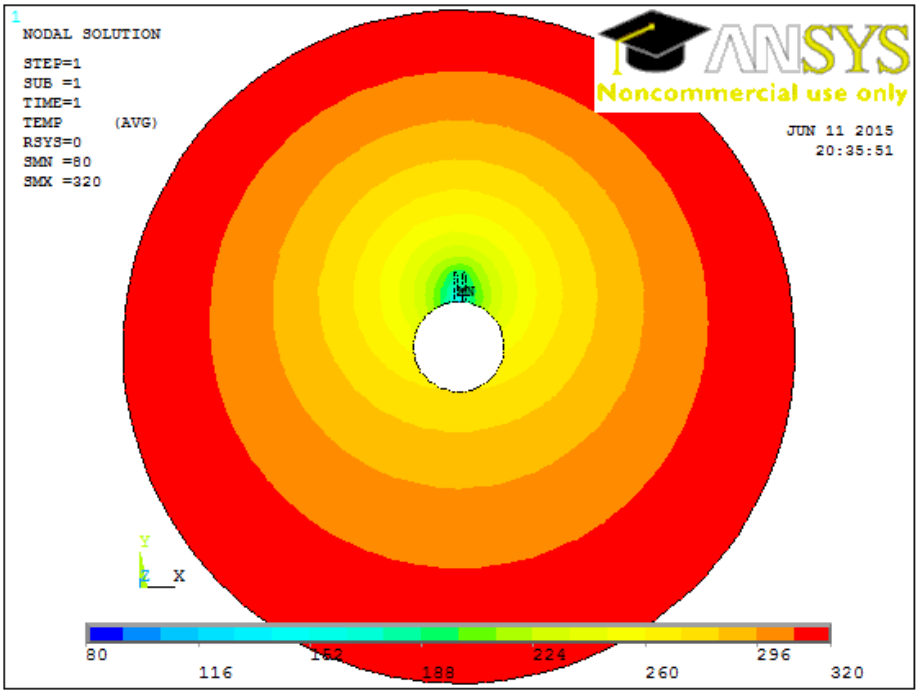

Figure 74: Isobaric contour plot

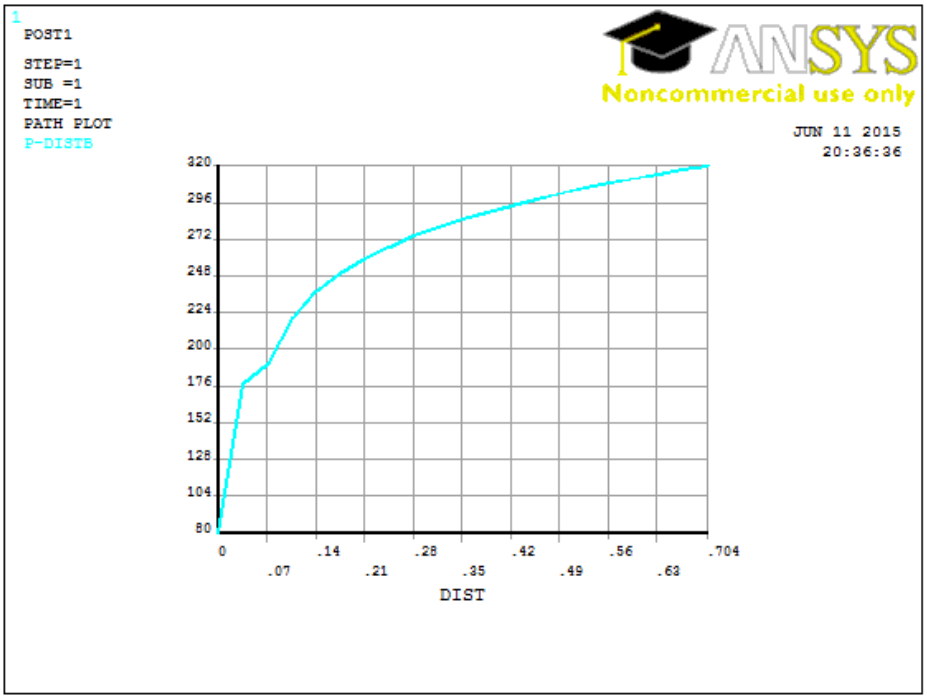

Figure 75: Pressure distribution from inner boundary to outer boundary

Well radius (inches)	4.3
Perforation length (inches) and type	6
Perforation phasing	350/10

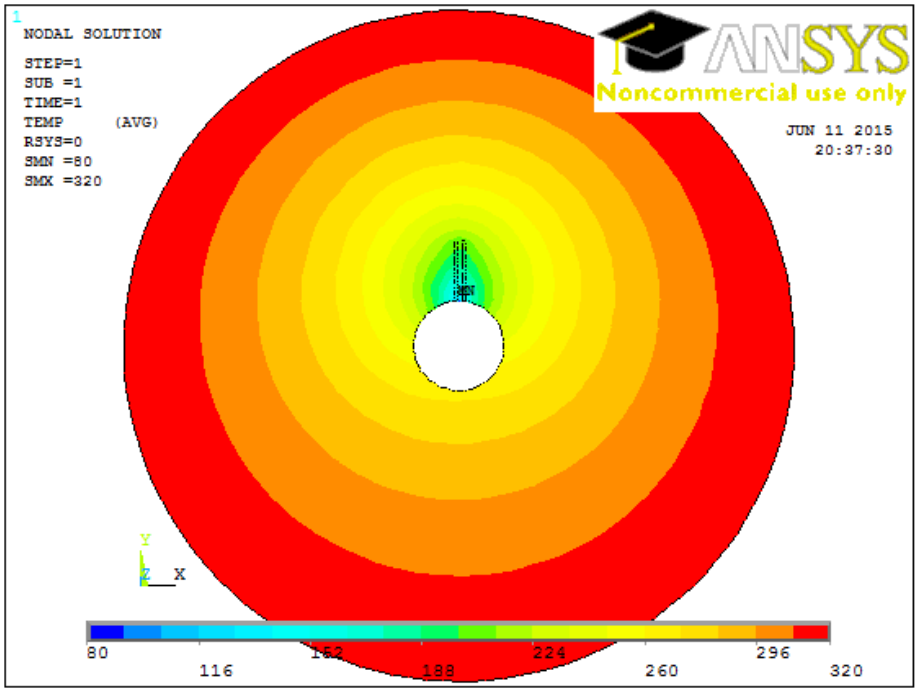

Figure 76: Isobaric contour plot

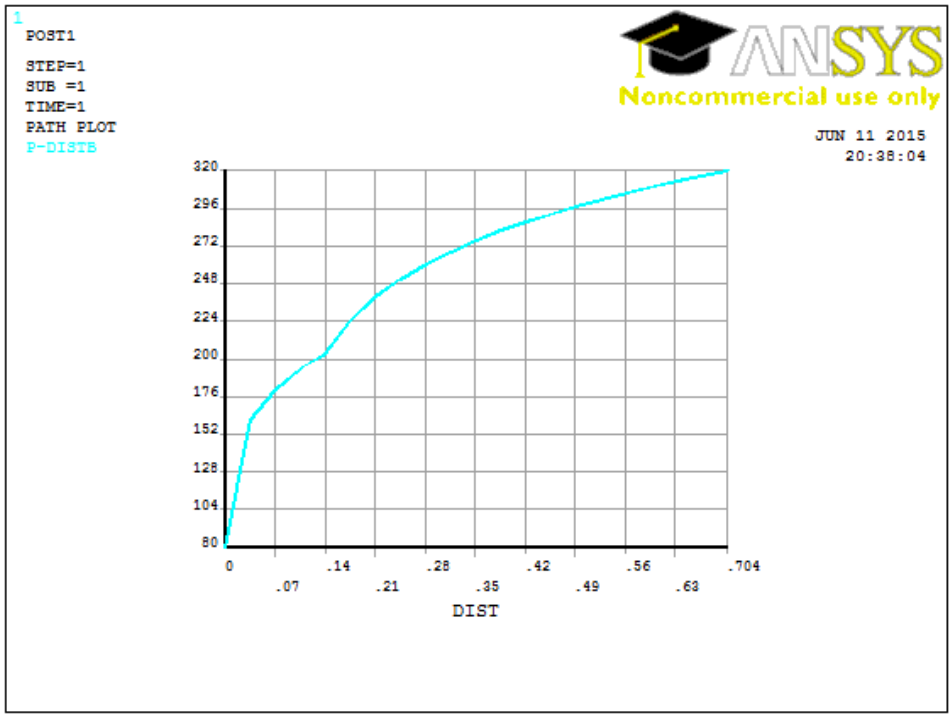

Figure 77: Pressure distribution from inner boundary to outer boundary

Well radius (inches)	4.3
Perforation length (inches) and type	9
Perforation phasing	350/10

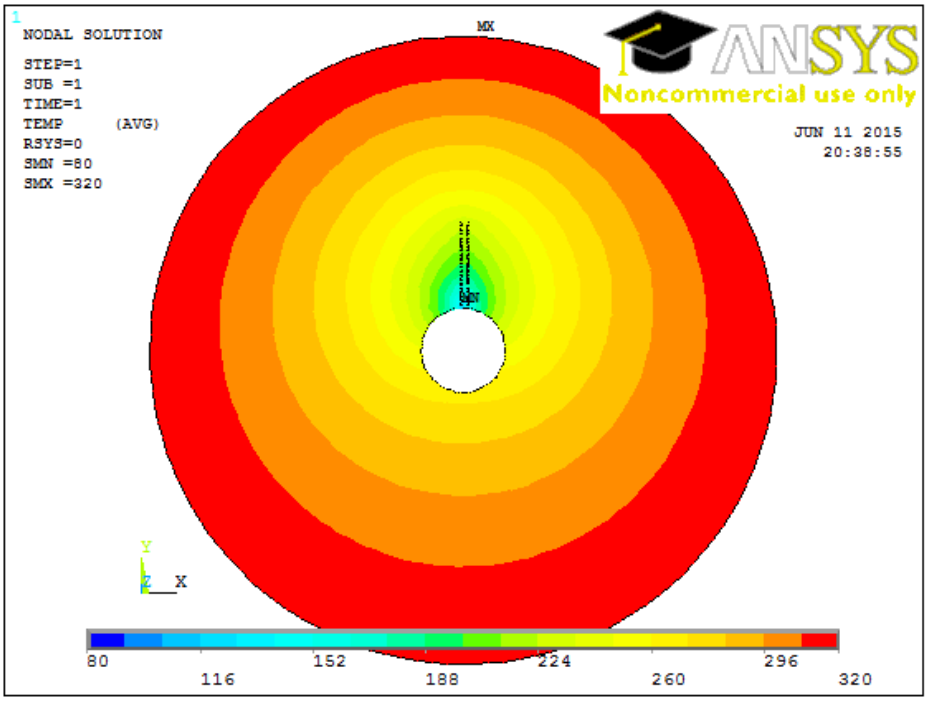

Figure 78: Isobaric contour plot

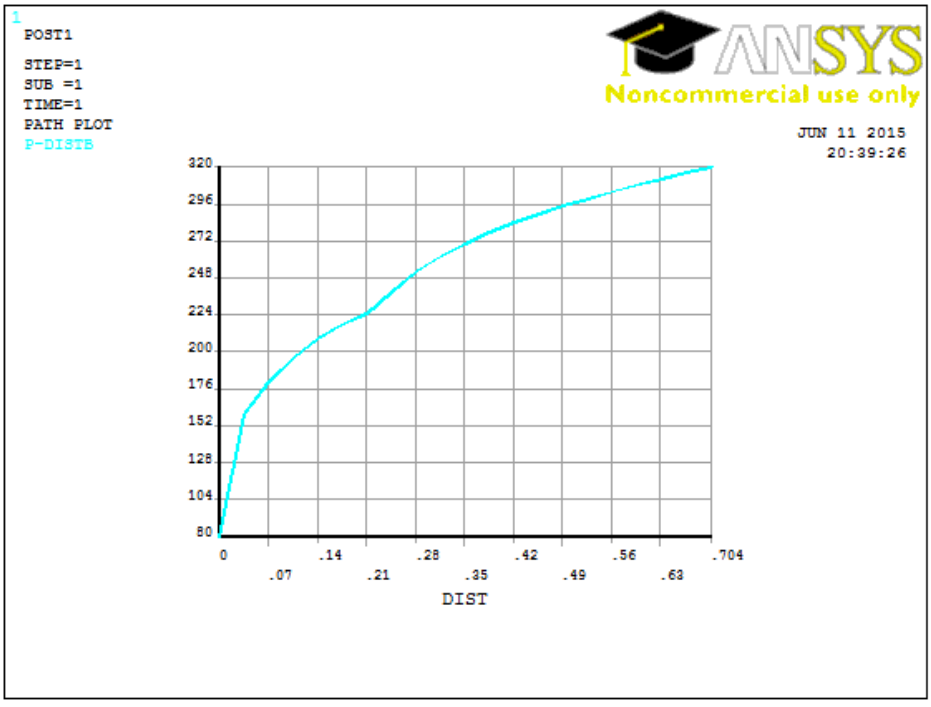

Figure 79: Pressure distribution from inner boundary to outer boundary

APPENDIX C: Finite element modeling simulation results for K_H/K_V = 1 (isotropic reservoir Case)

Well radius (inches)	2.4
Perforation length (inches)	3
Perforation phasing (degrees)	360

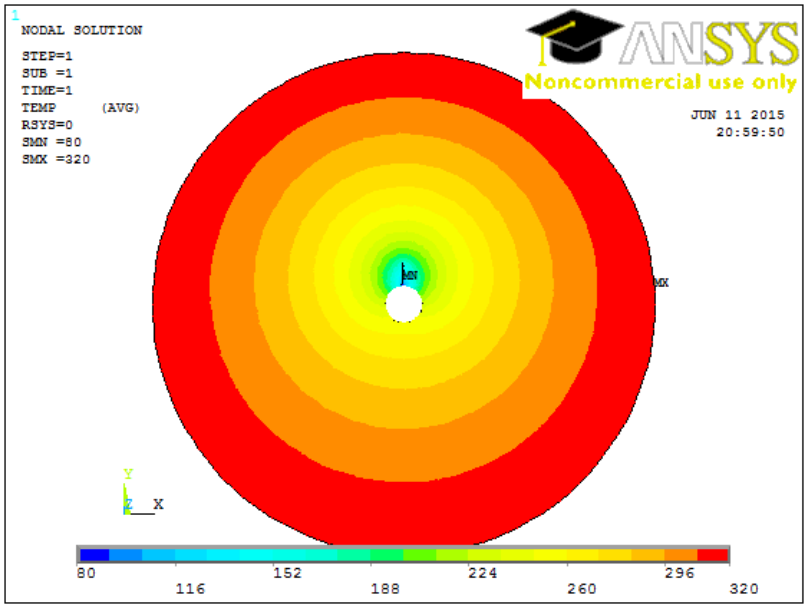

Figure 80: Isobaric contour plot

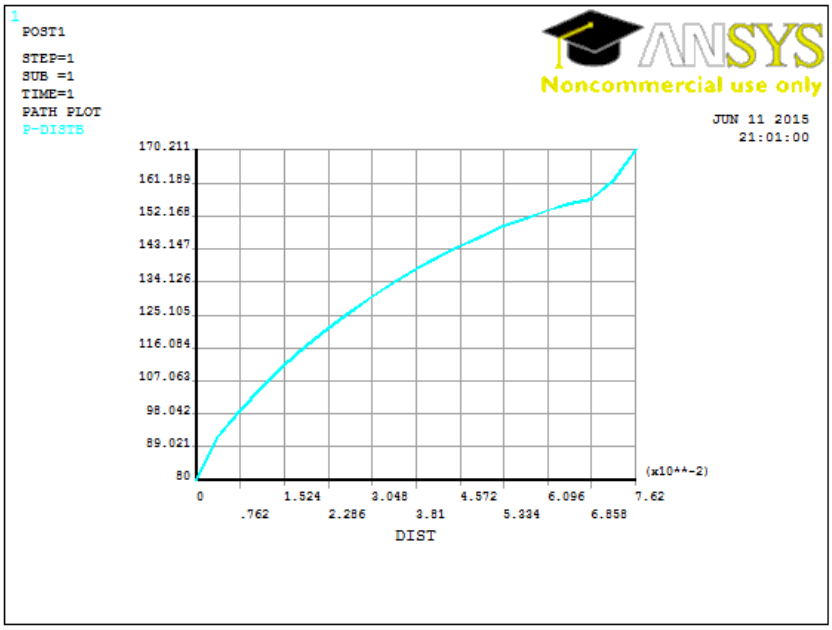

Figure 81: Pressure distribution from the inner boundary to the tip of perforation tunnel

Well radius (inches)	2.4
Perforation length (inches)	6
Perforation phasing (degrees)	360

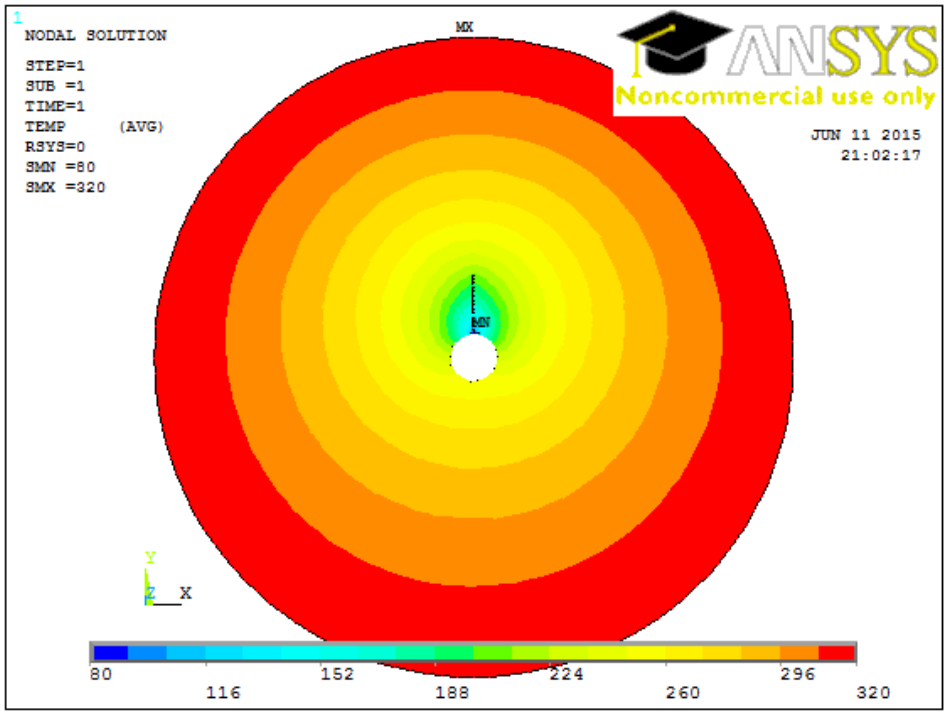

Figure 82: Isobaric contour plot

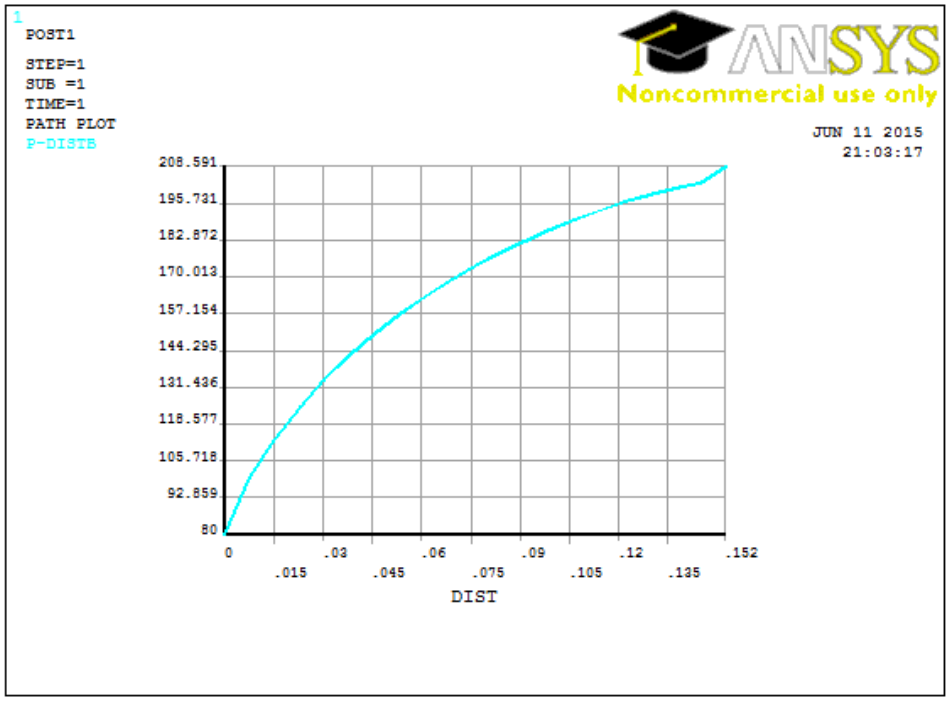

Figure 83: Pressure distribution from the inner boundary to the tip of perforation tunnel

Well radius (inches)	2.4
Perforation length (inches)	9
Perforation phasing (degrees)	360

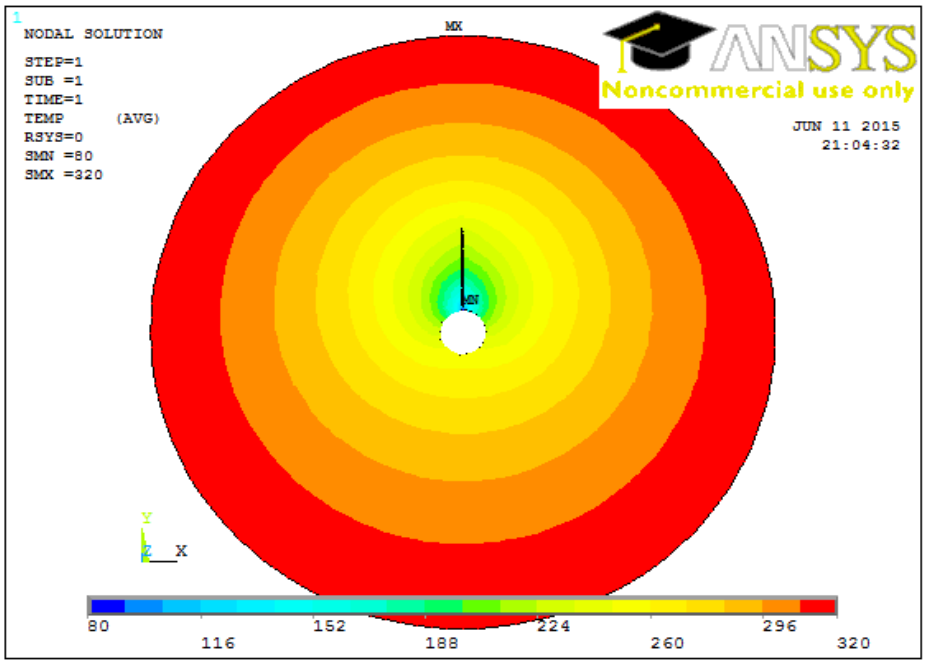

Figure 84: Isobaric contour plot

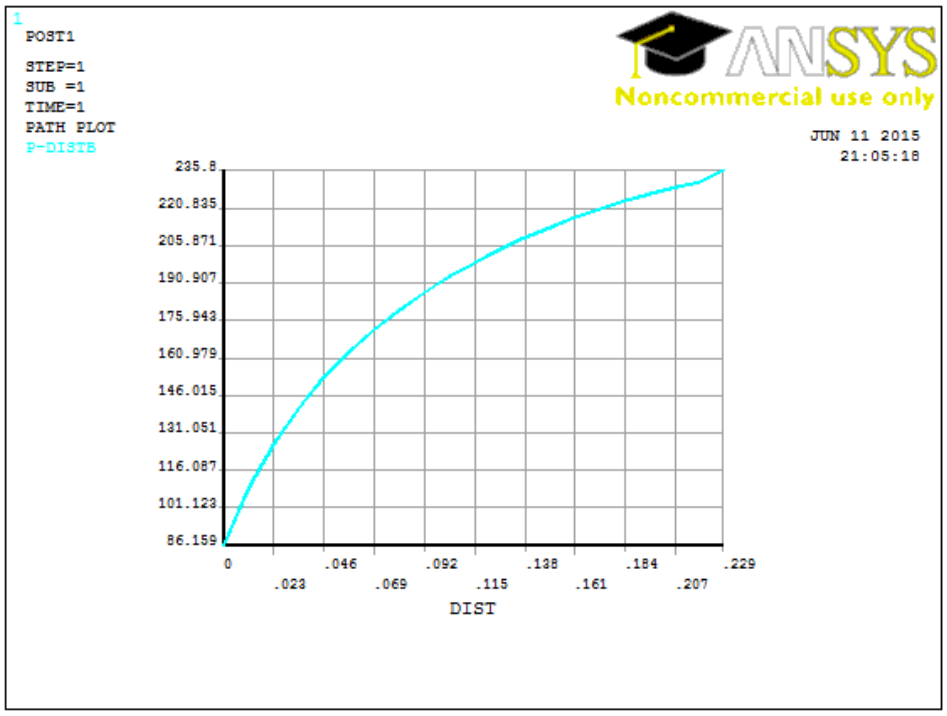

Figure 85: Pressure distribution from the inner boundary to the tip of perforation tunnel

Well radius (inches)	3
Perforation length (inches)	3
Perforation phasing (degrees)	360

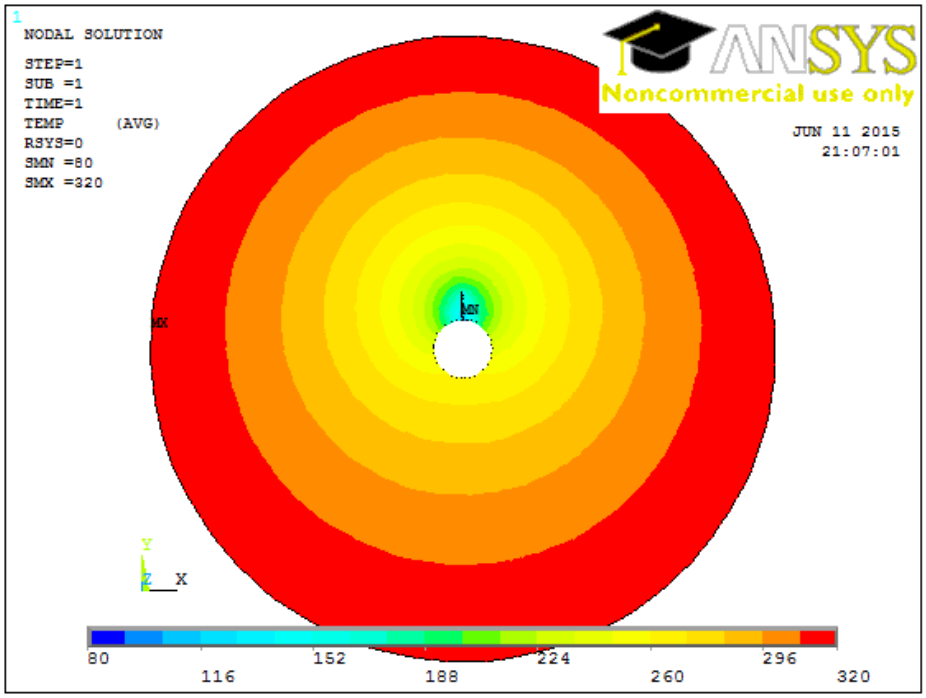

Figure 86: Isobaric contour plot

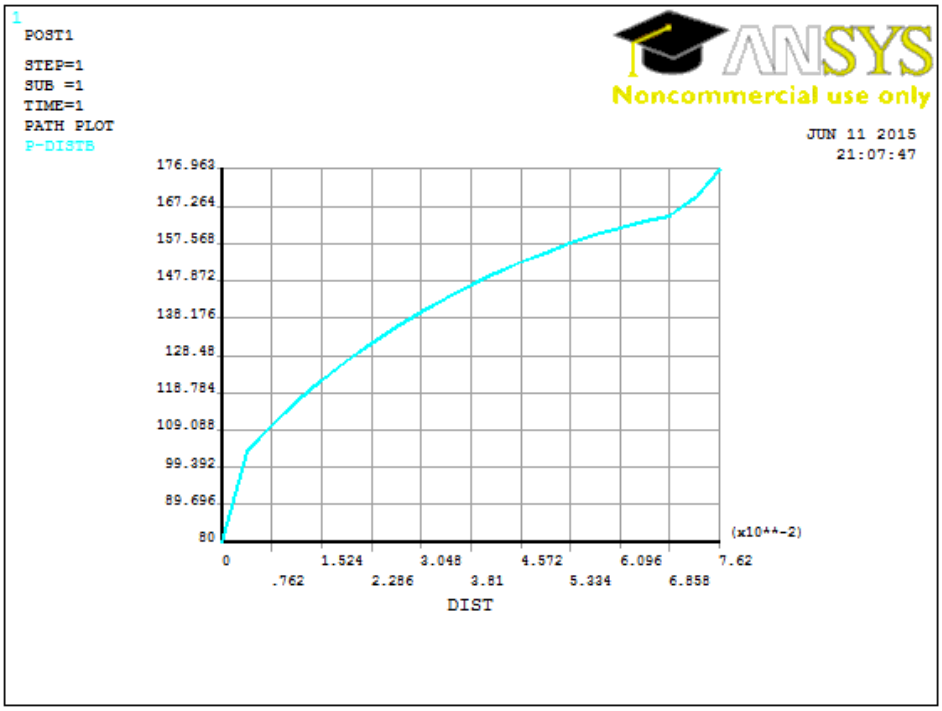

Figure 87: Pressure distribution from the inner boundary to the tip of perforation tunnel

Well radius (inches)	3
Perforation length (inches)	6
Perforation phasing (degrees)	360

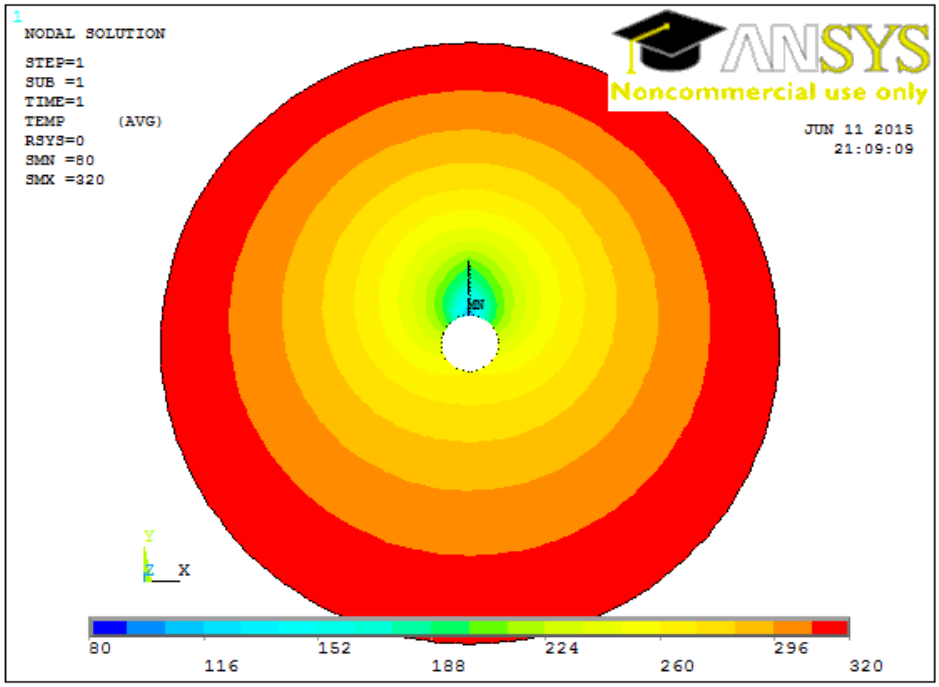

Figure 88: Isobaric contour plot

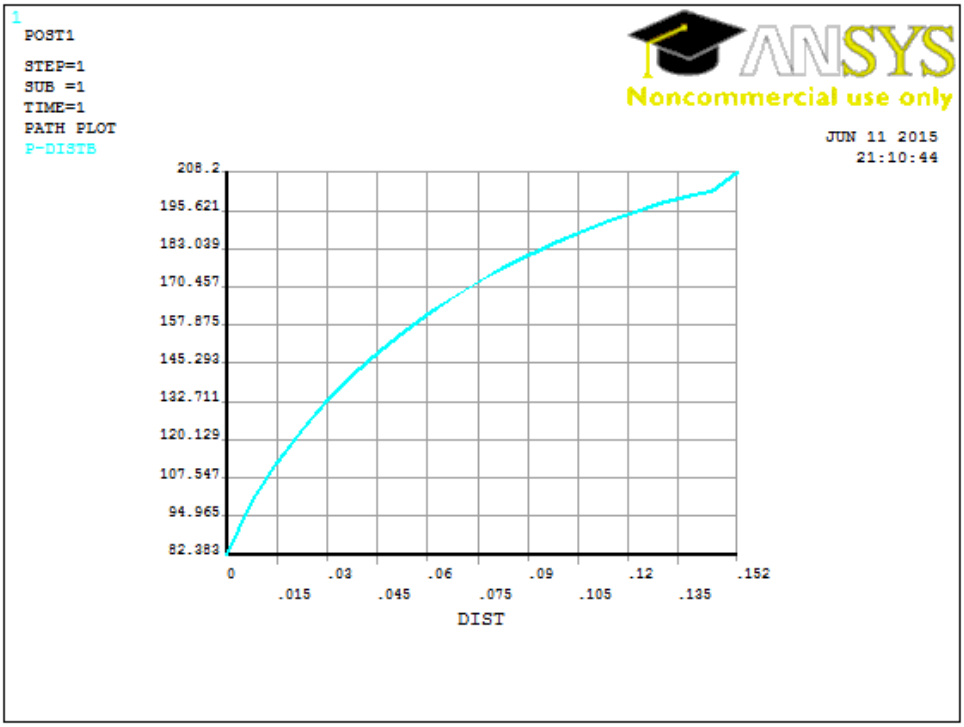

Figure 89: Pressure distribution from the inner boundary to the tip of perforation tunnel

Well radius (inches)	3
Perforation length (inches)	9
Perforation phasing (degrees)	360

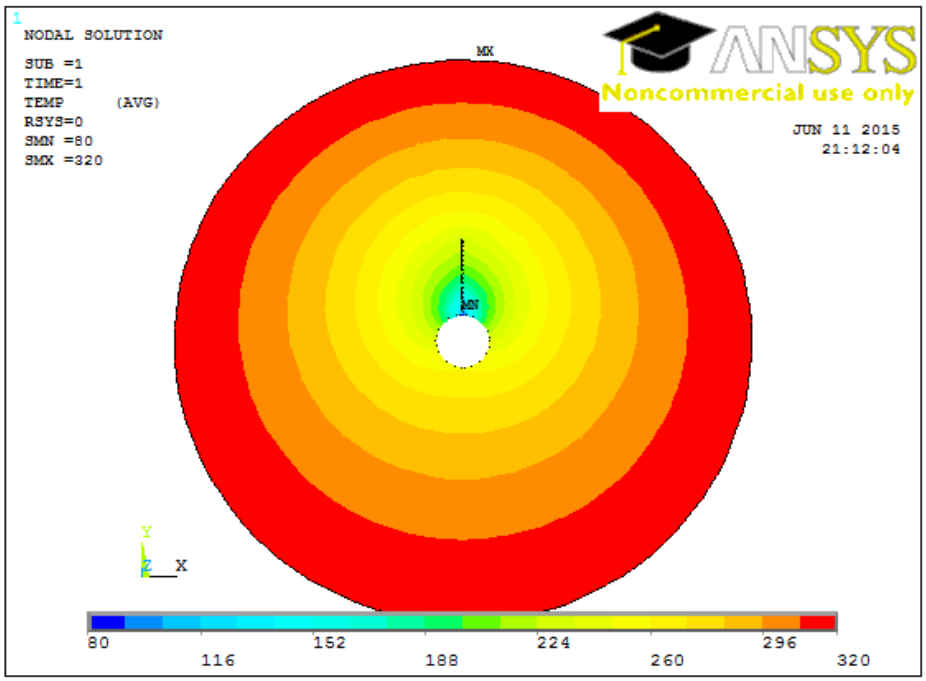

Figure 90: Isobaric contour plot

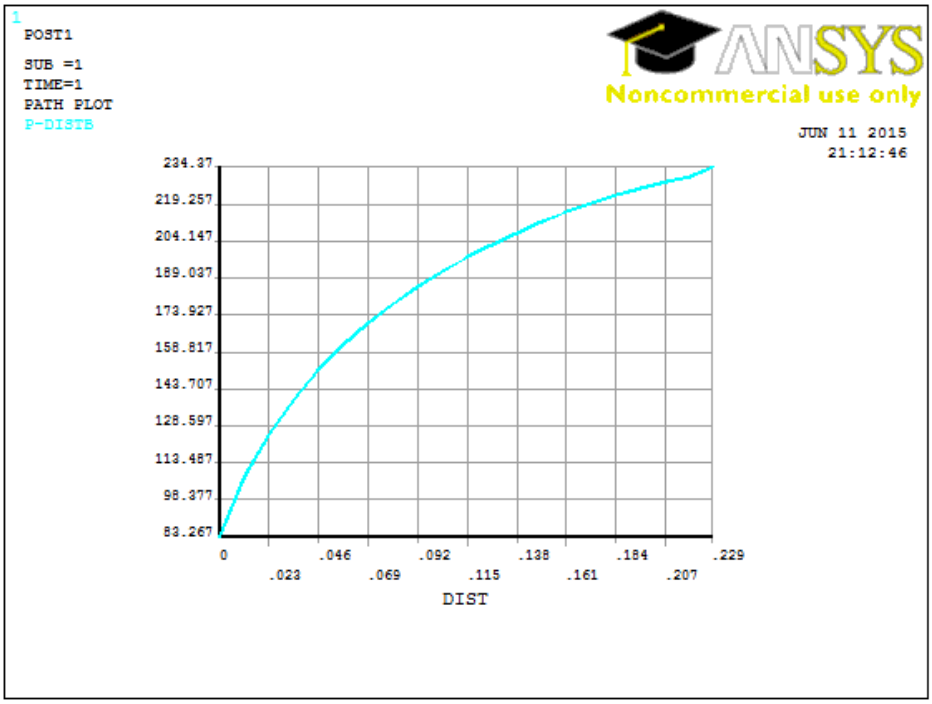

Figure 91: Pressure distribution from the inner boundary to the tip of perforation tunnel

Well radius (inches)	4.3
Perforation length (inches)	3
Perforation phasing (degrees)	360

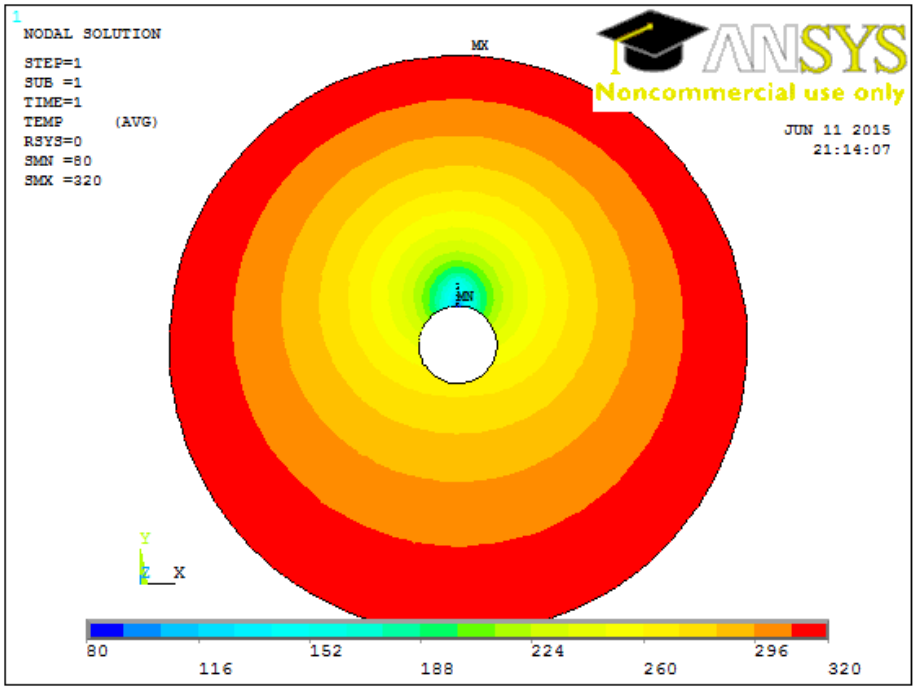

Figure 92: Isobaric contour plot

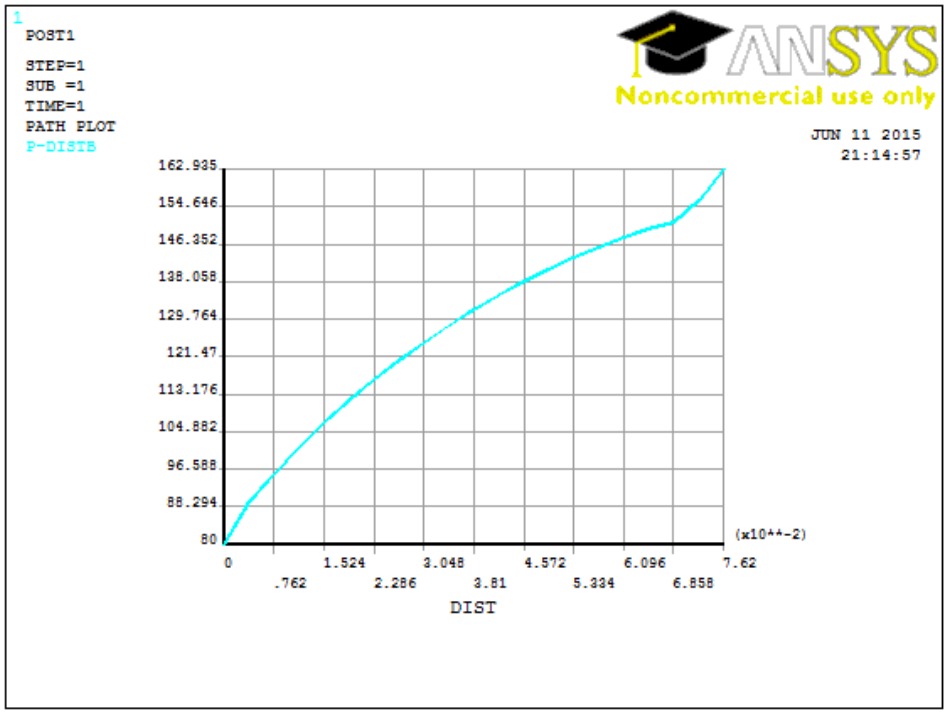

Figure 93: Pressure distribution from the inner boundary to the tip of perforation tunnel

Well radius (inches)	4.3
Perforation length (inches)	6
Perforation phasing (degrees)	360

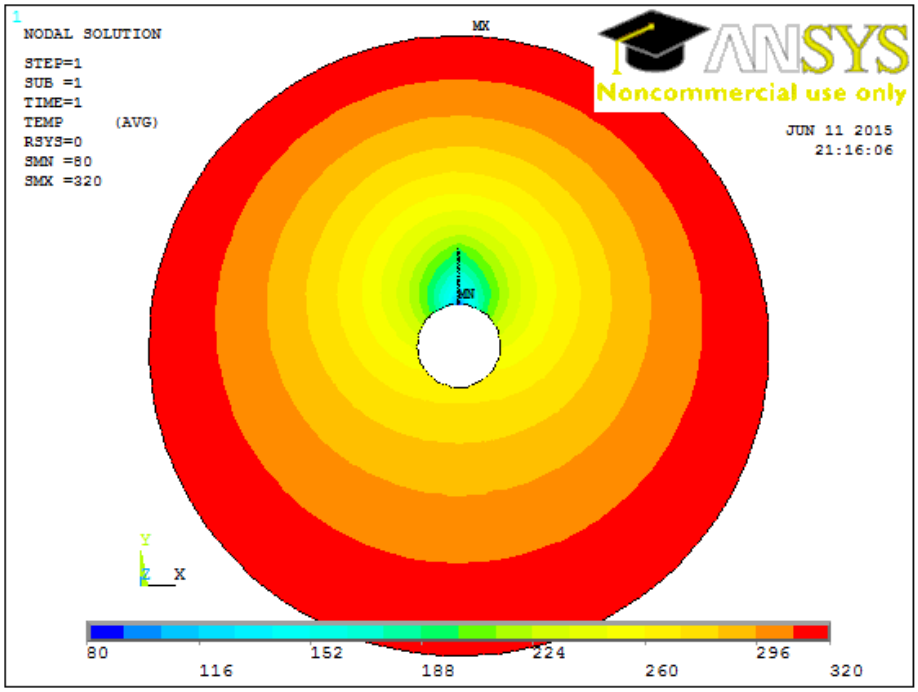

Figure 94: Isobaric contour plot

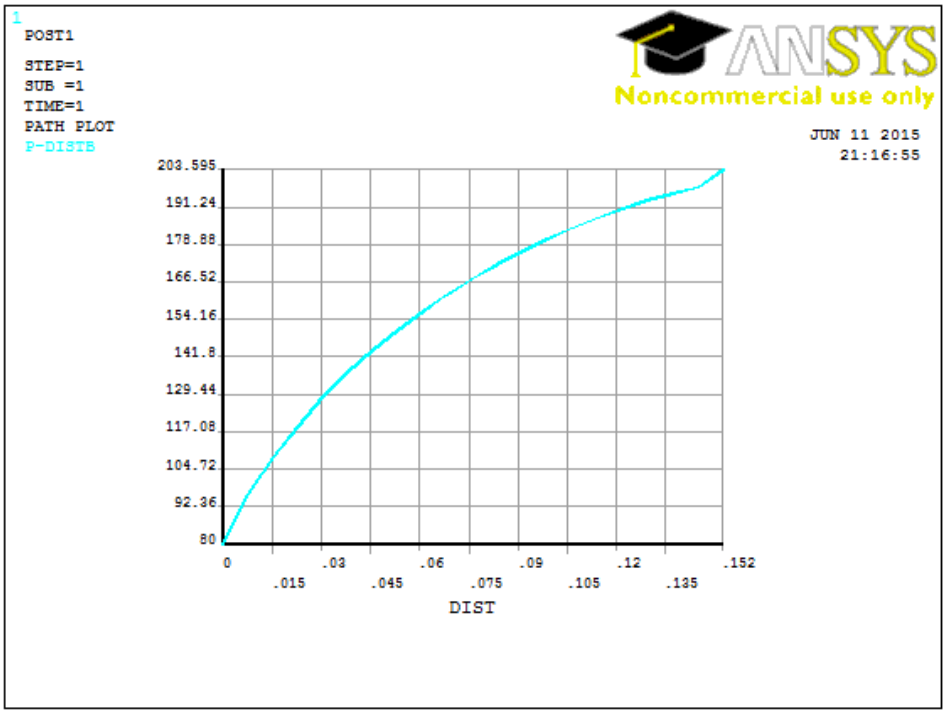

Figure 95: Pressure distribution from the inner boundary to the tip of perforation tunnel

Well radius (inches)	4.3
Perforation length (inches)	9
Perforation phasing (degrees)	360

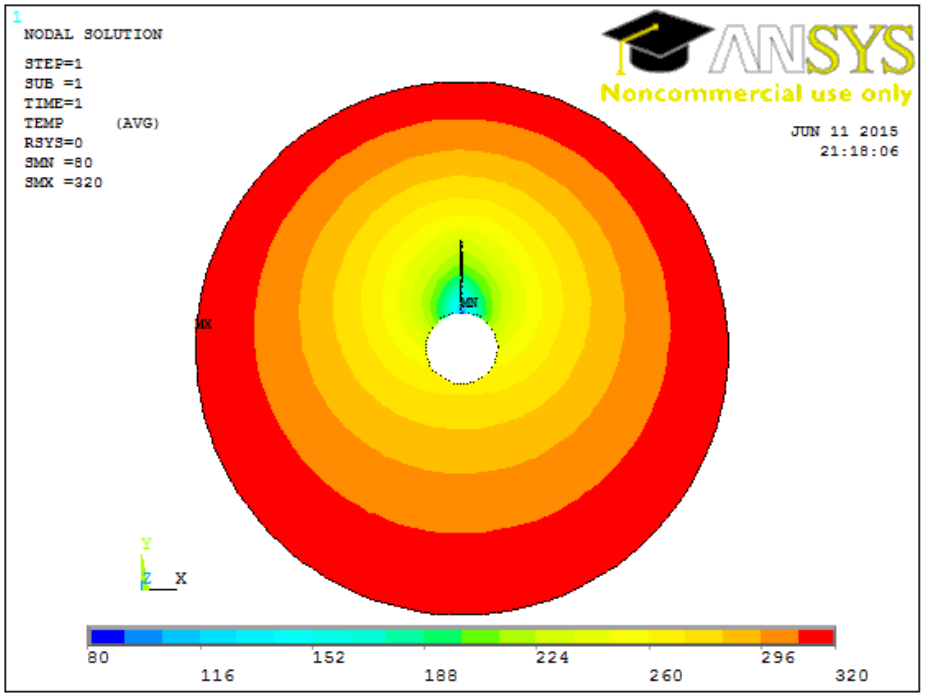

Figure 96: Isobaric contour plot

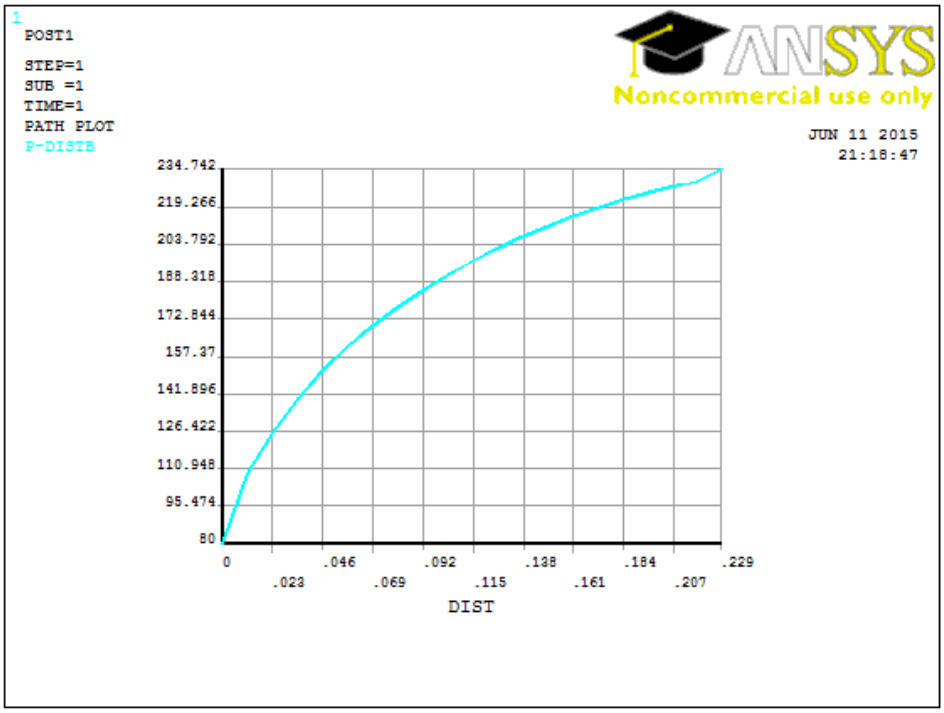

Figure 97: Pressure distribution from the inner boundary to the tip of perforation tunnel

Well radius (inches)	2.4
Perforation length (inches)	3
Perforation phasing (degrees)	350/10

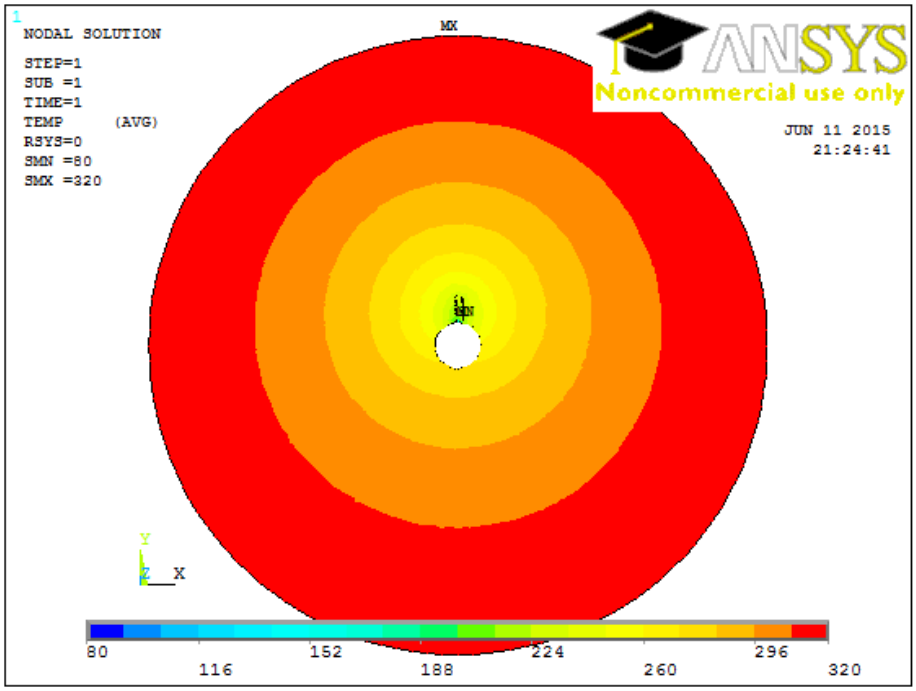

Figure 98: Isobaric contour plot

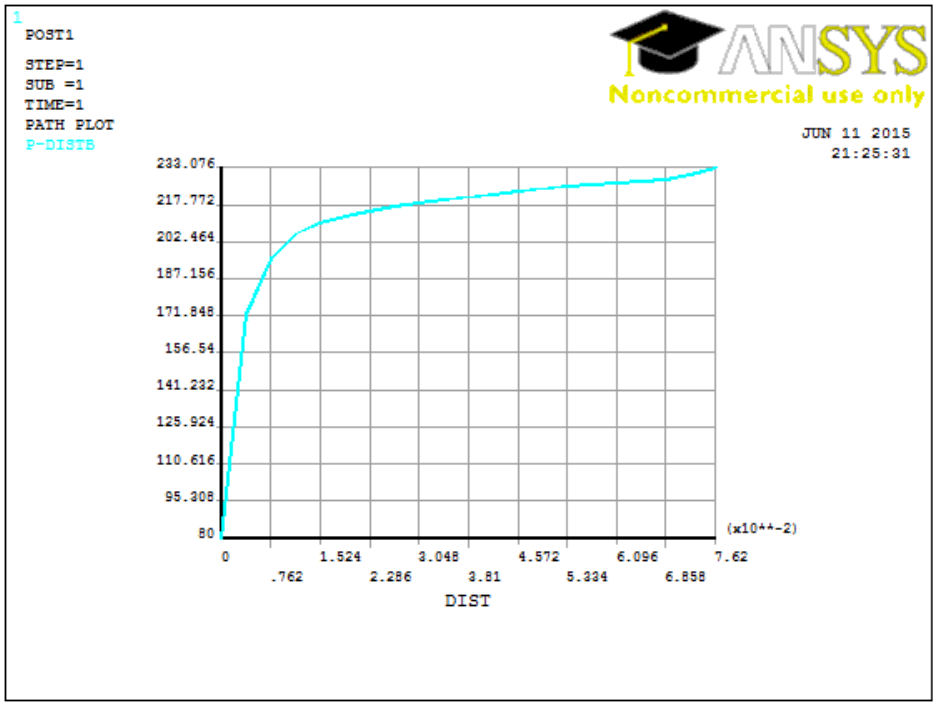

Figure 99: Pressure distribution from the inner boundary to the tip of perforation tunnel

Well radius (inches)	2.4
Perforation length (inches)	6
Perforation phasing (degrees)	350/10

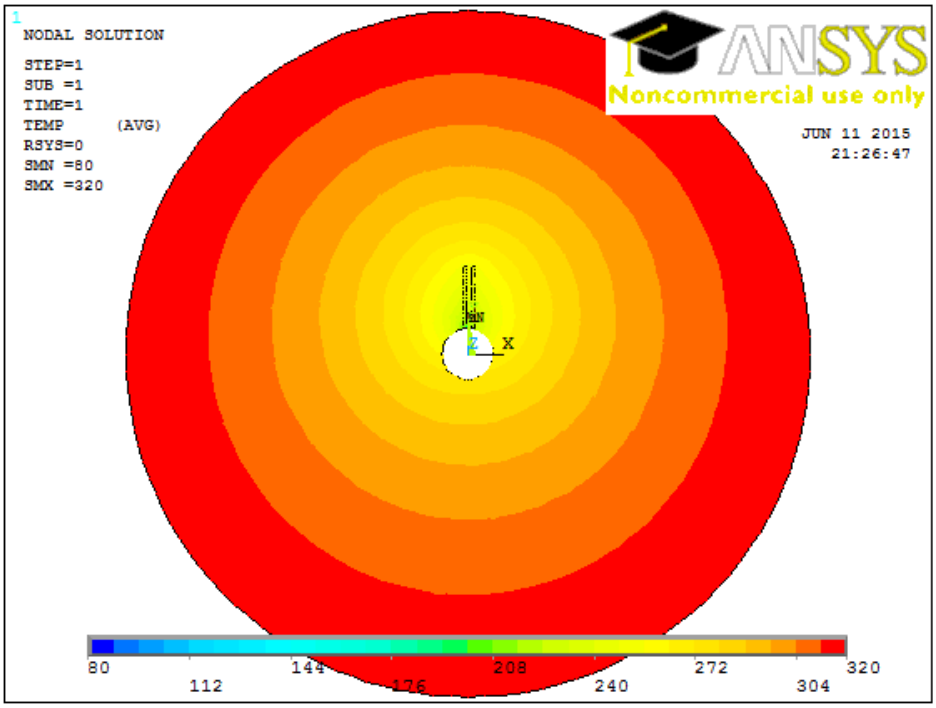

Figure 100: Isobaric contour plot

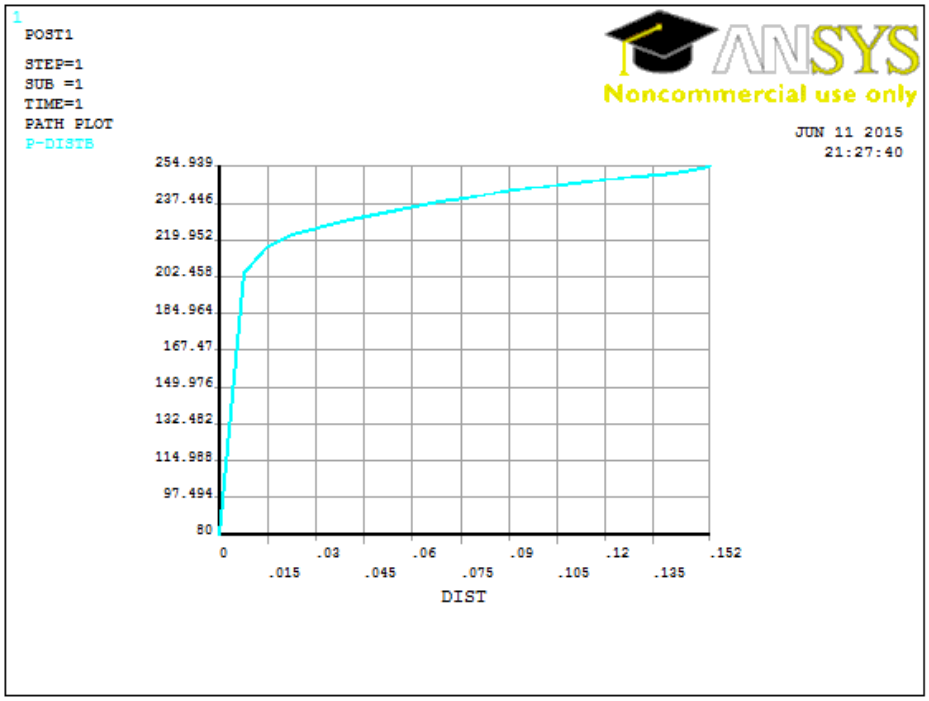

Figure 101: Pressure distribution from the inner boundary to the tip of perforation tunnel

Well radius (inches)	2.4
Perforation length (inches)	9
Perforation phasing (degrees)	350/10

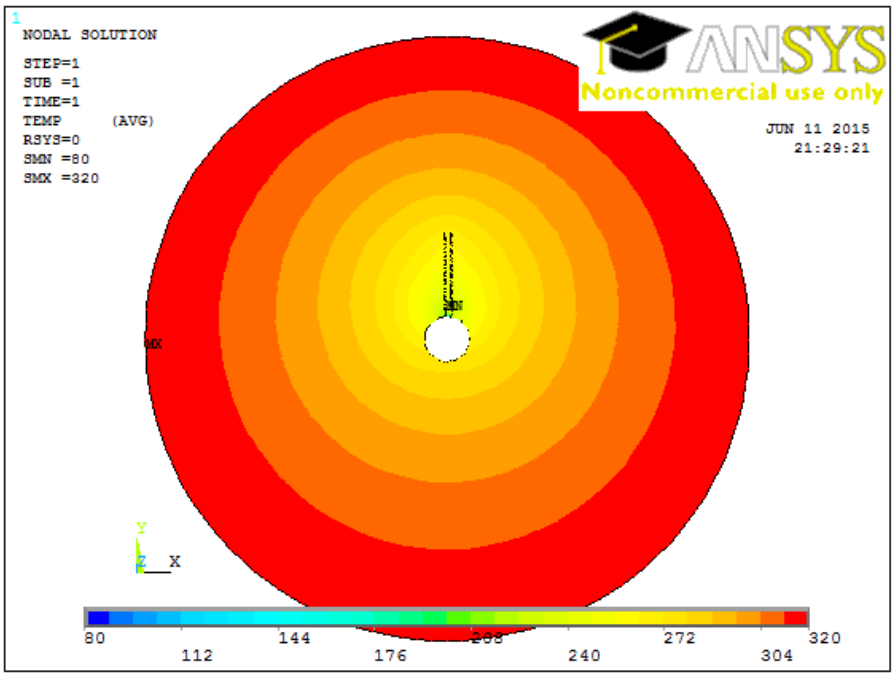

Figure 102: Isobaric contour plot

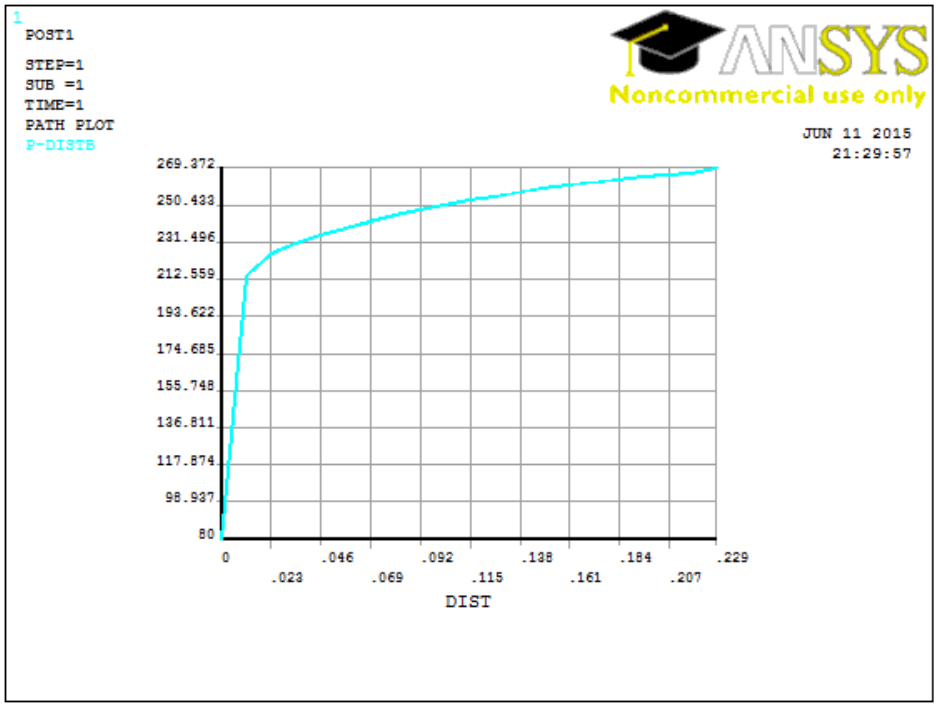

Figure 103: Pressure distribution from the inner boundary to the tip of perforation tunnel

Well radius (inches)	3
Perforation length (inches)	3
Perforation phasing (degrees)	350/10

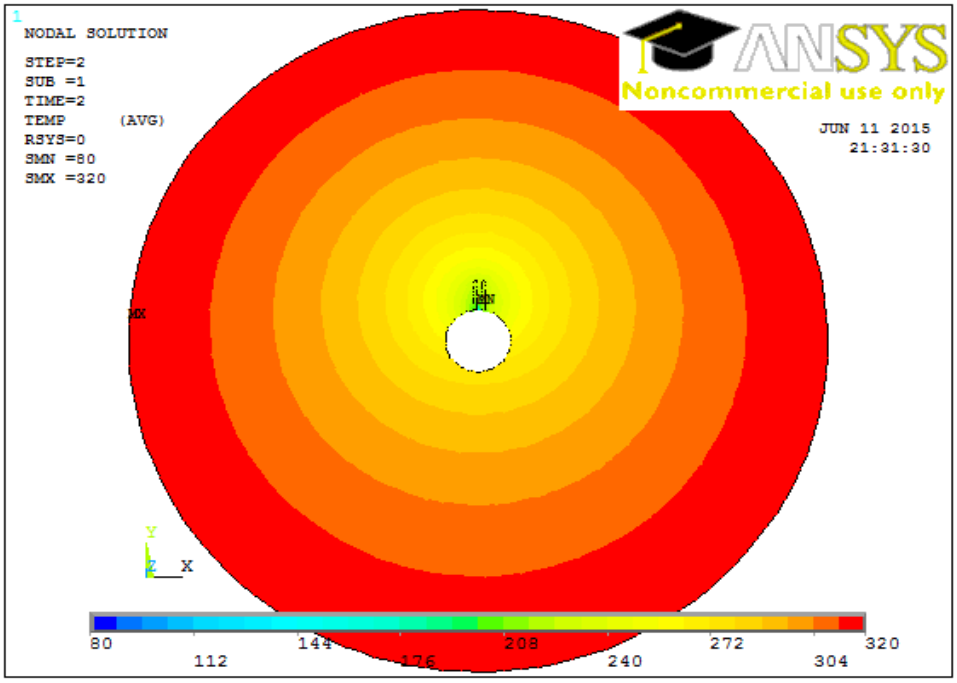

Figure 104: Isobaric contour plot

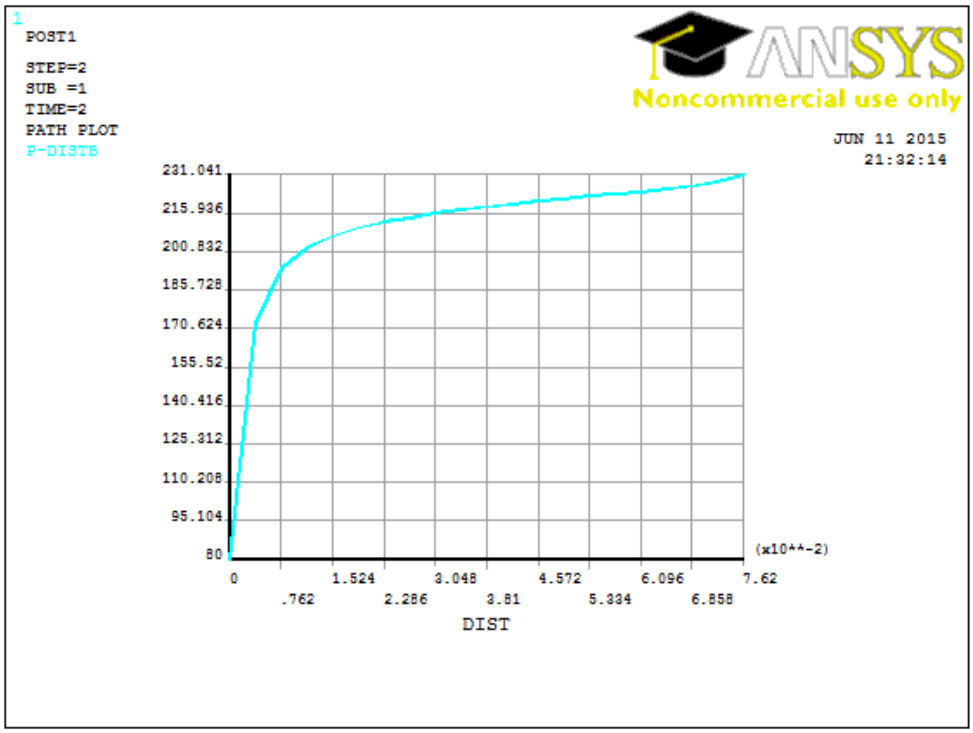

Figure 105: Pressure distribution from the inner boundary to the tip of perforation tunnel

Well radius (inches)	3
Perforation length (inches)	6
Perforation phasing (degrees)	350/10

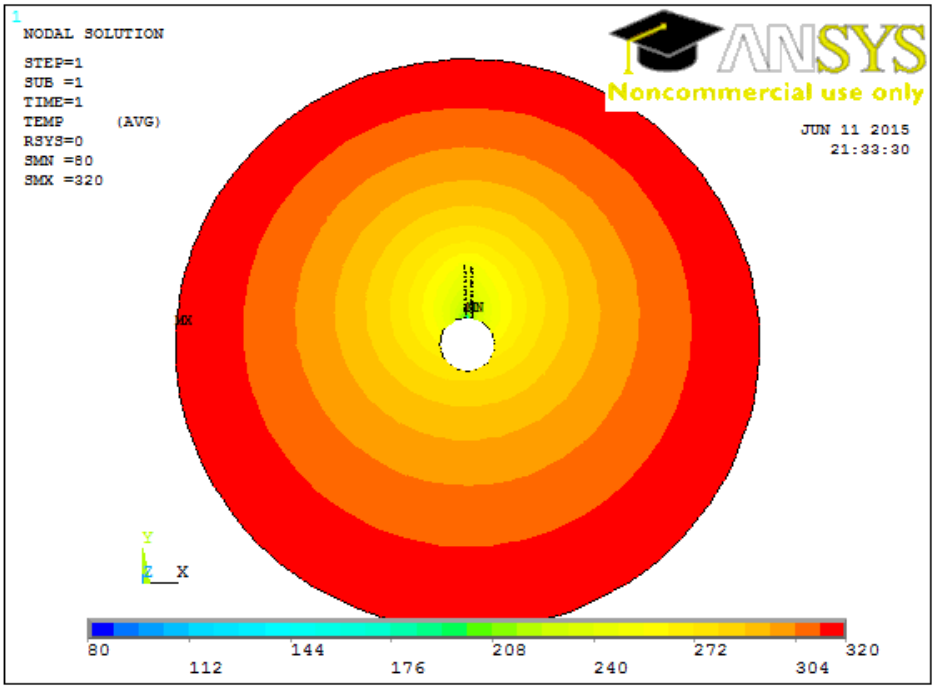

Figure 106: Isobaric contour plot

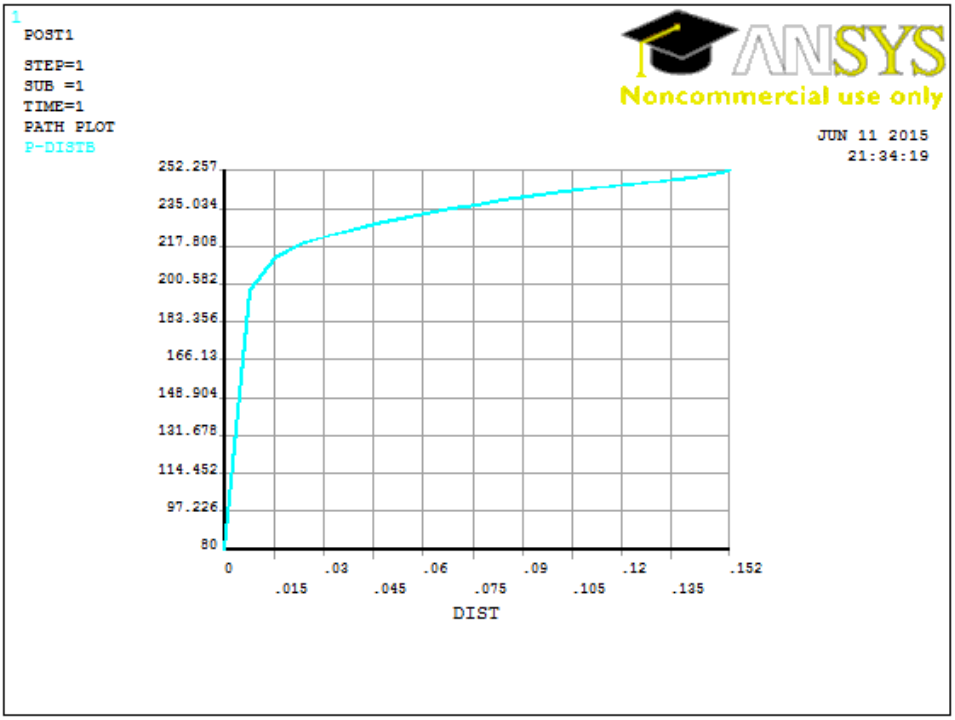

Figure 107: Pressure distribution from the inner boundary to the tip of perforation tunnel

Well radius (inches)	3
Perforation length (inches)	9
Perforation phasing (degrees)	350/10

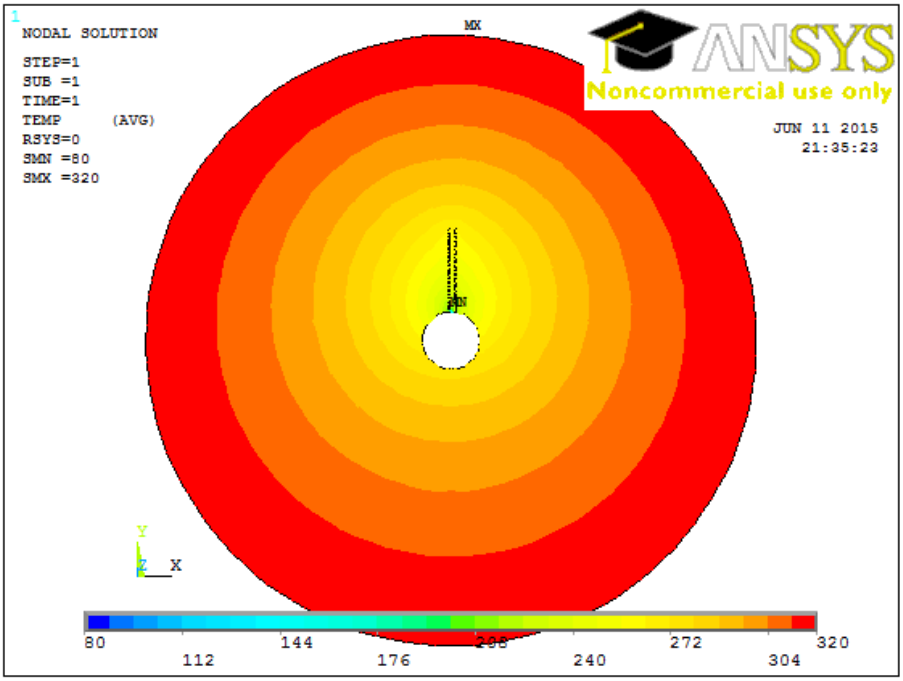

Figure 108: Isobaric contour plot

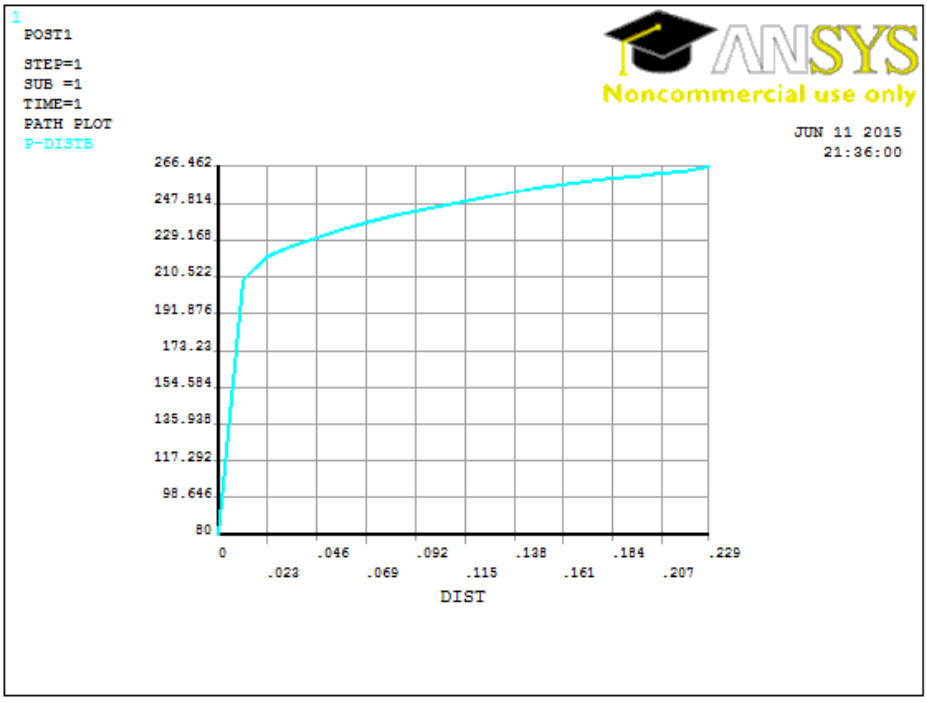

Figure 109: Pressure distribution from the inner boundary to the tip of perforation tunnel

Well radius (inches)	4.3
Perforation length (inches)	3
Perforation phasing (degrees)	350/10

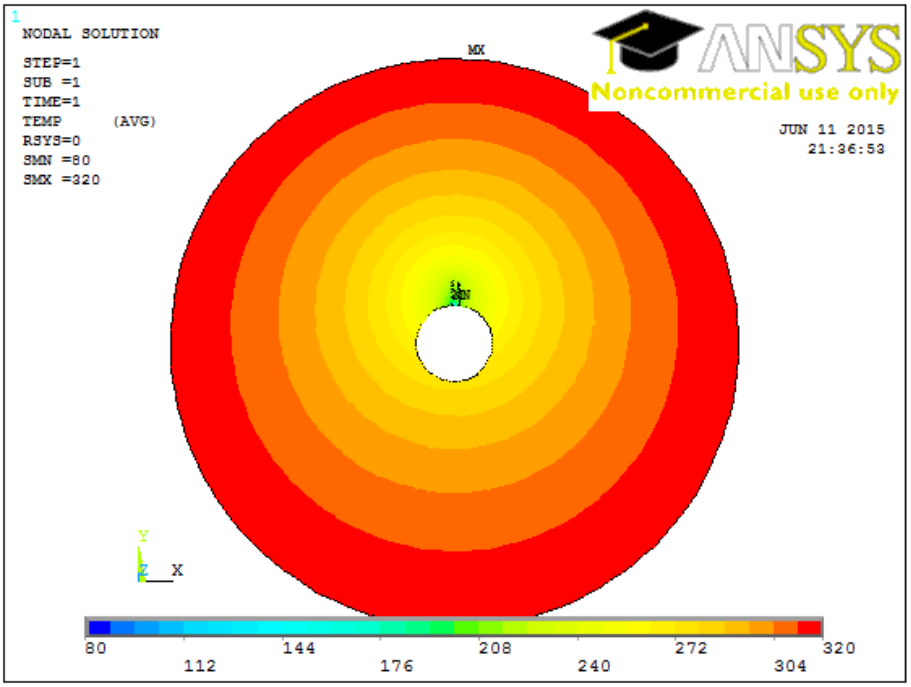

Figure 110: Isobaric contour plot

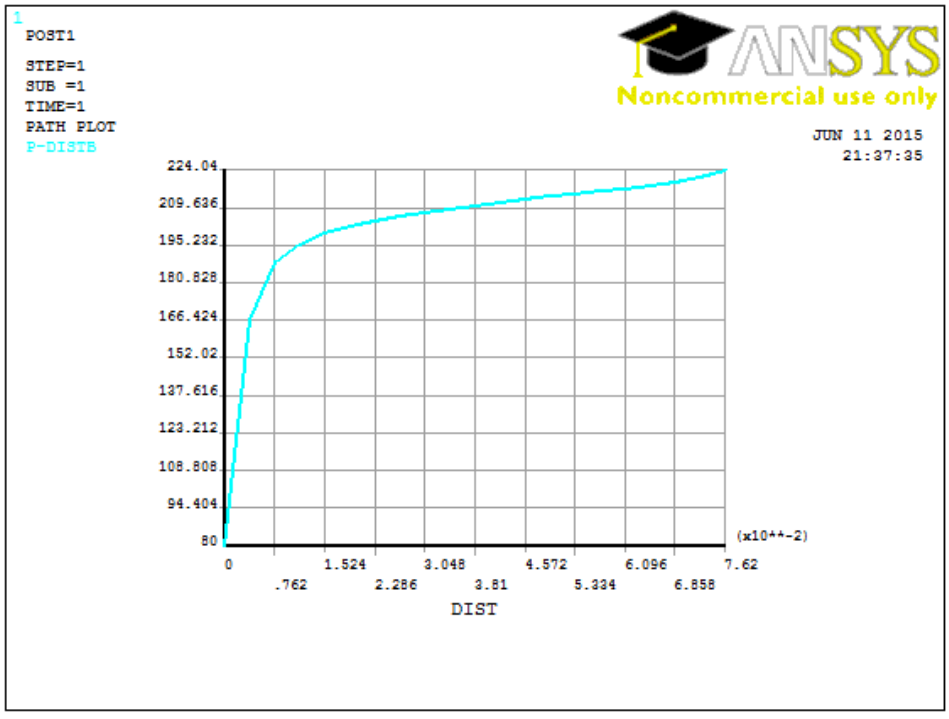

Figure 111: Pressure distribution from the inner boundary to the tip of perforation tunnel

Well radius (inches)	4.3
Perforation length (inches)	6
Perforation phasing (degrees)	350/10

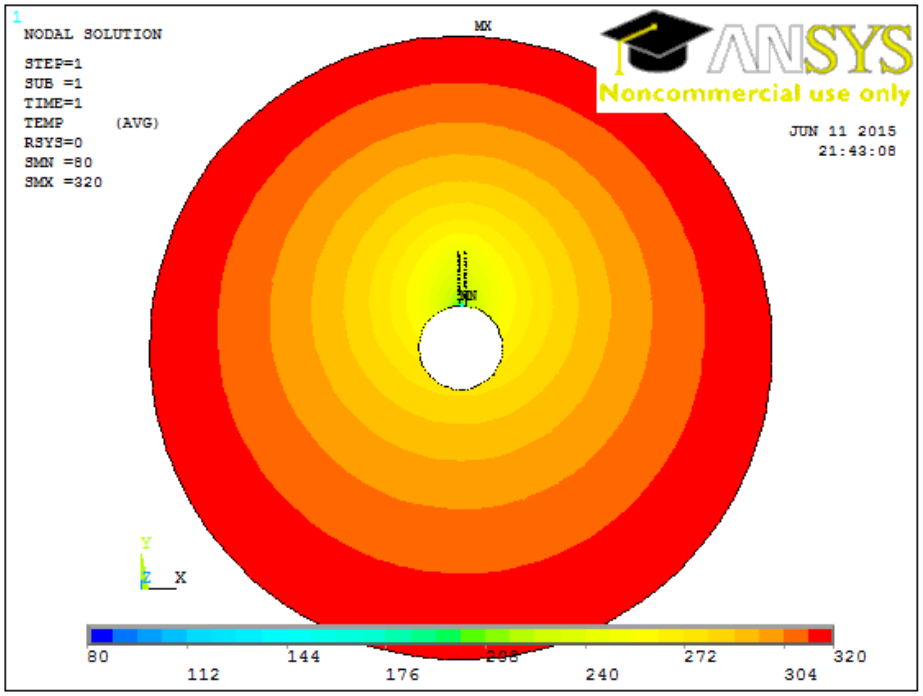

Figure 112: Isobaric contour plot

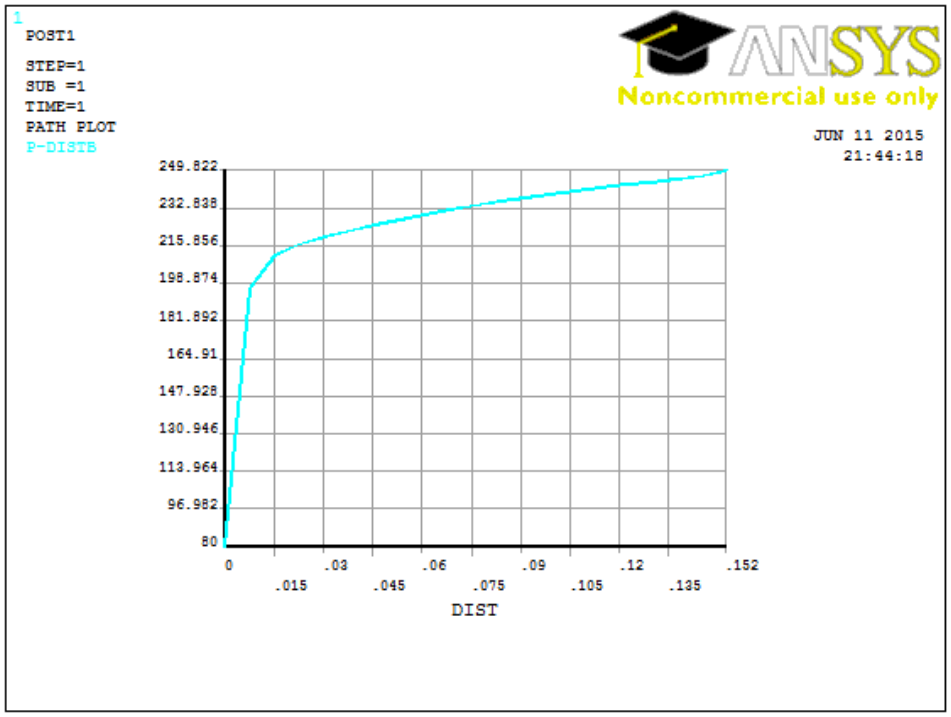

Figure 113: Pressure distribution from the inner boundary to the tip of perforation tunnel

Well radius (inches)	4.3
Perforation length (inches)	9
Perforation phasing (degrees)	350/10

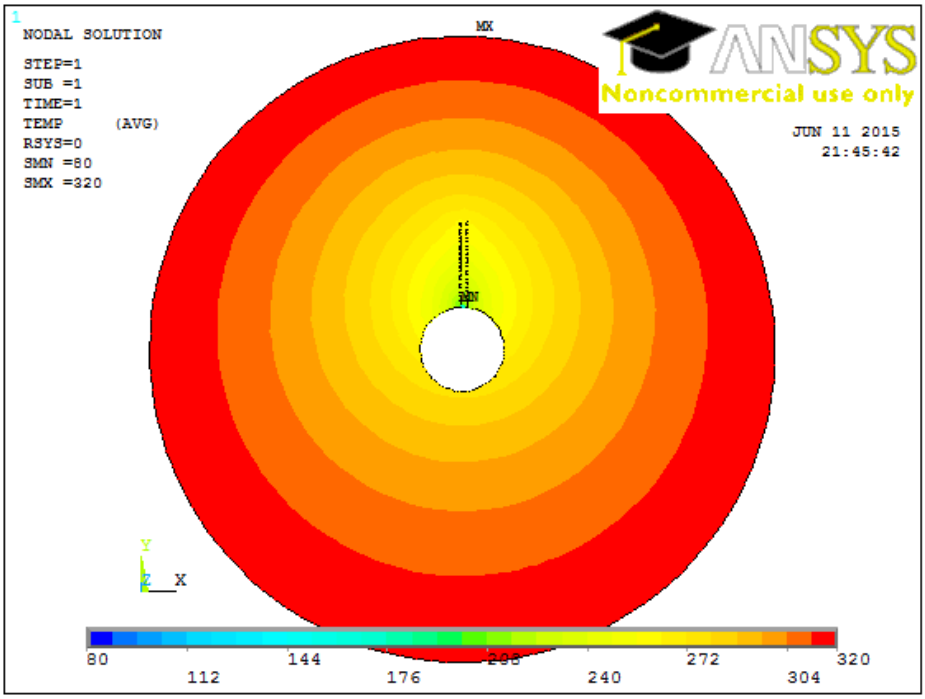

Figure 114: Isobaric contour plot

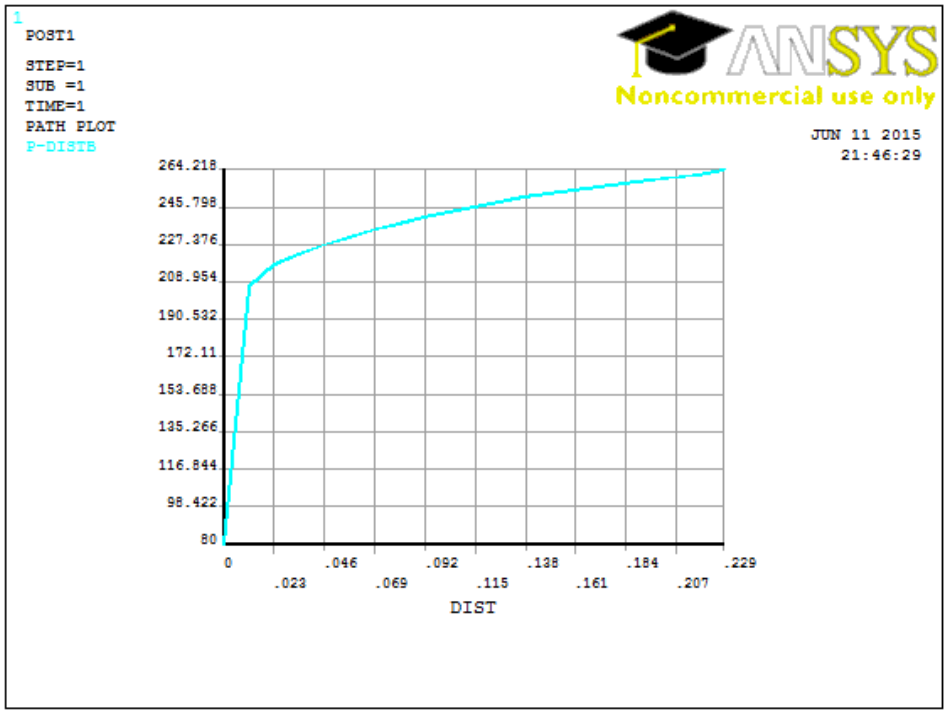

Figure 115: Pressure distribution from the inner boundary to the tip of perforation tunnel

APPENDIX D: Finite element modeling simulation results for K_H/K_V = 10 (anisotropic reservoir case)

Well radius (inches)	2.4
Perforation length (inches)	3
Perforation phasing (degrees)	360

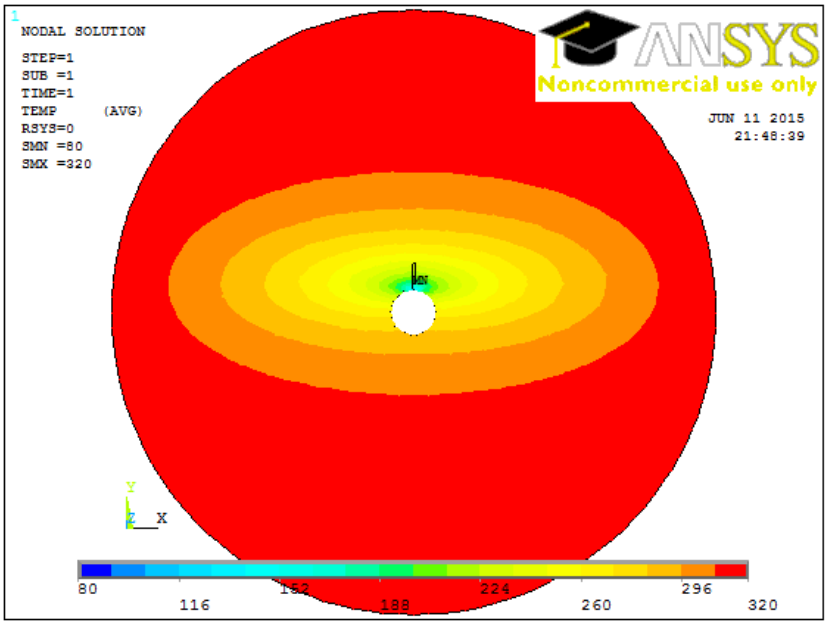

Figure 116: Isobaric contour plot

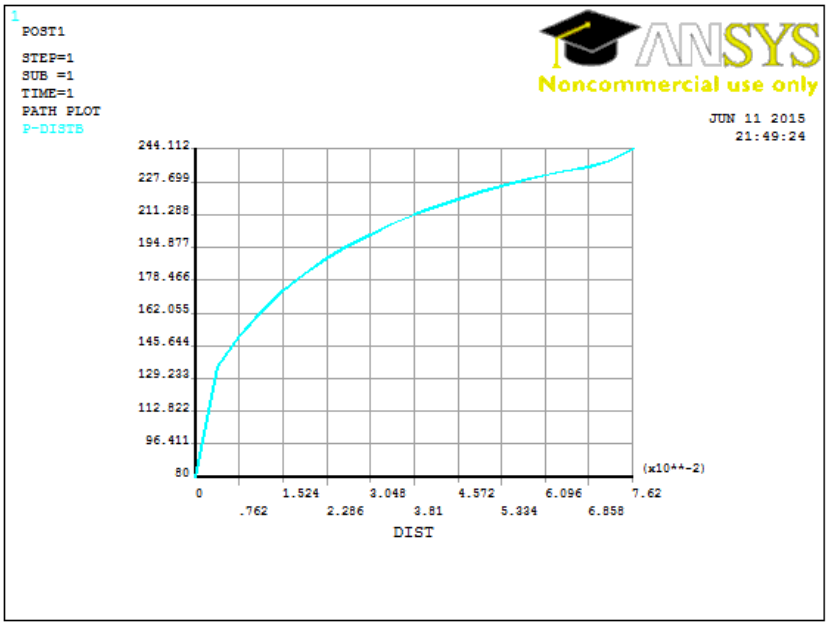

Figure 117: Pressure distribution from inner boundary to the tip of perforation tunnel

Well radius (inches)	2.4
Perforation length (inches)	6
Perforation phasing (degrees)	360

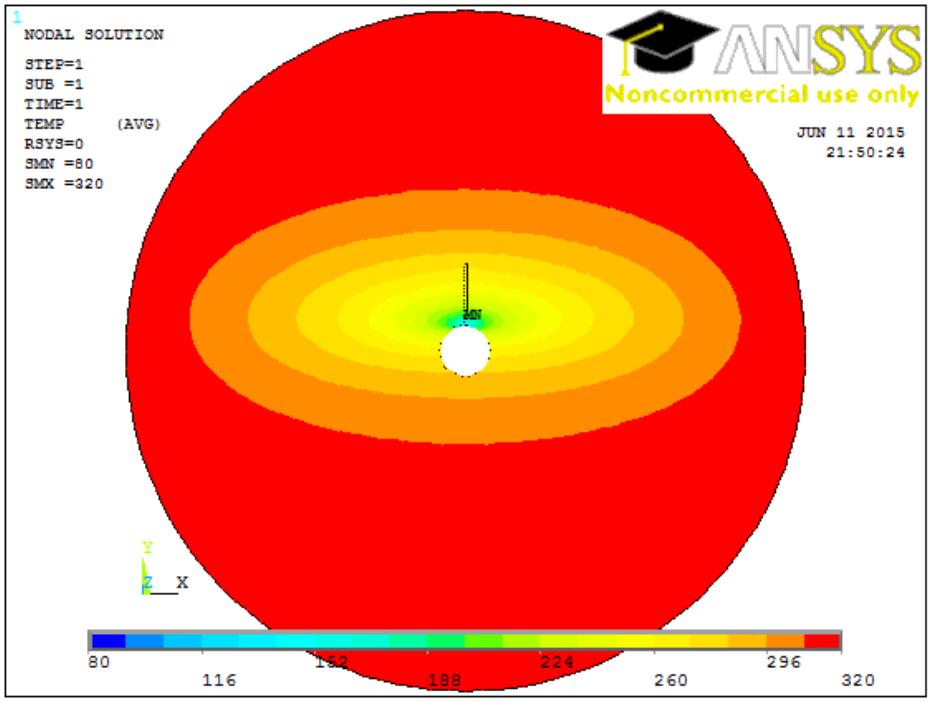

Figure 118: Isobaric contour plot

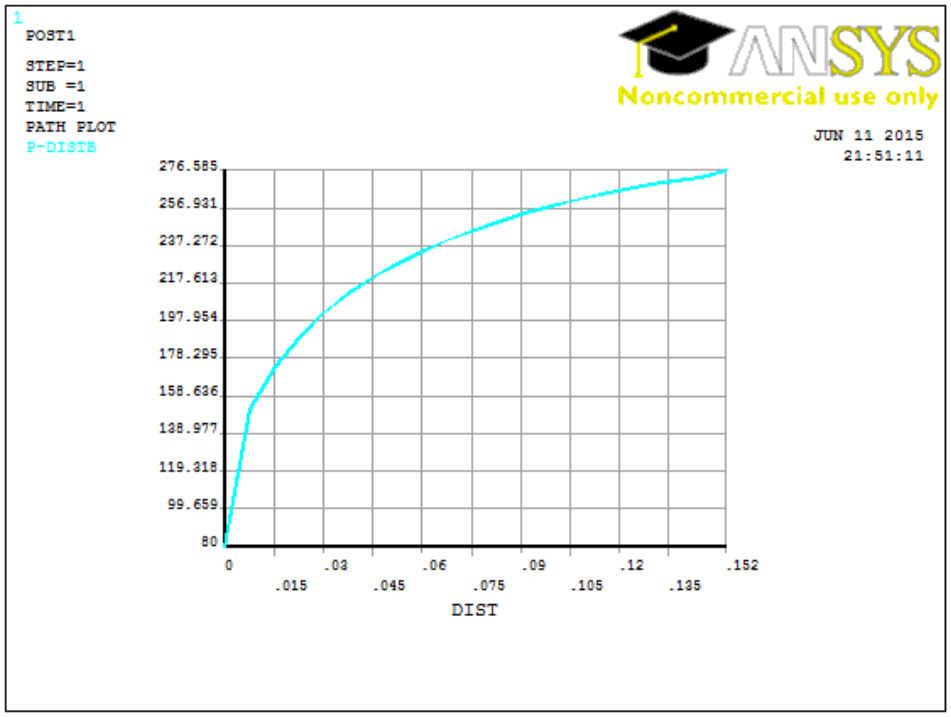

Figure 119: Pressure distribution from inner boundary to the tip of perforation tunnel

Well radius (inches)	2.4
Perforation length (inches)	9
Perforation phasing (degrees)	360

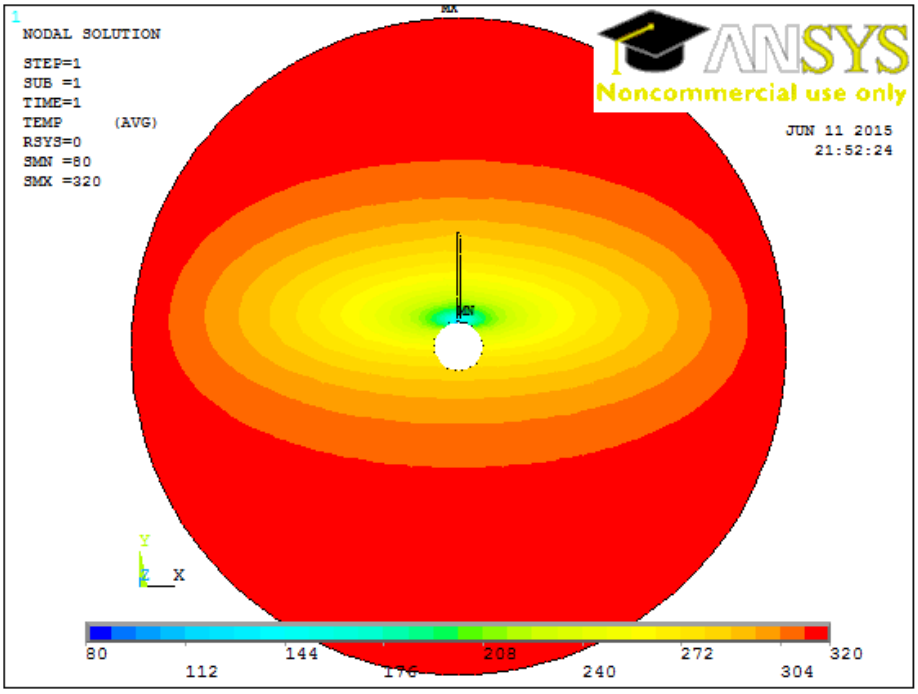

Figure 120: Isobaric contour plot

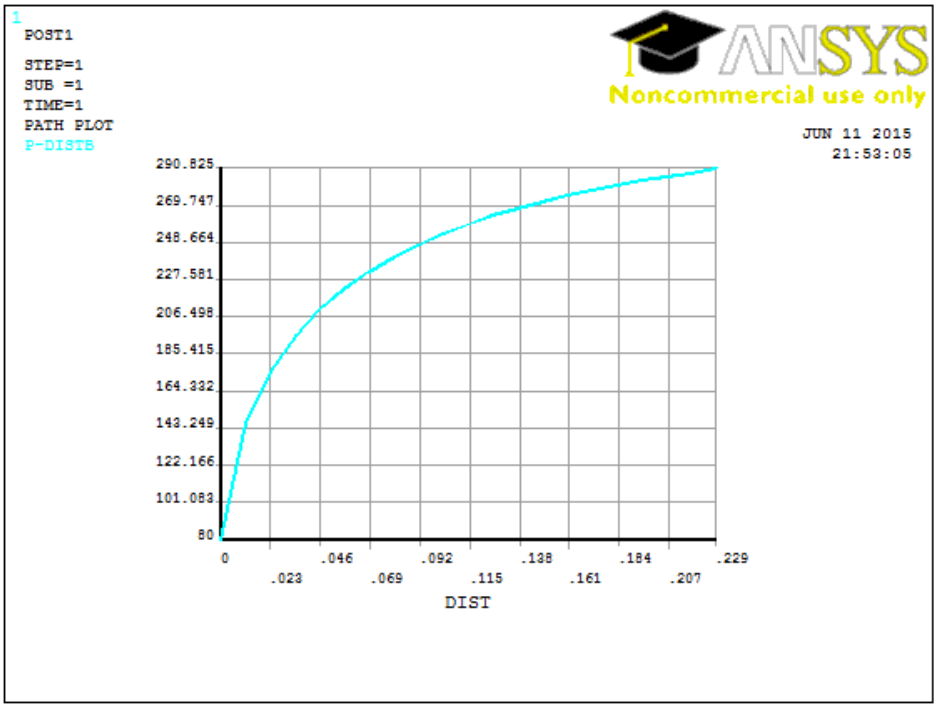

Figure 121: Pressure distribution from inner boundary to the tip of perforation tunnel

Well radius (inches)	3
Perforation length (inches)	3
Perforation phasing (degrees)	360

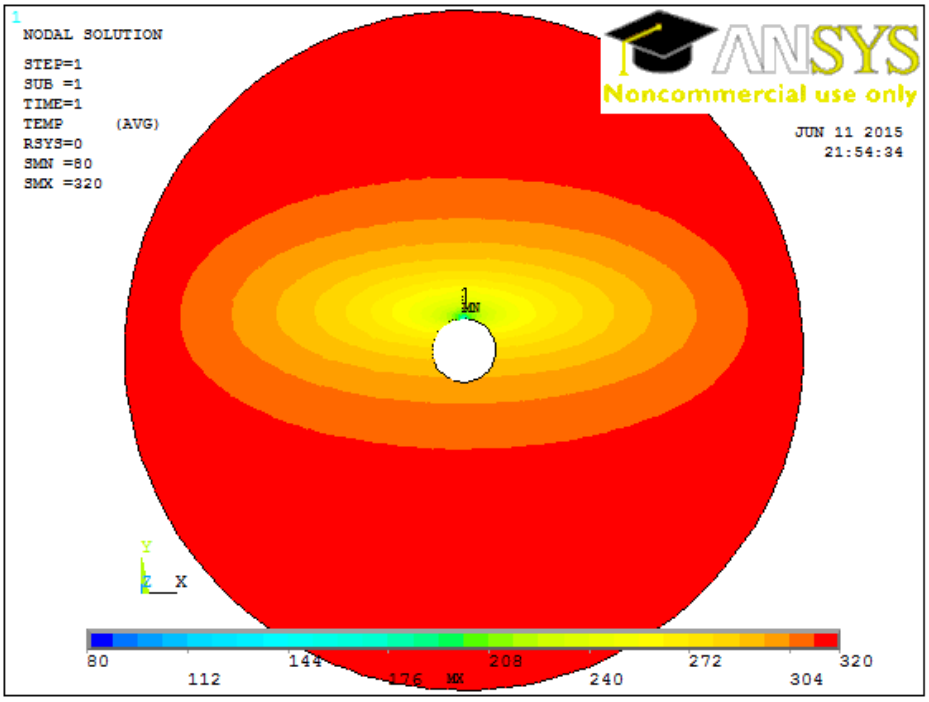

Figure 122: Isobaric contour plot

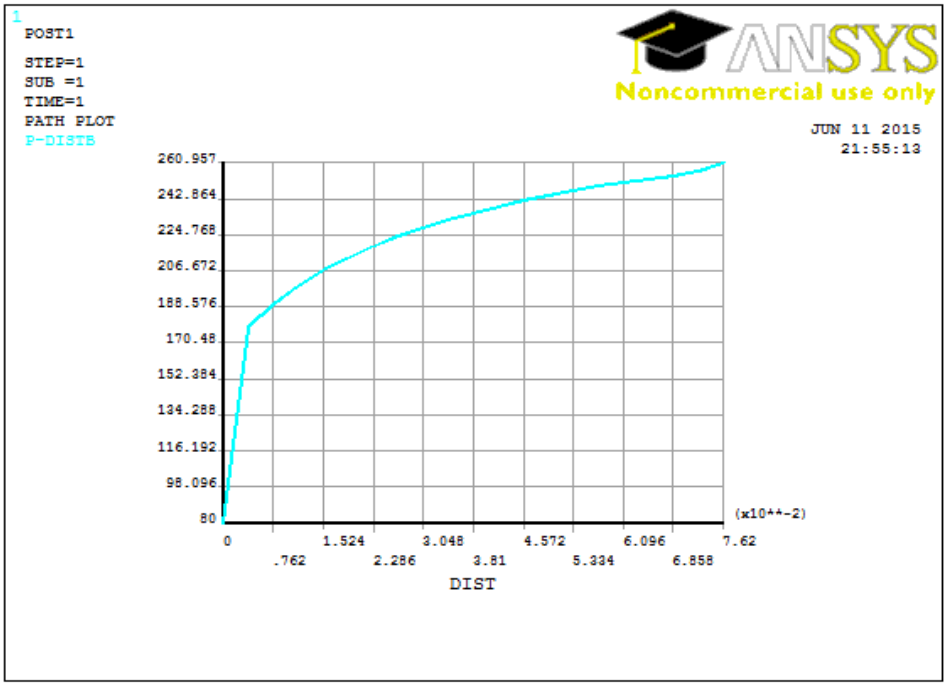

Figure 123: Pressure distribution from inner boundary to the tip of perforation tunnel

Well radius (inches)	3
Perforation length (inches)	6
Perforation phasing (degrees)	360

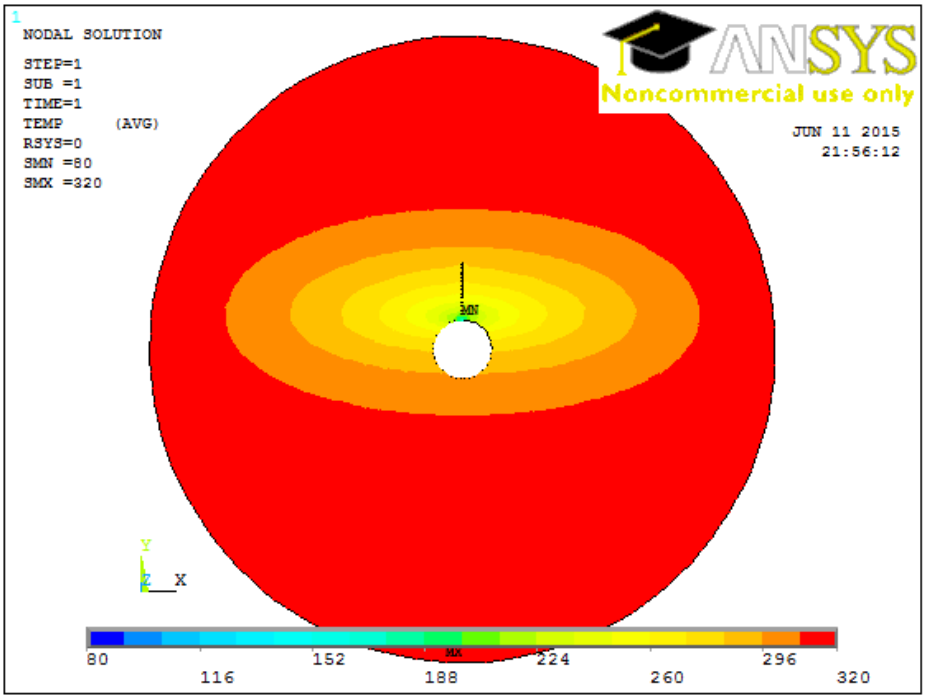

Figure 124: Isobaric contour plot

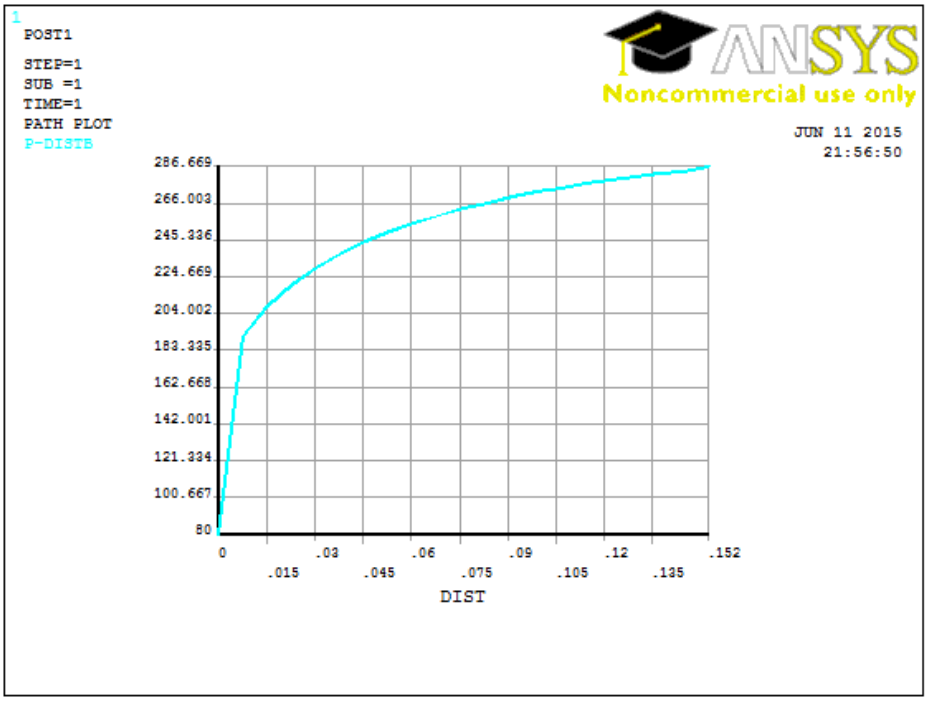

Figure 125: Pressure distribution from inner boundary to the tip of perforation tunnel

Well radius (inches)	3
Perforation length (inches)	9
Perforation phasing (degrees)	360

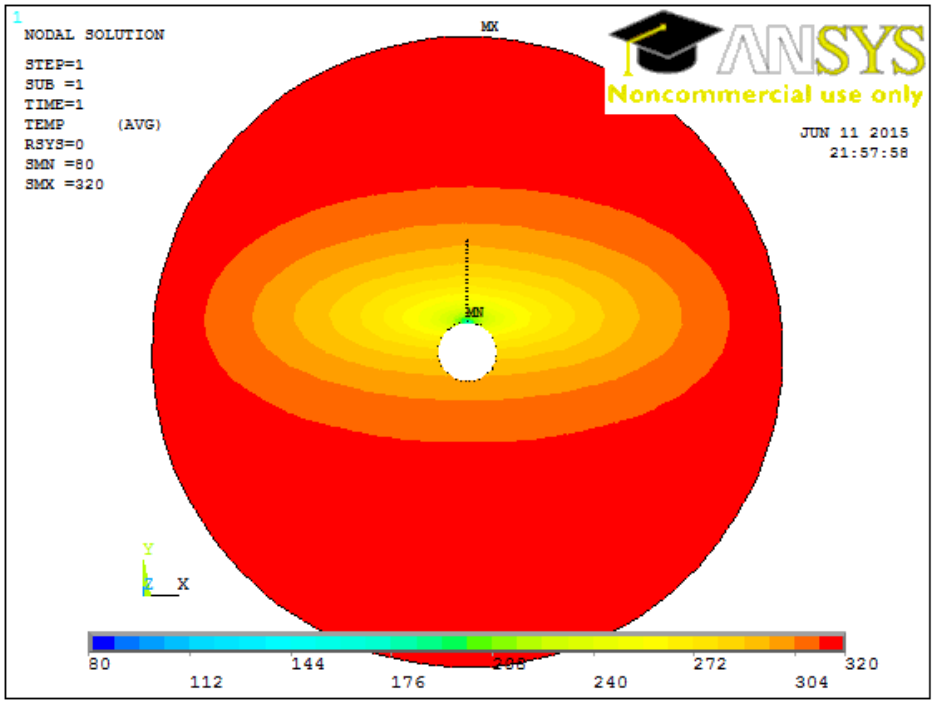

Figure 126: Isobaric contour plot

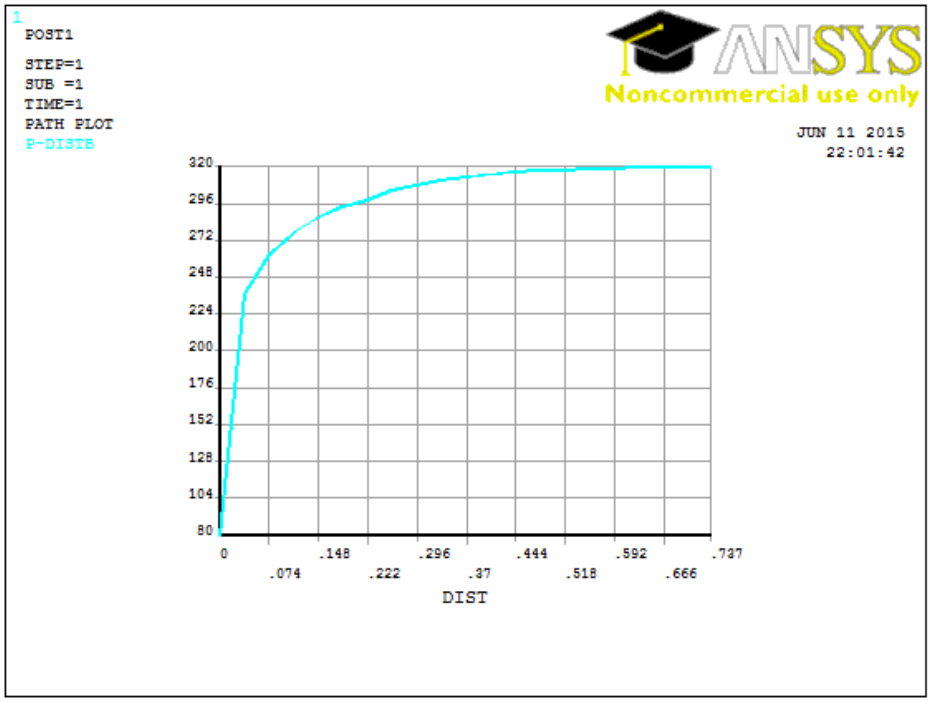

Figure 127: Pressure distribution from inner boundary to the tip of perforation tunnel

Well radius (inches)	4.3
Perforation length (inches)	3
Perforation phasing (degrees)	360

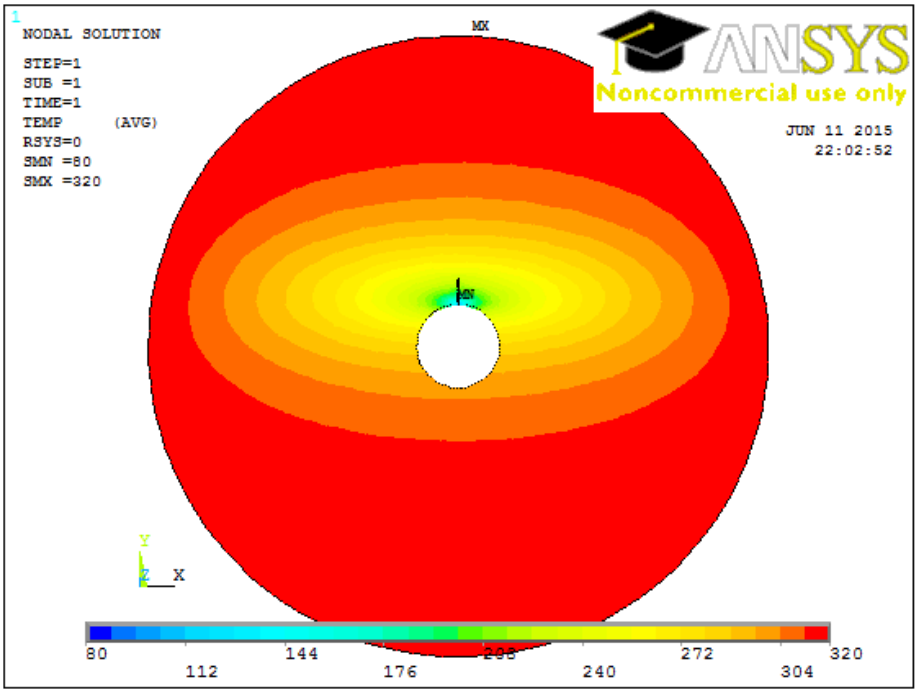

Figure 128: Isobaric contour plot

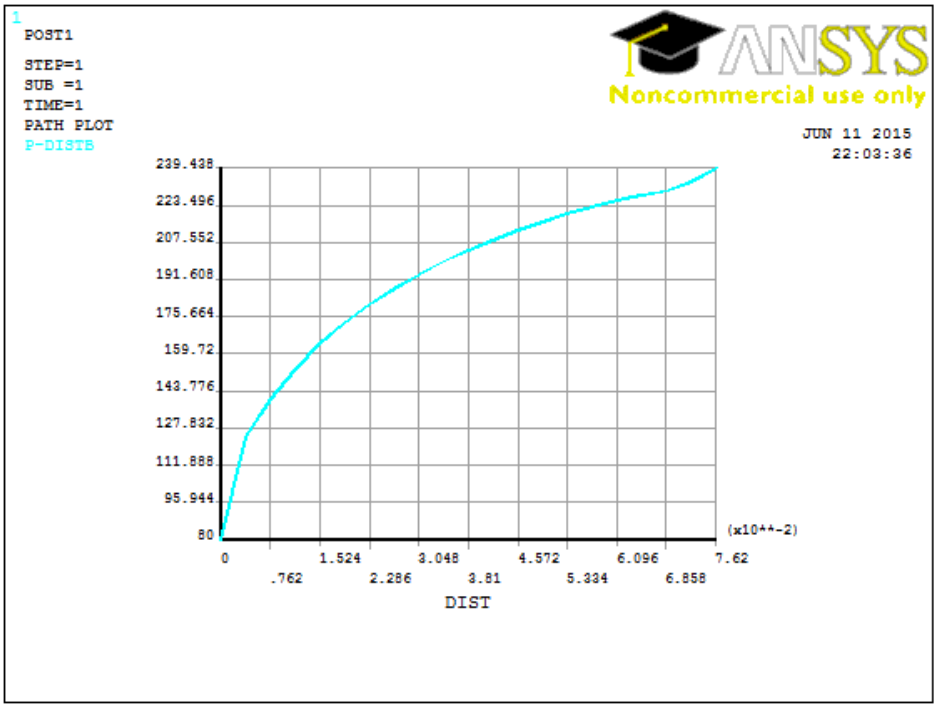

Figure 129: Pressure distribution from inner boundary to the tip of perforation tunnel

Well radius (inches)	4.3
Perforation length (inches)	6
Perforation phasing (degrees)	360

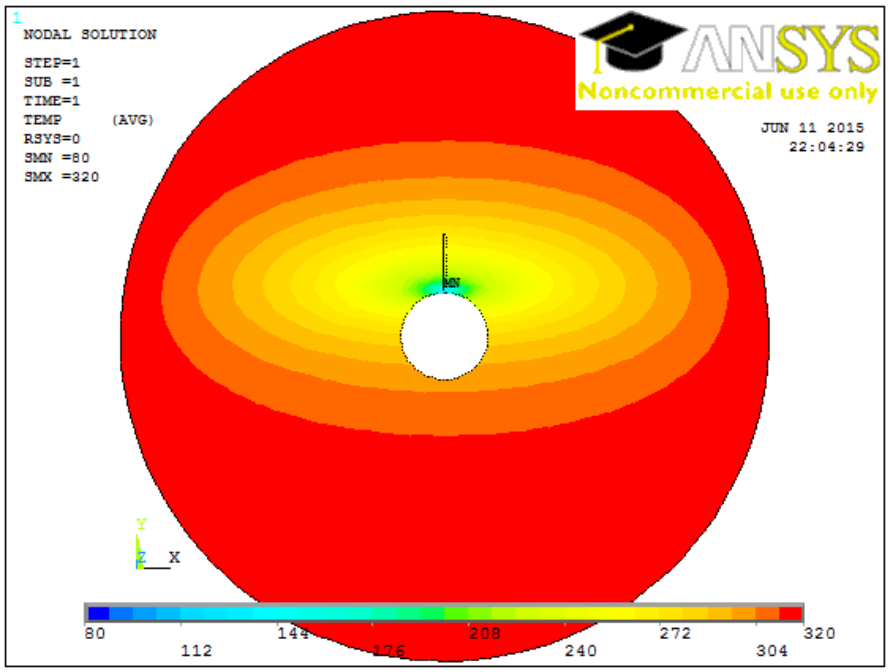

Figure 130: Isobaric contour plot

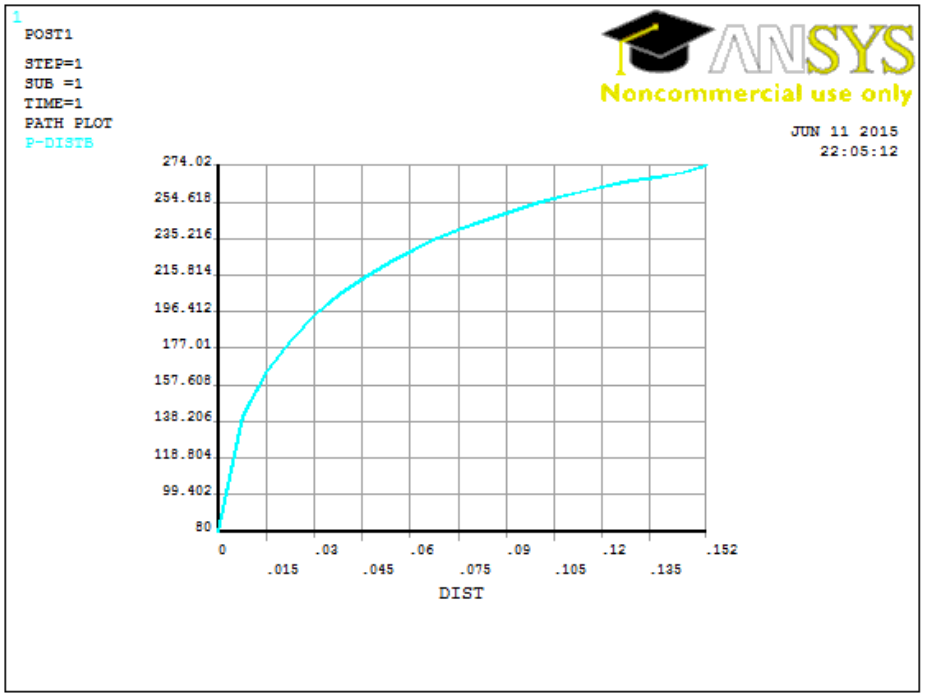

Figure 131: Pressure distribution from inner boundary to the tip of perforation tunnel

Well radius (inches)	4.3
Perforation length (inches)	9
Perforation phasing (degrees)	360

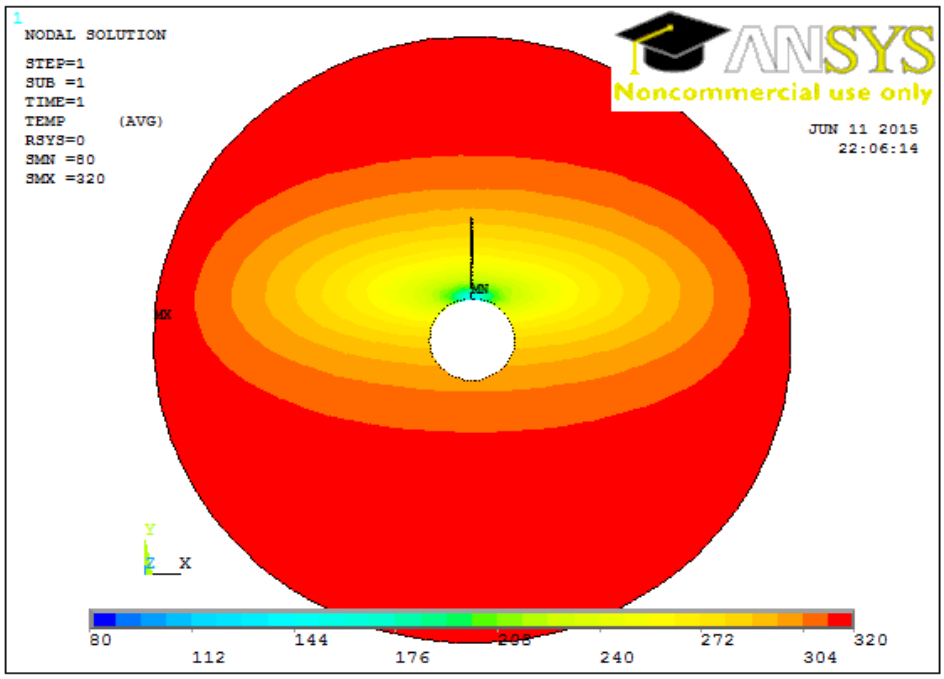

Figure 132: Isobaric contour plot

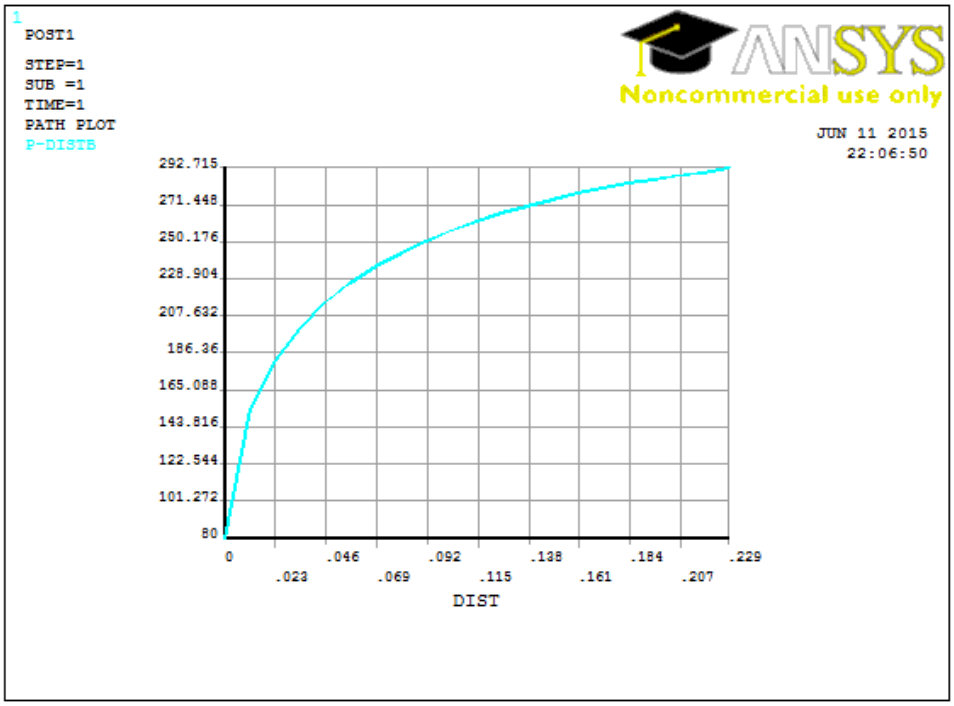

Figure 133: Pressure distribution from inner boundary to the tip of perforation tunnel

Well radius (inches)	2.4
Perforation length (inches)	3
Perforation phasing (degrees)	350/10

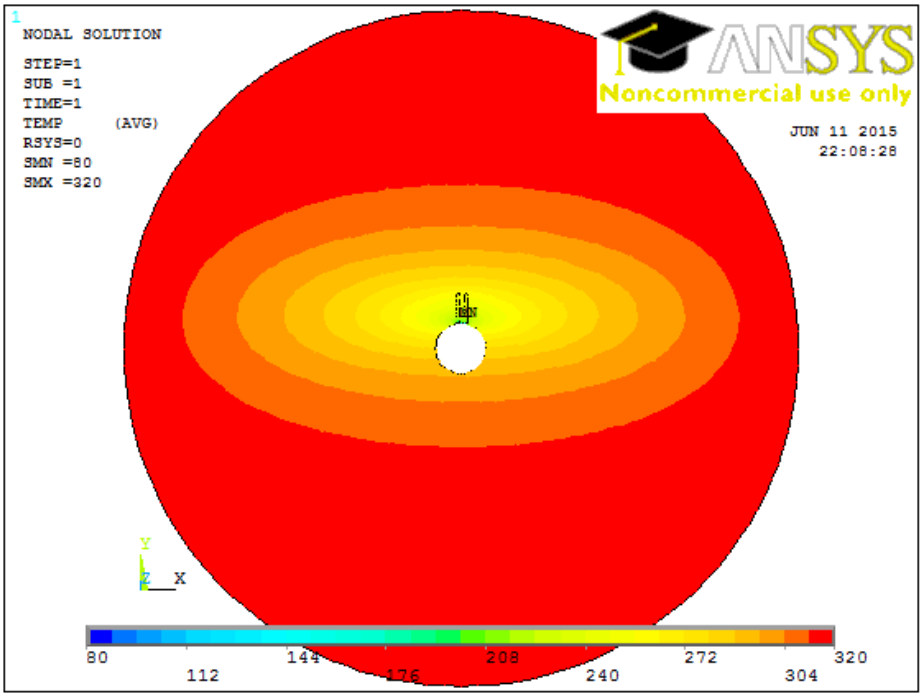

Figure 134: Isobaric contour plot

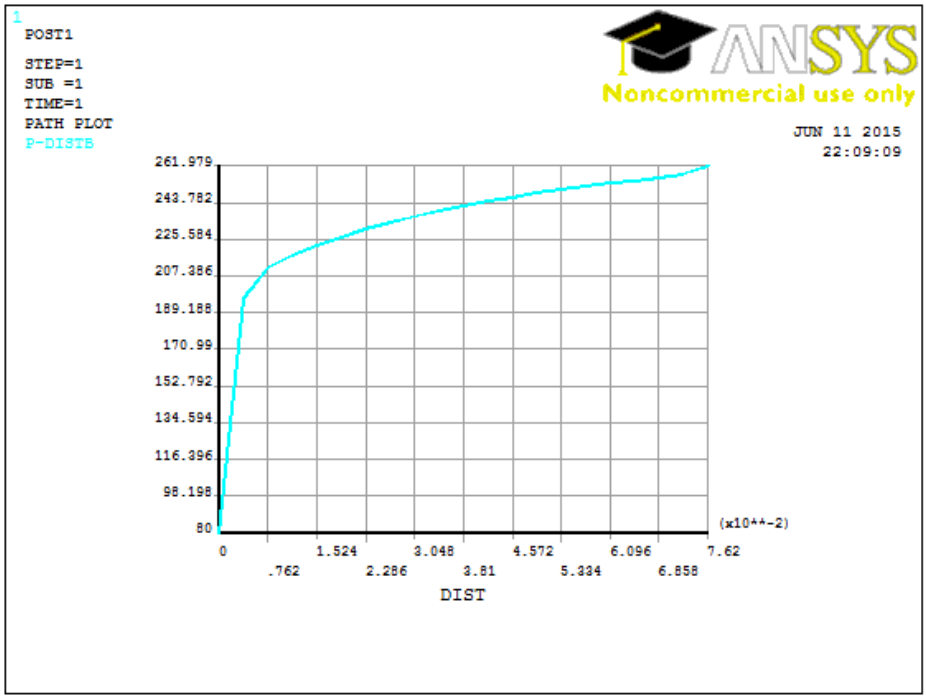

Figure 135: Pressure distribution from inner boundary to the tip of perforation tunnel

Well radius (inches)	2.4
Perforation length (inches)	6
Perforation phasing (degrees)	350/10

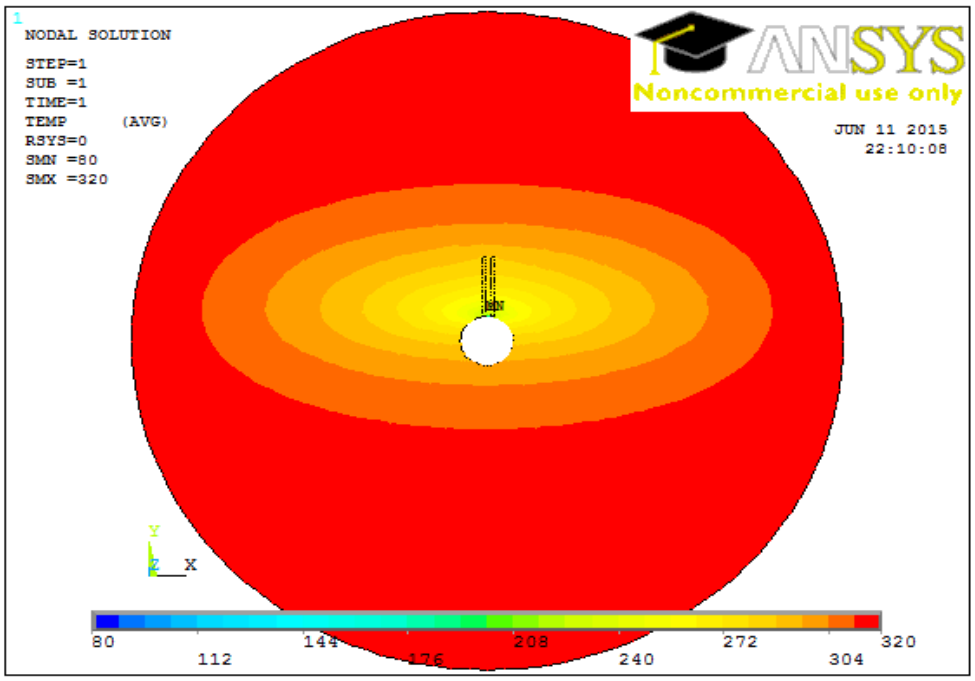

Figure 136: Isobaric contour plot

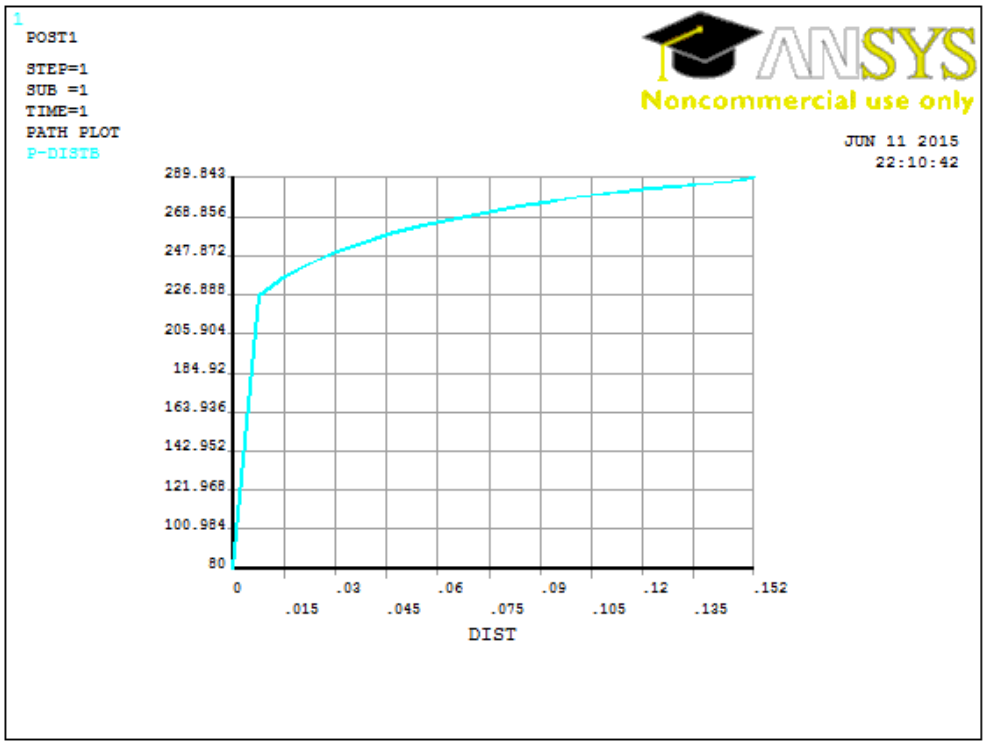

Figure 137: Pressure distribution from inner boundary to the tip of perforation tunnel

Well radius (inches)	2.4
Perforation length (inches)	9
Perforation phasing (degrees)	350/10

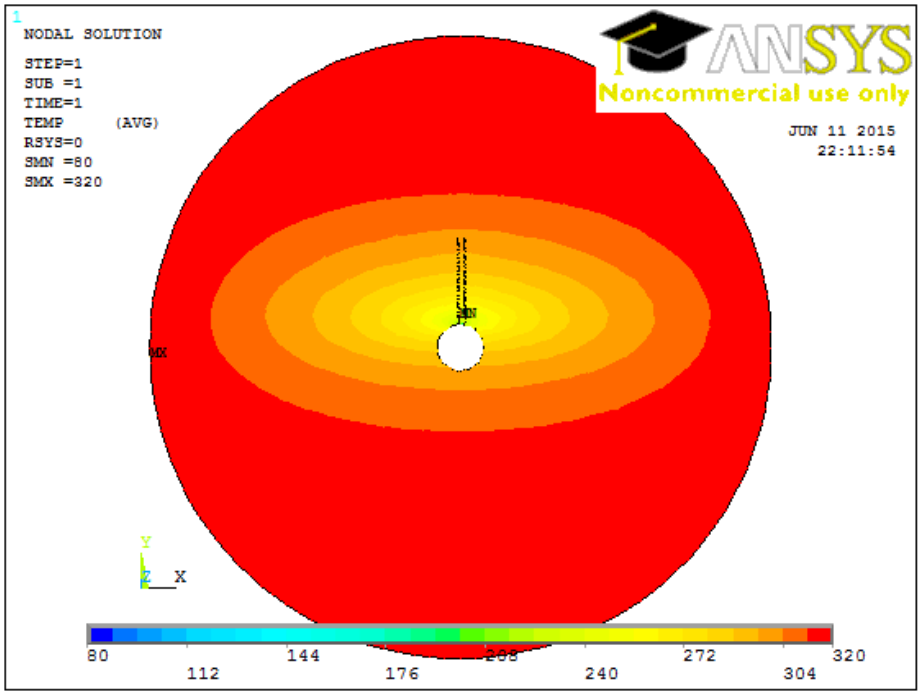

Figure 138: Isobaric contour plot

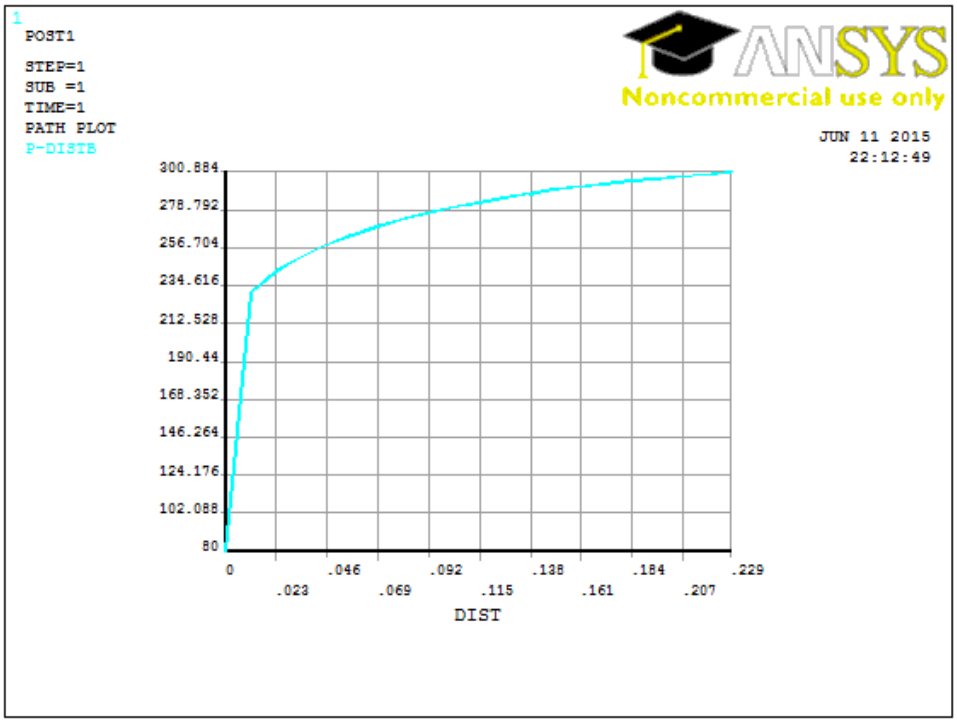

Figure 139: Pressure distribution from inner boundary to the tip of perforation tunnel

Well radius (inches)	3
Perforation length (inches)	3
Perforation phasing (degrees)	350/10

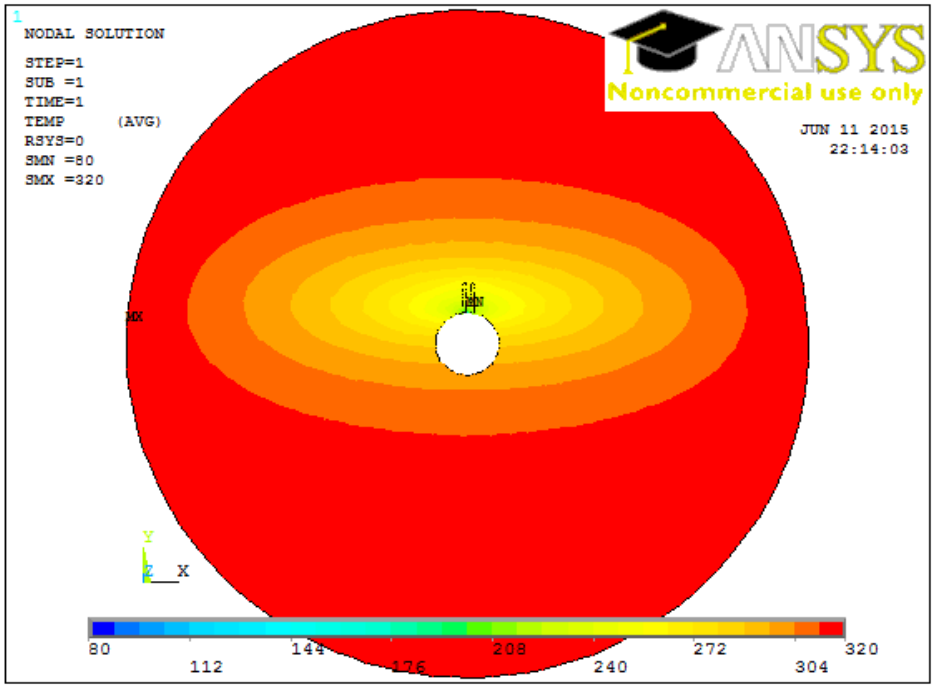

Figure 140: Isobaric contour plot

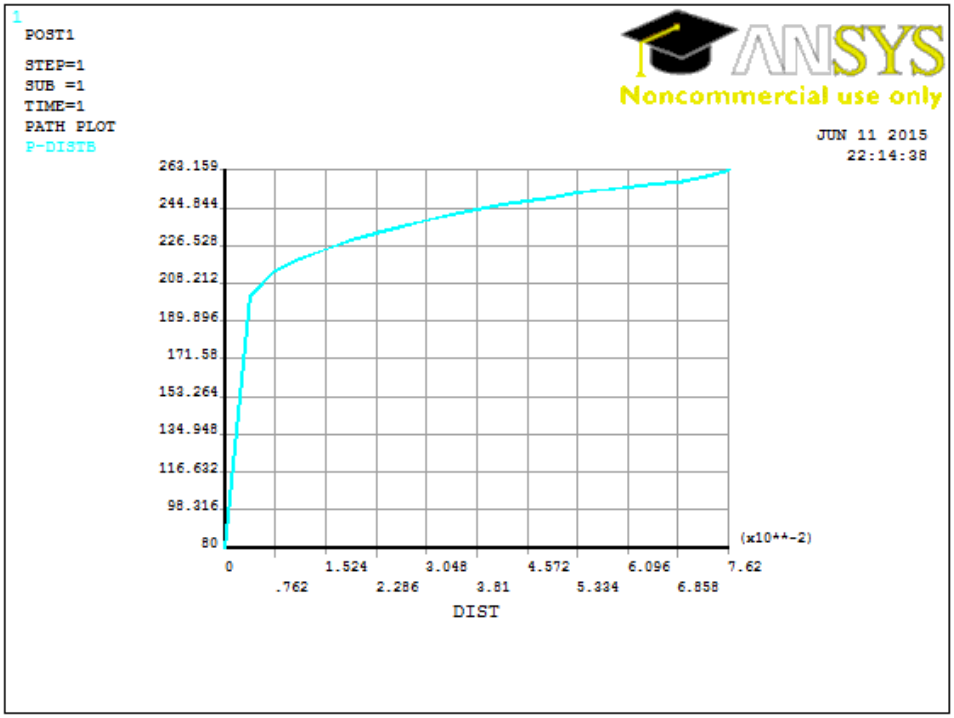

Figure 141: Pressure distribution from inner boundary to the tip of perforation tunnel

Well radius (inches)	3
Perforation length (inches)	6
Perforation phasing (degrees)	350/10

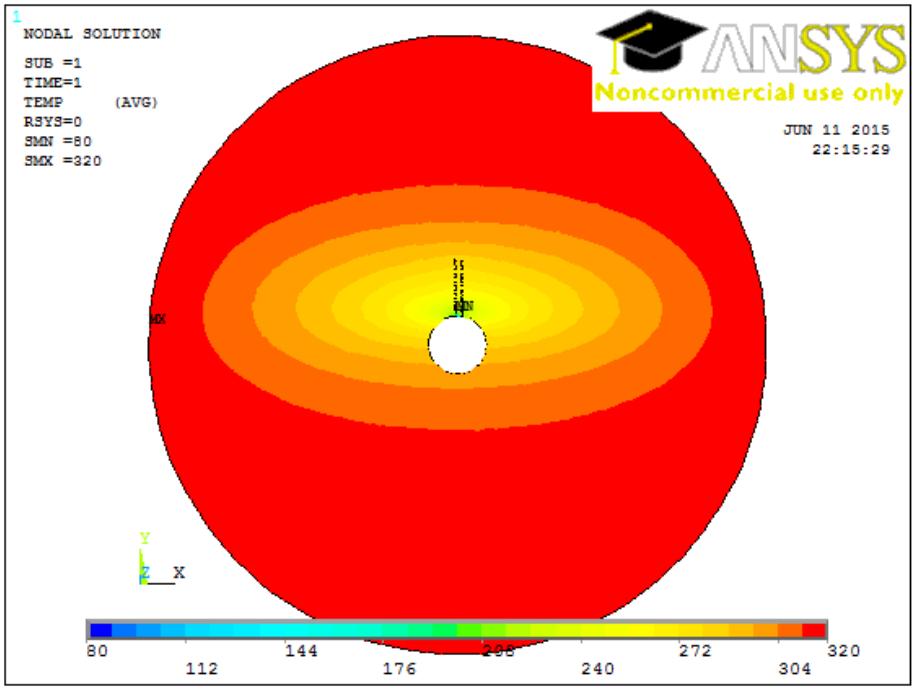

Figure 142: Isobaric contour plot

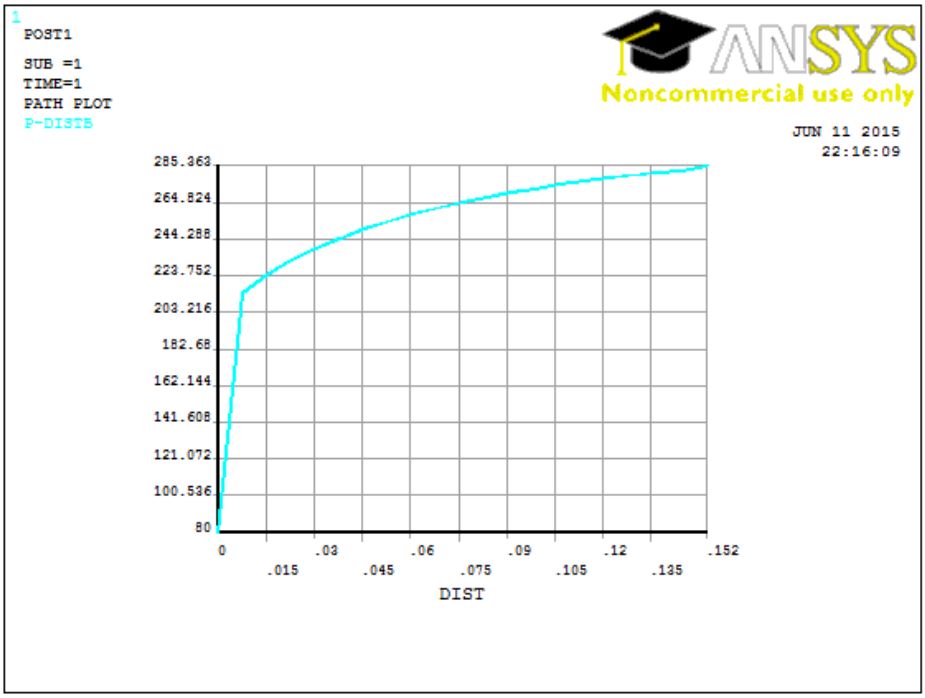

Figure 143: Pressure distribution from inner boundary to the tip of perforation tunnel

Well radius (inches)	3
Perforation length (inches)	9
Perforation phasing (degrees)	350/10

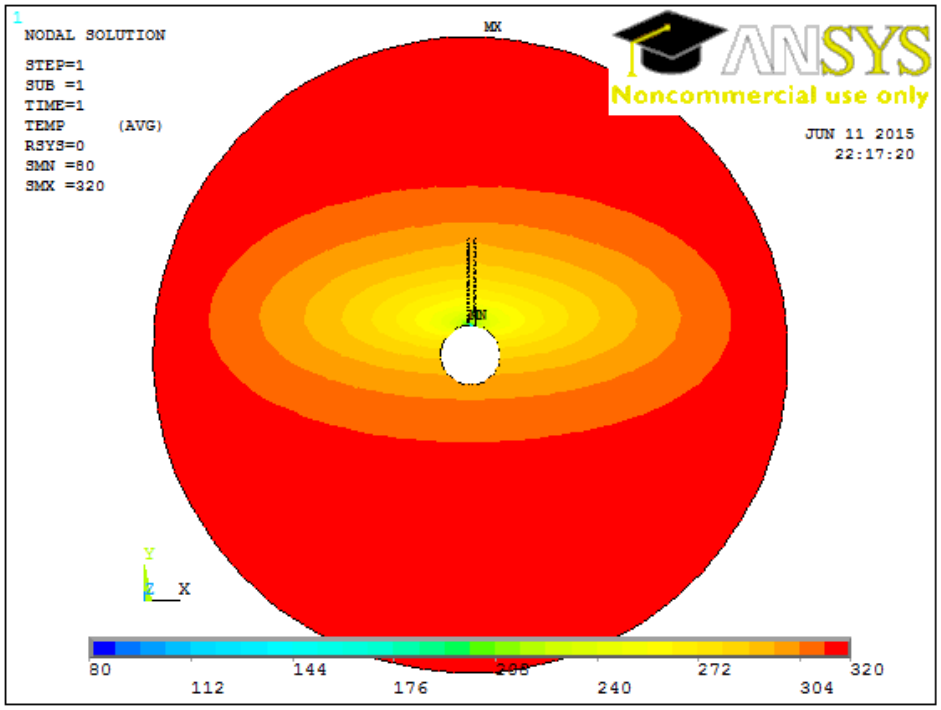

Figure 144: Isobaric contour plot

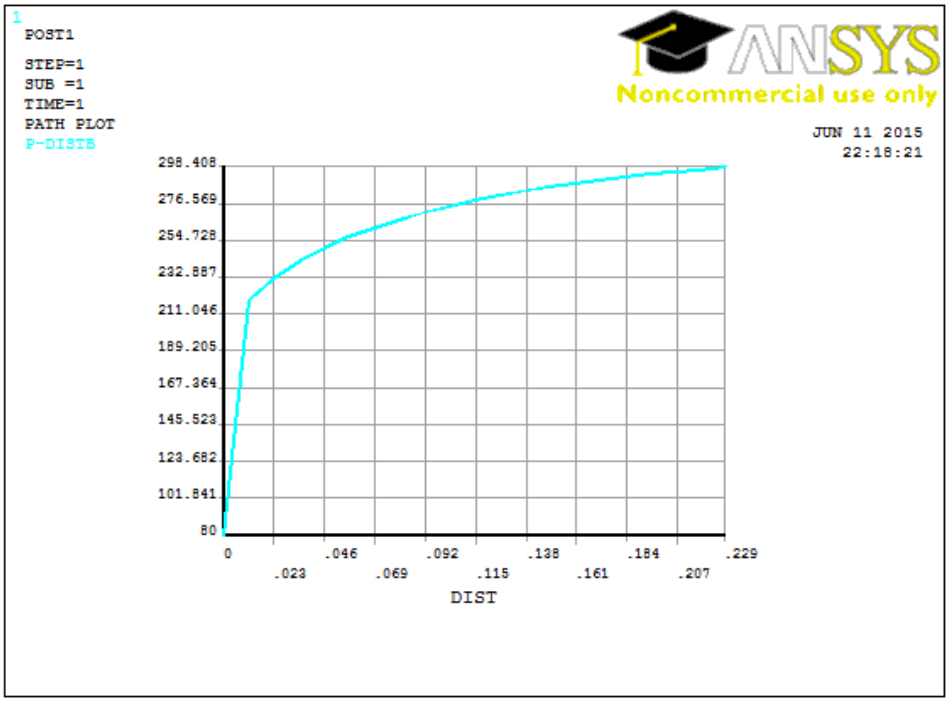

Figure 145: Pressure distribution from inner boundary to the tip of perforation tunnel

Well radius (inches)	4.3
Perforation length (inches)	3
Perforation phasing (degrees)	350/10

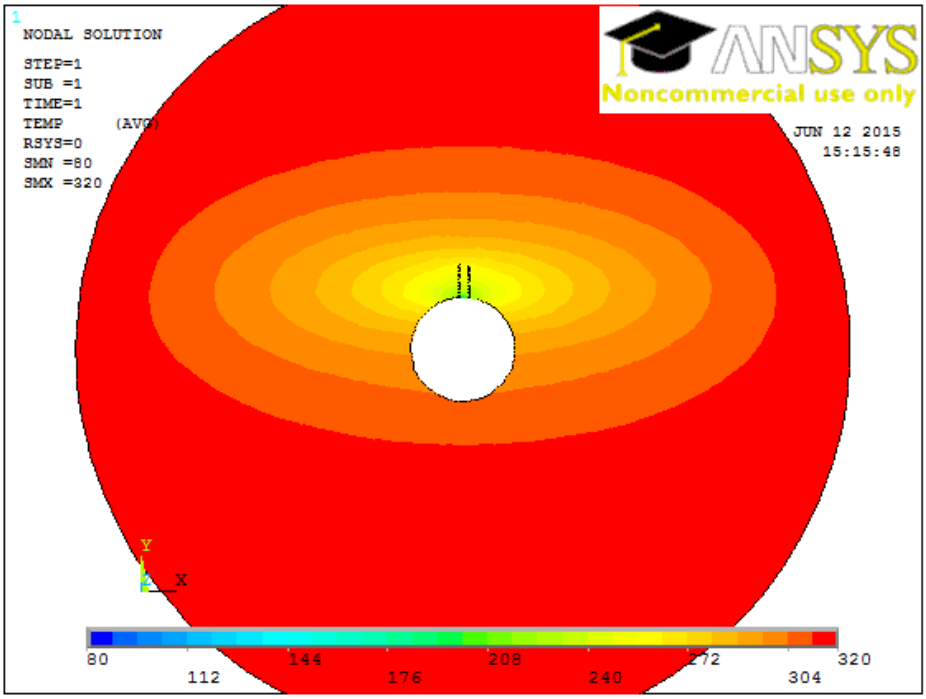

Figure 146: Isobaric contour plot

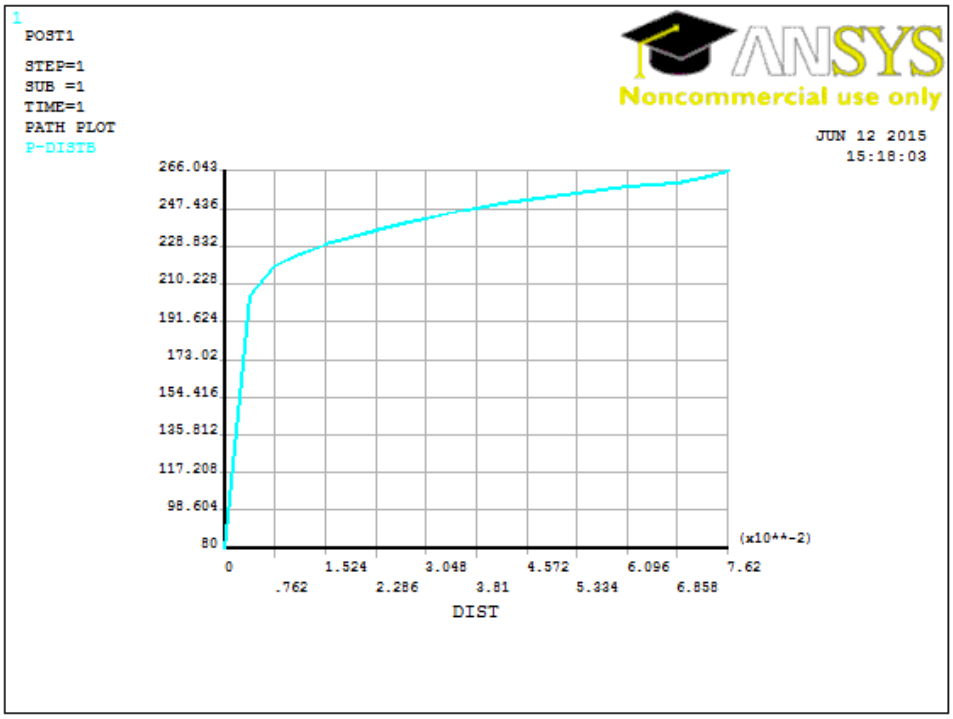

Figure 147: Pressure distribution from inner boundary to the tip of perforation tunnel

Well radius (inches)	4.3
Perforation length (inches)	6
Perforation phasing (degrees)	350/10

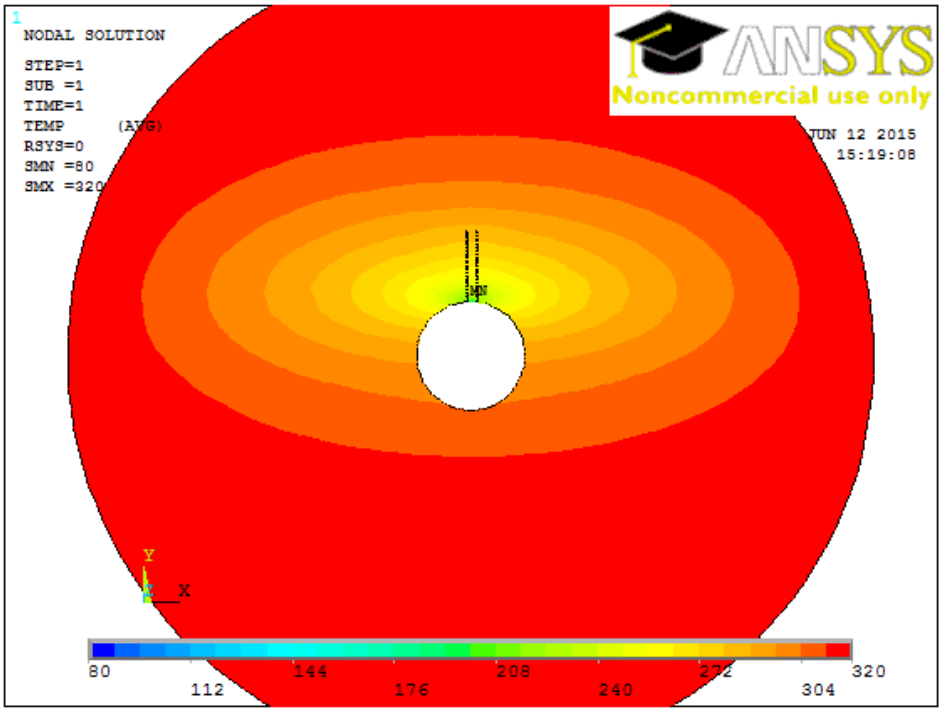

Figure 148: Isobaric contour plot

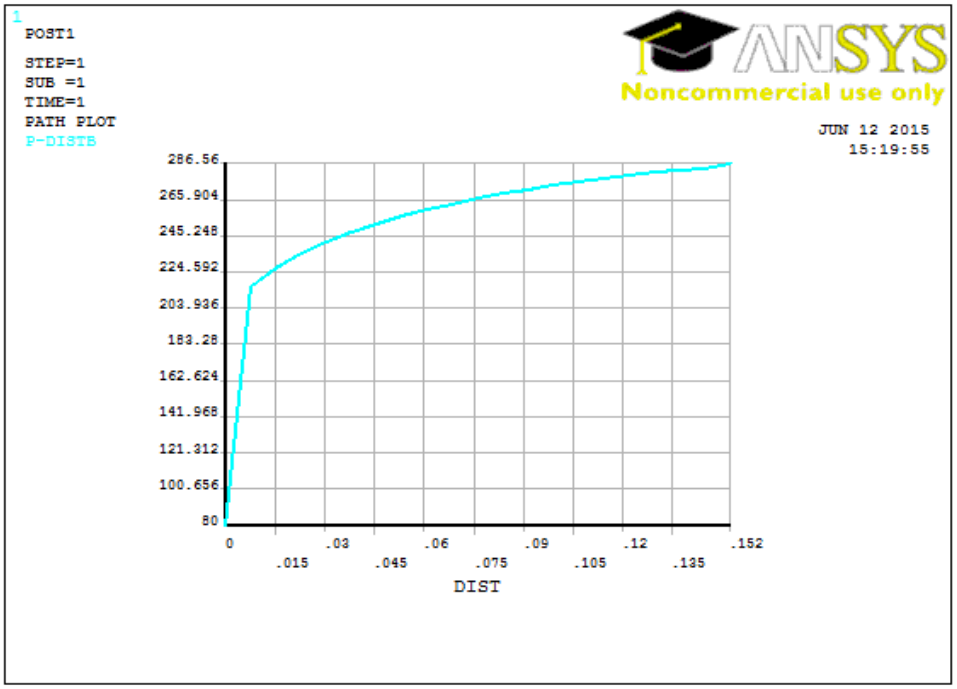

Figure 149: Pressure distribution from inner boundary to the tip of perforation tunnel

Well radius (inches)	4.3
Perforation length (inches)	9
Perforation phasing (degrees)	350/10

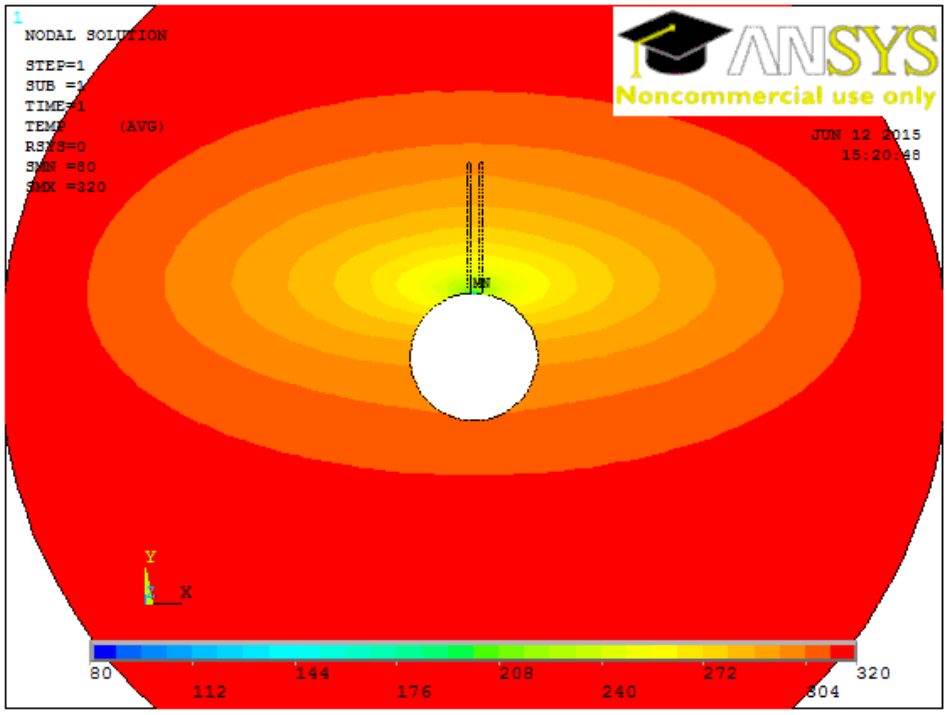

Figure 150: Isobaric contour plot

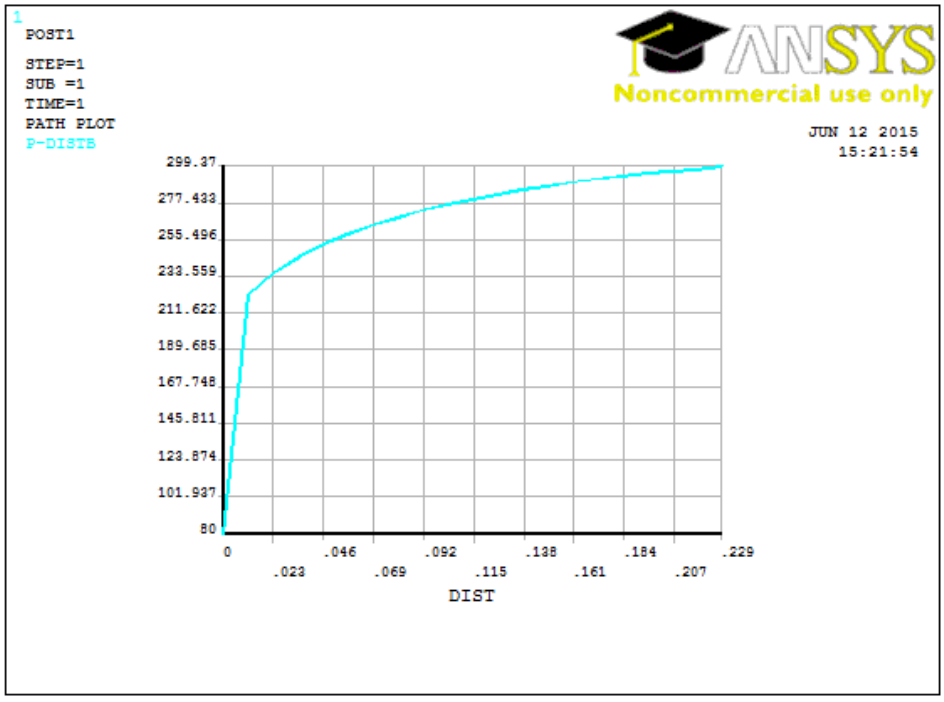

Figure 151: Pressure distribution from inner boundary to the tip of perforation tunnel